

**Due to the 2MB limit, I am unable to upload the original PDFs of the published papers,
and all of them can be viewed on my [homepage](#) or downloaded via this [link](#).**

PUBLICATIONS

GS-Planner: A Gaussian-Splatting-based Planning Framework for Active High-Fidelity Reconstruction

Rui Jin^{}, Yuman Gao^{*}, Haojian Lu, Fei Gao.*

Accepted by *IROS 2024*

- Proposed the first active 3D reconstruction system using 3DGS with online evaluation.
- Designed a feedback strategy of online model-consistent completeness and quality evaluation.
- Devised a planning framework for active reconstruction and safe navigation in the 3DGS map.

Unmanned Aerial Vehicle Mediated Drug Delivery for First Aid

Advanced Materials 2023

Sheng Tao^{}, Rui Jin^{*} (co-first author), et al, Fei Gao, Haojian Lu, Jichen Yu, Zhen Gu.*

(Frontispiece, IF: 29.4)

- Proposed a UAV-mediated first-aid system achieving autonomous administration of emergency medication without the involvement of bystander or the conscious patient.
- Designed a contact-triggered microneedle applicator capable of providing adequate force to insert microneedles upon contact with the skin, enabling fully autonomous first aid administration.

Canfly: A Can-sized Autonomous Mini Coaxial Helicopter

IROS 2023

Neng Pan, Rui Jin, Chao Xu, Fei Gao.

- Presented hardware design and control strategy for a mini coaxial helicopter, which occupies 62% less collision area compared to the state-of-the-art autonomous mini quadrotor.

Adaptive Tracking and Perching for Quadrotor in Dynamic Scenarios

T-RO 2024

Yuman Gao, Jialin Ji, Qianhao Wang, Rui Jin, Chao Xu, Fei Gao.

- UAV dynamic tracking and perching on 30 km/h high-speed SUV.
- UAV dynamic perching on high-speed 60-degree tilt plain.
- T-RO popular articles highest **Ranking No.5**, video with 35,000 views.

Other Publications

- Modeling and Force Control of a Variable-Length Continuum Robot with Variable Stiffness for Minimally Invasive Surgery, T-ASE 2024 (4th author)
- Soft Lightweight Small-Scale Parallel Robot With High-Precision Positioning, T-MECH 2023 (5th author)
- A Survey on Design, Actuation, Modeling, and Control of Continuum Robot, Cyborg and Bionic Systems 2022 (6th author, IF: 10.5)

GS-Planner: A Gaussian-Splatting-based Planning Framework for Active High-Fidelity Reconstruction

Rui Jin*, Yuman Gao*, Haojian Lu, and Fei Gao

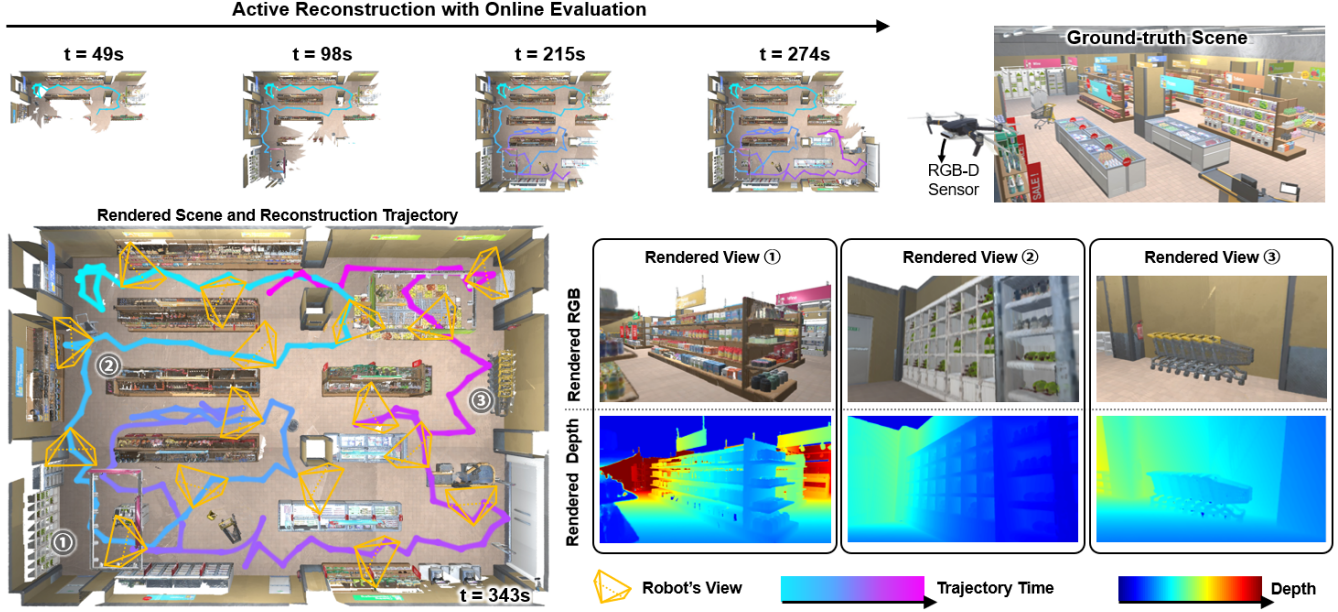


Fig. 1: The whole active reconstruction process in a simulated supermarket scene. We deployed our active high-fidelity reconstruction system on a simulated quadrotor with an RGB-D sensor. The colored curves illustrate the executed trajectories of the drones. We demonstrate the reconstruction result including the whole rendered scene and details rendered at three views.

Abstract— Active reconstruction technique enables robots to autonomously collect scene data for full coverage, relieving users from tedious and time-consuming data capturing process. However, designed based on unsuitable scene representations, existing methods show unrealistic reconstruction results or the inability of online quality evaluation. Due to the recent advancements in explicit radiance field technology, online active high-fidelity reconstruction has become achievable. In this paper, we propose GS-Planner, a planning framework for active high-fidelity reconstruction using 3D Gaussian Splatting. With improvement on 3DGS to recognize unobserved regions, we evaluate the reconstruction quality and completeness of 3DGS map online to guide the robot. Then we design a sampling-based active reconstruction strategy to explore the unobserved areas and improve the reconstruction geometric and textural quality. To establish a complete robot active reconstruction system, we choose quadrotor as the robotic platform for its high agility. Then we devise a safety constraint with 3DGS to generate executable trajectories for quadrotor navigation in the 3DGS map. To validate the effectiveness of our method, we conduct extensive experiments and ablation studies in highly realistic simulation scenes.

I. INTRODUCTION

Active high-fidelity 3D reconstruction involves robots creating an accurate, detailed, and realistic digital representation of an object or scene completely, efficiently, and safely. Maintaining intricate visual fidelity, this technique demonstrates significant practical value in scene inspection, virtual game development, and cultural heritage preservation.

The choice of an appropriate scene representation is the cornerstone of an active high-fidelity 3D reconstruction robotic system, with the following key requirements:

- **Precision and photorealism:** High-fidelity reconstruction requires the scene representation to accurately represent geometric and textural information, which enables a more realistic portrayal of the scene.
- **Real-time fusion:** New scene information is gathered step by step within the active reconstruction process. The scene representation should fuse the newly collected data in real time to guide the robot's reconstruction and provide information about occupied volumes for safe robot navigation.
- **Online evaluation:** To guide the robot in active reconstruction, the scene representation requires online evaluation of both reconstruction quality and completeness.

*Equal contribution. All authors are with the Institute of Cyber-Systems and Control, College of Control Science and Engineering, Zhejiang University, Hangzhou 310027, China, and also with the Huzhou Institute, Zhejiang University, Huzhou 313000, China. {fgaoaa}@zju.edu.cn.

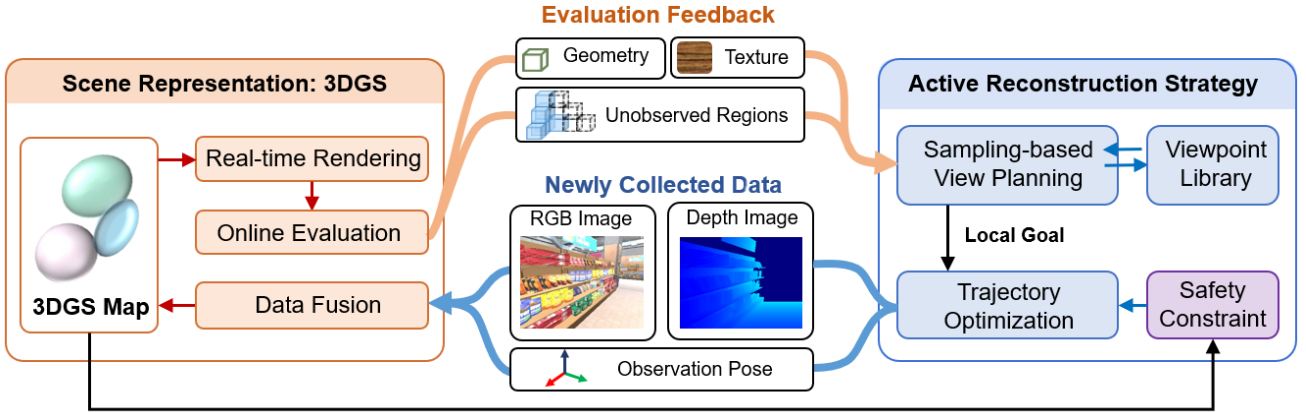


Fig. 2: An overview of our active high-fidelity reconstruction system. With 3DGS as scene representation, the unobserved regions, as well as the geometric and textural information of the built map can be feedback in real time for online reconstruction quality and completeness online evaluation. The proposed active reconstruction strategy guides the robot to collect new scene information to build a complete high-fidelity 3DGS map.

The quality assessment should include both geometric and textural aspects. The completeness evaluation demands the representation to identify observed and unobserved portions of the scene.

However, commonly used in traditional active reconstruction [1]–[3], grid map can only describe coarse structures and lack color and texture information. Mesh and surfel cloud fusion and optimization pose challenges due to their inherent complexities. Neural Radiance Field (NeRF) [4], which recently emerged as a high-fidelity scene representation, often requires extensive training times and substantial resources for rendering, making online evaluation difficult.

3D Gaussian Splatting (3DGS) [5], which recently emerged as a transformative technique in the explicit radiance field, fully meets the above requirements with specific advantages as follows: (a) High visual quality and precise geometry: 3DGS represents a scene with Gaussian blobs storing rich textural and explicit geometric information, ensuring high visual fidelity and precise geometry. More importantly, with learnable 3D Gaussians, 3DGS preserves properties of continuous volumetric radiance fields, which is essential for high-quality image synthesis. (b) Efficient fusion: Benefiting from explicit representation, 3DGS’s frustum culling strategy and adaptive Gaussian densification make it efficient to incrementally fuse the new observed data, showing comparable quality and superior efficiency surpassing neural-based methods. (c) Fast rendering: 3DGS’s highly parallel “splatting” rasterization, along with the avoidance of the computational overhead associated with rendering in empty space, enables fast frame rates and high-quality rendering for online evaluation.

Due to 3DGS’s appealing features, we propose a Gaussian-Splatting-based planning framework (GS-planner) to achieve active high-fidelity reconstruction with real-time quality and completeness evaluation to guide the robot’s reconstruction. Firstly, to evaluate the built 3DGS within the reconstruction process, we devise evaluation terms for both reconstruction completeness and quality. Existing 3DGS can only represent

occupied space, making it difficult to evaluate the completeness. To efficiently identify unobserved portions of the scene, we integrate the unknown voxels into the splatting-based rendering process. Secondly, we design a sampling-based active exploration strategy to guide the robot to explore the unobserved areas and improve the geometric and textural quality of the 3DGS map. Thirdly, to form a complete robotic active reconstruction system, we select quadrotor as the robotic platform for its high agility. Leveraging the differentiable nature and explicit representation properties of 3DGS, we devise a differentiable obstacle-avoidance cost with the 3DGS map. Furthermore, we form an autonomous navigation framework capable of generating collision-free and dynamic-feasible trajectories for quadrotors. Overall, based on the state-of-the-art dense 3DGS SLAM system SplaTam [6], we propose GS-Planner, a planning framework for active high-fidelity reconstruction with 3DGS as scene representation. In summary, the following are the contributions:

- 1) We propose the first active 3D reconstruction system using 3DGS with online evaluation.
- 2) We design evaluation metrics for reconstruction completeness and quality, applying them in a sampling-based autonomous reconstruction framework.
- 3) We devise a safety constraint with 3DGS and form a trajectory optimization framework in the 3DGS map.
- 4) We conduct extensive simulation experiments to validate the effectiveness of the proposed system.

II. RELATED WORKS

A. High-fidelity Reconstruction

To achieve high-fidelity reconstruction, several different scene representations have been employed, such as planes, meshes, and surfel clouds. Recently, Neural Radiance Field (NeRF) [4] has gained prominence in this field due to its exceptional capability of photorealistic rendering, which can be divided into three main types: MLP-based methods,

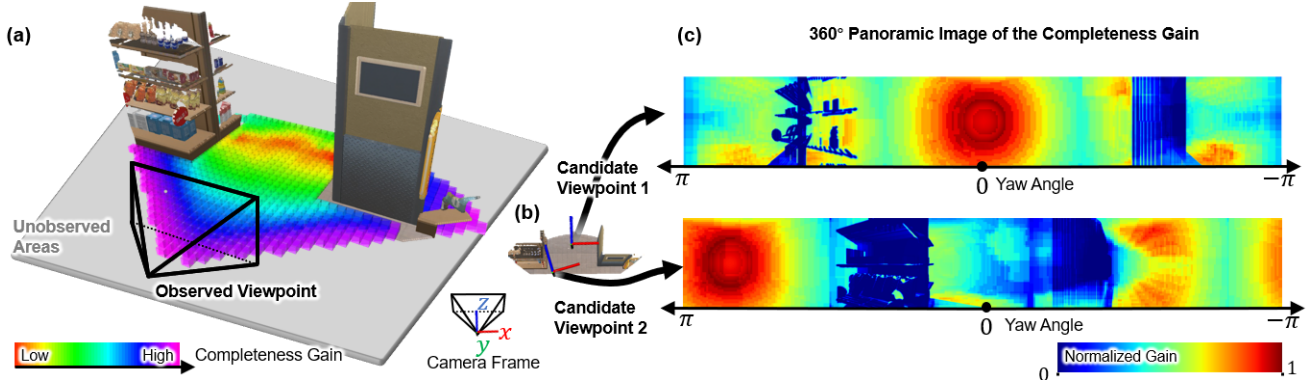


Fig. 3: An illustration of the completeness evaluation. (a). A partially reconstructed scene. Scene information has been collected only at the observed viewpoint. The colored grid illustrates the completeness gain from 360-degree summation at different positions at a height of $z = 1m$. (b). The location of two candidate viewpoints. The z-axis direction is aligned with the camera’s optical axis. (c). 360-degree panoramic image of the completeness gain of the candidate viewpoint 1 and 2. The generation of 360-degree gain facilitates the subsequent determination of the optimal viewpoint yaw direction.

hybrid representation methods, and explicit methods. MLP-based method [7] offers scalable and memory-efficient map representations but faces challenges with catastrophic forgetting in larger scenes. Hybrid representation [8, 9] methods combine the advantages of implicit MLPs and structure features, significantly enhancing the scene scalability and precision. As for the explicit method proposed in [10], it stores map features in voxel directly, without any MLPs, enabling faster optimization.

While NeRF excelled in photorealistic reconstruction [11], NeRF methods are computationally intensive [12]–[14]. NeRF often requires extensive training times and substantial resources for rendering, which contradicts the need to feed the model back into the active reconstruction decision loop in real time. Instead of representing maps with implicit features, 3DGS [5] enables real-time rendering of novel views by its pure explicit representation and the novel differential point-based splatting method. This technology has been applied in online dense SLAM with 3DGS as the scene representation and reconstructs the scene from RGB-D images [6, 15].

B. Active Reconstruction System

Active reconstruction systems put data acquisition in the decision loop, using the results for evaluation, and then guiding the robot for further data acquisition. Based on the representations of 3D models, these approaches can be categorized into voxel-based methods [1]–[3], surface-based approaches [16]–[18], and neural-based approaches [11].

Voxel-based methods [1, 3] aim to reconstruct the commonly used grid map, which is an axis-aligned and compact spatial representation. Surface-based approaches [16]–[18] model the environment with a set of surfaces. However, these methods only evaluate the reconstruction completeness but ignore color and texture information. There are also active reconstruction methods based on implicit neural representations. NeurAR [11] learns the neural uncertainty for view planning. However, limited by the high computation consumption of the implicit neural representation,

NeurAR takes about 50–120 seconds for model optimization and uncertainty evaluation between view steps, leading to frequent and prolonged halts in robot operation. 3DGS, as a newly emerged method, is well-suited for serving as a scene representation for active high-fidelity reconstruction. However, there is currently no active reconstruction robot system designed based on its excellent characteristics.

III. SYSTEM OVERVIEW

Active high-fidelity reconstruction requires a robot to visit a series of viewpoints to collect scene information and build a realistic digital representation. As shown in Fig. 2, the proposed active reconstruction system uses 3DGS as scene representation, and the robot can collect RGB-D images with the corresponding observation poses. Leveraging the efficient fusion and real-time rendering advantages of 3DGS, we conduct an online evaluation for possible future viewpoints. Such online evaluation feedback guides the active view planning module (Sec. IV) to generate a series of safe and high-information-gain viewpoints. To navigate the robot to the selected viewpoints, we further propose an autonomous navigation framework (Sec. V) with a safety constraint formulated with the 3DGS map.

IV. ACTIVE VIEW PLANNING WITH 3DGS MAP

In this section, we first introduce the 3DGS representation (Sec. IV-A). Then, a completeness evaluation method (Sec. IV-B) and a quality evaluation method (Sec. IV-C) are proposed to capture regions with poor coverage and quality respectively. In the following, we design a sampling-based active view planning algorithm to guide the robot to reconstruct unobserved regions and improve the quality of the built map (Sec. IV-D).

A. 3DGS Map Representation

We use the existing method SplatCam SLAM [6] for 3DGS real-time reconstruction. The scene is represented as a set of isotropic 3DGS. Each 3D GS is defined by center position

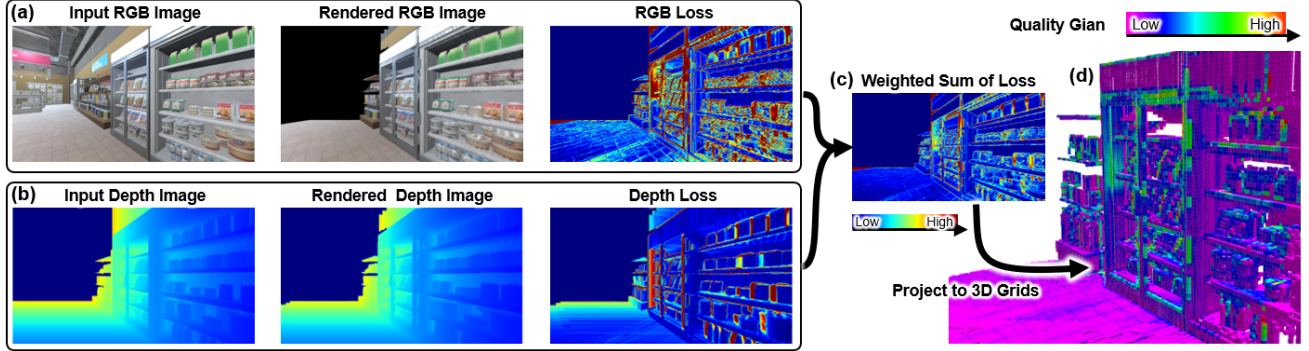


Fig. 4: An instance of the quality evaluation. (a). The generation of the RGB textural loss between the input RGB image and rendered RGB image. (b). The generation of the depth loss between the input depth image and rendered depth image. (c). The weighted sum of the RGB loss and depth loss. (d). We project the quality gain to the 3D grid in the world frame to store.

$\mu \in \mathbb{R}^3$, radius $r \in \mathbb{R}$, RGB color $c \in \mathbb{R}^3$, and opacity $o \in \mathbb{R}$. The opacity function α of a point $x \in \mathbb{R}^3$ computed from each 3DGS is described as:

$$\alpha(x, o) = o \exp\left(-\frac{|x - \mu|^2}{2r^2}\right). \quad (1)$$

In order to optimize the parameters of 3D Gaussians to represent the scene, we need to render them into images in a differentiable manner. The final rendered color can be formulated as the alpha-blending of N ordered points that overlap the pixel,

$$C_{pix} = \sum_{i=1}^N c_i \alpha_i \prod_{j=1}^{i-1} (1 - \alpha_j). \quad (2)$$

We render the depth in the same way

$$D_{pix} = \sum_{i=1}^N d_i \alpha_i \prod_{j=1}^{i-1} (1 - \alpha_j), \quad (3)$$

where d_i represents the depth of the i -th 3D Gaussian's center, which is equal to the z-coordinate of its center position in camera coordinate system.

B. Completeness Evaluation

To support full coverage of the scene, we introduce the completeness evaluation for candidate viewpoints. This evaluation requires to recognize unobserved space. However, the existing 3DGS only preserves information regarding the occupied volume. To address this limitation, we maintain a voxel map to represent unobserved volume, and integrate it into the splatting-based rendering. Then, we can efficiently calculate model-consistent pixel-level completeness gain within the 3DGS rendering process.

To be specific, given a collection of 3D Gaussians and a candidate viewpoint, first all Gaussians will be sorted by their depth. With the sorted Gaussians, depth image can be efficiently rendered by alpha-compositing the splatted 2D projection of each Gaussian in order in pixel space. In this rendering process, we can determine whether there exists an unobserved region between adjacent Gaussians

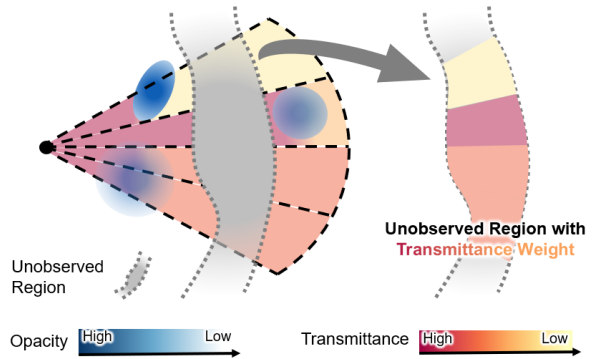


Fig. 5: A 2D illustration of the 3D completeness evaluation. Given a collection of 3D Gaussians and a candidate viewpoint, we can get unobserved regions within the splatting-based rendering. The unobserved regions are weighted by transmittance, which is equal to the accumulated Gaussians' opacity along the ray.

utilizing the maintained unobserved voxel. And the volume of the unobserved region corresponding to each pixel can be approximately calculated by the basic frustum volume formula. Furthermore, considering that Gaussians have different opacities, we evaluate the visibility of the unobserved volume by applying a transmittance weight, as shown in Fig. 5. Finally, we get the completeness information gain of each pixel as

$$V_{pix} = \sum_{i=1}^n V_i \prod_{j=1}^{m_i} (1 - \alpha_j), \quad (4)$$

where n is the number of unobserved volumes along the ray, m_i is the number of the related 3D Gaussians before the i -th unobserved volume V_i , $\prod_{j=1}^{m_i} (1 - \alpha_j)$ is the transmittance weight. For a certain unobserved volume V_i , as shown in Fig. 6, we approximate its volume as a frustum:

$$V_i = \frac{1}{3}(S_{in,i} + \sqrt{S_{in,i}S_{out,i}} + S_{out,i})(d_{out,i} - d_{in,i}), \quad (5)$$

where $d_{in,i}$ and $d_{out,i}$ respectively represent the depths of the entry and exit of the i -th unobserved volume. $S_{in,i}$ and $S_{out,i}$ represent the base areas of V_i , which are equal to the projected areas of the pixel at the entry plane of depth $d_{in,i}$

and the exit plane of depth $d_{out,i}$. $S = d^2/f^2$, where f is the camera focal length.

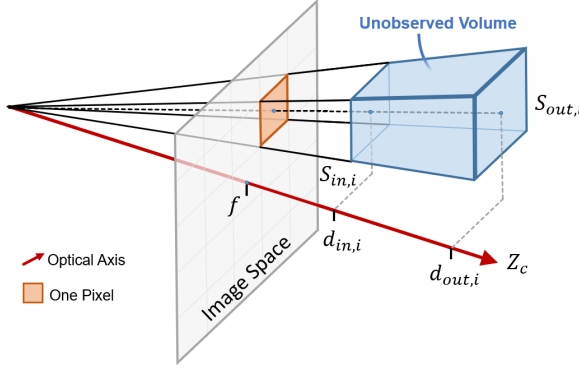


Fig. 6: A 3D illustration of the unobserved volume calculation.

Because we integrate the evaluation into the splatting-based rendering, this calculation process is parallelized and efficient. To illustrate the completeness evaluation intuitively, we give an instance shown in Fig. 3, demonstrating the guidance of completeness evaluation in viewpoint selection.

C. Quality Evaluation

Quality evaluation aims to identify reconstructed regions with poor texture and geometry accuracy. This evaluation includes two steps: loss caching and loss reprojection.

Loss caching: Leveraging the real-time rendering of 3DGS, it is straightforward to compute the disparity between the reconstructed model and the actual scene. As shown in Fig. 4, we project the loss L from the image space to the world space, and cache the loss into occupied voxels. Specifically, L is a weighted sum of L_1 loss both on the depth and the color renders:

$$L = L_1(D) + \lambda_C L_1(C), \quad (6)$$

where λ_C is the weight coefficient.

Loss reprojection: Given a candidate viewpoint, we reproject the loss cached in the occupied voxels to the image space by conducting 360-degree ray-tracing. The loss indicates the quality information gain of both texture and geometry:

According to Sec. IV-B and Sec. IV-C, we finally obtain an overall 360-degree information gain of a given viewpoint by calculating the weighted sum of completeness and quality. Then we use the sliding-window summation to find the optimal yaw angle of each viewpoint.

D. View Planning with a View Library

To enable a robot's full reconstruction of a scene in high quality, a series of reasonable viewpoints with position and yaw angle need to be generated for sequential navigation. We design a sampling-based view planning method with a view library to generate and cache viewpoints for evaluation. The whole view planning algorithm is listed as Alg. 1.

To be specific, we first acquire nearby cached viewpoints \mathbf{V}_{near} in the view library \mathbf{VL} , which stores unvisited viewpoints and their information gain (Line 1). Their information

Algorithm 1 Active View Planning with a View Library

```

Require: current pose  $\mathbf{p}$ , view library  $\mathbf{VL}$ ;
1:  $\mathbf{V}_{near}, \mathbf{G}_{near} \leftarrow$  subset of  $\mathbf{VL}$  nearby current pose  $\mathbf{p}$ ;
2: for  $v_i \in \mathbf{V}_{near}, g_i \in \mathbf{G}_{near}$  do
3:    $g_i = \text{UpdateGain}(v_i);$ 
4: end for
5:  $\mathbf{V}_c \leftarrow \text{RRTSample}(\mathbf{p}, \mathbf{V}_{near});$ 
6:  $\mathbf{G}_c \leftarrow \text{Evaluation}(\mathbf{V}_c);$ 
7: for  $v_i \in \mathbf{V}_c, g_i \in \mathbf{G}_c$  do
8:   if  $g_i < g_{lb}$  then
9:      $\mathbf{V}_c \leftarrow \mathbf{V}_c \setminus v_i;$ 
10:     $\mathbf{VL} \leftarrow \mathbf{VL} \setminus \{v_i, g_i\};$ 
11:    continue;
12:   end if
13:   if  $\text{Overlap}(v_i, \mathbf{V}_{near}) < \epsilon_{ol}$  and  $g_i > g_{thres}$  then
14:      $\mathbf{VL} = \mathbf{VL} \cup \{v_i, g_i\};$ 
15:   end if
16: end for
17: Result local goal:  $\mathbf{p}_{goal};$ 
18: if  $\mathbf{V}_c \neq \emptyset$  then
19:    $\mathbf{p}_{goal} = \text{BestBranchNode}(\mathbf{V}_c);$ 
20: else
21:    $\mathbf{p}_{goal} = \text{Select from } \mathbf{VL};$ 
22: end if
23: Return  $\mathbf{p}_{goal};$ 

```

gains are updated with new sensor data (Line 2-4). We use the expansion part of RRT* to sample potential future viewpoints \mathbf{V}_c (Line 5). The sampled viewpoints that are too close to obstacles will be deleted. And the optimal yaw angle of each viewpoint is determined by the above introduced sliding window method. \mathbf{V}_{near} are added and connected to the expanded trees in the sampling process. By real-time rendering at each viewpoint in \mathbf{V}_c via 3DGS, we calculate its information gain efficiently (Line 6). The viewpoints whose gain below threshold g_{lb} will be removed (Line 8-12). And high-information-gain viewpoints that are novel enough from others in \mathbf{VL} will be cached (Line 13-15). The node on the best branch will be selected as the next local goal (Line 19). Moreover, if there are no valid nearby candidates, the local goal will be selected from \mathbf{VL} (Line 21). When the \mathbf{VL} becomes empty, the reconstruction process is accomplished.

V. TRAJECTORY OPTIMIZATION IN 3DGS MAP

3DGs's explicit representation and precise geometry make safe robot navigation with the 3DGS map possible. Leveraging the differentiable nature of 3D Gaussian, we devise a safety constraint with the 3DGS map, and integrate it into a quadrotor trajectory optimization framework.

A. Safety Constraint with 3DGS

In 3DGS, Gaussians are defined with opacity as presented in Sec. IV-A. The opacity measures the probability of light being obstructed while passing through an object. We assume

the probability of terminating a light ray provides a strong indication of the probability of terminating a mass particle. Thus, for a robot pose p and a certain Gaussian with opacity o , we formulate a chance constraint to ensure safety:

$$\alpha(p, o) < c_{thr}, \quad (7)$$

where $\alpha(\cdot)$ presents the opacity function defined in Eq. 1, and c_{thr} presents the threshold of collision probability. c_{thr} is equal to the value of $\alpha(\cdot)$ at a distance of $(3r + R_{robot})$ (3σ rule) from its mean μ when the opacity $o = 1$:

$$c_{thr} = \exp\left(-\frac{3r + R_{robot}}{2r^2}\right), \quad (8)$$

where R_{robot} is the geometric bounding sphere radius. Intuitively, it means that we hope every point on the trajectory is at a distance greater than a safety radius R_s from the Gaussian mean point. R_s is weighted by o of the Gaussian, and equals to $(3r + R_{robot})$ when $o = 1$.

For the follow-up trajectory optimization, we provide the corresponding collision-avoidance cost for each point p on the trajectory as

$$\mathcal{J}_c(p) = \sum_{i=0}^k f(\alpha_i(p, o_i) - c_{thr}), \quad (9)$$

where $f(x) = \max(x, 0)^3$, and k is the number of nearby Gaussian elements in the 3DGS map. The collision-avoidance cost applied on the points on the trajectory during optimization with different opacity Gaussian is shown in Fig. 7. This differentiable cost is friendly for the follow-up trajectory optimization with analytical gradient written as

$$\frac{\partial \mathcal{J}_c(p)}{\partial p} = \sum_{i=0}^k 3(\alpha_i(p) - c_{thr})^2 o_i \exp\left(-\frac{|p - \mu_i|^2}{2r_i^2}\right) \left(\frac{\mu_i - p}{2r_i^2}\right). \quad (10)$$

B. Trajectory Optimization Formulation

Aimed to generate full-state collision-free and dynamic-feasible trajectories for quadrotors, we use MINCO [19]

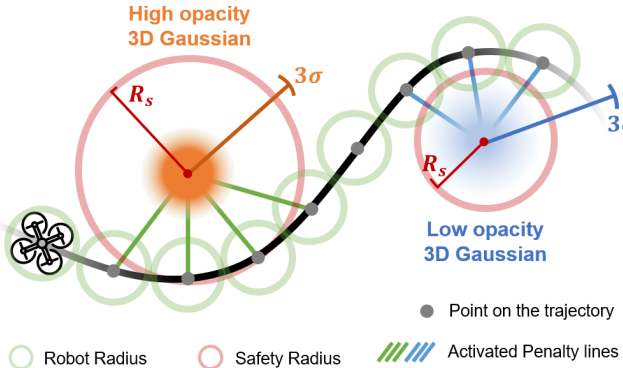


Fig. 7: The collision-avoidance cost applied on the trajectory with different opacity Gaussian. Each point on the trajectory is hoped to be at a distance greater than a safety radius R_s from the mean point of the Gaussian. R_s is weighted by the opacity o of different Gaussians.

as trajectory representation and optimize spatial-temporal trajectories in a reduced space with differential-flat outputs $\mathbf{z} = [\mathbf{p}^T, \phi]^T \in \mathbb{R}^3 \times \text{SO}(2)$, where ϕ is the Euler-yaw angle and position $\mathbf{p} = [p_x, p_y, p_z]^T$. And we further define the flat outputs and their derivatives $\mathbf{z}^{[s-1]} \in \mathbb{R}^{ms}$ as $\mathbf{z}^{[s-1]} := (\mathbf{z}^T, \dot{\mathbf{z}}^T, \dots, \mathbf{z}^{(s-1)}^T)^T$. To generate a trajectory $\mathbf{z}(t) : [0, T] \mapsto \mathbb{R}^m$, we formulate the trajectory optimization problem as

$$\min_{\mathbf{z}, \mathbf{T}} \mathcal{J}_E = \int_0^T \|\mathbf{z}^{(s)}(t)\|^2 dt + \rho T, \quad (11a)$$

$$\text{s.t. } \mathbf{z}^{[s-1]}(0) = \bar{\mathbf{z}}_s, \mathbf{z}^{[s-1]}(T) = \bar{\mathbf{z}}_e, \quad (11b)$$

$$\|\mathbf{p}^{(1)}(t)\| \leq v_{max}, \forall t \in [0, T], \quad (11c)$$

$$\|\mathbf{p}^{(2)}(t)\| \leq a_{max}, \forall t \in [0, T], \quad (11d)$$

$$\|\phi^{(1)}(t)\| \leq \phi_{max}, \forall t \in [0, T], \quad (11e)$$

$$\alpha_i(\mathbf{p}, o_i) < c_{thr}, \forall i \in \{1, \dots, k\}, \forall t \in [0, T], \quad (11f)$$

where Eq. 11a trade off the smoothness and aggressiveness, and ρ is the time regularization parameter. Here we adopt $s = 3$ for jerk integral minimization. Eq. 11b is the boundary conditions at start and end time. $\bar{\mathbf{z}}_s$ and $\bar{\mathbf{z}}_e$ are the initial and end state, respectively. Eq. 11c, Eq. 11d and Eq. 11e are the dynamic feasibility constraints, where v_{max} , a_{max} and ϕ_{max} are the velocity, acceleration and yaw rate limits. Eq. 11f is the safe constraint defined in Eq. 7. $\alpha_i(\cdot)$ is the opacity function of the i -th Gaussian element with opacity o_i .

This problem can be transformed into an unconstrained optimization problem [19] written as

$$\min_{\mathbf{z}, \mathbf{T}} \mathcal{J}_E + \int_0^T \mathcal{J}_G dt, \quad (12)$$

where \mathcal{J}_G is the penalty function corresponding to the inequality constraints Eq. 11c, Eq. 11d, and Eq. 11f. And \mathcal{J}_G includes \mathcal{J}_c defined in Eq. 10. With analytical gradients, the problem is then efficiently solved by the L-BFGS [20].

VI. EXPERIMENTS

A. Implementation Details

We run our active reconstruction system on a desktop PC with a 2.90GHz Intel i7-10700 CPU and an NVIDIA RTX 3090 GPU. And an additional laptop PC with a 2.50 GHz AMD Ryzen 9 7945HX and an NVIDIA GeForce RTX 4080 Laptop GPU is utilized to execute the high-fidelity simulation developed with Unity. The two devices are connected via a wired network connection. In Unity, the quadrotor equipped with an RGB-D sensor will provide real-time RGB-D images with a resolution of 640×480 and a perceptual range from $0.5m$ to $3m$. We add a uniform distribution noise of $2cm$ to the depth and assume the corresponding camera poses of the images are known.

The 3DGS mapping module builds upon SplaTam [6] by incorporating a real-time data streaming format. For view planning, we evaluate 10 viewpoints at each iteration and select the branch with the optimal viewpoint as the seed for the next iteration. For trajectory optimization, the robot

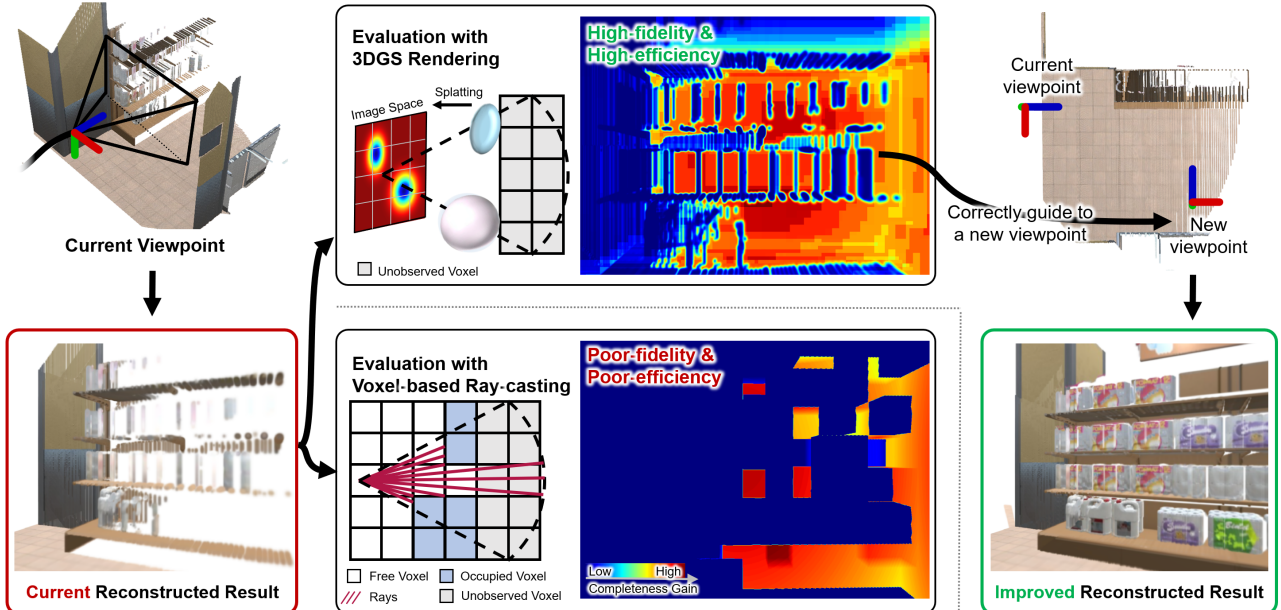


Fig. 8: Qualitative comparison of the completeness evaluation between using 3DGS rendering and using voxel-based ray-casting. When the robot arrives at the current viewpoint, due to its oblique view angle, the observation of items on the left front shelf is incomplete. The evaluation with 3DGS rendering is high-fidelity and high-efficiency, while the evaluation with voxel-based ray-casting is coarse and time-consuming. The fine completeness evaluation can correctly guide the robot to collect new information for improvement.

radius is fixed at 0.5m. And the safety constraint is computed by considering the 3DGS near the initial trajectory within the duration of [0s, 1s], selected using the Axis-aligned Bounding Box (AABB) method. The maximum velocity limit is 1.0m/s, the maximum acceleration limit is 2.0m/s², and the maximum yaw rate limit is $\pi rad/s$.

B. Simulation Result and Analysis

To validate our proposed method, we build a high-fidelity simulation environment via Unity engine. As shown in Fig. 1, this 22.0m × 14.0m × 3.2m supermarket scene contains a variety of items with rich texture information. We present the whole reconstruction process and the trajectory of the quadrotor. The quadrotor takes 343 seconds to complete the whole reconstruction. The reconstructed details are also demonstrated through rendered RGB and depth images. We can see from the reconstruction results that the reconstruction of the entire scene is complete and high-fidelity, retaining rich texture and structural information, and exhibiting a strong sense of realism.

C. Comparision and Ablation Study

To validate the effectiveness of the proposed reconstruction evaluations, we compare our method with traditional ones and conduct an ablation study.

1) *Completeness Evaluation*: Given a viewpoint, traditional methods for computing information gain typically rely on voxel-based raycasting [1]–[3]. This involves maintaining a grid map that represents observed and unobserved areas, and performing raycasting at candidate viewpoints to measure the volume of unobserved areas. However, this method is limited by the voxel resolution for occupied

TABLE I: Completeness Evaluation Methods Comparison

Voxel Resolution (m)	Scenario	Time (ms)	
		Voxel-based Raycast	Ours
0.1	Sparse	347.32	1.86
	Dense	342.10	2.11
0.15	Sparse	226.29	1.83
	Dense	230.21	2.33
0.2	Sparse	183.36	1.71
	Dense	176.01	2.31

and unobserved region representation, and its computational complexity is affected by discrete sampling steps. In contrast, we integrate the completeness evaluation calculation into the splatting process. Leveraging efficient Gaussian sorting and precise description of occupied geometry, we achieve high-fidelity high-efficiency completeness gain calculation. Fig. 8 shows an instance of the completeness gain calculation by different methods. Tab. I compares the computation speeds under various voxel resolutions, highlighting the notably higher efficiency of our 3DGS-based method. In the experiments, the raycasting step for the voxel-based method is half of the voxel resolution.

2) *Quality Evaluation*: To validate the impact of quality gain, we designed ablation experiments to calculate the information gain of candidate viewpoints with and without quality gain. And we further compute their corresponding optimal yaw angles. As the result shown in Fig. 9, the quality gain correctly guides the generation of the information gain and the optimal yaw angle. With quality consideration, our active reconstruction system can improve the regions of the built scene with poor geometry and texture.

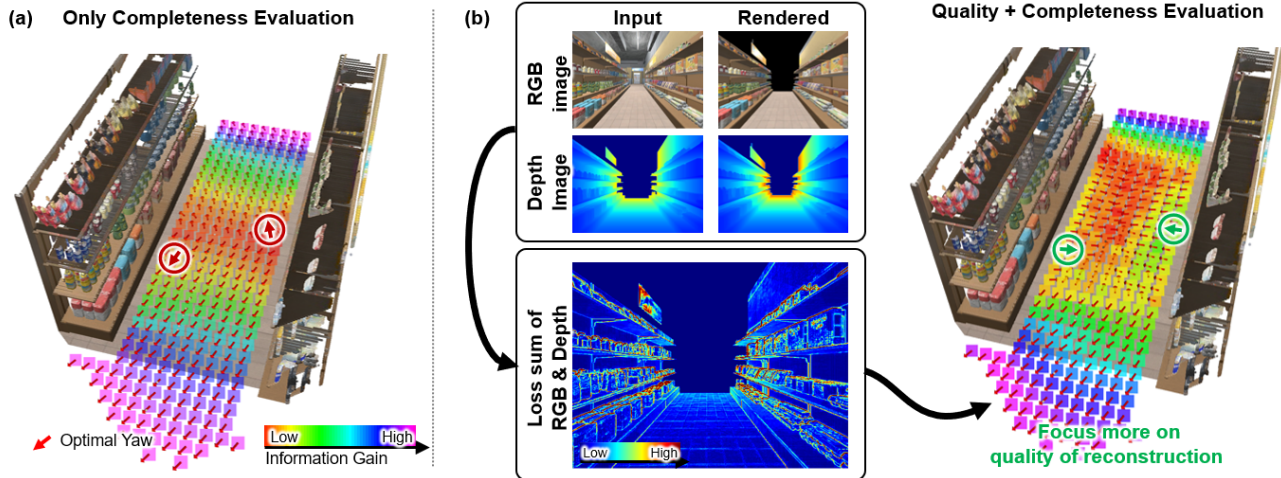


Fig. 9: Ablation of the quality gain. (a). The information gain regarding only completeness at the height of $z = 1$ m. Optimal yaw angles corresponding to the candidate viewpoints point towards unobserved areas. (b). Considering both quality and completeness in the information gain. It can be observed that, for viewpoints around two shelves, the quality gain tends to encourage further observation of shelves that can still improve the reconstruction quality.

VII. CONCLUSION AND FUTURE WORK

In this paper, we adopt the recently emerged 3DGS technique to achieve an active high-fidelity reconstruction system. To online evaluate the reconstruction result as reconstruction strategy feedback, we respectively design completeness and quality evaluation methods with 3DGS. Then we propose a sampling-based active view planning method to generate a series of optimal viewpoints. For robot navigation in 3DGS map, we design a differentiable chance constraint to ensure safety, and form a quadrotor trajectory optimization framework. For future work, we are going to deploy our system on real robotic platforms and try to reduce the GPU memory consumption of 3DGS and improve its efficiency.

REFERENCES

- [1] S. Isler, R. Sabzevari, J. Delmerico, and D. Scaramuzza, “An information gain formulation for active volumetric 3d reconstruction,” in *IEEE International Conference on Robotics and Automation (ICRA)*, 2016, pp. 3477–3484.
- [2] T. Dang, F. Mascarich, S. Khattak, C. Papachristos, and K. Alexis, “Graph-based path planning for autonomous robotic exploration in subterranean environments,” in *IEEE/RSJ International Conference on Intelligent Robots and Systems (IROS)*, 2019, pp. 3105–3112.
- [3] B. Zhou, Y. Zhang, X. Chen, and S. Shen, “Fuel: Fast uav exploration using incremental frontier structure and hierarchical planning,” *IEEE Robotics and Automation Letters*, vol. 6, no. 2, pp. 779–786, 2021.
- [4] B. Mildenhall, P. P. Srinivasan, M. Tancik, J. T. Barron, R. Ramamoorthi, and R. Ng, “Nerf: Representing scenes as neural radiance fields for view synthesis,” *Communications of the ACM*, vol. 65, no. 1, pp. 99–106, 2021.
- [5] B. Kerbl, G. Kopanas, T. Leimkühler, and G. Drettakis, “3d gaussian splatting for real-time radiance field rendering,” *ACM Transactions on Graphics*, vol. 42, no. 4, 2023.
- [6] N. Keetha, J. Karhade, K. M. Jatavallabhula, G. Yang, S. Scherer, D. Ramanan, and J. Luiten, “Splatam: Splat, track & map 3d gaussians for dense rgb-d slam,” *arXiv preprint arXiv:2312.02126*, 2023.
- [7] E. Sucar, S. Liu, J. Ortiz, and A. J. Davison, “imap: Implicit mapping and positioning in real-time,” in *Proceedings of the IEEE/CVF International Conference on Computer Vision*, 2021, pp. 6229–6238.
- [8] Z. Zhu, S. Peng, V. Larsson, W. Xu, H. Bao, Z. Cui, M. R. Oswald, and M. Pollefeys, “Nice-slam: Neural implicit scalable encoding for slam,” in *Proceedings of the IEEE/CVF Conference on Computer Vision and Pattern Recognition*, 2022, pp. 12 786–12 796.
- [9] C. Jiang, H. Zhang, P. Liu, Z. Yu, H. Cheng, B. Zhou, and S. Shen, “H2-mapping: Real-time dense mapping using hierarchical hybrid representation,” *IEEE Robotics and Automation Letters*, vol. 8, no. 10, pp. 6787–6794, 2023.
- [10] S. Fridovich-Keil, A. Yu, M. Tancik, Q. Chen, B. Recht, and A. Kanazawa, “Plenoxels: Radiance fields without neural networks,” in *Proceedings of the IEEE/CVF Conference on Computer Vision and Pattern Recognition*, 2022, pp. 5501–5510.
- [11] Y. Ran, J. Zeng, S. He, J. Chen, L. Li, Y. Chen, G. Lee, and Q. Ye, “Neurar: Neural uncertainty for autonomous 3d reconstruction with implicit neural representations,” *IEEE Robotics and Automation Letters*, vol. 8, no. 2, pp. 1125–1132, 2023.
- [12] T. Takikawa, J. Litalien, K. Yin, K. Kreis, C. Loop, D. Nowrouzezahrai, A. Jacobson, M. McGuire, and S. Fidler, “Neural geometric level of detail: Real-time rendering with implicit 3d shapes,” in *Proceedings of the IEEE/CVF Conference on Computer Vision and Pattern Recognition*, 2021, pp. 11 358–11 367.
- [13] C. Reiser, S. Peng, Y. Liao, and A. Geiger, “Kilonerf: Speeding up neural radiance fields with thousands of tiny mlps,” in *Proceedings of the IEEE/CVF International Conference on Computer Vision*, 2021, pp. 14 335–14 345.
- [14] T. Müller, A. Evans, C. Schied, and A. Keller, “Instant neural graphics primitives with a multiresolution hash encoding,” *ACM Transactions on Graphics*, vol. 41, no. 4, pp. 1–15, 2022.
- [15] C. Yan, D. Qu, D. Wang, D. Xu, Z. Wang, B. Zhao, and X. Li, “Gsslam: Dense visual slam with 3d gaussian splatting,” *arXiv preprint arXiv:2311.11700*, 2023.
- [16] R. Huang, D. Zou, R. Vaughan, and P. Tan, “Active image-based modeling with a toy drone,” in *IEEE International Conference on Robotics and Automation (ICRA)*, 2018, pp. 6124–6131.
- [17] L. Schmid, M. Pantic, R. Khanna, L. Ott, R. Siegwart, and J. Nieto, “An efficient sampling-based method for online informative path planning in unknown environments,” *IEEE Robotics and Automation Letters*, vol. 5, no. 2, pp. 1500–1507, 2020.
- [18] Y. Gao, Y. Wang, X. Zhong, T. Yang, M. Wang, Z. Xu, Y. Wang, Y. Lin, C. Xu, and F. Gao, “Meeting-merging-mission: A multi-robot coordinate framework for large-scale communication-limited exploration,” in *IEEE/RSJ International Conference on Intelligent Robots and Systems (IROS)*, 2022, pp. 13 700–13 707.
- [19] Z. Wang, X. Zhou, C. Xu, and F. Gao, “Geometrically constrained trajectory optimization for multicopters,” *IEEE Transactions on Robotics*, vol. 38, no. 5, pp. 3259–3278, 2022.
- [20] D. C. Liu and J. Nocedal, “On the limited memory bfgs method for large scale optimization,” *Mathematical programming*, vol. 45, no. 1-3, pp. 503–528, 1989.

Unmanned Aerial Vehicle Mediated Drug Delivery for First Aid

Tao Sheng, Rui Jin, Changwei Yang, Ke Qiu, Mingyang Wang, Jiaqi Shi, Jingyu Zhang, Yuman Gao, Qing Wu, Xin Zhou, Hao Wang, Juan Zhang, Qin Fang, Neng Pan, Yanan Xue, Yue Wang, Rong Xiong, Fei Gao, Yuqi Zhang, Haojian Lu,* Jicheng Yu,* and Zhen Gu*

Acknowledgements Page 9

T.S. and R.J. contributed equally to this work.

Timely administration of key medications toward patients with sudden diseases is critical to saving lives. However, slow transport of first-aid therapeutics and the potential absence of trained people for drug usage can lead to severe injuries or even death. Herein, an unmanned aerial vehicle (UAV)-mediated first-aid system for targeted delivery (*uFAST*) is developed. It allows unattended administration of emergency therapeutics-loaded transdermal microneedle (MN) patches toward patients to relieve symptoms by a contact-triggered microneedle applicator (CTMA). The implementability and safety of the *uFAST* for first aid is demonstrated in a severe hypoglycemic pig model by automatically delivering a glucagon patch with immediate and bioresponsive dual release modes. This platform technique may facilitate the development of UAV-mediated first-aid treatments for other sudden diseases.

1. Introduction

First aid is crucial for patients with sudden illnesses, such as myocardial infarction, severe hypoglycemia, and stroke.^[1] In these situations, the patients may face an extreme risk of death if treatment is not provided promptly; thus, time is life in these cases.^[2] However, there are still a large number of deaths worldwide caused by a lack of timely resuscitation, which results from the shortage of emergency equipment around the patient, the inability of the patient to call for help, or traffic congestion.^[3] Moreover, drug-based first aid is mainly dependent on intravenous or subcutaneous injection of

T. Sheng, C. Yang, J. Shi, Q. Wu, H. Wang, J. Zhang, Y. Zhang, J. Yu, Z. Gu
Key Laboratory of Advanced Drug Delivery Systems of Zhejiang Province
College of Pharmaceutical Sciences

Zhejiang University
Hangzhou 310058, China
E-mail: yujicheng@zju.edu.cn; guzhen@zju.edu.cn

R. Jin, K. Qiu, M. Wang, J. Zhang, Y. Gao, X. Zhou, Q. Fang, N. Pan,
Y. Xue, Y. Wang, R. Xiong, F. Gao, H. Lu
State Key Laboratory of Industrial Control and Technology
Zhejiang University
Hangzhou 310027, China
E-mail: luhaojian@zju.edu.cn

R. Jin, K. Qiu, M. Wang, J. Zhang, Y. Gao, X. Zhou, Q. Fang, N. Pan,
Y. Xue, Y. Wang, R. Xiong, F. Gao, H. Lu
Institute of Cyber-Systems and Control
the Department of Control Science and Engineering
Zhejiang University
Hangzhou 310027, China

R. Jin, M. Wang, Y. Gao, X. Zhou, N. Pan, F. Gao
Huzhou Institute of Zhejiang University
Huzhou 313000, China

Y. Zhang
Department of Burns and Wound Center
Second Affiliated Hospital
School of Medicine
Zhejiang University
Hangzhou 310009, China

H. Lu
Stomatology Hospital, School of Stomatology
Zhejiang University School of Medicine
Clinical Reach Center for Oral Disease of Zhejiang Province
Key Laboratory of Oral Biomedical Research of Zhejiang Province
Cancer Center of Zhejiang University
Hangzhou 310006, China

J. Yu, Z. Gu
Liangzhu Laboratory
Zhejiang University Medical Center
Hangzhou 311121, China

J. Yu, Z. Gu
Department of General Surgery
Sir Run Run Shaw Hospital
School of Medicine
Zhejiang University
Hangzhou 310016, China

J. Yu, Z. Gu
Jinhua Institute of Zhejiang University
Jinhua 321299, China

Z. Gu
MOE Key Laboratory of Macromolecular Synthesis
and Functionalization
Department of Polymer Science
Zhejiang University
Hangzhou 310027, China

 The ORCID identification number(s) for the author(s) of this article
can be found under <https://doi.org/10.1002/adma.202208648>.

DOI: 10.1002/adma.202208648

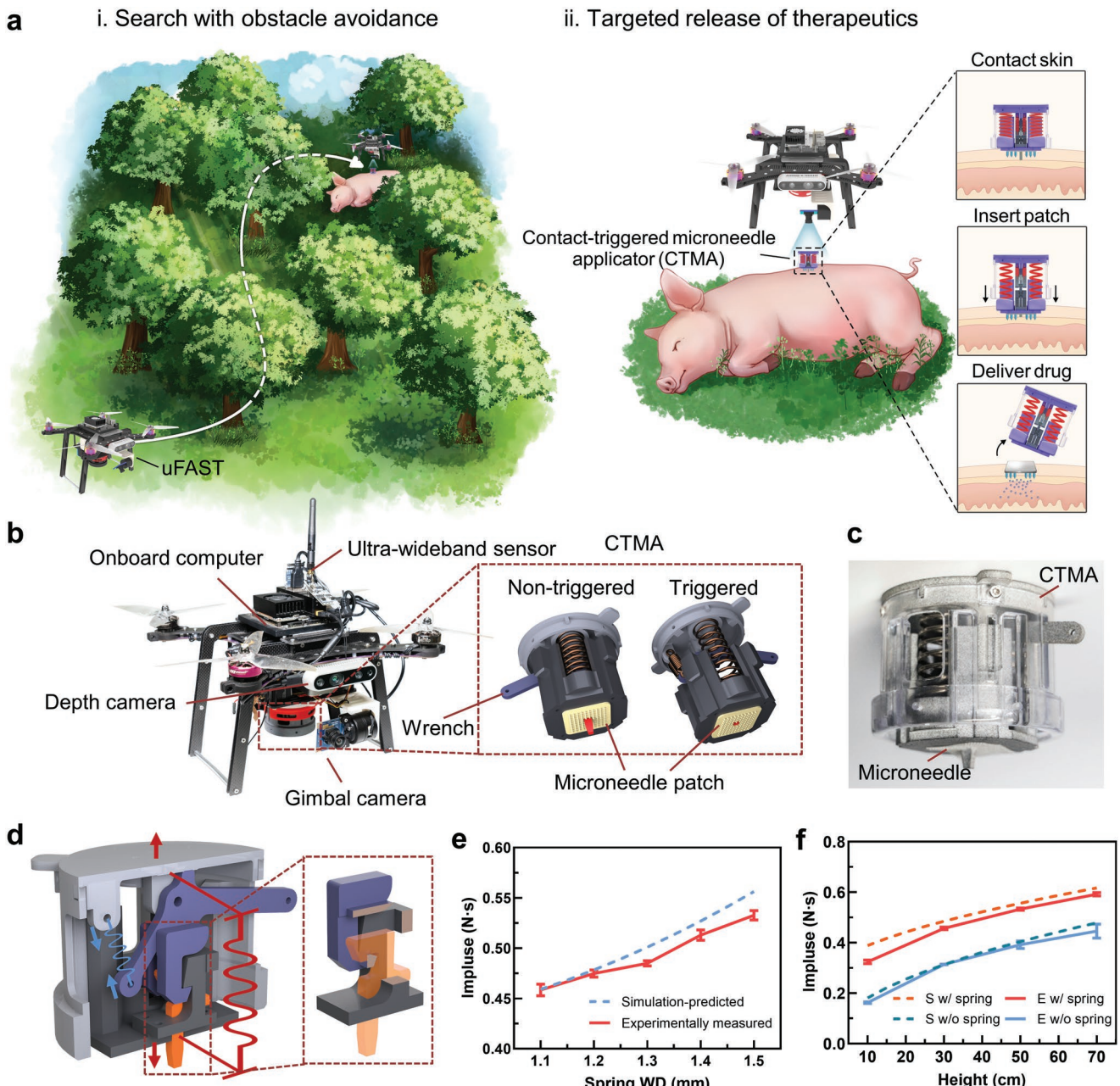


Figure 1. Schematic and characterization of UAV-mediated first-aid system for targeted drug delivery (uFAST). a) Schematic of uFAST. Once the UAV receives the emergency signal, it takes off immediately and reaches the patient to release the CTMA, which subsequently autonomously administers the MN patch into the skin for targeted drug delivery. b) Schematic of the components of the uFAST, including a UAV, a CTMA, and an MN patch. The MN patch is fixed onto the CTMA, which is secured in the UAV. c) Physical diagram of the CTMA and MN patch. d) Schematic of the CTMA. When the CTMA is untriggered, the pre-compressed spring (red) pushes the slidable base (black), and the tension spring (blue) pulls the bridge (purple) that is locked by the trigger (orange) and prevents the base from sliding out. Once the trigger touches the skin surface, it rises up to unlock the bridge, and the base is ejected out by the compressed spring. e) Simulation-predicted (dashed line) and experimentally measured (solid line) impulse of the CTMA with different spring wire diameters (WD) at RH of 0.5 m ($n = 4$). f) Simulation-predicted (S, dashed line) and experimentally measured (E, solid line) impulse of the CTMA with and without spring (1.5 mm WD) at RH from 0.1 m to 0.7 m ($n = 4$). In (e,f), data are presented as mean \pm standard deviation (s.d.).

emergency drugs, while this process always needs to be operated by professionals. In addition, inappropriate administration of the syringe needles for injections by patients may cause secondary injury, such as the risk of residual needle fracture in the skin, infection, as well as inflammation.^[4]

Herein, we describe an unmanned aerial vehicle (UAV)-mediated first-aid system for targeted delivery (uFAST) that can achieve autonomous administration of emergency medication without the involvement of additional or conscious persons (Figure 1a). The UAV can be initiated by an emergency signal

with the positioning information from the patients, and it is able to reach the vicinity of the positioning signal based on an online calculated trajectory with real-time obstacle avoidance capability. In this system, we utilize a microneedle (MN) patch as an emergency device because MNs can provide convenient, safe, and efficient administration. Such transdermal formats can be tailored to achieve rapid drug release from a dissolvable tip as well as bioresponsive controlled release from a crosslinked matrix.^[5] Of note, in order to adapt the MN patch to the UAV and realize UAV-mediated drug administration, a contact-triggered microneedle applicator (CTMA) is designed to provide a sufficient force to insert MNs upon contact with the skin (Figure 1b,c). When the UAV searches and identifies the patient, it hovers at a proper height and subsequently releases the CTMA to apply the drug-loaded MNs into the skin for emergency care.

We further demonstrate the implementability and safety of the uFAST for first aid in a severe hypoglycemia disease model. Hypoglycemia is a common side effect occurring in people with diabetes receiving insulin treatment, and severe hypoglycemia may lead to coma, brain damage, or even death.^[6] As severe hypoglycemia often leads to sudden fainting or occurs while sleeping at night,^[7] the continuous glucose monitoring system (CGMS) on diabetic people that is able to real-time alert hypoglycemia could serve as the danger signal source to pair the uFAST for timely administration of the glucose-elevating drug (glucagon).^[8] In order to ensure accurate dosing of glucagon, a dual-mode microneedle patch (DM-MN) is developed to realize an immediate release of a basal dose as well as a sustained glucose-dependent release of a subsequent dose. In an insulin-overdosing hypoglycemic diabetic minipig model, we further substantiate that the uFAST integrated with DM-MN could facilitate a timely aid in minutes, to alleviate the risk of severe hypoglycemia.

2. Results

2.1. Design and Characterization of the Autonomous Drug Delivery System

The autonomous drug delivery system consists of the CTMA, the release unit, the gimbal camera unit, and the base platform attached to the bottom of the UAV. The detailed delivery gear design for the UAV is shown in Figure 1b. We equipped the release unit for locating the CTMA (Figure S1, Supporting Information), the onboard ultra-wideband (UWB) sensor for measuring the relative distance to correct the position of the patient, and the gimbal camera for identifying the patient to obtain the releasing point. The core part of the drug delivery module is the CTMA which administers the therapeutics into the body via a MN array patch (Figure 1c). The CTMA was designed and built to be lightweight (75 g), reducing the payload during flight to increase the first-aid distance. Meanwhile, due to the necessity of the powerful force in MN patch application, a contact-triggered system was designed to release the pre-stored energy. The CTMA is mainly composed of trigger elements, energy storage elements, and a MN patch. The schematic diagram of the CTMA is shown in Figure 1d and

Figure S2, Supporting Information. When the trigger at the bottom of CTMA touches the skin surface, the springs can release sufficient energy to eject the slidible base so that the MN patch attached can be inserted into the skin. After completing the first-aid task, the CTMA can be readily reused by pulling back the wrench.

Considering the administration mode of the MN patch, sufficient pressure lasting for a period of time is essential for successful penetration. To this end, we evaluated the insertion performance of the CTMA by the integral of force with time (impulse). The impulse

I generated by the CTMA was calculated as $I = mv_1 - mv_0$, where m was the mass of the CTMA, and v_0 and v_1 were the velocities of the CTMA before and after applying respectively.

The simulation (see details in the Experimental Section; Equation (S1) and Figure S3, Supporting Information) predicted that the CTMA with the thicker springs or released from a higher position could generate a greater impulse (Figure 1e,f).^[9] Real-world experiments were further conducted to validate the hypothesis (Figure 1e,f; Videos S1 and S2, Supporting Information). The high-speed camera was used to measure the velocity of the CTMA (Figure S4, Supporting Information). As it was difficult to reset the CTMA when wire diameter (WD) > 1.5 mm, the springs of 1.5 mm WD were selected in the following study to evaluate the performance of CTMA at different release heights (RHs).

In the final process of identification, the height of the uFAST determines the accuracy of the operating localization position. Due to the ground effect, the uFAST cannot hover stably at a relatively low position. Considering the magnitude of generated impulse, an optimized RH value of 50 cm was selected in the following experiments.

2.2. Combination of CTMA and Microneedle Patch

The MN patch was immobilized on the CTMA through frictional force by cutting a pinhole in the MN patch slightly larger than the bottom area of the trigger element. Taking advantage of the pressure-sensitive films, the MN patches implementation comparison on the minipig skin between manually pressing and CTMA could be revealed directly, indicating the pressure generated by CTMA was uniform compared to that generated manually (Figure 2a). In addition, the hematoxylin and eosin (H&E)-stained section image further validated the insertion of the MNs into the minipig skin by CTMA (Figure 2b).

Furthermore, the MN insertion process was captured under high-speed photography (Figure 2c; Video S3, Supporting Information). The slow-motion video of the MN insertion process exhibited three main stages, that is, descending, triggering, and inserting. In Figure 2d and Video S4, Supporting Information, the device fixed by glue (springs were invalid) was tested under the same experimental conditions but could hardly insert the MNs. With the aid of the high-speed camera, it could be perceived that the base corner touched the skin first in most cases, resulting in the putting straight of CTMA. After that, the springs could eject the base out during pose adjusting and provide sufficient force to deform the skin to fit the MN patch (Figure 2e).

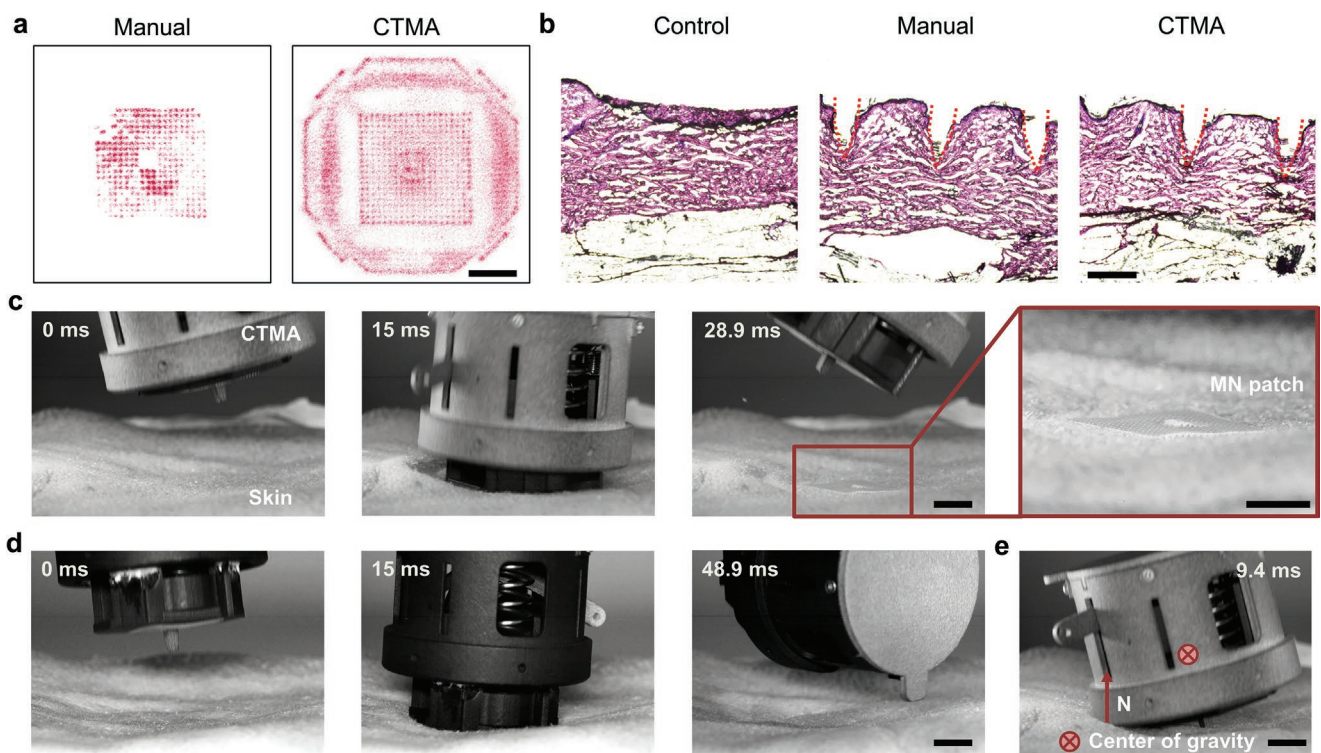


Figure 2. Combined administration of the CTMA and MN patch. a) Visualization of the contact force by the pressure-sensitive films. Scale bar: 1 cm. b) Representative hematoxylin and eosin (H&E) stained sections of MNs penetrating into the minipig skin by different methods (manually and CTMA). Scale bar: 500 μ m. c,d) The process of the MN patch administration by the CTMA with spring (c) and without spring (d) through the high-speed photography (imaging at 1800 frames per s). Scale bar: 1.2 cm. e) Representative force diagram of the CTMA with spring when it touched the skin surface. Scale bar: 1.2 cm.

As the RHs may influence the CTMA drop position, we tested the positioning accuracy of CTMA-delivered MN patch both in vitro and in vivo. It demonstrated that the MN patch drop position was moved away from the release position as the RH was increased (Figure S5A,B, Supporting Information). With the RH of 50 cm, the average releasing position error (distance from the release position to the center of the MN path drop position) could be controlled within 2.44 cm in vitro (Figure S5A, Supporting Information) and 4.6 cm in vivo (Figure S5C,D, Supporting Information), respectively. The minimum circle area encompassing all MN patch positions was considered as the minimal dimension, which could be controlled in a circle with a radius of 4.31 cm in vitro (Figure S5A, Supporting Information) and 9.22 cm in vivo (Figure S5D, Supporting Information). These results suggested that precise and area targeted drug delivery with the MN patch could be achieved by CTMA.

2.3. Preparation and Characterization of the Glucagon-Loaded DM-MN Patch

Glucagon is available as an emergency medication to treat severe hypoglycemia by stimulating the breakdown of liver glycogen to increase blood glucose levels.^[10] In order to prevent an overdose of glucagon, a DM-MN patch with a bilayer structure was developed. The DM-MN was comprised of two action

modules: the MN tip made by the water-soluble polymer could immediately release glucagon to rapidly raise the blood glucose once inserted into the skin; the MN body made by glucose-responsive polymeric matrix could sustainably provide additional glucagon subsequently in a glucose-dependent manner to achieve better blood glucose regulation and prevent the blood glucose becoming too high or staying too low. The DM-MN patch was prepared by a two-step fabrication method based on two types of silicone MN molds. The immediate release module of DM-MN was first prepared from a mixture of glucagon (GC) and N-vinylpyrrolidone (NVP) by the in situ photopolymerization at 4 °C, and the glucose-responsive release module was subsequently fabricated from the mixture of the glucagon analog (GA), NVP, ethylene glycol dimethacrylate (EGDMA), (4-((2-acrylamidoethyl) carbamoyl)-3-fluorophenyl) boronic acid (3FPBA), and 2-(dimethylamino) ethyl acrylate (DMAEA) by the same method (Figure 3a,b; Figure S6, Supporting Information).

The prepared DM-MN patch was made up of a 20 × 20 array of microstructures with a central spacing of 800 μ m between the adjacent needles. The base width and height of the needle tip arrays were 400 and 500 μ m, and the base width and height of the needle body array were 400 and 400 μ m, respectively (Figure S6, Supporting Information). The fluorescence microscopy images of the DM-MN revealed the bilayer structure of the fluorescein isothiocyanate (FITC)-labeled GC loaded needle tip and the rhodamine-B-labelled GA loaded needle body (Figure 3c). The successful assembling of the two modules

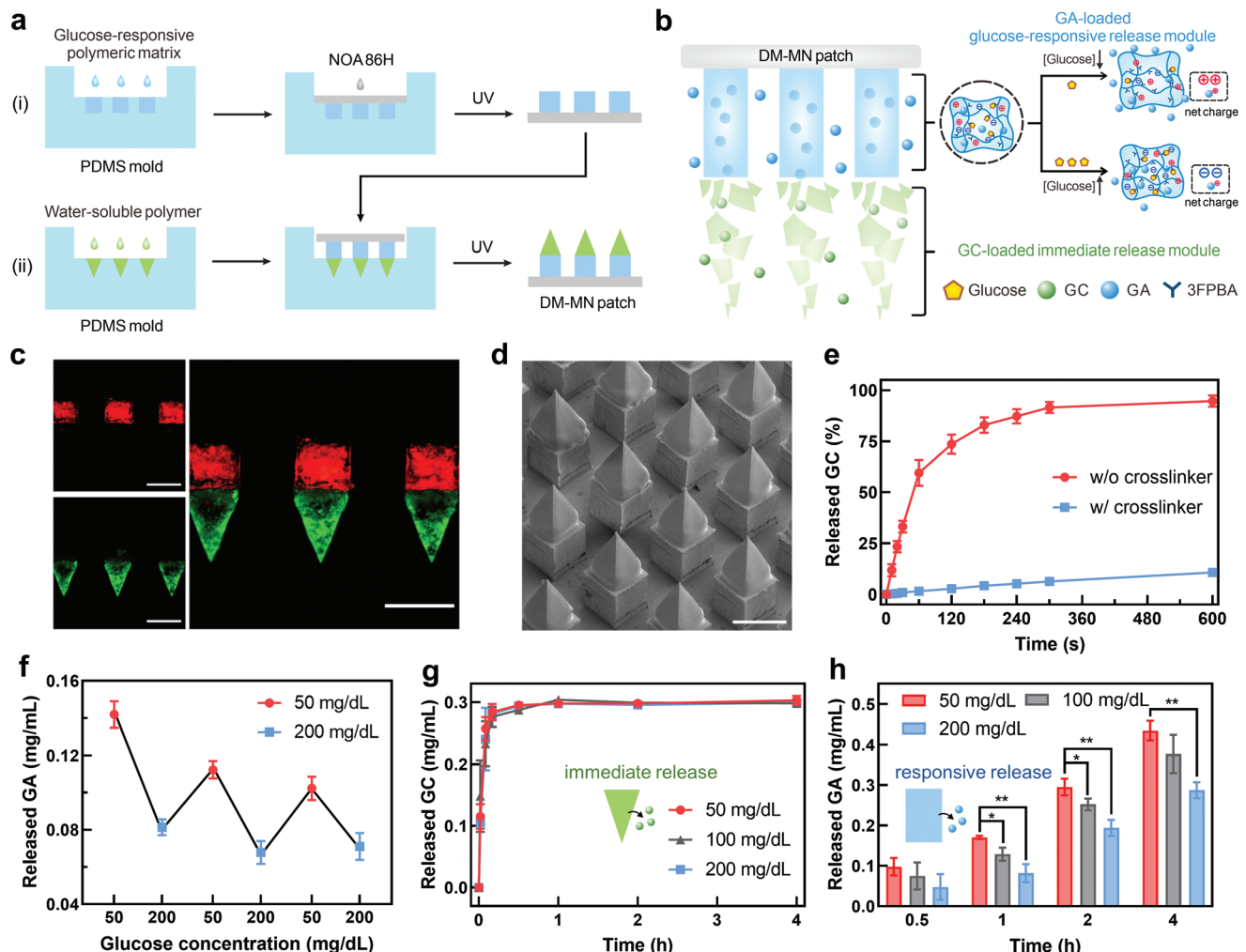


Figure 3. Characterization of the glucagon-loaded DM-MN patch. a) Schematic of the fabrication process of a DM-MN patch from silicone molds using an in situ photopolymerization method. b) Mechanism of immediate GC release and GA glucose-responsive release from DM-MNs. c) Representative fluorescence microscopy images of the DM-MN patch containing the immediate release module (FITC-GC) and glucose-responsive release module (Rhodamine B-GA). Scale bar: 500 μ m. d) Representative scanning electron microscopy images of the DM-MN patch. Scale bar: 500 μ m. e) In vitro accumulated release of GC from the immediate release polymeric matrix with (w/) and without (w/o) the crosslinker of EGDMA in PBS at 37 °C ($n = 3$). f) Pulsatile release pattern of GA by incubating in solution with different glucose concentrations of 50 and 200 mg dL⁻¹ alternately. Each incubation time is 20 min. g,h) In vitro accumulated release of GC (g) and GA (h) from the DM-MNs in varying glucose concentrations at 37 °C, pH 7.4 ($n = 3$). In (e-h), data are presented as mean \pm s.d. Statistical significance was determined by a two-tailed Student's *t* test. **P* < 0.05, ***P* < 0.01.

was further confirmed by scanning electron microscopy (SEM) images (Figure 3d), whereby the two modules were tightly connected (Figure S7, Supporting Information). In addition, the fracture force of the DM-MN was determined as 0.307 ± 0.013 N per needle by a tensile compression machine (Figure S8, Supporting Information), which was sufficient to penetrate the skin.^[5g,h]

To achieve immediate release of GC for hypoglycemic emergencies, the MN tip was fabricated by the polymerization of NVP without the crosslinker. As shown in Figure 3e, more than 75% of GC could be released in ≈ 2 min, while less than 20% of GC was released even in 10 min from the polymeric matrix crosslinked by EGDMA. Phenylboronic acid was selected as the glucose-sensitive unit in the glucose-responsive release module. It could reversibly interact with glucose to form negatively charged cyclic boronic esters under hyperglycemic conditions,

while dissociating to the uncharged group under hypoglycemic conditions, which led to an increased positive net charge within the MN polymeric matrix due to the presence of amino groups in DMAEA units (Figure 3b). As the isoelectric point (pI) of natural glucagon is ≈ 7.1 ,^[11] it has weak electrostatic interaction with the charge-switchable MN matrix in a physiological environment (pH 7.4). Therefore, a positively charged glucagon analog was synthesized by introducing two basic amino acids, arginine, to the C-terminus of glucagon. The resulting GA had an isoelectric point of ≈ 9.3 (Figure S9, Supporting Information). In vivo studies revealed that GA had a similar glucose-raising capacity compared to native glucagon (Figure S10, Supporting Information). In the glucose-responsive release module with a 1:0.8 ratio of 3FPBA to DMAEA, GA could be quickly released due to the electrostatic repulsion by the positively charged MN matrix under hypoglycemia, while the release rate slowed down

once returned to normoglycemia (Figure 3f; Figure S11, Supporting Information).

The dual-mode release behavior of DM-MN patches was further assessed in solutions with varying concentrations of glucose. As shown in Figure 3g,h, the resultant DM-MN patches could realize a rapid release of glucagon and a sustained glucose-dependent release of GA. In addition, the activity of the released GC and GA was similar to freshly dissolved native GC and GA in healthy mice (Figure S10, Supporting Information) because no additional extra organic solvent and the elevated temperature were involved during the fabrication process. The matrix-assisted laser desorption/ionization time-of-flight mass spectrum (MALDI-TOF-MS) analysis further confirmed that the released GC and GA remained intact throughout the polymerization process (Figure S12, Supporting Information). Moreover, the immediate release module showed insignificant toxicity at the various concentrations studied (Figure S13, Supporting Information), and the glucose-responsive release module that was not dissolvable in vivo could be intactly removed from the skin.

2.4. In Vivo Studies of DM-MN Integrated uFAST in the Hypoglycemic Diabetic Pig Model

We further assessed the performance of the uFAST in an insulin-overdosing hypoglycemic diabetic minipig model regarding the minipig skin structure being similar to human skin.^[12] Acute severe hypoglycemia in the streptozotocin-induced type 1 diabetic minipig was developed by subcutaneous overdosing of insulin (0.035 mg kg^{-1}). To achieve real-time and continuous recording of glucose levels in minipigs, a continuous glucose monitoring system (CGMS) was affixed to the inside of the hind legs of the minipigs. When hypoglycemia occurred, the CGMS could alert and generate a danger signal to be transmitted to the uFAST. In this study, a manual signal containing the coordinate information was sent to the uFAST when the minipig got hypoglycemia. We used a visual-inertial system (VINS), a robust visual-inertial odometry (VIO) framework, to localize the UAV,^[13] and a newly developed trajectory representation named minimum control (MINCO) for trajectory planning.^[14] Once the signal was sensed, the UAV took off equipped with the DM-MN patch. According to the target location signal and the obstacle map built from the real world, the UAV (FAST 330) could achieve automatic trajectory planning with obstacle avoidance capability.^[15] Meanwhile, the destination was corrected online by relocating the signal source through onboard UWB sensors (Equation (S2) and Figure S14, Supporting Information). When the UAV reached the source of the signal, the UAV could accurately hover over the minipig through auto-identification based on the pre-trained YOLOv5 neural network. Then, the UAV fell to 50 cm above the center of the minipig, and released the CTMA to achieve DM-MN application into the skin of the minipig (Figure 4a; Video S5, Supporting Information). As shown in Figure 4b, the DM-MN effectively penetrated the skin of the minipig by uFAST.

Following the application of the DM-MN patch via uFAST, the blood glucose of the hypoglycemic minipig rapidly returned

to the normoglycemic range within 90 min, which was similar to the groups that received DM-MN patches by pressing manually (Figure 4c). However, the minipigs without any treatment remained in the hypoglycemic state for more than 6 h (Figure S15, Supporting Information). Through comparing the different first-aid manners, the DM-MN integrated uFAST was able to achieve a fast glucose-raising effect as well as the manual pressing method, significantly minimizing the duration of hypoglycemia and reducing the risk of fatal danger (Figure 4d).

We further examined the plasma concentrations of GC and GA in the minipigs. As shown in Figure 4e,f, the DM-MN patches administered by either uFAST or manual pressing could achieve a similar rapid release of GC and the responsive release of GA (Figure S16, Supporting Information). GC released from the immediate release module reached the maximum blood concentration in 30 min, while GA from the glucose-responsive module reached the maximum blood concentration in 45–60 min, and the release rate of GA gradually decreased with the rise of blood glucose. We also monitored the change of the glucose levels in the blood using both the CGMS and glucometer, and found that blood glucose could reach the normal blood glucose range ≈60 min after the use of DM-MN, indicating a corresponding dependence on the concentration of GC and GA in plasma. The time for CGMS to detect the rise of blood glucose to the normal range was ≈90 minutes (Figure S17, Supporting Information), which may be related to the existence of lag in the detection of blood glucose by CGMS.^[16] Insignificant neutrophil infiltration and inflammatory response were noted after treatment with the DM-MN by both uFAST and manual pressing (Figure 4g).

3. Conclusion

In the last decade, the rapid development of unmanned aerial vehicles (UAVs) has realized the remarkably effective transport of medicines and emergency equipment due to their capability of spatially unrestricted, terrain-independent, and rapid arrival at targeted locations, greatly improving the survival rate of emergency patients.^[17] Besides the rapid transport of emergency medicine, a timely medication administration is also indispensable for preserving life. Nonetheless, the current medical UAVs still require emergency patients to administer drugs on their own or other people around them to help, which is not feasible in many situations. Therefore, there is an urgent need to develop a UAV-based system that can not only identify the position of patients and reach them immediately but also achieve autonomous drug administration to relieve symptoms.

We have developed a UAV-assisted autonomous drug delivery system for first aid. Our uFAST consists of the UAV, the CTMA, and the MN patch containing emergency therapeutics. Among them, the UAV could complete the reception of the emergency signal, generating trajectory to the target location, obstacle avoidance, and target recognition; the CTMA enables autonomous drug delivery to provide first aid without additional assistant; the MN patch offers a fast-acting and smart drug delivery for the emergency patient. Both simulation and real-world experiments indicated that CTMA could

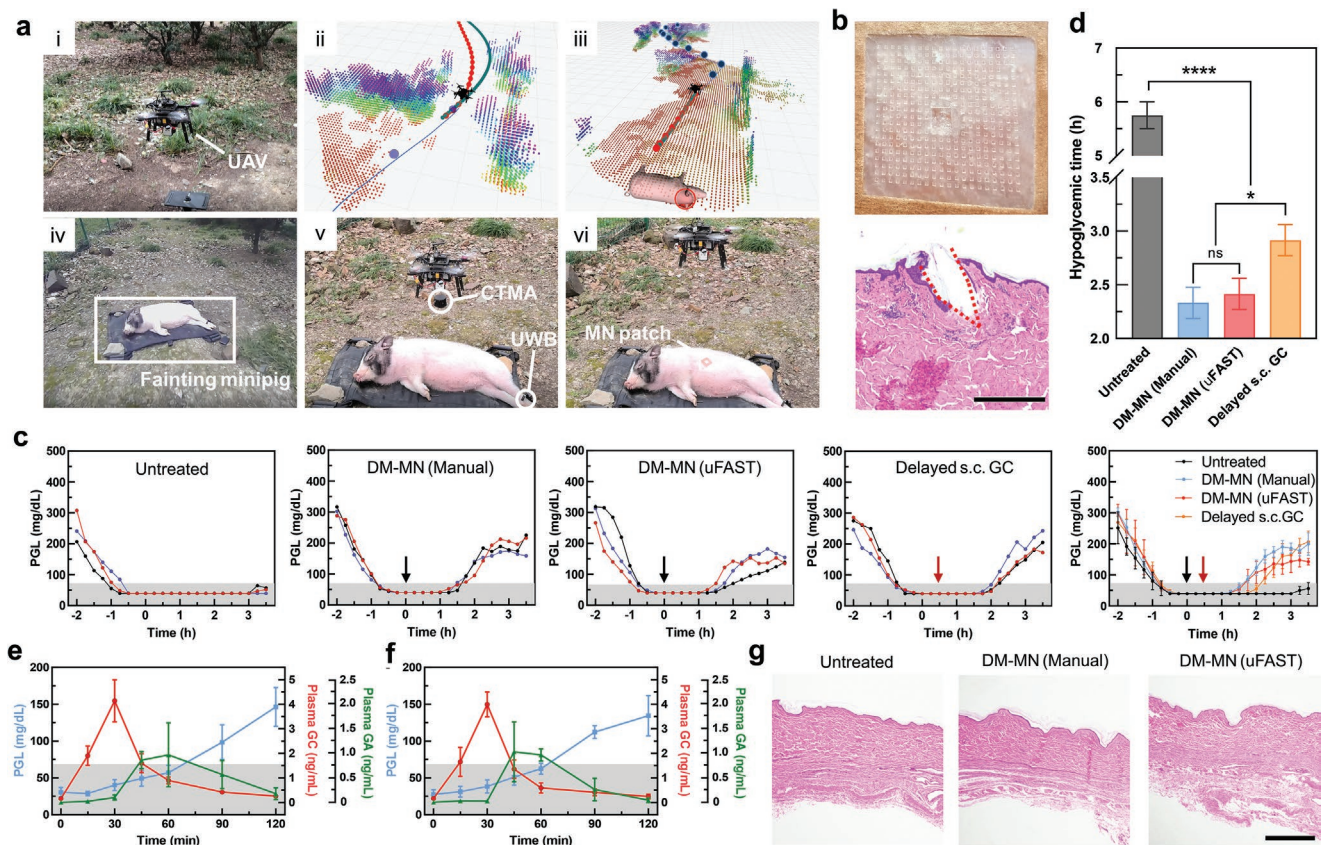


Figure 4. In vivo performance of the DM-MNs-integrated uFAST in an insulin-overdosing hypoglycemic diabetic minipig model. a) The working process of the DM-MN integrated uFAST in the minipig model. a-i) Autonomous take-off once the alert signal is received. a-ii) Automatic trajectory planning. Red track: optimized trajectory; Green track: global trajectory; Blue track: flight trajectory. Blue point: UWB sampling points. a-iii) Re-location. Blue point: UWB sampling points; Red point: corrected localization of minipig (the patient model). a-iv) Identification. a-v) Release of the CTMA. a-vi) Administration of the DM-MN patch toward the minipig skin. b) Top: photograph of DM-MN patch applied to the skin of the minipig by uFAST in (a), bottom: H&E-stained section of minipig skin penetrated by the DM-MN patch. Scale bar: 300 μ m. c) Plasma glucose levels (PGLs) in insulin-overdosing hypoglycemic diabetic minipigs ($n = 3$) without treatment or with treatments by different methods, including the DM-MN patches administered manually or by uFAST as well as subcutaneous GC injection delayed by 30 min. Patch size: 2 cm \times 2 cm. Insulin dose: 0.035 mg kg $^{-1}$. GC dose in DM-MNs: 1 mg. GA dose in DM-MNs: 3 mg. GC dose in injection: 1 mg. Black arrow, the time point of the DM-MNs administration. Red arrow, the time point of subcutaneous injection of GC. Gray area, PGLs below 70 mg dL $^{-1}$ (hypoglycemic range). d) Duration of hypoglycemia in minipigs ($n = 3$) received different treatments. e,f) PGLs and plasma concentrations of GC and GA in minipigs ($n = 3$) treated with the DM-MN patches manually (e) or by uFAST (f). g) H&E-stained skin sections of minipig skin pre- and post-treatment of DM-MNs. Scale bar: 1 mm. In (c-f), data are presented as mean \pm s.d. Statistical significance was determined by a two-tailed Student's t test. * $P < 0.05$ and *** $P < 0.0001$.

provide a uniform and sufficiently powerful force for the microneedle to be firmly inserted into the skin. Moreover, the MN patch with dual modes could not only offer a basal dose of the emergency drug at the first time but also support with a subsequent glucose-dependent dose to prevent the potential side effect of overdosing. In vivo studies confirmed that the uFAST successfully implemented autonomous first aid in a hypoglycemic minipig model, which effectively prevented the continuous decrease in blood glucose and promoted its rise to the normal range.

Furthermore, in order to improve the insertion rate of the MNs into the uneven skin, the flexible materials could be integrated at the bottom of CTMA, ensuring that CTMA can well fit the skin during the administration. In addition, wearable monitoring devices such as smart watches that can monitor physiological signals including blood pressure and heart rate, can be further paired with the uFAST.^[18] Once a dan-

gerous signal is identified by the wearable monitoring device, it could transmit the alert and position information to initiate the uFAST for first aid. Considering the impact of environment and positioning accuracy, several advanced detection or analysis regions could also be further combined with the uFAST. For example, the radar-based system (OUSTER OS0) and thermal images could be applied for detection in difficult weather conditions.^[14,19] The OpenPose system and Instance Mask Projection system could integrate for detecting real-time pose and delivering drugs to the targeted area (e.g., bare skin) to enhance the accuracy.^[20] Meanwhile, other formulations and administration approaches of drugs, such as transdermal creams and aerosols, even new delivery devices^[21] can be integrated with the uFAST to extend this platform of UAV-mediated drug delivery for emergency treatment of other sudden diseases and dangerous occasions associated with fires.

4. Experimental Section

Materials: All of the non-standard parts of CTMA were processed by nylon 3D printing made by WeNext. The UWB sensors (LinkTrack PS-B and LinkTrck PTag) were purchased from Noooploop. The USB camera (KS2A543) was purchased from Kingcent. The servo motor (HT-S-2806) was purchased from Haitai Electromechanical. The steering motor (LX-15D) was purchased from Hiwonder. All chemicals were purchased from Aladdin unless otherwise specified and used as received. Glucagon analog (sequence: HSQGTFTSDYSKYLDSSRRAQDFVQWLMNTRR) was ordered from GL Biochem Ltd. (Shanghai, China). Human glucagon (GC) was purchased from Bidet Pharmaceuticals (Catalog No. BD132093). Coomassie (Bradford) Protein Assay Kit was purchased from Thermo Fisher Scientific (Catalog No. 23200). Norland Optical Adhesive 86H was purchased from Edmund Optics (Catalog No. 12-848). Glucagon human enzyme-linked immunosorbent assay (ELISA) kit was purchased from Thermo Fisher Scientific (Catalog No. EHGCG). (4-((2-acrylamidoethyl) carbamoyl)-3-fluorophenyl) boronic acid was purchased from AmBeed (Catalog No. A1194179). Streptozocin (STZ) was purchased from MACKLIN (Catalog No. S817944).

Autonomous UAV-Mediated Microneedle Delivery in the Forest: The FAST 330 UAV was utilized to integrate the autonomous medicine delivery system in this study. The quadrotor was equipped with an Nvidia Xavier NX for onboard computing, an Intel RealSense D435 stereo camera pair for imagery and depth sensing, and a PX4 autopilot for stabilizing the drone and feeding inertial measurement unit data. A manual estimate was applied as a danger signal (based on CGMS) to send the initial approximate position information of the patient (minipig). To estimate and correct the localization of the patient, the relative distance between uFAST and the patient was measured by using the onboard UWB sensor. To further smooth the position of the patient based on the detection of YOLOv5, a lowpass filter was applied. Once the uFAST hovered stably at the expected position, the CTMA was released.

CTMA Characterizations: To keep the consistency of the experiment conditions, the CTMA was released from the release device, and the device without spring was made by fixing the CTMA with its slideable base with glue. The impulse measuring test was performed using a high-speed camera (PHANTOM Miro C210) to record images at the rate of 4000 fps (Figure S4, Supporting Information), whose interval time Δt was 250 μs . The initial velocity v_0 was determined by the RH h calculated as $v_0 = \sqrt{2gh}$. The initial and the final frame numbers were manually determined with the interval of $n = 40$. The initial frame referred to a frame at which the base of the CTMA first left the skin. The displacement Δx was defined as the distance between the center of gravity of the CTMA at the selected frame numbers. The generated impulse was calculated as: $I = m\Delta v$, where $\Delta v = v_1 - v_0 = (\Delta x/n\Delta t) - (\sqrt{2gh}(g/l|g|))$.

Positioning Accuracy of CTMA: In the *in vitro* experiment, to precisely locate the MN patch position after using the CTMA, 40% gelatin was chosen as the skin model for the MNs position recording. The MN patch was fixed on the CTMA. After releasing the CTMA at different heights, the MN patch lodged into the gelatin to leave an imprint. Photographs of the gelatin with the MNs imprint were subsequently taken and the location of the MN patch position was depicted by CorelDraw for further analysis. In the *in vivo* experiment, the CTMA was assembled on the UAV. The CTMA was released when the UAV reached above the minipig by identifying the minipig. The release process of the CTMA and the position of the MN patch were recorded by the camera fixed on the UAV.

Blood-Glucose-Raising Effect of GA: GA and GC were dissolved in 0.01 M HCl solution and configured into 1 mg mL⁻¹ solution, respectively. The initial blood glucose of each mouse was measured by a glucometer (Accu-Chek Aviva). The GC and GA were injected subcutaneously into healthy C57BL/6 mice at a dose of 15 mg kg⁻¹, followed by a measurement of blood glucose level after 15 min of injection. The animal study protocol was approved by the Institutional Animal Care and Use Committee at Zhejiang University.

Fabrication of DM-MN Patch: The DM-MN patch was prepared by press alignment and twice polymerization under ultraviolet irradiation. In brief, to prepare the DM-MN, a total of two microneedle molds were

used: a 400 × 400 μm base and 500 μm height pyramid mold and a 400 × 400 μm base and 400 μm height square prism mold, respectively. The needles in both molds were arranged in a 20 × 20 array with a spacing of 400 μm . The glucose-responsive part of the DM-MN was first prepared. The ethylene glycol dimethacrylate (EGDMA) (0.5 wt%) as the crosslinker and 2-hydroxy-4'-(2-hydroxyethoxy)-2-methylpropiophenone (Irgacure 2959) (1.5 wt%) as the photoinitiator were dissolved in *N*-vinylpyrrolidone (NVP) solution, followed by the addition of (4-((2-acrylamidoethyl) carbamoyl)-3-fluorophenyl) boronic acid (3FPBA) and 2-(dimethylamino) ethyl acrylate (DMAEA) in a molar ratio of 1:0.8 to the mixture. The mixture then placed under ultrasound until completely dissolved. Afterward, the GA (12 wt%) was dispersed in the prepared monomer, mixed thoroughly under ultrasonication, and the solution was directly deposited by pipette onto the surface of the square prism molds. Then, the molds were placed under vacuum for 20 min to allow the solution to fill the mold cavities. After removing the excess solution, the mold on an ice bath was placed under a UV curing lamp for 5 min of photopolymerization (135 mW cm⁻², 365 nm). The UV curable substrate (NOA 86H) was then added dropwise to the mold and cured under a UV lamp for 5 min to obtain the glucose-responsive module of DM-MN. The immediate release module of the DM-MN was subsequently prepared in a similar manner. The mixture of the immediate release part contained only NVP, Irgacure 2959 (1.5 wt%), and GC (10 wt%), and was deposited by pipette onto the surface of the pyramid mold. To integrate the immediate release module and glucose-responsive release module, the glucose-responsive release part was aligned and inserted into the pyramid microneedle mold filled with the immediate release module of the monomer solution under a stereomicroscope, and the mold was placed on an ice bath under a UV curing lamp for 5 min for photopolymerization (135 mW cm⁻², 365 nm). The resulting patch was carefully separated from the mold and stored in the vacuum desiccator for further studies.

Microneedle Characterizations: The fluorescence images of the DM-MN were observed using a fluorescence microscope (Nikon). Nova Nano 450 field-emission scanning electron microscope (SEM) was applied to characterize the DM-MN patch. The DM-MN patch was sputtered with a gold/palladium target for 30 s prior to imaging. The mechanical strength of the microneedle was measured by pressing the microneedle against a stainless-steel plate. The initial gauge between the microneedle tip and the stainless-steel plate was set at 1.00 mm and the load cell capacity was 10.00 N. The top stainless-steel plate was moved toward the microneedle at a speed of 0.1 mm s⁻¹. The failure force of the microneedles was recorded when the needles began to buckle.

MALDI-TOF Spectra: GC was extracted from the immediate release part of the prepared DM-MN patch in PBS solution for 5 min, and GA was extracted from the glucose-responsive release part of DM-MN in 0.01 M HCl at 4 °C for 24 h. The spectra of the released GC, GC, the released GA, and GA were detected using an Ultraflextreme MALDI-TOF/TOF system.

In Vitro Release Studies: To assess the immediate release of GC and glucose-responsive release of GA, the immediate release and responsive-release modules of the DM-MN patch were placed in 1 mL of PBS solution (pH 7.4), respectively, and incubated at 37 °C with gentle shaking (400 rpm) at different glucose concentrations (50, 100, and 200 mg dL⁻¹). At predetermined time points, 10 μL of supernatant was collected into 96-well plates and released GC or GA was quantified using the Coomassie (Bradford) protein assay (Thermo Fisher Scientific). Absorbance was detected at 595 nm on the Synergy H1 microplate reader (BioTek) and concentrations were calculated using GC (8–500 μg mL⁻¹) or GA (8–500 μg mL⁻¹) standard curves. The release patterns of GC and GA integrated in the DM-MN patch were performed in the same way, where the GC and GA were labeled with FITC and rhodamine B, respectively. The release of GC and GA was detected by a fluorometric method (GC: excitation wavelength: 490 nm, emission wavelength: 520 nm; GA: excitation wavelength: 540 nm, emission wavelength: 593 nm), and the concentration of FITC-labeled GC (0–500 μg mL⁻¹) and rhodamine-B-labeled GA (0–500 μg mL⁻¹) standard curve were used to calculate the concentration.

Cytotoxicity of the DM-MN: The immediate release part of DM-MN was re-dissolved in DMEM medium and added to B16F10 cells for 24 h, and cell viability was detected using the CCK-8 kit.

In Vivo Studies Using an Insulin-Overdosing Hypoglycemic Diabetic Minipig Model: The animal study protocol was approved by the Institutional Animal Care and Use Committee at Zhejiang University. Three male Bama minipigs were used. Insulin-deficient diabetes was induced in minipigs by intravenous administration of STZ (150 mg kg⁻¹). STZ was dissolved in freshly prepared sodium citrate–disodium citrate buffer (pH 4.5) under light-protected conditions at a final intravenous concentration of 75 mg mL⁻¹ and was administered intravenously within 10 min. The successful establishment of an insulin-deficient diabetes minipig model was confirmed by monitoring glucose levels with a continuous glucose monitor system (CGMS, FreeStyle Libre, Abbott) affixed to the inner hind limbs of the minipig after 7 days of STZ injection. Diabetic minipigs were treated once daily with glargin insulin (0.3–0.8 U kg⁻¹; Lantus; Sanofi) for glycemic control. Daily treatment was stopped 36 h before the experiment. All minipigs (25–30 kg) were fasted overnight before the experiment and an overdose of insulin (0.035 mg kg⁻¹) was injected subcutaneously on the following day. After blood glucose level was at a hypoglycemic level (<70 mg dL⁻¹), DM-MN was applied to the flanks of the minipigs by using different methods, and the doses of GC and GA in each patch were 1.0 and 3.0 mg, respectively. The minipigs were under anesthesia during the application of the patch. Before applying DM-MN, the hair on the lateral side of the minipig was shaved, and the microneedle was inserted into the shaved skin by hand pressing or by uFAST. To secure the patch on the skin surface, a 3M Tegaderm transparent film dressing was used to cover the patch. Before applying DM-MN through the uFAST, DM-MN was attached to a 3 M film dressing and secured to the CTMA. Blood glucose changes were continuously monitored by CGMS during the experiment. To verify that the elevated glucose and drug release were correlated, the concentrations of GC and GA in plasma were measured by ELISA and fluorometric methods, respectively. After applying the DM-MN patch in different ways, blood was collected from the anterior vena cava at the indicated time points and blood glucose levels were measured by using a glucometer (Accu-Chek Aviva glucometer, Roche Diabetes Care Inc.). The plasma was then extracted from blood by centrifugation (3000 rpm, 20 min) and stored at –20 °C until it was assayed.

H&E Staining: DM-MN patches were applied to the shaved skin of minipigs using different methods (manually and by uFAST), and 1 day after removal of DM-MN, the skin was obtained from the treatment site, fixed in 4% formaldehyde for 24 h, and sectioned and stained with H&E.

Statistical Analysis: All the results are presented as mean ± s.d. Statistical analysis was performed using a two-tailed Student's t-test. The differences between experimental groups and control groups were considered statistically significant at *P*<0.05.

Supporting Information

Supporting Information is available from the Wiley Online Library or from the author.

Acknowledgements

T.S. and R.J. contributed equally to this work. The authors acknowledge Deyue Xu (Laboratory Animal Center, Zhejiang University), Mengke Zhang, Liua Pei, Chengzhang Gong, Haoxiong Xu, and Kunyi Zhang for helping in animal field experiments. The authors appreciate Chao Sun (Analysis Center of Agrobiology and Environmental Sciences, Zhejiang University) for the help of MALDI mass analysis and Guizhen Zhu, Dandan Song (Cryo-EM center, Zhejiang University) for help in processing of samples for scanning electron microscopy. This work

was supported by the grants from the National Key R&D Program of China (2021YFA0909900) to Z.G., National Science Foundation of China (62173293) to R.X., Zhejiang Provincial Natural Science Foundation of China (LD22E050007), the Fundamental Research Funds for the Zhejiang Provincial Universities (2021XZX021) to H.L., and the grants from the Startup Package of Zhejiang University to and Y.Z., H.L., J.Y., and Z.G.

Conflict of Interest

Z.G., J.Y., H.L., Y.Z., F.G., T.S., and R.J. have applied for patents related to this study. Z.G. is the co-founder of Zenomics Inc., Zencapsule Inc., Lizen Inc., Wskin Inc., and ZCapsule Inc. Z.G. and Y.Z. are the co-founders of μZen Pharma Co., Ltd., and the other authors declare no conflict of interest.

Data Availability Statement

The data that support the findings of this study are available from the corresponding author upon reasonable request.

Keywords

drug delivery, first aid, microneedles, unmanned aerial vehicles

Received: September 20, 2022

Revised: October 31, 2022

Published online: January 29, 2023

- [1] a) P. Deedwania, *J. Am. Coll. Cardiol.* **2018**, *72*, 1787; b) E. M. Singletary, D. A. Zideman, J. C. Bendall, D. C. Berry, V. Borra, J. N. Carlson, P. Cassan, W. T. Chang, N. P. Charlton, T. Djavari, M. J. Douma, J. L. Epstein, N. A. Hood, D. S. Markenson, D. Meyran, A. M. Orkin, T. Sakamoto, J. M. Swain, J. A. Woodin, F. A. S. Collaborators, *Circulation* **2020**, *142*, S284; c) C. Andersson, R. S. Vasan, *Nat. Rev. Cardiol.* **2018**, *15*, 230.
- [2] a) G. De Luca, H. Suryapranata, J. P. Ottavanger, E. M. Antman, *Circulation* **2004**, *109*, 1223; b) J. Emberson, K. R. Lees, P. Lyden, L. Blackwell, G. Albers, E. Bluhmki, T. Brott, G. Cohen, S. Davis, G. Donnan, J. Grotta, G. Howard, M. Kaste, M. Koga, R. von Kummer, M. Lansberg, R. I. Lindley, G. Murray, J. M. Olivot, M. Parsons, B. Tilley, D. Toni, K. Toyoda, N. Wahlgren, J. Wardlaw, W. Whiteley, G. J. del Zoppo, C. Baigent, P. Sandercock, W. Hacke, et al., *Lancet* **2014**, *384*, 1929; c) C. P. Cannon, C. M. Gibson, C. T. Lambrew, D. A. Shoultz, D. Levy, W. J. French, J. M. Gore, W. D. Weaver, W. J. Rogers, A. J. Tiefenbrunn, *JAMA, J. Am. Med. Assoc.* **2000**, *283*, 2941.
- [3] a) A. B. Jena, C. Mann, L. N. Wedlund, A. Olenski, *N. Engl. J. Med.* **2017**, *376*, 1441; b) Z. Kmietowicz, *BMJ* **2017**, *358*, j4339; c) J. S. Baekgaard, S. Viereck, T. P. Moller, A. K. Ersboll, F. Lippert, F. Folke, *Circulation* **2017**, *136*, 954.
- [4] C. Vergari, J. C. Mansfield, D. Chan, A. Clarke, J. R. Meakin, P. C. Winlove, *Acta Biomater.* **2017**, *63*, 274.
- [5] a) E. Kochba, Y. Levin, I. Raz, A. Cahn, *Diabetes Technol. Ther.* **2016**, *18*, 525; b) Y. Ye, J. Yu, D. Wen, A. R. Kahkoska, Z. Gu, *Adv. Drug Delivery Rev.* **2018**, *127*, 106; c) S. P. Sullivan, D. G. Koutsonanos, M. D. Martin, J. W. Lee, V. Zarnitsyn, S. O. Choi, N. Murthy, R. W. Compans, I. Skountzou, M. R. Prausnitz, *Nat. Med.* **2010**, *16*, 915; d) A. Abramson, E. Caffarel-Salvador, V. Soares, D. Minahan, R. Y. Tian, X. Y. Lu, D. Dellal, Y. Gao, S. Kim, J. Wainer, J. Collins, S. Tamang, A. Hayward, T. Yoshitake,

- H. C. Lee, J. Fujimoto, J. Fels, M. R. Frederiksen, U. Rahbek, N. Roxhed, R. Langer, G. Traverso, *Nat. Med.* **2019**, *25*, 1512; e) M. R. Prausnitz, R. Langer, *Nat. Biotechnol.* **2008**, *26*, 1261; f) W. Li, R. N. Terry, J. Tang, M. H. R. Feng, S. P. Schwendeman, M. R. Prausnitz, *Nat. Biomed. Eng.* **2019**, *3*, 220; g) J. C. Yu, Y. Q. Zhang, Y. Q. Ye, R. DiSanto, W. J. Sun, D. Ranson, F. S. Ligler, J. B. Buse, Z. Gu, *Proc. Natl. Acad. Sci. U. S. A.* **2015**, *112*, 8260; h) J. C. Yu, J. Q. Wang, Y. Q. Zhang, G. J. Chen, W. W. Mao, Y. Q. Ye, A. R. Kahkoska, J. B. Buse, R. Langer, Z. Gu, *Nat. Biomed. Eng.* **2020**, *4*, 499; i) P. C. DeMuth, Y. J. Min, B. Huang, J. A. Kramer, A. D. Miller, D. H. Barouch, P. T. Hammond, D. J. Irvine, *Nat. Mater.* **2013**, *12*, 367; j) K. Lee, M. J. Goudie, P. Tebon, W. J. Sun, Z. M. Luo, J. Lee, S. M. Zhang, K. Fetah, H. J. Kim, Y. M. Xue, M. A. Darabi, S. Ahadian, E. Sarikhani, W. Ryu, Z. Gu, P. S. Weiss, M. R. Dokmeci, N. Ashammakhi, A. Khademhosseini, *Adv. Drug Delivery Rev.* **2020**, *165–166*, 41.
- [6] K. V. Allen, B. M. Frier, *Endocr. Pract.* **2003**, *9*, 530.
- [7] a) J. Geddes, J. E. Schopman, N. N. Zammit, B. M. Frier, *Diabetic Med.* **2008**, *25*, 501; b) E. W. M. T. ter Braak, A. M. M. F. Appelman, M. F. van de Laak, R. P. Stolk, T. W. van Haeften, D. W. Erkelens, *Diabetes Care* **2000**, *23*, 1467.
- [8] T. A. Hitt, J. Smith, E. L. Forth, P. Garren, D. Olivos-Stewart, M. De la Vega, F. Stuart, C. P. Hawkes, S. M. Willi, J. Gettings, *Diabetes* **2020**, *69*, 1292.
- [9] S. Diridollou, F. Patat, F. Gens, L. Vaillant, D. Black, J. M. Lagarde, Y. Gall, M. Berson, *Skin Res. Technol.* **2000**, *6*, 214.
- [10] M. C. Jaklevic, *JAMA, J. Am. Med. Assoc.* **2021**, *325*, 613.
- [11] a) S. S. Steiner, M. Li, R. Hauser, R. Pohl, J. *Diabetes Sci. Technol.* **2010**, *4*, 1332; b) Z. Wang, J. Wang, H. Li, J. Yu, G. Chen, A. R. Kahkoska, V. Wu, Y. Zeng, D. Wen, J. R. Miedema, J. B. Buse, Z. Gu, *Proc. Natl. Acad. Sci. U. S. A.* **2020**, *117*, 29512.
- [12] A. Surnmerfield, F. Meurens, M. E. Ricklin, *Mol. Immunol.* **2015**, *66*, 14.
- [13] T. Qin, P. L. Li, S. J. Shen, *IEEE Trans. Rob.* **2018**, *34*, 1004.
- [14] Z. Wang, X. Zhou, C. Xu, F. Gao, *IEEE Trans. Rob.* **2022**, *38*, 3259.
- [15] X. Zhou, Z. P. Wang, H. K. Ye, C. Xu, F. Gao, *IEEE Rob. Autom. Lett.* **2021**, *6*, 478.
- [16] D. P. Zaharieva, K. Turksoy, S. M. McGaugh, R. Pooni, T. Vienneau, T. Ly, M. C. Riddell, *Diabetes Technol. Ther.* **2019**, *21*, 313.
- [17] a) D. C. Schedl, I. Kurmi, O. Bimber, *Sci. Rob.* **2021**, *6*, eabg1188.
b) A. Claesson, A. Backman, M. Ringh, L. Svensson, P. Nordberg, T. Djärv, J. Hollenberg, *JAMA, J. Am. Med. Assoc.* **2017**, *317*, 2332;
c) S. Schierbeck, J. Hollenberg, A. Nord, L. Svensson, P. Nordberg, M. Ringh, S. Forsberg, P. Lundgren, C. Axelsson, A. Claesson, *Eur. Heart J.* **2021**, *42*, 656; d) M. P. Nisingizwe, P. Ndishimye, K. Swaibu, L. Nshimiyimana, P. Karame, V. Dushimiyimana, J. P. Musabyimana, C. Musanabaganwa, S. Nsanizimana, M. R. Law, *Lancet Global Health* **2022**, *10*, e564.
- [18] M. A. C. Gil, *Eur. Heart J.* **2021**, *42*, 3046.
- [19] M. Krišto, M. Ivasic-Kos, M. Pobar, *IEEE Access* **2020**, *8*, 125459.
- [20] a) Z. Cao, T. Simon, S.-E. Wei, Y. Sheikh, in *2017 IEEE Conf. on Computer Vision and Pattern Recognition (CVPR)*, IEEE, Piscataway, NJ, USA **2017**, pp. 1302–1310. b) C. Fu, T. Berg, A. Berg, in *2019 IEEE/CVF Int. Conf. on Computer Vision (ICCV)*, IEEE, Piscataway, NJ, USA **2019**, pp. 5177–5186.
- [21] A. Abramson, E. Caffarel-Salvador, M. Khang, D. Dellal, D. Silverstein, Y. Gao, M. R. Frederiksen, A. Vegge, F. Hubalek, J. J. Water, A. V. Friderichsen, J. Fels, R. K. Kirk, C. Cleveland, J. Collins, S. Tamang, A. Hayward, T. Landh, S. T. Buckley, N. Roxhed, U. Rahbek, R. Langer, G. Traverso, *Science* **2019**, *363*, 611.

Canfly: A Can-sized Autonomous Mini Coaxial Helicopter

Neng Pan, Rui Jin, Chao Xu, and Fei Gao



Fig. 1: The proposed coaxial helicopter (a) autonomously navigates through an unknown cluttered environment, (b) possesses a miniature size slightly larger than a can of soda, (c) deftly crosses through a narrow gap of 125mm wide.

Abstract— The development of autonomous rotary-wing UAVs has shown an evident tendency in miniaturization. However, the side effects brought by miniaturization, such as decreased load capability, shorter flight duration and reduced autonomous ability, seriously hinder its process. In this paper, we first investigate the configurations of different rotary-wing aircraft and optimize the configuration selection. Afterward, with several elaborate mechanisms contributing to the miniaturization, we present the hardware design and control strategy of a mini coaxial helicopter, which is 62% smaller than the state-of-the-art autonomous mini quadrotor so far in collision area [1]. Meanwhile, abundant experiments reveal that it achieves impressive traversability and is capable of conducting autonomous tasks in unknown dense scenarios, while maintaining satisfactory performance regarding loadability and flight duration.

I. INTRODUCTION

In recent years, due to rotary-wing UAVs' hovering capability and impressive agility, they have attracted significant attention across numerous fields, such as aerial photography, rescue operation, collaborative exploration, and formation shows. Meanwhile, the development of UAVs has shown an evident tendency in miniaturization [1]–[4], because the smaller size brings higher mobility, greater traversability, and enhanced safety, thus broadening their application. For example, the ruins after an earthquake are too rugged and dense with obstacles for any ground vehicles or medium-sized UAVs to pass through, while agile mini UAVs can squeeze into the debris and deliver hope for the victims. However, miniaturization also brings challenges, including

All authors are with the State Key Laboratory of Industrial Control Technology, Zhejiang University, Hangzhou 310027, China and Huzhou Institute, Zhejiang University, Huzhou 313000, China. This work was supported by the National Natural Science Foundation of China under grant no. 62003299 and the Fundamental Research Funds for the Central Universities.

E-mail:{panneng_zju, fgaoaa}@zju.edu.cn

weaker load capability, shorter flight duration and poorer autonomous ability.

To explore the boundary of miniaturization without sacrificing the flight duration and autonomous ability, an elaborate investigation and thorough design of the hardware configuration are essential. Thanks to quadrotors' compact mechanism and simple control strategy, previous researchers have developed several impressive mini quadrotor systems [1, 3, 4]. However, quadrotors are not the best choice for miniaturization. In the later discussion in Sec. III-A, we demonstrate that helicopters enjoy the highest power efficiency among all kinds of rotary-wing aircraft.

So it's an intuitive idea to draw inspiration from the development of helicopters. During the last few decades, we have seen various configurations of helicopters [2], all showing great potential in different fields. However, most of them suffer from complicated mechanisms, poor controllability or high energy consumption, bringing great difficulties to miniaturization, as discussed in Sec. II.

Based on the reflection of previous works, we develop a mini configuration of UAVs. We name it as Canfly, meaning it has a similar size to a soda can, as shown in Fig. 1(b). Sufficient work is made to minimize Canfly's size, while guaranteeing its loadability and flight duration. The dynamic model and control strategy are presented later in Sec. V. Finally, in Sec. VI Canfly is challenged to navigate through an unknown environment setup with dense obstacles and cross through a narrow gap of 125mm wide, revealing its satisfactory controllability and impressive traversability.

We summarize our contributions as follows:

- 1) A comprehensive investigation into different kinds of rotary-wing UAV configuration, supporting the view that coaxial helicopters based on control surfaces are the most suitable configuration for mini autonomous UAVs.
- 2) The hardware design and control strategy of a coaxial

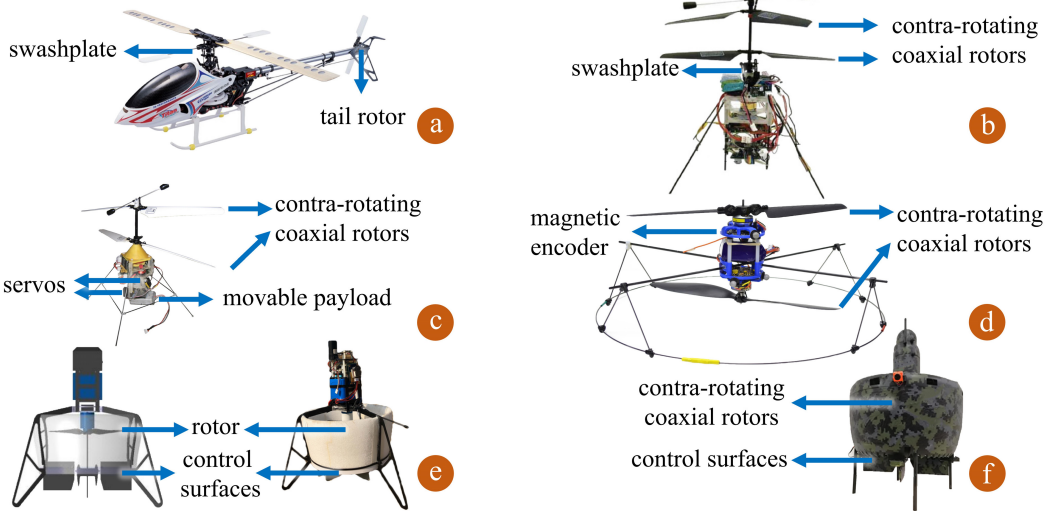


Fig. 2: (a) A conventional electric helicopter with a swashplate and a tail rotor proposed by Schafroth et al. [5]. (b) A coaxial helicopter without a tail rotor proposed by Bouabdallah et al. [6, 7]. (d) A coaxial helicopter with only two motors proposed by Paulos et al. [8, 9]. (e) A homotaxial helicopter controlled by control surfaces, proposed by Deng et al. [10]. (f) A coaxial helicopter controlled by control surfaces, proposed by Deng et al. [11].

helicopter based on control surfaces, which is 62% smaller than the state-of-the-art smallest autonomous UAV platform in collision area [1].

- 3) Sufficient experiments validating the controllability, autonomous ability and traversability of Canfly.

II. RELATED WORKS

A. Miniaturization Process of Quadrotors

Many researchers have explored the miniaturization of autonomous UAVs [1, 3, 4]. One of the representative works is the Crazyflie series proposed by Giernacki et al. [4]. Crazyflie is a nano quadrotor whose minimum circumscribed circle's diameter is 137mm, which is very impressive for an autonomous UAV. However, due to the usage of coreless DC motors, the maximum payload of Crazyflie is limited to 15g. The poor load capability tightly restricts the introduction of vision sensors with higher precision, onboard computers with higher computational power, or batteries with larger capacity, which is necessary for most autonomous tasks. As a result, Crazyflies can only conduct low-level autonomous tasks, waypoints tracking for example.

To make the UAVs qualified for high-level autonomous tasks, researchers [3] equip a brushless-motor-driven quadrotor with a DJI Manifold2-C onboard computer and a Realsense D435 stereo camera. This quadrotor is 377mm wide in circumscribed circle's diameter, and capable of carrying a payload up to 1kg. Later, Zhou et al. [1] integrate the system into a more compact configuration whose width is 188mm and the payload is 200g, making it the smallest autonomous UAV system qualified for high-level tasks so far.

However, previous works tend to dig into the configurations of quadrotors. In the later discussion in Sec. III-A, we prove that helicopters are the preferred configurations for mini UAVs, and we should focus more on the development of helicopters.

B. Development of Helicopters

During the last few decades, various configurations of helicopters [2] have sprung up, all showing great potential in different fields. The most commonly seen helicopter [12], as shown in Fig. 2(a), consists of a swashplate and a tail rotor. The swashplate is a delicate mechanism that can control the orientation of the thrust vector, but its complicated structure makes it rather challenging to be applied in mini UAVs. Moreover, the extra tail rotor also increases the body length, bringing more difficulty to miniaturization.

To get rid of the tail rotor, researchers have come up with a coaxial helicopter with a swashplate [5, 13], as shown in Fig. 2(b). Its contra-rotating coaxial rotors can provide thrust while generating little reaction torque and gyroscopic torque, which means it can achieve full controllability of yaw without the help of the tail rotor. However, the generation of pitch torque and roll torque still relies on the cyclic control of the swashplate, making the miniaturization process still challenging. On the other hand, the integrated contra-rotating rotors present an additional complexity to the mechanism.

To avoid the introduction of the swashplate, Bouabdallah et al. [6, 7] propose a coaxial helicopter whose steering is achieved by controlling the center of gravity with two servos, as shown in Fig. 2(c). Such designs greatly reduce the size of the vehicle, but the price is that it suffers from little control margin and poor controllability.

Other researchers propose a coaxial helicopter that can emulate full actuation over forces and torques using only two motors [8, 9], as shown in Fig. 2(d). It is realized by exciting the motors with a cyclic flapping response to control the orientation of the thrust vector. Unfortunately, the motors will overheat during high-frequency accelerations and decelerations, where much energy is wasted. Moreover, the introduction of magnetic encoders in this configuration is not a practical choice for miniaturization, either.

Another way to gain pitch and roll torque is by adopting aerodynamic control surfaces. Researchers [10, 14] discuss the design and control strategy of a homotaxial helicopter that consists of one motor and four individual control surfaces, as shown in Fig. 2(e). The motor provides the thrust and the control surfaces provide the torque in roll, pitch and yaw. Researchers [11] propose a similar helicopter with coaxial rotors, which can naturally get rid of the reaction torque and gyroscopic torque, as shown in Fig. 2(f). Such designs based on control surfaces abandon all complicated transmission mechanisms, have few fatal drawbacks, and are in our favor for miniaturization. We will discuss the difference between them in detail in Sec. III-B.

III. CONFIGURATION COMPARISON AND OPTIMIZATION

A. Efficiency of Different Configurations of Rotary-Wings

As mentioned above, the main purpose of the hardware design is to minimize the valid size while maintaining satisfactory hover efficiency. In this paper, we take the minimum circumscribed circle's area of the horizontal projection as the valid size of a UAV, because the vehicle is modeled as a sphere or a circle in most path planning algorithms [15, 16]. On the other hand, we focus more on the horizontal area because there is more vertical free space than horizontal free space in most structured and unstructured scenarios, cities with dense buildings, narrow windows and forests for example. In this section, we will demonstrate that the helicopters enjoy the maximum hover efficiency among the commonly used configurations of rotary-wing aircraft.

According to the momentum theory [17] and the verification in work [18], we know that the ideal power P of a rotor to produce a thrust F_T is

$$P(F_T) = F_T \sqrt{\frac{F_T}{2S\rho}}, \quad (1)$$

where S is the swept area of the rotor, and ρ is the density of air. For a rotary-wing aircraft with n rotors and total mass of m_l , the hover efficiency E_h is

$$E_h(n) = \frac{MASS}{POWER} = \frac{m_l}{n \cdot P(m_l g/n)} = \sqrt{\frac{2S n \rho}{m_l g^3}}. \quad (2)$$

Given a circumscribed circle of radius R , the radius r of the helicopter's propeller is simply R . As for a multicopter whose number of rotors $n \geq 2$, assume the rotors are tangent to the adjacent rotors¹, which should maximize the valid rotor area. The circumstance is shown in Fig. 3, where O is the center of the circumscribed circle, and $O_k(k \in N_+)$ is the center of the k^{th} rotor.

As for $O_1 O_2 O_3 \dots O_n$ is an equilateral polygon, we know

$$\begin{aligned} \angle O_2 O O_3 &= \frac{2\pi}{n}, \\ OO_2 &= \frac{O_2 O_3}{2 \sin(\pi/n)} = \frac{r}{\sin(\pi/n)}. \end{aligned} \quad (3)$$

¹In practice, we have to leave some spaces between each rotor, which will result in a less valid rotor area for multicopters.

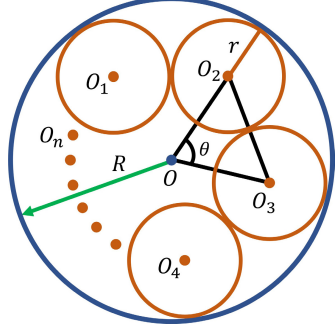


Fig. 3: Circumscribed circle of a multicopter with n rotors. O is the center of the circumscribed circle, and $O_k(k \in N_+)$ is the center of the k^{th} rotor.

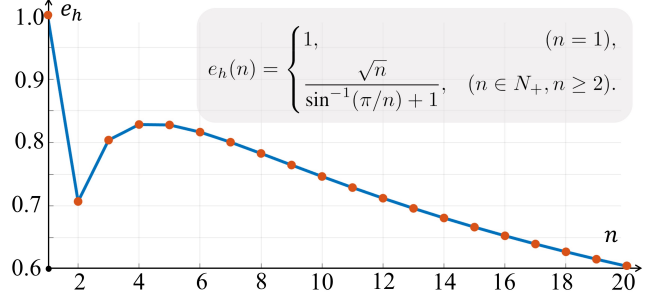


Fig. 4: The figure of $e_h(n)$, a dimensionless coefficient indicating the hover efficiency of a rotary-wing aircraft with n rotors.

Together with $R = OO_2 + r, (n \in N_+, n \geq 2)$, we have

$$r = \begin{cases} R, & (n = 1), \\ \frac{R}{1 + \sin^{-1}(\pi/n)}, & (n \in N_+, n \geq 2). \end{cases} \quad (4)$$

Given $S = \pi r^2$, substituting Equ. (4) to Equ. (1) gives us

$$E_h(n) = \begin{cases} \sqrt{\frac{2\pi\rho}{m_l g^3}} R, & (n = 1), \\ \sqrt{\frac{2\pi\rho}{m_l g^3}} R \cdot \frac{\sqrt{n}}{\sin^{-1}(\pi/n) + 1}, & (n \in N_+, n \geq 2). \end{cases} \quad (5)$$

Assuming the load m_l is the same for every multicopter, the term $\sqrt{2\pi\rho/m_l g^3} R$ is a constant value, and Equ. (5) indicates that the hover efficiency is proportional to

$$e_h(n) = \begin{cases} 1, & (n = 1), \\ \frac{\sqrt{n}}{\sin^{-1}(\pi/n) + 1}, & (n \in N_+, n \geq 2). \end{cases} \quad (6)$$

By drawing the figure of $e_h(n)$ shown in Fig. 4, we know $e_h(n)$ is a function whose two maximum values locate in

$$\begin{aligned} e_{h\max 1} &= e_h(1) = 1, \\ e_{h\max 2} &= e_h(4) = \frac{2}{\sqrt{2} + 1} \approx 0.828, \end{aligned} \quad (7)$$

which indicates that the hover efficiency of a helicopter is higher than any other rotary-wing aircraft.



Fig. 5: The comparison between a coaxial helicopter and a homotaxial helicopter.

B. Coaxial Helicopters vs. Homotaxial Helicopters

As we discuss in Sec. II and Sec. III-A, we find out that helicopters based on control surfaces are the preferred choice for mini UAVs. In this subsection, we discuss whether a homotaxial one or a coaxial one is a more suitable configuration for the desired mini autonomous UAV.

The typical coaxial helicopter design consists of two motors and two servos, and the typical homotaxial helicopter design consists of one motor and four servos, as shown in Fig. 5. In a coaxial helicopter, the contra-rotating rotors provide thrust and yaw torque, and the control surfaces provide roll and pitch torque. The opposite control surfaces move in the same direction, so they can be driven by the same servo. While in a homotaxial helicopter, the reaction torque of the rotor has to be balanced by the control surfaces, so the opposite control surfaces may move in different directions, which means they have to be driven individually. Thus we know that coaxial helicopters have fewer actuators and a more compact mechanism than homotaxial helicopters.

Meanwhile, coaxial helicopters enjoy higher hover efficiency and maximum thrust than homotaxial helicopters. Assume that a coaxial helicopter and a homotaxial helicopter have the same mass m and propeller radius R . Rewrite Equ. (5) as

$$E_h(m_l) = \sqrt{\frac{2\pi\rho}{g^3}} R \cdot \frac{1}{\sqrt{m_l}}. \quad (8)$$

According to Equ. (8), we know $E_h(m_l)$ is a decreasing function with respect to the load m_l . The power of the coaxial helicopter P_{coax} is the sum of the two rotors whose load is $m/2$,

$$P_{coax}(m) = 2 \cdot \frac{\frac{m}{2}}{E_h(\frac{m}{2})} = \frac{m}{E_h(\frac{m}{2})}. \quad (9)$$

$$E_{coax}(m_l) = E_h(\frac{m_l}{2}). \quad (10)$$

As for the homotaxial helicopter, the power is simply

$$P_{homo}(m) = \frac{m}{E_h(m)}, \quad E_{homo}(m_l) = E_h(m_l). \quad (11)$$

Combining Equ. (10) and Equ. (11) gives

$$E_{coax}(m_l) = \sqrt{2}E_{homo}(m_l), \quad (12)$$

which indicates coaxial helicopters are 41.4% more efficient than homotaxial helicopters ideally.

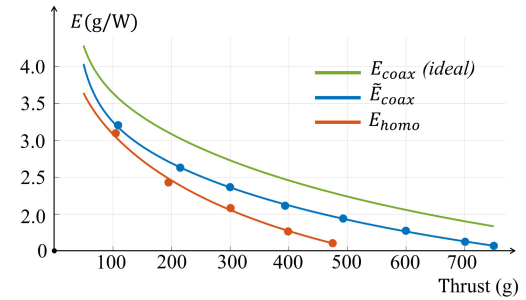


Fig. 6: The hover efficiency of ideal coaxial rotor, corrected coaxial rotors and a homotaxial rotor at different thrusts.

C. Aerodynamic Power Loss and Rotor Efficiency

In practice, we know there exists a nonnegligible aerodynamic disturbance between the coaxial rotors, which will result in reduced power efficiency [19]. If we take the aerodynamic power loss η_{AL} into consideration, we have the corrected hover efficiency \tilde{E}_{coax} and power of the coaxial helicopter \tilde{P}_{coax} ,

$$\tilde{P}_{coax}(m) = \frac{m}{E_h(\frac{m}{2})(1 - \eta_{AL})}, \quad (13)$$

$$\tilde{E}_{coax}(m) = E_h(\frac{m}{2})(1 - \eta_{AL}). \quad (14)$$

To measure η_{AL} , we conduct an experiment and measure the power of the homotaxial rotor and coaxial rotors at different thrusts. The motor and propeller setup is presented in Sec. IV. Afterward, we use a second-order polynomial to fit the hover efficiency with respect to the thrust and calculate the ideal coaxial hover efficiency according to Equ. (10). The result is shown in Fig. 6.

From the result, we know that η_{AL} is around 13.8% in our configuration, and the corrected coaxial hover efficiency \tilde{E}_{coax} is 19.5% higher than the homotaxial helicopter's efficiency E_{homo} . Furthermore, the experiment also reveals that the maximum thrust of the coaxial rotors is 58.2% higher than the single rotor, providing abundant thrust for aggressive flight and extra payloads.

IV. HARDWARE DESIGN AND IMPLEMENTATION

Based on the reflection of previous works in Sec. II and analysis in Sec. III, we know that coaxial helicopters based on control surfaces are the most suitable configuration for the desired mini autonomous UAVs. In this section, we present our implementation and design details of the mini coaxial helicopters Canfly.

A. Hardware Implementation

The illustration of the hardware is shown in Fig. 7. The motors are mounted on the same carbon fiber board, where a 3D print component with counter bores is used to avoid the interference of bolts. Compared with conventional integrated contra-rotating motors [5]–[7, 11, 13] where the two motors share the same shaft, such split-type installation can greatly simplify the structure and can be applied to any kind of commercial motors. To avoid interference between

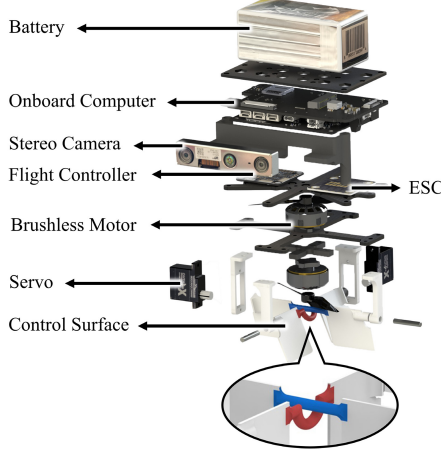


Fig. 7: Illustration of the proposed system's hardware.

TABLE I: Weight and model of each component

Component	Model	Weight (g)
Battery	GNB 1700mAh Li-Hv 4S	160
Onboard computer	NVIDIA Xavier NX	72
Motor	T-Motor F2004	65
Stereo camera	Intel Realsense D430	30
Control surface	3D print	20
Servo	BlueArrow X-4	15
Frame	Carbon fiber	15
Bolts&wires		10
Flight controller	Holybro Kakute Mini	8
ESC	Holybro Tekko32 45A	7
Propeller	Gemfan D76	6
Total		408

the two control surfaces while not increasing the height of the vehicle, we bend one of the control surfaces' connecting shafts, as the red and blue highlights in Fig. 7 show.

The total weight of Canfly is 408g, and the maximum payload is 150g. The weight and model of each component are listed in Table. I. The flight duration is up to 8 minutes, which is satisfactory for such a mini vehicle with a relatively large payload.

B. Ductless Design

Other helicopters with larger sizes tend to adopt a duct to increase the hover efficiency [10, 11, 14]. However, in this work we discard the duct design mainly based on the following reasons. From work [20] we know the gap between the propeller's tip and the duct's inwall has to be smaller than 3% of the propeller's height to provide a beneficial effect on the system, which in our case is

$$4mm * 3\% = 0.12mm.$$

However, the typical precision of 3D printing is around 0.2mm, which makes manufacturing rather hard. On the other hand, a slight deformation can easily destroy the delicate gap and leads to a crush, weakening the robustness of the system. Finally, the proposed system is mainly designed for hovering and low-speed cruising, where the duct introduces

much air drag while providing little lift force. In conclusion, the duct design is not practical or beneficial to the proposed system with miniature size.

C. Size and Efficiency Comparison

In this subsection, we compare the valid size described in Sec. III-A as well as hover efficiency between Canfly and the state-of-the-art mini UAV system that shares the similar autonomous ability to Canfly [1].

The diameter of the minimum circumscribed circle of Canfly is 116mm, while Zhou's is 188mm. The area of the valid collision size of Canfly is 62% less than Zhou's. The illustration is shown in Fig. 8.

As for the hover efficiency, we can calculate it with the battery capacity C , voltage U , flight duration T and total weight m , which can be found in the corresponding paper,

$$E = \frac{UC}{Tm}. \quad (15)$$

The hover efficiency of Zhou's is 2.50g/W, while Canfly's is 2.16g/W, indicating that our system can achieve similar hover efficiency with remarkably reduced size.

V. CONTROL

A. Dynamic Model

We introduce two frames for later discussion: body frame ($\mathbf{x}_b - \mathbf{y}_b - \mathbf{z}_b$) and FLU (Forward- Left- Up) world frame ($\mathbf{x}_w - \mathbf{y}_w - \mathbf{z}_w$).

Assume that the aerodynamic forces generated by the control surfaces are horizontal and the vertical drag part is relatively small and can be neglected.

The force analysis is shown in Fig.9, where CoM is the center of mass, f is the collective thrust, F_{CS_i} is the horizontal force generated by the control surfaces, α, β are the angle of the control surfaces respective to \mathbf{z}_b , and H is the vertical distance between CoM and control surfaces.

Consider the state of the vehicle $\mathbf{x} = \{\mathbf{r}, \mathbf{R}\}$, where \mathbf{r} is the position of the vehicle's center of mass in the world frame, and \mathbf{R} is the rotation of the body with respect to the world frame. The input is $\mathbf{u} = \{f, \tau\}$, where f is the collective thrust, and τ is the torque generated by the actuators. Then we have the dynamic model based on Newton-Euler Equation,

$$m\ddot{\mathbf{r}} = -mg\mathbf{e}_3 + f\mathbf{R}\mathbf{e}_3 + \mathbf{F}_{CS}, \quad (16)$$

$$\mathbf{J}\dot{\boldsymbol{\omega}} = \boldsymbol{\tau} - \boldsymbol{\omega} \times \mathbf{J}\boldsymbol{\omega}. \quad (17)$$

In Equ. (16), m is the total mass of the vehicle, g is the gravitational acceleration, $\mathbf{e}_3 = (0, 0, 1)^T$, and \mathbf{F}_{CS} is the force generated by the control surfaces in the body frame. In Equ. (17), \mathbf{J} is the inertia matrix, $\boldsymbol{\omega}$ is the angular rate in body frame.

B. Control Surface

In the proposed system, we adopt two flat planes driven by the servos as control surfaces to generate torque in \mathbf{x}_b and

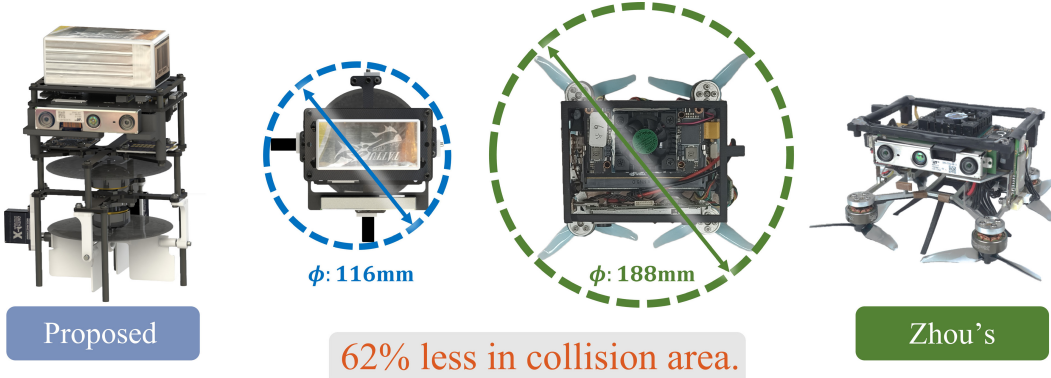


Fig. 8: Comparison with Zhou's quadrotor platform [1], the smallest UAV system so far that share similar autonomous ability with our system. The area of the valid collision size of the proposed system is 62% less than Zhou's.

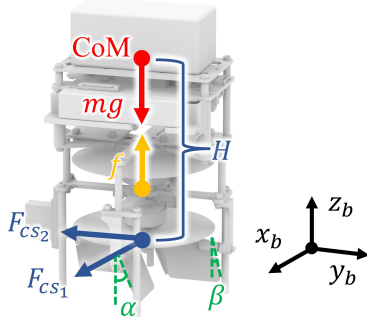


Fig. 9: The force analysis and frame definition of the proposed system.

\mathbf{y}_b . According to the work [21], we know the force acting on the control surface can be expressed as

$$F_{CS} = \frac{1}{2} \rho V_a^2 S C_L, \quad (18)$$

where ρ is the density of the air, V_a is the velocity of the inflow air, S is the platform area of the control surface, and C_L is the aerodynamic coefficient.

Assuming that the vehicle travel at a low speed and the velocity of the wind can be ignored, we know that V_a equals the speed of the airflow accelerated by the propellers. On the other hand, according to [21] we know the thrust generated by the propeller is proportional to the square of the accelerated airflow's speed ,

$$f = K_v V_a^2, \quad (19)$$

where K_v is a constant coefficient.

Assume that the angle of control surfaces θ is small, which is acceptable for low-speed traveling, the aerodynamic coefficients C_L can be linearized by Taylor expansion as,

$$C_L(\theta) = C_{L0} + C_{L\theta}\theta, \quad (20)$$

where C_{L0} is the value of C_L when $\alpha = 0$, and $C_{L\theta}$ is a constant coefficient. Note that $C_{L0} = 0$, because the control surface generates no force when it is vertical, we can rewrite Equ. (20) as

$$C_L(\theta) = C_{L\theta}\theta. \quad (21)$$

Combine Equ. (18), Equ. (19) and Equ. (21), we can conclude that F_{CS} is proportional to the product of θ and f ,

$$F_{CS} = K_{CS}f\theta, \quad K_{CS} = \frac{\rho S C_{L\theta}}{2K_v}. \quad (22)$$

where K_{CS} is a constant coefficient that can be identified in static conditions. This way, the \mathbf{F}_{CS} in Equ. (16) can be defined as

$$\mathbf{F}_{CS} = [K_{CS}f\beta, \quad K_{CS}f\alpha, \quad 0]^T \quad (23)$$

C. Mixer

We use $\mathbf{u} = [f, \tau]^T$ to denote the control input. Given the standard motor model,

$$f_i = K_F \omega_i^2, \quad \tau_i = K_M \omega_i^2, \quad (24)$$

where f_i is the produced force, τ_i is the reaction torque, ω_i is the motor's angular velocity, K_F is the thrust coefficient and K_M is the reaction torque coefficient, we have

$$\mathbf{u} = \begin{bmatrix} K_F & K_F & 0 & 0 \\ 0 & 0 & K_{CS}H & 0 \\ 0 & 0 & 0 & K_{CS}H \\ K_M & -K_M & 0 & 0 \end{bmatrix} \begin{bmatrix} \omega_u^2 \\ \omega_l^2 \\ \alpha u_0 \\ \beta u_0 \end{bmatrix}, \quad (25)$$

where ω_u is the angular velocity of the upper motor, and ω_l is the angular velocity of the lower motor.

From Equ. (25), we can derive the actuator output

$$\begin{aligned} \omega_u &= \sqrt{\frac{1}{2} \left(\frac{u_0}{K_F} + \frac{u_3}{K_M} \right)}, \\ \omega_l &= \sqrt{\frac{1}{2} \left(\frac{u_0}{K_F} - \frac{u_3}{K_M} \right)}, \\ \alpha &= \frac{u_1}{K_{CS}H u_0}, \\ \beta &= \frac{u_2}{K_{CS}H u_0}. \end{aligned} \quad (26)$$

D. Attitude Control

We use a cascade control structure to control the attitude, as shown in Fig. 10. The attitude-angular-rate loop is a proportional controller based on the quaternion error described in [22], and the angular-rate-torque loop is a PID controller.

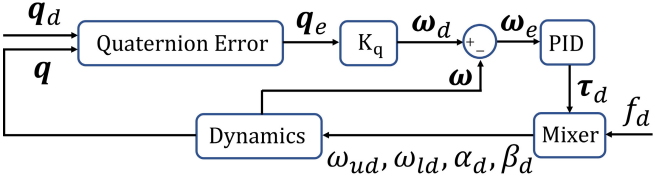


Fig. 10: The control pipeline of the proposed system's attitude control, where a cascade PID controller is applied.

Firstly, we obtain the quaternion \mathbf{q} and angular velocity $\boldsymbol{\omega}$ of the vehicle from the IMU, and calculate the quaternion error \mathbf{q}_e between \mathbf{q} and desired quaternion \mathbf{q}_d ,

$$\mathbf{q}_e = \mathbf{q}^{-1} \mathbf{q}_d. \quad (27)$$

Next, we calculate the desired angular rate $\boldsymbol{\omega}_d$ using the proportional gain \mathbf{K}_q ,

$$\mathbf{K}_q = \text{diag}(K_{q1}, K_{q2}, K_{q3}), \quad (28)$$

$$\boldsymbol{\omega}_d = \mathbf{K}_q \text{sgn}(\mathbf{q}_{e,0}) \mathbf{q}_{e,1:3}, \quad (29)$$

where

$$\text{sgn}(x) = \begin{cases} 1, & (x \geq 0), \\ -1, & (x < 0). \end{cases} \quad (30)$$

Afterwards, we calculate the desired torque τ_d using PID gains $\{\mathbf{K}_{P\omega}, \mathbf{K}_{I\omega}, \mathbf{K}_{D\omega}\}$

$$\begin{aligned} \mathbf{K}_{P\omega} &= \text{diag}(K_{P\omega 1}, K_{P\omega 2}, K_{P\omega 3}), \\ \mathbf{K}_{I\omega} &= \text{diag}(K_{I\omega 1}, K_{I\omega 2}, K_{I\omega 3}), \\ \mathbf{K}_{D\omega} &= \text{diag}(K_{D\omega 1}, K_{D\omega 2}, K_{D\omega 3}), \end{aligned} \quad (31)$$

$$\tau_d = \left(\mathbf{K}_{P\omega} + \mathbf{K}_{I\omega} \frac{1}{s} + \mathbf{K}_{D\omega} s \right) (\boldsymbol{\omega}_d - \boldsymbol{\omega}). \quad (32)$$

Together with the desired thrust f_d , we can obtain the desired actuator output $\{\omega_{ud}, \omega_{ld}, \alpha_d, \beta_d\}$ according to the mixer in Equ. (26).

E. Trajectory Tracking

In the research for trajectory tracking of quadrotors, a technique called differential flatness is widely used, which means the states and the inputs of the vehicle can be written as algebraic functions of some carefully selected flat outputs and their derivatives. This can help simplify the control and planning process.

In our case, the combined external forces

$$\mathbf{f}_{ex} = f \mathbf{R} \mathbf{e}_3 + \mathbf{R} \mathbf{F}_{CS}, \quad (33)$$

is not always aligned with \mathbf{z}_b of the body. However, the \mathbf{F}_{CS} term is relatively small with respect to the thrust, so it's reasonable and practical to assume \mathbf{f}_{ex} is parallel to \mathbf{z}_b . This way, the dynamic of the proposed system is the same as quadrotors' and quadrotors' derived property of differential flatness can be directly applied [23], equipping Canfly with the compatibility for the popular path planners designed for quadrotors [1, 15].

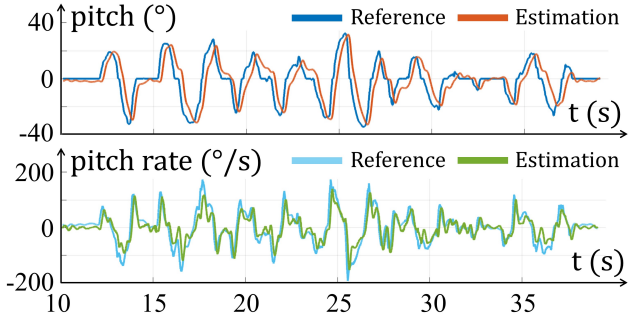


Fig. 11: The result of pitch and pitch rate tracking.

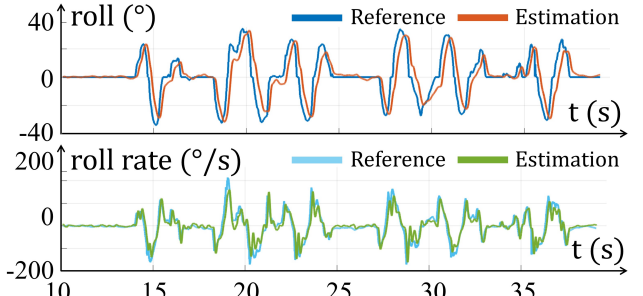


Fig. 12: The result of roll and roll rate tracking.

VI. EXPERIMENTS

A. Attitude Control Validation

In this experiment, we validate the proposed system's attitude control performance. The attitude setpoint signal is given by a remote controller, and the control series is an imitation of a typical aggressive flight, where the maximum pitch angle and roll angle can reach up to 34° . The results are shown in Fig. 11, Fig. 12 and Fig. 13.

From the result we can tell the drone can track the attitude series well. However, the delay between the estimation and reference is around $180ms$, which is relatively big compared with typical quadrotors (around $50ms \sim 100ms$). This is mainly brought by the dynamics of the servos where a pure delay is introduced, and stands as a common problem in most servo-based aircrafts.

B. Autonomous Navigation in Unknown Scenarios

In this experiment, we validate the proposed system's autonomous ability. The environment is set up with dense obstacles and the drone is demanded to travel $15m$ ahead at the maximum speed of $1m/s$. The localization is given by the visual-inertial-odometry system VINS-Fusion [24], and the local planner is Ego-Planner [16]. The illustration of the environment and the navigation path is shown in Fig. 1(a). The position tracking error results are shown in Fig.14, and the $RMSE$ is $0.070m$.

C. Crossing a Narrow Gap

In this experiment, we have the drone cross a narrow gap of $125mm$ wide, even shorter than the height of a typical

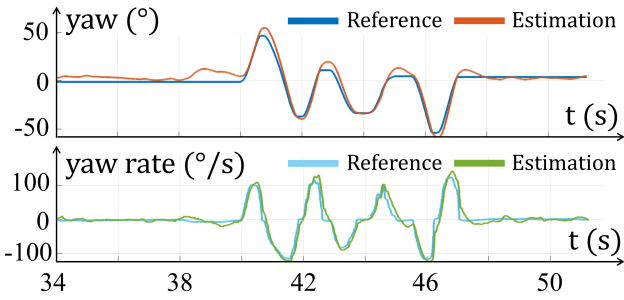


Fig. 13: The result of yaw and yaw rate tracking.

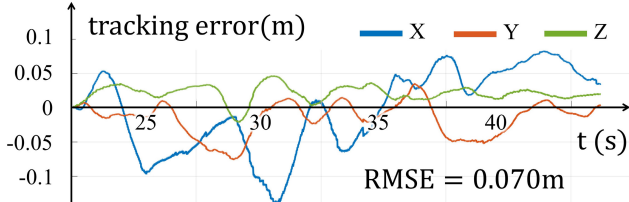


Fig. 14: The tracking error result of autonomous navigation experiment, where the $RMSE$ is $0.070m$.

smartphone. The position setpoint is given by the remote controller. The illustration is shown in Fig. 1(c).

We recommend the readers refer to the attached video for more details of the experiments.

VII. CONCLUSION

In this work, we first compare the pros and cons among different configurations of rotary-wing aircraft and demonstrate that coaxial helicopters based on control surfaces are the preferred choice for mini UAVs. Afterward, we propose the hardware design of the coaxial helicopter Canfly, with several elaborate mechanisms to minimize its size. Later, we present the dynamic model and control strategy of the proposed system. Finally, abundant experiments are carried out to validate the proposed system's controllability, autonomous ability and traversability, showing its convincing potential to be applied in various fields.

However, there still exist some problems that need further exploration. On the one hand, as the horizontal projection's area decreases, the height of the proposed system increases due to the stacking of the components, which weakens its traversability in the face of horizontal narrow gaps. On the other hand, the arrangement of the mechanism is not optimized, where the air flow inlet of the propeller is partially blocked, resulting in a higher aerodynamic loss. In the future, we aim to optimize the mechanism of Canfly to broaden its application to wider fields.

REFERENCES

- [1] Xin Zhou, Xiangyong Wen, Zhepei Wang, Yuman Gao, Haojia Li, Qianhao Wang, Tiankai Yang, Haojian Lu, Yanjun Cao, Chao Xu, et al. Swarm of micro flying robots in the wild. *Science Robotics*, 7(66):eabm5954, 2022.
- [2] Shahin Darvishpoor, Jafar Roshanian, Ali Raissi, and Mostafa Hasanian. Configurations, flight mechanisms, and applications of unmanned aerial systems: A review. *Progress in Aerospace Sciences*, 121:100694, 2020.
- [3] Fei Gao, Luqi Wang, Boyu Zhou, Xin Zhou, Jie Pan, and Shaojie Shen. Teach-repeat-replan: A complete and robust system for aggressive flight in complex environments. *IEEE Transactions on Robotics*, 36(5):1526–1545, 2020.
- [4] Wojciech Giernacki, Mateusz Skwierczyński, Wojciech Witwicki, Paweł Wroński, and Piotr Kozierski. Crazyflie 2.0 quadrotor as a platform for research and education in robotics and control engineering. In *2017 22nd International Conference on Methods and Models in Automation and Robotics (MMAR)*, pages 37–42. IEEE, 2017.
- [5] Modeling, system identification and robust control of a coaxial micro helicopter. *Control Engineering Practice*, 18(7):700–711, 2010.
- [6] Samir Bouabdallah, Roland Siegwart, and Gilles Caprari. Design and control of an indoor coaxial helicopter. In *2006 IEEE/RSJ International Conference on Intelligent Robots and Systems*, pages 2930–2935. IEEE, 2006.
- [7] Christian Bermes, Stefan Leutenegger, Samir Bouabdallah, Dario Schafroth, and Roland Siegwart. New design of the steering mechanism for a mini coaxial helicopter. In *2008 IEEE/RSJ International Conference on Intelligent Robots and Systems*, pages 1236–1241. IEEE, 2008.
- [8] James Paulos and Mark Yim. Flight performance of a swashplateless micro air vehicle. In *2015 IEEE International Conference on Robotics and Automation (ICRA)*, pages 5284–5289. IEEE, 2015.
- [9] James Paulos, Bennet Caraher, and Mark Yim. Emulating a fully actuated aerial vehicle using two actuators. In *2018 IEEE International Conference on Robotics and Automation (ICRA)*, pages 7011–7016. IEEE, 2018.
- [10] Zihuan Cheng and Hailong Pei. Flight transition control for ducted fan uav with saturation on control surfaces. In *2021 International Conference on Unmanned Aircraft Systems (ICUAS)*, pages 439–446. IEEE, 2021.
- [11] Shuanghou Deng, Siwei Wang, and Zheng Zhang. Aerodynamic performance assessment of a ducted fan uav for vtol applications. *Aerospace Science and Technology*, 103:105895, 2020.
- [12] Wayne Johnson. *Helicopter theory*. Courier Corporation, 2012.
- [13] Havard Fjaer Grip, Wayne Johnson, Carlos Malpica, Daniel P Scharf, Milan Mandic, Larry Young, Brian Allan, Bérénice Mettler, and Miguel San Martin. Flight dynamics of mars helicopter. 2017.
- [14] Larry Lipera, Jason D Colbourne, Mark B Tischler, M Hossein Mansur, Michael C Rotkowitz, and Paul Patangui. The micro craft istar micro air vehicle: Control system design and testing. In *Annual Forum Proceedings-American Helicopter Society*, volume 57, pages 1998–2008. AMERICAN HELICOPTER SOCIETY, INC, 2001.
- [15] B. Zhou, F. Gao, L. Wang, C. Liu, and S. Shen. Robust and efficient quadrotor trajectory generation for fast autonomous flight. *IEEE Robotics and Automation Letters*, 4(4):3529–3536, 2019.
- [16] Xin Zhou, Zhepei Wang, Hongkai Ye, Chao Xu, and Fei Gao. Ego-planner: An esdf-free gradient-based local planner for quadrotors. *IEEE Robotics and Automation Letters*, 6(2):478–485, 2021.
- [17] Gordon J Leishman. *Principles of helicopter aerodynamics with CD extra*. Cambridge university press, 2006.
- [18] Youming Qin, Wei Xu, Adrian Lee, and Fu Zhang. Gemini: A compact yet efficient bi-copter uav for indoor applications. *IEEE Robotics and Automation Letters*, 5(2):3213–3220, 2020.
- [19] Vinod K Lakshminarayanan and James D Baeder. Computational investigation of microscale coaxial-rotor aerodynamics in hover. *Journal of aircraft*, 47(3):940–955, 2010.
- [20] Ali Akturk and Cengiz Camci. Tip clearance investigation of a ducted fan used in vtol uavs: Part 1—baseline experiments and computational validation. In *Turbo Expo: Power for Land, Sea, and Air*, volume 54679, pages 331–344, 2011.
- [21] Randal W Beard and Timothy W McLain. *Small unmanned aircraft: Theory and practice*. Princeton university press, 2012.
- [22] Dario Brescianini, Markus Hehn, and Raffaello D'Andrea. Nonlinear quadrocopter attitude control: Technical report. Technical report, ETH Zurich, 2013.
- [23] Daniel Mellinger and Vijay Kumar. Minimum snap trajectory generation and control for quadrotors. In *2011 IEEE International Conference on Robotics and Automation(ICRA)*, pages 2520–2525. IEEE, 2011.
- [24] Tong Qin, Peiliang Li, and Shaojie Shen. Vins-mono: A robust and versatile monocular visual-inertial state estimator. *IEEE Transactions on Robotics*, 34(4):1004–1020, 2018.

Adaptive Tracking and Perching for Quadrotor in Dynamic Scenarios

Yuman Gao^{ID}, Jialin Ji^{ID}, Qianhao Wang^{ID}, *Student Member, IEEE*, Rui Jin^{ID}, Yi Lin^{ID}, Zhimeng Shang^{ID}, Yanjun Cao^{ID}, Shaojie Shen^{ID}, Chao Xu^{ID}, *Senior Member, IEEE*, and Fei Gao^{ID}, *Member, IEEE*

Abstract—Perching on the moving platforms is a promising solution to enhance the endurance and operational range of quadrotors, which could benefit the efficiency of a variety of air-ground cooperative tasks. To ensure robust perching, tracking with a steady relative state and reliable perception is a prerequisite. This paper presents an adaptive dynamic tracking and perching scheme for autonomous quadrotors to achieve tight integration with moving platforms. For reliable perception of dynamic targets, we introduce elastic visibility aware planning to actively avoid occlusion and target loss. Additionally, we propose a flexible terminal adjustment method that adapts the changes in flight duration and the coupled terminal states, ensuring full state synchronization with the time varying perching surface at various angles. A relaxation strategy is developed by optimizing the tangential relative speed to address the dynamics and safety violations brought by hard boundary conditions. Moreover, we take SE(3) motion planning into account to ensure no collision until the contact moment. Furthermore, we propose an efficient spatiotemporal trajectory optimization framework considering full state dynamics. The proposed method is extensively tested through benchmark comparisons and ablation studies. To facilitate the application of academic research to industry and to validate the efficiency under strictly limited computational resources, we deploy our system on a commercial drone (DJI MAVIC3) with a full size sport utility vehicle (SUV). We conduct extensive real world experiments, where the drone successfully tracks and perches at 30 km/h (8.3 m/s) on the top of the SUV, and at 3.5~m/s with 60° inclined into the trunk of the SUV.

Manuscript received 14 June 2023; accepted 31 October 2023. Date of publication 24 November 2023; date of current version 15 December 2023. This paper was recommended for publication by Associate Editor Giuseppe Loianno and Editor Paolo Robuffo Giordano upon evaluation of the reviewers' comments. This work was supported in part by the National Natural Science Foundation of China under Grant 62322314, in part by DJI-ZJU FAST Autonomous Drone Research Funding, and in part by the Fundamental Research Funds for the Central Universities. (Yuman Gao and Jialin Ji are co-first authors.) (Corresponding author: Fei Gao.)

Yuman Gao, Jialin Ji, Qianhao Wang, Rui Jin, Yanjun Cao, Chao Xu, and Fei Gao are with the Key Laboratory of Industrial Control Technology, Institute of Cyber-Systems and Control, Zhejiang University, Hangzhou 310027, China, and also with Huzhou Institute, Zhejiang University, Huzhou 313000, China (e-mail: ymgao@zju.edu.cn; jlji@zju.edu.cn; qhwangaa@zju.edu.cn; bbbbigrui@163.com; yanjundream@outlook.com; cxu@zju.edu.cn; fgaoaa@zju.edu.cn).

Yi Lin and Zhimeng Shang are with DJI Technology Company, Shenzhen 510810, China (e-mail: ylinax@connect.ust.hk; shangzhimeng@gmail.com).

Shaojie Shen is with the Department of Electronic and Computer Engineering, Hong Kong University of Science and Technology, Hong Kong, SAR, China (e-mail: eeshaojie@ust.hk).

This article has supplementary downloadable material available at <https://doi.org/10.1109/TRO.2023.3335670>, provided by the authors.

Digital Object Identifier 10.1109/TRO.2023.3335670

Index Terms—Aerial system, motion and path planning, perception and autonomy, trajectory optimization.

I. INTRODUCTION

UNCREWED aerial vehicles (UAVs) that operate in conjunction with mobile platforms have recently emerged in a variety of applications, such as truck-drone delivery systems [1], [2], [3], car-drone inspection systems [4], [5], [6], and air-ground search and rescue systems [7], [8], [9]. In these applications, due to the short flight duration of UAVs, they need to frequently perch on the mobile platform for resting or recharging, which necessitates the platform to come to a complete stop or interrupt its ongoing operations. For higher automation and task efficiency, it is necessary to let the UAV smoothly attach to moving platforms without interruption. This demands the UAV to track the moving and various angled platforms with steady relative state and reliable perception, and perch on it at the proper moment. For an ideal planner promising successful tracking and perching applied in dynamic real-world scenarios, *adaptability* must be explicitly considered and modeled to cope with several practical challenges analyzed as follows.

The first challenge is how to maintain stable observations during agile flight. For a quadrotor chasing a high-speed ground vehicle, the noncooperative movements of these two agents result in fluctuating relative motions. Such relative motion easily makes the target out of the limited field of view (FoV) of the drone's sensory device, causing target loss. Moreover, irregular obstacle distributions or dynamic objects often block direct observations from the quadrotor to its target, producing occlusion. To avoid the above situations, the trajectory of the drone should be adjusted adaptively according to the target movement and the surrounding environments, summarized as *visibility* requirement.

The second challenge is how to smoothly and quickly attach to the dynamic platform. A desired perching requires the quadrotor to synchronize its position, velocity, and attitude adaptively with the perching surface at a proper contact moment. Since a quadrotor's attitude and motion are coupled, a time-varying terminal state introduces cross-dependent temporal and spatial conditions for the quadrotor's trajectory. To cope with such conditions, the quadrotor should flexibly adjust its flight duration and the coupled terminal states during trajectory generation. Furthermore, strict terminal constraints may contain conflicts

with the quadrotor's safety and dynamics, resulting in no feasible solution. Therefore, a relaxation approach is hoped for reasonably adjusting the final perching state. The above requirements are summarized as *flexibility*.

The third challenge is how to react to sudden changes in complicated situations. In a dynamic scenario without global information, obstacles that appear suddenly, target states that change quickly, and external disturbances that act severely would make the latest generated trajectory deprecated. To let the quadrotor react adaptively in time, high-frequency replanning based on the onboard perception is necessary. However, for a quadrotor with limited onboard resources, it is difficult to satisfy the planning efficiency, the modeling fidelity, and the solving completeness at the same time. Therefore, the *responsiveness* is another critical requirement for planning.

Apart from the above requirements, *safety* and *dynamic feasibility* are also fundamental considerations for conducting an ideal aerial tracking and perching. The generated trajectory should avoid any possible collisions with obstacles, and can only contact the target until the final moment. Moreover, perching maneuvers with large attitudes often push the actuators toward their physical limits, making dynamic feasibility essential. However, constraints on high-order dynamic states usually demand high computation.

Based on the above observations and analysis, and built upon our previous conference papers [10], [11], we propose a complete aerial system with an adaptive tracking-perching scheme for dynamic targets. In our proposed system, to actively enhance *visibility*, we design a series of differentiable metrics considering the occlusion of obstacles, relative distance, and angle, with the limited 3-D FoV of quadrotors. Based on the surrounding environment, the tracking distance can be elastically adjusted. Moreover, to maintain high-quality observation, the quadrotor's position and attitude are jointly adjusted to lock the target centrally in the image space while perching. Second, to provide *flexibility* in determining the flight duration and the coupled terminal states, we propose a flexible terminal adjustment approach to ensure full-state synchronization with the time-varying perching surface. This approach eliminates the terminal constraints along with reducing optimization variables. Additionally, a relaxation strategy is developed by optimizing the tangential relative speed, addressing the conflict between terminal restrictions, safety, and dynamic feasibility. Third, to ensure *safety* around the contact moment precisely, we geometrically model the quadrotor and platform to prevent collision, and further construct a concise geometric constraint. Furthermore, *dynamic feasibility* is guaranteed by constrained on high-order states, including angular velocity and thrust, with an efficient flatness mapping. To collectively involve the above aspects in trajectory generation, we propose an efficient spatiotemporal trajectory optimization framework. Concise metrics and compact trajectory representation benefit the solving efficiency, ensuring *responsiveness*. Finally, to facilitate the application of academic research to industry and to validate our system in the real world, we deploy our adaptive tracking and perching scheme on a commercial drone (DJI-MAVIC 3) with a sport-utility vehicle (SUV) as the moving platform. Efficient trajectory optimization



Fig. 1. Simulations and real-world experiments of our adaptive tracking and perching system. Please watch our attached videos for more information at: youtu.be/5XKm7qkp2Xs, youtu.be/fBwW93Zq9ss.

enables high-frequency replanning even in embedded processors with severely limited resources. We present experiments in a variety of dynamic scenarios partly shown in Fig. 1, including successful tracking and perching on the SUV with a speed up to 30 km/h (8.3 m/s). Contributions of this article are listed as follows.

- 1) A series of differentiable planning metrics that enable visibility awareness against occlusion and target loss in aggressive flight efficiently.
- 2) A concise approach that flexibly adjusts the terminal perching states with safety and feasibility guaranteed by terminal constraint relaxation.
- 3) An efficient trajectory optimization framework considering full state dynamics and complex collision constraints for tracking and perching.
- 4) A variety of simulations and real-world tests that validate the proposed methods with a commercialized quadrotor.

This article consolidates the preliminary conference papers presented in [10] and [11] with significant functionality extension, performance improvements, as well as application promotion. Compared to our previous work [10], which relies on external facilities for perception, we build a fully autonomous tracking and perching system with solely onboard sensors. To better exploit the limited sensing capability of onboard vision,

we propose a visibility-aware planner to deform the trajectory for improving the target's observation quality. Besides, our previous tracking method [11] employed a decoupled way to generate a trajectory, where the temporal profile is optimized after its spatial shape. In this article, we jointly optimize the trajectory in space and time and result in much higher optimality. Finally, by deploying our method in a commercial quadrotor and testing it with a full-sized vehicle, we demonstrate that our system can be successfully deployed outside the laboratory. We consider this as an important step forward from our previous works, which are only validated in human-controlled environments.

II. RELATED WORKS

A. Aerial Tracking System

Several previous vision-based tracking works [12], [13] formulate the trajectory planning and control integrally as a reactive control problem, and take the tracking error defined on image space as the feedback. These reactive methods can achieve real-time performance but are too shortsighted to consider safety and occlusion constraints. To overcome these drawbacks, model predictive control (MPC) planners [14], [15] and differential-flatness-based planners [16], [17], [18], [19], [20], [21] with receding horizon formulations emerge. Nageli et al. [14] design a modular visibility cost function based on the reprojection error of targets, and integrate it into an MPC planner. However, this method has a strong assumption that the obstacles are elliptical and thus cannot avoid arbitrarily shaped obstacles well. Penin et al. [15] formulate a nonlinear MPC optimization problem with a visibility term in image space. Lacking environmental perception, this approach requires complete knowledge of the environment. Optimizing trajectories in flat-output space, Bonatti et al. [17] tradeoff shot smoothness, safety, occlusion, and cinematography guidelines. Nevertheless, they avoid occlusions by making the connection line between the target and robot obstacle-free, neglecting the conical FoV shape of sensors. Han et al. [18] propose a safe tracking trajectory planner consisting of a kinodynamic searching front-end and a spatiotemporal optimal trajectory planning back-end. Without visibility considerations, it is prone to fail due to the target being out of the FoV or too close in relative distance. The authors of [19] and [20] propose a graph-search-based preplanning procedure to cover safety and visibility, but carry out path smoothing afterward. Such inconsistency makes the trajectories may not meet all the constraints. Ji et al. [21] use a series of 2-D fans to represent the visible region for tracking planning. But the fans are only generated at the specified height, making this method pseudo-3-D. These recent works address that visibility is significant in determining tracking success rate and robustness. In contrast with the above works, our proposed differentiable metrics comprehensively consider the factors that affect visibility, including the 3-D shape of the conical FoV, the relative observation distance and angle, and obstacle occlusion.

B. Dynamic Landing and Perching

For clarity, we refer to the methods that can merely adjust the end position and velocity as "landing," and methods that

can additionally adjust the end attitude as "perching." Dynamic landing on a moving platform has been widely studied in UAV research. Previous studies typically adopt control-level methods, which directly construct a state deviation term based on target observation. Controllers designed with the proportional-integral-derivative method or Lyapunov-function-based methods are widely adopted [22], [23], [24]. Besides, the image-based visual servoing (IBVS) method [25], [26], [27] is another group of control-level methods that define the visual error in image space with less computational complexity. However, the above methods are often shortsighted and face difficulties in introducing state constraints related to interacting objects. To compensate for these drawbacks, most of the recent works address dynamic landing issues with MPC [28], [29], [30] or differential-flatness-based trajectory planning approaches [31], [32], both with a receding planning horizon. However, all these above studies only aim to reach the landing position, lacking the ability to adjust desired attitudes at the contact moment. Furthermore, the coordinated landing of quadrotors with moving platforms is also widely studied [33], [34], where the joint planning and control are designed to accomplish rendezvous and landing. These methods require control of the platform, introducing a higher system complexity, and have limited application scenarios.

Many previous perching works [35], [36], [37], [38], [39], [40], [41] study the problem of perching on stationary inclined surfaces. Most of these works [35], [36], [37], [38] rely on particular mechanisms, such as suction or adhesive grippers, to bypass the terminal attitude requirement. Thomas et al. [39] propose a planning and control strategy fully considering actuator constraints and formulates a quadratic programming (QP) problem using a series of linear approximations. However, this approach cannot adjust the perching duration, and the linearization is oversimplified. Based on this approach, Mao et al. [40] propose a global-bound-checking method to check the dynamic feasibility efficiently, then increase the trajectory duration and recursively solve a QP problem until actuator constraints are satisfied. However, the method ignores that the spatial profile of trajectories also affects dynamic feasibility, which can result in this constraint being unsatisfied. Moreover, Panque et al. [41] formulate a discrete-time multiple-shooting nonlinear programming (NLP) problem for perching on powerlines, with a task-specific perception-aware term. Nevertheless, this method adjusts terminal states by computationally expensive multiple shooting, resulting in an excessive computation time for orders of magnitude longer than ours.

For dynamic perching, Vlantis et al. [42] study the problem of landing a quadrotor on an inclined moving platform. By solving a discrete time nonlinear MPC, the drone approaches the platform, while maintaining it within the camera's FoV, and finally perches on it. However, such a computationally demanding problem is computed on a ground station. Moreover, the quite small inclined angle (27°) and quite slow speed (0.5 m/s) are inadequate for validation. Hu and Mishra [43] achieve the differentially flat spatiotemporal optimization considering the actuator constraints and collision constraints. But it is only for 3-DOF quadrotors in the 2-D coordinate system. Liu et al. [44] design a suction

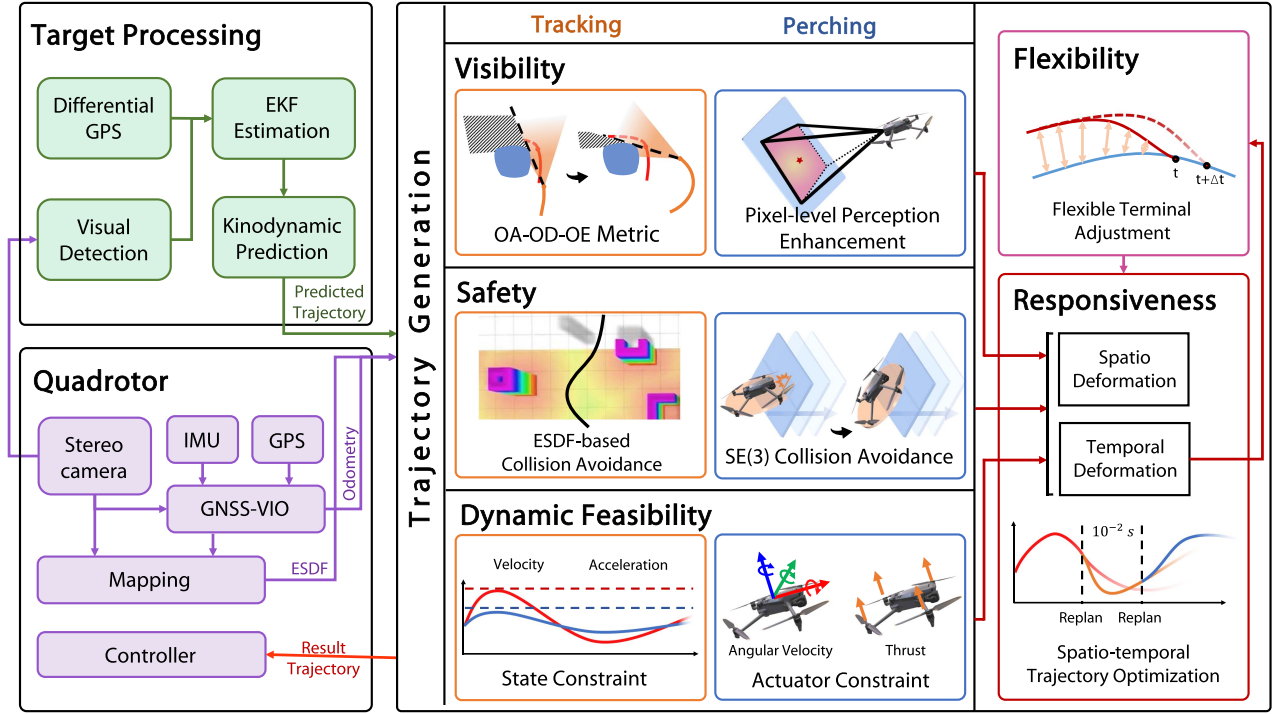


Fig. 2. Overview of our complete aerial system with dynamic tracking and perching scheme. The trajectory generation module takes all the requirements mentioned in Section I into account and provides spatiotemporal optimal feasible trajectory for stable tracking and dynamic perching.

cup gripper for quadrotors to perch on a moving target, but this work focus more on the novel mechanical design and simply use minimum-jerk-based trajectory generation without safety, actuator limit, and visibility considerations.

III. SYSTEM OVERVIEW AND PRELIMINARIES

A. System Architecture

The overall architecture of our aerial system with the adaptive tracking and perching scheme is illustrated in Fig. 2. The target position is obtained by the fusion of coarser differential-GPS-based relative localization (meter-level error) and finer visual detection (centimeter-level error). After obtaining the target position, we conduct an extended Kalman filter (EKF) based estimation and predict the target trajectory in the future (Section III-C). To meet the five aspects of requirements stated in Section I, we design comprehensive constraints of visibility, safety, and dynamic feasibility, respectively, for tracking (Section IV) and perching (Section V). Collectively considering these constraints, we simultaneously optimize the spatial and temporal profile of the trajectory with high efficiency (Section VI). When trajectory duration changes in temporal deformation, a flexible terminal adjustment approach is adopted to adaptively synchronize the full states of the quadrotor with the time-varying states of the perching surface (Section V-D).

B. Dynamic Model and Differential Flatness

In this article, we use the simplified dynamics proposed by [45] for a quadrotor, whose configuration is defined by its

translation $\mathbf{p} = (p_x, p_y, p_z)^T \in \mathbb{R}^3$ and rotation $\mathbf{R} \in \text{SO}(3)$. Translational motion depends on the gravitational acceleration \bar{g} as well as the thrust \tilde{f} . Rotational motion takes the body rate $\dot{\omega} \in \mathbb{R}^3$ as input. The simplified model is written as

$$\begin{cases} \tau = \tilde{f}\mathbf{e}_3/m \\ \ddot{\mathbf{p}} = \boldsymbol{\tau} - \bar{g}\mathbf{e}_3 \\ \dot{\mathbf{R}} = \mathbf{R}\dot{\boldsymbol{\omega}} \end{cases} \quad (1)$$

where $\boldsymbol{\tau}$ denotes the mass-normalized net thrust, \mathbf{e}_i is the i th column of \mathbf{I}_3 , such as $\mathbf{e}_3 = [0, 0, 1]^T$, and $\hat{\cdot}$ is the skew-symmetric matrix form of the vector cross product.

Exploiting the differential flatness property of the quadrotor, the state and input variables of quadrotors can be parameterized by finite derivatives of flat outputs [45]. The flat output of quadrotors is

$$\mathbf{z} = (p_x, p_y, p_z, \psi)^T \in \mathbb{R}^3 \times \text{SO}(2) \quad (2)$$

where $\psi \in \text{SO}(2)$ is the Euler-yaw angle. We further define the flat outputs and their derivatives $\mathbf{z}^{[s-1]} \in \mathbb{R}^{ms}$ as

$$\mathbf{z}^{[s-1]} := (\mathbf{z}^T, \dot{\mathbf{z}}^T, \dots, \mathbf{z}^{(s-1)T})^T. \quad (3)$$

This makes it possible for us to optimize a trajectory $\mathbf{z}(t) : [0, T] \mapsto \mathbb{R}^m$ in the low-dimension flat-output space.

C. Target Prediction Model

Given measurements on the target position $(\varrho_x, \varrho_y, \varrho_z)$, we aim to estimate the full state of the target vehicle. Estimating high-order states will amplify the observation error from the position measurement noise. Therefore, we adopt the constant

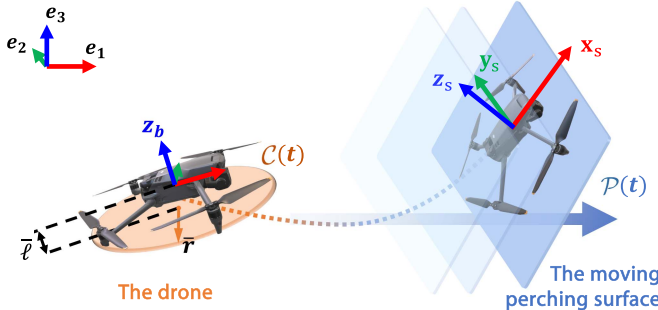


Fig. 3. Illustration of the geometry model. The quadrotor is modeled as a disc $\mathcal{C}(t)$, and the perching surface is modeled as a half-space $\mathcal{P}(t)$.

turn rate and velocity (CTRV) model [46] for state estimation, and the states of the target vehicle are written as

$$\chi(t) = (\varrho_x, \varrho_y, \varrho_z, \theta, v_h, v_v, \omega_\varrho)^T \quad (4)$$

where θ is the heading angle of the vehicle, ω_ϱ is the angular velocity, v_h is the horizontal velocity, and v_v is the vertical velocity, which is usually small and used to estimate uphill and downhill motion. Then we use EKF with this model for the state estimation.

To combine environmental information for target prediction, given the estimated current states, we use a kinodynamic motion primitive method considering collision. Given a prediction duration, by expanding motion primitives using the constant turn rate and acceleration (CTRA) model [46] under different control inputs with a time step Δt , we choose the collision-free one with the least control effort. Expanding until the prediction duration is reached, we obtain the predicted trajectory $\varrho(t) \in \mathbb{R}^3$ with yaw angle $\theta(t) \in SO(2)$ and a series of corresponding discrete target positions denoted as

$$\Psi = \{\varrho_k = \varrho(k\Delta t) \mid k = [0, 1, \dots, M]\}. \quad (5)$$

D. Geometric Model

To avoid collision with the perching surface, we model the underside of a symmetric quadrotor as a disc, shown in Fig. 3, denoted by

$$\mathcal{C} = \left\{ \mathbf{x} = \mathbf{R}\bar{B}\bar{r}\mathbf{u} + \mathbf{o} \mid \|\mathbf{u}\| \leq 1, \mathbf{u} \in \mathbb{R}_2, \mathbf{x} \in \mathbb{R}_3 \right\} \quad (6)$$

where $\mathbf{B} = (\mathbf{e}_1, \mathbf{e}_2) \in \mathbb{R}_{3 \times 2}$ and \bar{r} denotes the radius of the disc. We use \bar{l} to denote the thickness of the centroid of the quadrotor to the bottom. Thus, the center of the disc $\mathbf{o} = \mathbf{p} - \bar{l}\mathbf{z}_b$, where \mathbf{z}_b is the normal vector corresponding to the z -axis of the body frame.

We assume that the estimated position and yaw angle of the moving platform is denoted as ϱ and θ , and the normal vectors corresponding to the perching surface frame are denoted by $\mathbf{x}_s, \mathbf{y}_s$, and \mathbf{z}_s . Therefore, the feasible half-space divided by the perching surface is written as

$$\mathcal{P} = \left\{ \mathbf{h}^T \mathbf{x} \leq b \mid \mathbf{x} \in \mathbb{R}_3 \right\} \quad (7)$$

where $\mathbf{h} = -\mathbf{z}_s$, $b = \mathbf{h}^T \varrho$, and $\mathbf{z}_s = \mathbf{R}_z(\theta)\bar{\mathbf{z}}_s$, where $\mathbf{R}_z(\theta) \in SO(3)$ represents the basic rotation by angle θ around ego z -axis, and $\bar{\mathbf{z}}_s$ is the current normal vector obtained by detection. The other normal vectors can be similarly calculated.

IV. VISIBILITY-AWARE TRACKING PLANNING

As analyzed in Section I, planning with visibility consideration is essential for conducting long-term stable target tracking. To this end, we define several metrics to comprehensively model visibility in this section. Observing typical tracking failures, we can summarize that they are mainly due to observation distance (OD), observation angle (OA), and occlusion effect (OE). In this section, we explicitly model the above OD, OA, and OE metrics, design their penalty functions, and derive corresponding gradients for trajectory optimization. In what follows, the drone's position and yaw angle are denoted as $\mathbf{p} \in \mathbb{R}^3$ and $\psi \in SO(2)$, with the target position $\varrho \in \mathbb{R}^3$.

A. Observation Distance Restriction

A target is expected to be observed within a proper distance range from a drone. Since target ground platforms usually have more aggressive horizontal motion, we separately constrain the horizontal (δ^h) and vertical (δ^v) components of the tracking distance with different margins

$$d_\ell^* \leq \delta^* \leq d_u^*, * = \{h, v\} \quad (8)$$

where the d_ℓ and d_u are the lower and upper bounds of the optimal distance of observation. To make this metric analytically differentiable, we design penalty functions for the OD constraint

$$\mathcal{J}_{OD^v} = g(d_\ell^v - \delta^v) + g(\delta^v - d_u^v) \quad (9a)$$

$$\mathcal{J}_{OD^h} = g(d_\ell^h - \delta^h) + \mathcal{L}_\mu(\delta^h - d_u^h) \quad (9b)$$

where $g(x) = \max(x, 0)^3$ and $\mathcal{L}_\mu(\cdot)$ is a C^2 -smoothing linear penalty function denoted by

$$\mathcal{L}_\mu(x) = \begin{cases} 0, & x \leq 0 \\ (\mu - x/2)(x/\mu)^3, & 0 < x \leq \mu \\ x - \mu/2, & x > \mu \end{cases} \quad (10)$$

When the horizontal distance surpasses the upper bound μ , we apply a linearly increasing penalty function $L_\mu(\cdot)$. We choose a more severe penalty $g(\cdot)$ to prevent the drone from getting the target too close and possibly causing a collision.

B. Observation Angle Restriction

In order to keep the observation angle straight toward the target, the expected yaw angle ψ_e is defined as

$$\psi_e(\mathbf{p}, \varrho) = \text{atan2}(\mathbf{e}_2^T(\varrho - \mathbf{p}), \mathbf{e}_1^T(\varrho - \mathbf{p})) \quad (11)$$

where \mathbf{e}_i is the i th column of \mathbf{I}_3 . The cost of this term is written as

$$\mathcal{J}_{OA} = (\psi - \psi_e)^2. \quad (12)$$

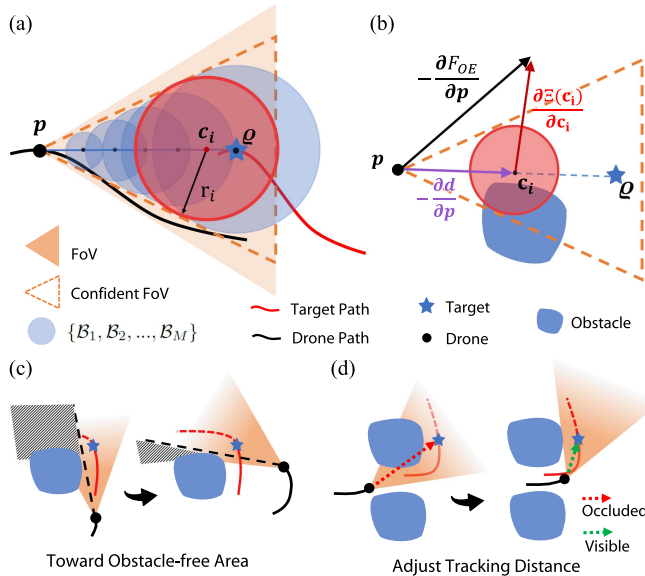


Fig. 4. (a) Illustration of the OE metric. The drone at position \mathbf{p} observes the target \mathbf{q} . A sequence of ball-shaped areas in blue are used to approximate the confident FoV expected to be obstacle-free. (b) Example of the two decomposition parts of the negative F_{OE} 's gradient, driving the drone to move toward obstacle-free areas and adjust the tracking distance elastically. (c) Drone moves toward obstacle-free areas for less occlusion probability. (d) Drone adjusts the tracking distance in obstacle-rich areas for less occlusion probability.

Note that the drone could adjust both its position and yaw angle to reach ψ_e . The gradient of \mathcal{J}_{OA} affects both \mathbf{p} and ψ . Here, we present the gradient w.r.t. \mathbf{p} written as¹

$$\frac{\partial \mathcal{J}_{OA}}{\partial \mathbf{p}} = \left[\frac{\partial \mathcal{J}_{OA}}{\partial p_x}, \frac{\partial \mathcal{J}_{OA}}{\partial p_y}, 0 \right]^T \quad (13)$$

where

$$\frac{\partial \mathcal{J}_{OA}}{\partial p_x} = \frac{2(\psi - \psi_e)}{(\mathbf{e}_1^T(\mathbf{p} - \mathbf{q}))^2 + (\mathbf{e}_2^T(\mathbf{p} - \mathbf{q}))^2} \cdot \mathbf{e}_2^T(\mathbf{p} - \mathbf{q}). \quad (14)$$

$\partial \mathcal{J}_{OA}/\partial p_y$ can be calculated similarly.

C. Elastic Occlusion Effect Avoidance

Complex environments increase the possibility of occlusion during tracking, easily causing target loss. Considering the conical FoV and arbitrarily shaped obstacles, we formulate the OE metric as follows. As shown in Fig. 4(a), the *confident FoV* embedded in the real FoV represents the region that is expected TO BE obstacle-free around the line of sight. To formulate analytically, we approximate the confident FoV with a sequence of ball-shaped areas $\{\mathcal{B}_1, \mathcal{B}_2, \dots, \mathcal{B}_M\}$, where M is the number of the areas. For each ball, its center \mathbf{c}_i and radius r_i are calculated by

$$\mathbf{c}_i = \mathbf{p} + \lambda_i(\mathbf{q} - \mathbf{p}) \quad (15)$$

$$r_i = \rho \cdot \lambda_i \cdot \|\mathbf{p} - \mathbf{q}\| \quad (16)$$

where $\lambda_i = i/M \in [0, 1]$, and ρ is a constant determined by the size of the confident FoV. Then we guarantee OE analytically

¹Note that we adopt the denominator layout for gradients in this article.

by forcing constraint

$$r_i < \Xi(\mathbf{c}_i) \quad (17)$$

for each ball-shaped area, where $\Xi(\mathbf{c}_i) : \mathbb{R}^3 \rightarrow \mathbb{R}$ is the distance between \mathbf{c}_i and its closest obstacle, which is obtained from Euclidean signed distance field (ESDF). Then, the OE cost is concisely written as

$$\mathcal{J}_{OE} = \sum_{i=1}^M g(F_{OE}(\mathbf{p})) \quad (18a)$$

$$F_{OE}(\mathbf{p}) = r_i - \Xi(\mathbf{c}_i). \quad (18b)$$

The gradient of F_{OE} can be written as

$$\frac{\partial F_{OE}}{\partial \mathbf{p}} = \rho \lambda_i \cdot \frac{\partial d}{\partial \mathbf{p}} - (1 - \lambda_i) \frac{\partial \Xi(\mathbf{c}_i)}{\partial \mathbf{c}_i} \quad (19)$$

where $d = \|\mathbf{p} - \mathbf{q}\|$, and $\partial \Xi(\mathbf{c}_i)/\partial \mathbf{c}_i$ is obtained from ESDF.

To further analyze the metric, an example of the gradient of F_{OE} is presented in Fig. 4(b). As the two directions of the decomposition parts of $-\partial F_{OE}/\partial \mathbf{p}$ shown, the OE metric can not only make the drone move toward obstacle-free areas [see Fig. 4(c)] but also adjust the tracking distance elastically according to the environment [see Fig. 4(d)]. Both of the two actions can prevent occlusion, especially when a target moves in obstacle-rich regions shown in Fig. 4(d), with a small positional adjustment margin, getting closer to the target is a reasonable way. Such characteristic is further demonstrated in simulation experiments in Section VII-B.

V. AGGRESSIVE AND FLEXIBLE PERCHING PLANNING

To smoothly attach to the perching surface, it is essential to get a full-state alignment at the contact moment, with safety, dynamic feasibility, and continuous target observation guaranteed. To this end, in this section, we detail the specific constraints involving the above factors for aggressive and flexible perching planning. In what follows, the position trajectory of the drone and the target are denoted as $\mathbf{p} \in \mathbb{R}^3$ and $\mathbf{q} \in \mathbb{R}^3$, respectively. The attitude quaternion of the quadrotor is denoted as $\mathbf{q} \in \mathcal{S}^3$.

A. SE(3) Collision Avoidance

Considering the geometry of a quadrotor, adjusting its attitude is critical for collision avoidance with the perching surface, necessitating SE(3) trajectory planning. Given the description of \mathcal{C} (6) and \mathcal{P} (7), to avoid the quadrotor having intersection of the surface, the SE(3) collision avoidance constraint is written as

$$\mathcal{C} \subset \mathcal{P} \quad (20)$$

which is equivalent to

$$\mathbf{h}^T (\mathbf{R} \mathbf{B} \bar{\mathbf{r}} \mathbf{u} + \mathbf{o}) - b \leq 0 \quad (21a)$$

$$\sup_{\|\mathbf{u}\| \leq 1} \mathbf{h}^T (\mathbf{R} \mathbf{B} \bar{\mathbf{r}} \mathbf{u}) + \mathbf{h}^T \mathbf{o} - b \leq 0 \quad (21b)$$

$$\bar{r} \|\mathbf{B}^T \mathbf{R}^T \mathbf{h}\| + \mathbf{h}^T \mathbf{o} - b \leq 0. \quad (21c)$$

Since we are utilizing the flat output \mathbf{z} as the state representation, we should first recover \mathbf{R} from \mathbf{z} before computing the constraint

(21c). First, the mass-normalized net thrust can be directly obtained from the trajectory

$$\tau = \mathbf{p}^{(2)} + \bar{g}\mathbf{e}_3. \quad (22)$$

Then, since the z -axis of the body frame \mathbf{z}_b is aligned with the direction of the mass-normalized net thrust according to the simplified dynamics [45], we can obtain

$$\mathbf{z}_b = \tau / \|\tau\|_2. \quad (23)$$

To recover \mathbf{R} from \mathbf{z}_b , denoting that $\mathbf{z}_b = [a_z, b_z, c_z]^T$, we utilize an efficient mapping according to Hopf fibration [47], which is written as

$$\mathbf{q}_{abc} = \frac{1}{\sqrt{2(c_z + 1)}} \begin{pmatrix} c_z + 1 \\ -b_z \\ a_z \\ 0 \end{pmatrix} \quad (24)$$

where the unit quaternion \mathbf{q}_{abc} satisfies $\mathbf{R}(\mathbf{q}_{abc})\mathbf{e}_3 = \mathbf{z}_b$. Since this collision avoidance metric is independent of the yaw angle ψ , the rotation of the quadrotor can be obtained by $\mathbf{R} = \mathbf{R}(\mathbf{q}_{abc})$. Adopting this differential flatness with Hopf fibration can reduce computation and reduce the singularities to the best case possible. Finally, we can easily calculate $\mathbf{B}^T \mathbf{R}^T$ in (21c) through \mathbf{z}_b

$$\mathbf{B}^T \mathbf{R}^T = \begin{pmatrix} 1 - \frac{a_z^2}{c_z + 1} & -\frac{a_z b_z}{c_z + 1} & -a_z \\ -\frac{a_z b_z}{c_z + 1} & 1 - \frac{b_z^2}{c_z + 1} & -b_z \end{pmatrix}. \quad (25)$$

However, the constraint (21c) should only be activated when $\|\mathbf{p} - \boldsymbol{\varrho}\| \leq \bar{d}$, that is, the drone is close to the platform. This constitutes a mixed-integer nonlinear programming problem. Here, we design a smoothed logistic function $\mathcal{L}_\epsilon(\cdot)$ to incorporate the integer variable into our NLP, which is denoted by

$$\mathcal{L}_\epsilon(x) = \begin{cases} 0, & x \leq -\epsilon \\ \frac{1}{2\epsilon^4}(x + \epsilon)^3(\epsilon - x), & -\epsilon < x \leq 0 \\ \frac{1}{2\epsilon^4}(x - \epsilon)^3(\epsilon + x) + 1, & 0 < x \leq \epsilon \\ 1, & x > \epsilon \end{cases} \quad (26)$$

where ϵ is a tunable positive parameter. Then the penalty function of collision avoidance can be written as

$$\mathcal{J}_c = \mathcal{L}_\epsilon(\mathcal{F}_{\bar{d}}) \cdot \mathcal{L}_\mu(\mathcal{F}_c) \quad (27)$$

where $\mathcal{F}_{\bar{d}}$ and \mathcal{F}_c are denoted by

$$\mathcal{F}_{\bar{d}} = \|\mathbf{p} - \boldsymbol{\varrho}\|^2 - \bar{d}^2 \quad (28a)$$

$$\mathcal{F}_c = \bar{r} \|\mathbf{B}^T \mathbf{R}^T \mathbf{h}\| + \mathbf{h}^T \mathbf{o} - b. \quad (28b)$$

Additionally, to limit the drone within a safe relative height range and prevent the drone from hitting the ground, we define a relative height cost $\mathcal{J}_{\Delta z}$ written as

$$\mathcal{J}_{\Delta z} = \mathcal{L}_\mu(z_{\min} - \Delta z) + \mathcal{L}_\mu(\Delta z - z_{\max}) \quad (29)$$

where relative height $\Delta z = \mathbf{e}_3^T (\mathbf{p} - \boldsymbol{\varrho})$, z_{\min} and z_{\max} are the expected minimum and maximum relative heights.

B. Image Space Pixel-Level Perception Enhancement

For accurate perching, high-quality observation is a fundamental factor. With a visual tag that remarks the perching

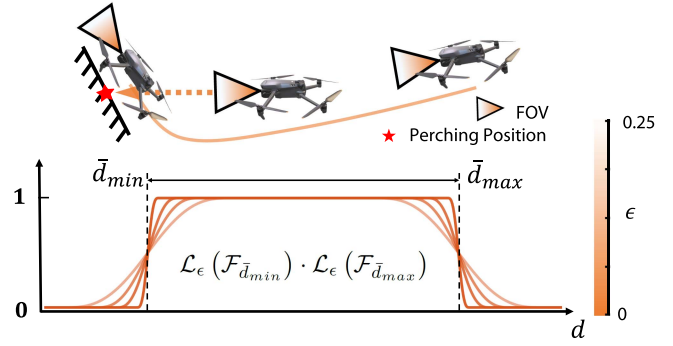


Fig. 5. Illustration of the perception distance range selection function with a front camera. The perception metric is only activated within the setting range $[\bar{d}_{\min}, \bar{d}_{\max}]$. Overly constraining at a close relative distance can lead to violations of terminal attitude constraints.

position, the quadrotor is expected to keep it central in the camera image. Denoting the tag position that coincided with the perching position in the world frame as ${}^w\boldsymbol{\varrho}$, we first transform it to the camera frame

$${}^b\boldsymbol{\varrho} = \mathbf{R}({}^b_w\mathbf{q})({}^w\boldsymbol{\varrho} - \mathbf{p}) \quad (30a)$$

$${}^c\boldsymbol{\varrho} = \mathbf{R}({}^c_b\mathbf{q})({}^b\boldsymbol{\varrho} - {}^b_t) \quad (30b)$$

where we denote index w as world frame, c as camera frame, and b as body frame. ${}^c_b\mathbf{q}$ and b_t are the rotation quaternion and the translation between the body frame and the camera frame, respectively. ${}^b_w\mathbf{q}$ is the rotation quaternion between the world frame and the body frame.

Using the pinhole camera model, the tag position in the camera frame, with the center of the image as the origin, can be written as

$$\begin{bmatrix} u_c \\ v_c \end{bmatrix} = \begin{bmatrix} f_x {}^c\boldsymbol{\varrho}_x / {}^c\boldsymbol{\varrho}_z \\ f_y {}^c\boldsymbol{\varrho}_y / {}^c\boldsymbol{\varrho}_z \end{bmatrix} \quad (31)$$

where f_x, f_y are the known camera intrinsics. Excessive constraints at a far distance limit the spatial freedom of trajectories, while overly constraining at a close distance might lead to violations of terminal attitude constraints, as shown in Fig. 5. Therefore, perception constraint should be activated only when the drone is within $[\bar{d}_{\min}, \bar{d}_{\max}]$ distance range from the perching surface, introducing mix-integer programming problem. We still resort to $\mathcal{L}_\epsilon(\cdot)$ defined in (26) to incorporate the integer variable. Then, the penalty function of tag perception is written as

$$\mathcal{J}_p = \mathcal{L}_\epsilon(\mathcal{F}_{\bar{d}_{\min}}) \cdot \mathcal{L}_\epsilon(\mathcal{F}_{\bar{d}_{\max}}) \cdot \mathcal{F}_p \quad (32)$$

where \mathcal{F}_p , $\mathcal{F}_{\bar{d}_{\min}}$, and $\mathcal{F}_{\bar{d}_{\max}}$ are denoted by

$$\mathcal{F}_p = u_c^2 + v_c^2 \quad (33a)$$

$$\mathcal{F}_{\bar{d}_{\min}} = \|\mathbf{p} - {}^w\boldsymbol{\varrho}\|^2 - \bar{d}_{\min}^2 \quad (33b)$$

$$\mathcal{F}_{\bar{d}_{\max}} = \bar{d}_{\max}^2 - \|\mathbf{p} - {}^w\boldsymbol{\varrho}\|^2. \quad (33c)$$

As \mathcal{F}_p implies, the drone position \mathbf{p} and attitude \mathbf{q} jointly affect the perception quality. But the coupled attitude and motion of the quadrotor further hinder perception enhancement, as shown in Fig. 6. To address the problem, we provide the gradients of

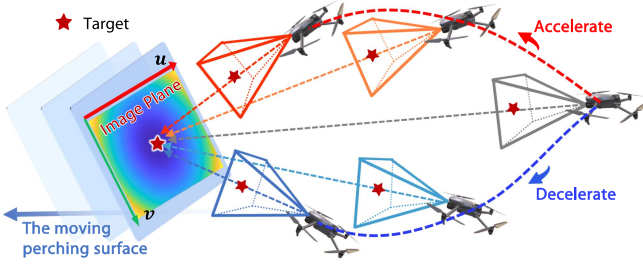


Fig. 6. For perception enhancement, the target is expected to be locked centrally in the image space. Since the motion and view attitude of a quadrotor are coupled, during acceleration or deceleration, the quadrotor needs to jointly adjust its attitude and position as shown to guarantee the perception quality.

\mathcal{F}_p w.r.t. \mathbf{p} and \mathbf{q} here, and optimize the trajectory in quadrotor flat-output space in latter Section VI-B. The gradient w.r.t. \mathbf{p} is written as

$$\frac{\partial \mathcal{F}_p}{\partial \mathbf{p}} = \frac{\partial^c \boldsymbol{\varrho}}{\partial \mathbf{p}} \frac{\partial \mathcal{F}_p}{\partial^c \boldsymbol{\varrho}} \quad (34)$$

where $\frac{\partial^c \boldsymbol{\varrho}}{\partial \mathbf{p}} = -(\overset{c}{\mathbf{R}} \cdot \overset{b}{\mathbf{R}})^T$. Moreover, the gradient w.r.t. the drone's attitude quaternion can be written as

$$\frac{\partial \mathcal{F}_p}{\partial^w \mathbf{q}} = \left(\frac{\partial^b \boldsymbol{\varrho}}{\partial_w^b \mathbf{q}} \frac{\partial^c \boldsymbol{\varrho}}{\partial^b \boldsymbol{\varrho}} \frac{\partial \mathcal{F}_p}{\partial^c \boldsymbol{\varrho}} \right)^{-1} \quad (35)$$

where $\frac{\partial^b \boldsymbol{\varrho}}{\partial_w^b \mathbf{q}}$ is the jacobian matrix of a quaternion rotation w.r.t. the quaternion, $\frac{\partial^c \boldsymbol{\varrho}}{\partial^b \boldsymbol{\varrho}} = \overset{b}{\mathbf{R}}$, and $(\cdot)^{-1}$ is the inversion of quaternion. The gradient w.r.t. attitude quaternion can be further transformed to gradients w.r.t. the flat-output states of the drone according to [47].

C. Actuator Constraints

To ensure dynamic feasibility during agile flight, we constrain the quadrotor's thrust and angular velocity within a reasonable range. First, the mass-normalized net thrust calculated by (22) is bounded as

$$\tau_{\min} \leq \|\boldsymbol{\tau}\| \leq \tau_{\max} \quad (36)$$

which can be constrained by constructing such a penalty function

$$\mathcal{J}_\tau = \mathcal{L}_\mu (\|\boldsymbol{\tau}\|^2 - \tau_{\max}^2) + \mathcal{L}_\mu (\tau_{\min}^2 - \|\boldsymbol{\tau}\|^2). \quad (37)$$

Second, the limitation of body rate $\boldsymbol{\omega} = [\omega_x, \omega_y, \omega_z]^T = \mathbf{R}^T \dot{\mathbf{R}}$ can also be constrained by penalty function

$$\mathcal{J}_\omega = \mathcal{L}_\mu (\|\boldsymbol{\omega}_{xy}\|^2 - \omega_{xy,\max}^2) \quad (38)$$

$$+ \mathcal{L}_\mu (\|\omega_z\|^2 - \omega_{z,\max}^2) \quad (39)$$

where $\boldsymbol{\omega}_{xy} = [\omega_x, \omega_y]^T$, $\omega_{xy,\max}$ is the x - y body axis maximum angular velocity and $\omega_{z,\max}$ is the z -axis part. To reduce singularities and simplify calculation, we enforce the constraint with Hopf fibration angle velocity decompose [47]

$$\|\boldsymbol{\omega}_{xy}\|^2 = \omega_x^2 + \omega_y^2 = \|\dot{\mathbf{z}}_b\| \quad (40)$$

where $\dot{\mathbf{z}}_b$ is calculated by

$$\dot{\mathbf{z}}_b = f_{DN}(\boldsymbol{\tau}) \mathbf{p}^{(3)} \quad (41)$$

where $\mathbf{p}^{(3)}$ represents the jerk of the drone on the trajectory, and $f_{DN}(\cdot)$ is given by

$$f_{DN}(x) = \left(\mathbf{I}_3 - \frac{xx^T}{x^T x} \right) / \|x\|_2. \quad (42)$$

Since the yaw angle ψ changes a little while perching, we approximately adopt $\omega_z = \dot{\psi}$.

D. Flexible Terminal Adjustment

To attach to the moving perching platform quickly and smoothly, the quadrotor should align its terminal states with the perching surface at a proper moment. During trajectory optimization, the temporal profile is affected by the above dynamics, safety constraints, and the time regularization introduced later in Section VI-B, determining the contact moment. As the flight duration changes, the desired terminal states of the quadrotor vary due to the motion of the perching surface. To flexibly synchronize the quadrotor's position, velocity, and attitude with the time-varying states of the perching surface, we formulate the terminal constraints of the drone trajectory as a function of the predicted target trajectory as follows.

At the contact moment, which corresponds to the end of the perching trajectory, the quadrotor should exactly coincide with the perching pose

$$\mathbf{p}(T) = \boldsymbol{\varrho}(T) - \bar{l} \mathbf{z}_s(T) \quad (43)$$

where T is the trajectory duration. Additionally, we expect the heading of the quadrotor to coincide with the estimated target's heading

$$\psi(T) = \theta(T). \quad (44)$$

Ideally, the drone needs to stay relatively still from the target

$$\mathbf{p}^{(1)}(T) = \boldsymbol{\varrho}^{(1)}(T) - \bar{v}_n \mathbf{z}_s(T) \quad (45)$$

where $\mathbf{p}^{(1)}$ and $\boldsymbol{\varrho}^{(1)}$ are the velocity trajectory of the drone and the target, \bar{v}_n is a preset small normal relative speed that helps the drone to stick to the perching surface at the end. However, the hard constraints of the relative end state may conflict with either the safety or the actuator constraints, as shown in Fig. 7. The conflicting constraints will result in no feasible trajectories. Moreover, considering the observation error, the strict terminal velocity constraint may lead to attitude shaking. Therefore, we relax the end velocity constraint by adding the tangential relative speed $\boldsymbol{\nu} = [\nu_x, \nu_y]^T \in \mathbb{R}^2$ as a new variable to be optimized into (45)

$$\mathbf{p}^{(1)}(T) = \boldsymbol{\varrho}^{(1)}(T) + \boldsymbol{\delta}_v(T) \quad (46a)$$

$$\boldsymbol{\delta}_v(T) = [\nu_x \mathbf{x}_s(T), \nu_y \mathbf{y}_s(T), -\bar{v}_n \mathbf{z}_s(T)]^T \quad (46b)$$

where ν_x and ν_y are the relative speed along the direction of \mathbf{x}_s and \mathbf{y}_s , respectively. We minimize the tangential relative speed by introducing a regulation term

$$\mathcal{J}_\nu = \|\boldsymbol{\nu}\|^2. \quad (47)$$

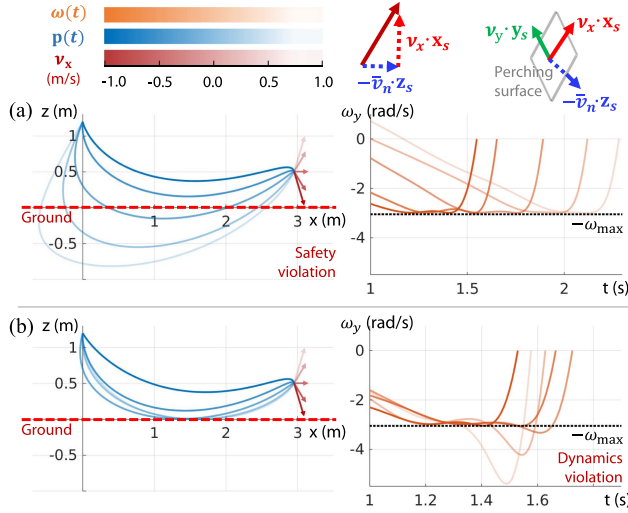


Fig. 7. Optimized perching trajectories for 1.5 rad terminal attitude with different tangential relative speeds along \mathbf{x}_s : $\nu_x = \{-1.0, -0.5, 0.0, 0.5, 1.0\}$ (m/s). This instance shows the relative end speed constraint can conflict with safety and actuator constraints. (a) With a hard actuator constraint, trajectories with $\nu_x = \{0.0, 0.5, 1.0\}$ (m/s) violate the safety constraint and hit the ground ($z = 0$). (b) With a hard safety constraint, trajectories with $\nu_x = \{0.0, 0.5, 1.0\}$ (m/s) violate the actuator constraint $\omega_{\max} = 3$ rad/s. Hence, it is necessary to optimize the tangential relative velocity ν to simultaneously satisfy safety and actuator constraints.

For attitude alignment, the z -axis of the drone body frame should coincide with the normal vector of the perching surface

$$\mathbf{z}_b(T) = \mathbf{z}_s(T) \quad (48)$$

which is equivalent to

$$\boldsymbol{\tau}(T)/\|\boldsymbol{\tau}(T)\|_2 = \mathbf{z}_s(T). \quad (49)$$

To deal with the coupled motion and attitude of the quadrotor, we transform the attitude constraint to the final acceleration $\mathbf{p}^{(2)}(T)$ in flat-out space. Considering this constraint and the thrust limit for terminal states, we design a transformation

$$\mathbf{p}^{(2)}(T) = \boldsymbol{\tau}_e \cdot \mathbf{z}_s(T) - \bar{g}\mathbf{e}_3 \quad (50a)$$

$$\boldsymbol{\tau}_e = \boldsymbol{\tau}_m + \boldsymbol{\tau}_r \cdot \sin(\boldsymbol{\tau}_f) \quad (50b)$$

where $\boldsymbol{\tau}_m = (\boldsymbol{\tau}_{\max} + \boldsymbol{\tau}_{\min})/2$ and $\boldsymbol{\tau}_r = (\boldsymbol{\tau}_{\max} - \boldsymbol{\tau}_{\min})/2$. By introducing a new variable $\boldsymbol{\tau}_f \in \mathbb{R}$, the terminal thrust $\boldsymbol{\tau}_e$ is limited within $[\boldsymbol{\tau}_{\min}, \boldsymbol{\tau}_{\max}]$ implicitly. The terminal attitude constraint is eliminated by this transformation.

As for terminal jerk, since it is related to the terminal angular velocity according to (41), we should set the final jerk $\mathbf{p}^{(3)}(T) = \mathbf{0}$ to make the relative angular velocity of the robot small when it touches the surface. Finally, the above terminal state constraints are collectively written as

$$\mathbf{z}^{[s-1]}(T) = F(\boldsymbol{\varrho}(T)). \quad (51)$$

VI. SPATIAL-TEMPORAL TRAJECTORY OPTIMIZATION

A. Occlusion-Aware Path Finding

To provide a reasonable initial path for tracking trajectory optimization, we design an occlusion-aware path-finding method

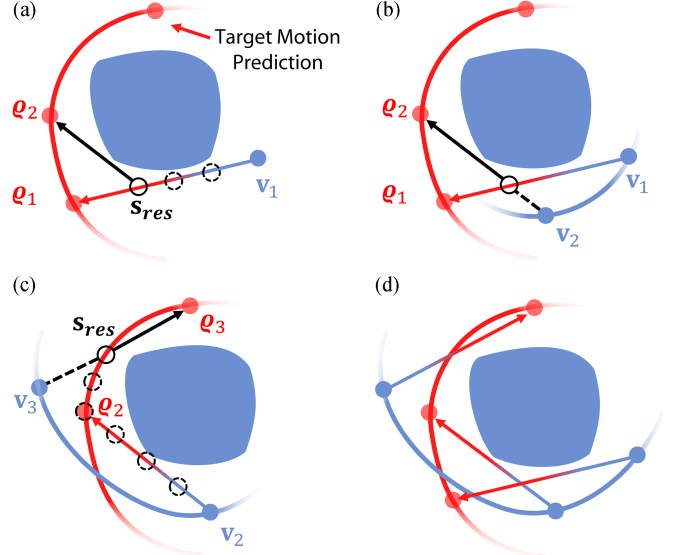


Fig. 8. Illustration of the occlusion-aware multigoal path-finding method.

Algorithm 1: Visibility-aware Tracking Trajectory Generation

Notation: target trajectory $\boldsymbol{\varrho}(t)$ and corresponding series $\Psi = [\boldsymbol{\varrho}_1, \dots, \boldsymbol{\varrho}_K]$, current state \mathbf{z} , desired tracking distance \bar{d} , viewpoint series \mathbf{V} , tracking trajectory \mathfrak{T} ;

- 1: $\mathbf{V}.\text{clear}; \mathit{Path}.\text{clear};$
- 2: $\mathbf{v}_1 = \mathbf{z};$
- 3: **for** $i = 2$ to K **do**
- 4: $\mathit{Ray}_{i-1} = \boldsymbol{\varrho}_{i-1} - \mathbf{v}_{i-1};$
- 5: $\mathit{Traj}_{i-1} \leftarrow \text{TrajSegment}(\boldsymbol{\varrho}(t), \boldsymbol{\varrho}_{i-1}, \boldsymbol{\varrho}_i);$
- 6: **for** \mathbf{s}_j on Ray_{i-1} and Traj_{i-1} **do**
- 7: **if** $\text{CheckRay}(\mathbf{s}_j, \boldsymbol{\varrho}_i)$ **then**
- 8: $\mathbf{s}_{res} = \mathbf{s}_j;$
- 9: **break**;
- 10: **end if**
- 11: **end for**
- 12: $\mathit{Dir}_i = \mathbf{s}_{res} - \boldsymbol{\varrho}_i;$
- 13: $\mathbf{v}_i \leftarrow \text{Extend}(\mathbf{s}_{res}, \mathit{Dir}_i, \bar{d});$
- 14: $\mathbf{V}.\text{push_back}(\mathbf{v}_i);$
- 15: $\mathit{Path}.\text{push_back}(\text{SearchPath}(\mathbf{v}_{i-1}, \mathbf{v}_i));$
- 16: **end for**
- 17: $\mathfrak{T} \leftarrow \text{TrackingTrajOpt}(\mathit{Path}, \Psi, \mathbf{V});$
- 18: **Return** $\mathfrak{T};$

that considers both tracking distance and occlusion. Given the target predicted trajectory $\boldsymbol{\varrho}(t)$ and corresponding target series $\Psi = [\boldsymbol{\varrho}_1, \dots, \boldsymbol{\varrho}_K]$ by (5), the path-finding method is aimed at offering a viewpoint series $\mathbf{V} = [\mathbf{v}_1, \dots, \mathbf{v}_K]$ corresponding to Ψ and a path connecting all viewpoints \mathbf{V} for subsequent trajectory optimization. The whole tracking trajectory generation algorithm is listed as Algorithm 1.

Considering efficiency, we use the greedy method, decoupling the whole path-finding problem into smaller multigoal path-searching problems. As an example shown in Fig. 8(a) ($i = 2$)

in this example), given the last viewpoint \mathbf{v}_{i-1} and target point $\boldsymbol{\varrho}_{i-1}$, we first traverse the ray from \mathbf{v}_{i-1} to $\boldsymbol{\varrho}_{i-1}$ to get sample points. Then we check the line-of-sight from the sample point \mathbf{s}_j to the current target point $\boldsymbol{\varrho}_i$ in function **CheckRay()**, and select the first no-occlusion one as \mathbf{s}_{res} (Lines 4–11). To keep the expected tracking distance, as shown in Fig. 8(b), we then extend \mathbf{s}_{res} along $\overline{\boldsymbol{\varrho}_i \mathbf{s}_{\text{res}}}$ in function **Extend()**, until the length of $\overline{\mathbf{v}_i \boldsymbol{\varrho}_i}$ equals to the expected tracking distance \bar{d} or reach an obstacle (Lines 12–13). If no valid sample point on the ray, we continue sample points on the target trajectory segment between $\boldsymbol{\varrho}_{i-1}$ to $\boldsymbol{\varrho}_i$, which is obtained by the function **TrajSegment()**. An example is shown in Fig. 8(c) ($i = 3$ in this example). Thus, we obtain an occlusion-free viewpoint and simply use A* algorithm on the grid map to obtain the path from \mathbf{v}_{i-1} to \mathbf{v}_i in function **SearchPath()** (Line 15). Subsequent viewpoints can be iteratively found. The found path and viewpoints set are used for later tracking trajectory optimization (Line 17).

B. Trajectory Optimization Problem Formulation

Here, we present the general trajectory optimization formulation, and the detailed design for specific stages of tracking and perching is described in Sections VI-E and VI-F, respectively. We use the M -piece polynomial to represent the piecewise flat-output trajectory $\mathbf{z}(t)$. $\mathbf{T} = (T_1, \dots, T_M)^T \in \mathbb{R}_{>0}^M$ are the durations of each piece, and $\mathbf{c} = (\mathbf{c}_1^T, \dots, \mathbf{c}_M^T)^T \in \mathbb{R}^{(N+1) \times 4M}$ are the coefficient matrices of each piece. Then, the i th piece is an N -degree polynomial

$$\mathbf{z}_i(t) = \mathbf{c}_i^T \boldsymbol{\beta}(t) \quad \forall t \in [0, T_i] \quad (52)$$

where $\boldsymbol{\beta}(t) = [t^0, t^1, \dots, t^N]^T$ is the natural basis. The trajectory optimization problem can be formulated as follows:

$$\min_{\mathbf{c}, \mathbf{T}} \mathcal{J}_E = \int_0^T \|\mathbf{z}^{(s)}(t)\|^2 dt + \rho T \quad (53a)$$

$$\text{s.t. } T \geq T_\ell \quad (53b)$$

$$\mathbf{z}^{[s-1]}(0) = \bar{\mathbf{z}}_0 \quad (53c)$$

$$\mathbf{z}^{[s-1]}(T) = F(\boldsymbol{\varrho}(T)) \quad (53d)$$

$$\mathcal{G}(\mathbf{z}^{[s-1]}(t), \boldsymbol{\varrho}(t)) \preceq \mathbf{0} \quad \forall t \in [0, T] \quad (53e)$$

$$\mathcal{H}(\mathbf{z}^{[s-1]}(t), \boldsymbol{\varrho}(t)) \preceq \mathbf{0} \quad \forall t \in \mathcal{T} \quad (53f)$$

where $T = \sum_{i=1}^M T_i$, cost function (53a) tradeoffs the smoothness and aggressiveness, and ρ is the time regularization parameter. Equation (53b) guarantees the entire duration greater than the lower bound T_ℓ . Equations (53c) and (53d) are the boundary conditions. Equation (53c) guarantees the trajectory starting from initial state $\bar{\mathbf{z}}_0 = \{\mathbf{z}_0, \dots, \mathbf{z}_0^{(s-1)}\}$. Equation (53d), which is explained in Section V-D, constrains the final state determined by the predicted target trajectory. For different trajectory requirements, we design different additional constraints: (53e) are the inequality constraints that are continuously forced on the entire time, and (53f) are the inequality constraints that are discretely forced on the specific time series \mathcal{T} . The discrete-time constraints are designed to ensure consistency with the discrete results of the path-finding method.

To deform the spatial and temporal profiles of the trajectory during optimization efficiently, we adopt $\mathfrak{T}_{\text{MINCO}}$ [48], a state-of-the-art minimum control effort polynomial trajectory class. MINCO efficiently conducts spatiotemporal deformation of the M -piece flat-output trajectory $\mathbf{z}(t)$ by decoupling the space and time parameters with a linear-complexity mapping

$$\mathbf{z}(t) = \mathcal{M}_{\mathbf{m}, \mathbf{T}}(t) \quad (54)$$

where $\mathbf{T} \in \mathbb{R}_{>0}^M$ are the durations defined as aforementioned and $\mathbf{m} = (\mathbf{m}_1, \dots, \mathbf{m}_{M-1})^T \in \mathbb{R}^{4 \times (M-1)}$ are the adjacent intermediate points between connected pieces. The s -order $\mathfrak{T}_{\text{MINCO}}^s$ consisting of $(2s-1)$ -degree polynomials can represent an s -integrator chain dynamics system. Furthermore, MINCO is advanced in converting $\{\mathbf{m}, \mathbf{T}\}$ to $\{\mathbf{c}, \mathbf{T}\}$ by the parameter mapping $\mathbf{c} = C(\mathbf{m}, \mathbf{T})$ with linear time and space complexity via *banded PLU factorization*. Meanwhile, the gradients for $\{\mathbf{c}, \mathbf{T}\}$ are also propagated to MINCO parameters $\{\mathbf{m}, \mathbf{T}\}$ in linear time. We refer readers to [48] for more details.

To solve the continuous constrained optimization problem conveniently, we convert it to an unconstrained optimization problem. All kinds of equality constraints are implicitly satisfied by using the variable of MINCO for optimization. To eliminate the inequality constraints (53e)–(53f), we use penalty function method introduced in Section VI-C. We adopt appropriate penalty weights and a fast postoptimization check for safety and dynamic feasibility to prevent unreasonable inequality constraint violations. The temporal constraint (53b) is eliminated by diffeomorphic variable substitution, which is introduced in Section VI-D. Finally, (53) is transformed to an unconstrained optimization problem written as

$$\min_{\mathbf{m}, \mathbf{T}} \mathcal{J}_E + \int_0^T \mathcal{J}_G dt + \sum_{t \in \mathcal{T}} \mathcal{J}_H \quad (55)$$

where \mathcal{J}_G is the continuous-time penalty function corresponding to (53e), and \mathcal{J}_H is the discrete-time penalty function corresponding to (53f).

C. Inequality Constraints Elimination

Inspired by the constraint transcription method [49], the inequality constraints (53e) and (53f) are formulated into penalty functions.

1) *Continuous Relative-Time Penalty*: For the constraint (53e) forced over the entire continuous trajectory, the derivatives between pieces are independent of each other. We transform them into finite constraints via the integral of constraint violation, which is further transformed into the penalized sampled function $\mathcal{J}_{\mathcal{I}}$

$$\mathcal{J}_{\mathcal{I}} = \int_0^T \mathcal{J}_G dt = \sum_{i=1}^M \mathcal{I}_i \quad (56a)$$

$$\mathcal{I}_i = \frac{T_i}{\kappa_i} \sum_{j=0}^{\kappa_i} \bar{\omega}_j \mathcal{J}_G \left(\mathbf{z}_i^{[s-1]}(t_j), \boldsymbol{\varrho}(t_j) \right) \quad (56b)$$

where κ_i is the sample number, $(\bar{\omega}_0, \bar{\omega}_1, \dots, \bar{\omega}_{\kappa_i-1}, \bar{\omega}_{\kappa_i}) = (1/2, 1, \dots, 1, 1/2)$ are the quadrature coefficients following

the trapezoidal rule [50], and $t_i = \frac{j}{\kappa_i} T_i$. Then the gradient of \mathcal{J}_i w.r.t. \mathbf{c} and \mathbf{T} can be easily derived

$$\frac{\partial \mathcal{J}_i}{\partial \mathbf{c}_i} = \frac{T_i}{\kappa_i} \sum_{j=0}^{\kappa_i} \left(\bar{\omega}_j \frac{\partial \mathcal{J}_G}{\partial \mathbf{c}_i} \right) \quad (57a)$$

$$\frac{\partial \mathcal{J}_i}{\partial T_i} = \frac{\mathcal{I}_i}{T_i} + \frac{T_i}{\kappa_i} \sum_{j=0}^{\kappa_i} \left(\bar{\omega}_j \frac{j}{\kappa_i} \frac{\partial \mathcal{J}_G}{\partial t_i} \right). \quad (57b)$$

For $\partial \mathcal{J}_G / \partial \mathbf{c}_i$, the total derivative of it is written as

$$\frac{\partial \mathcal{J}_G}{\partial \mathbf{c}_i} = \sum_{k=0}^{s-1} \boldsymbol{\beta}^{(k)} \frac{\partial \mathcal{J}_G}{\partial \mathbf{z}_i^{(k)}}. \quad (58)$$

Similar for $\partial \mathcal{J}_G / \partial t_i$ that can be written as

$$\frac{\partial \mathcal{J}_G}{\partial t_i} = \sum_{k=0}^{s-1} \mathbf{z}_i^{(k+1)} \frac{\partial \mathcal{J}_G}{\partial \mathbf{z}_i^{(k)}} + \dot{\varrho} \frac{\partial \mathcal{J}_G}{\partial \varrho} + \dot{\theta} \frac{\partial \mathcal{J}_G}{\partial \theta}. \quad (59)$$

2) *Discrete Absolute-Time Penalty*: To ensure consistency with the discrete results of the path-finding method, we formulate the corresponding constraint (53f) forced on the trajectory over specific discrete moments. The cost of a piece of the trajectory at a discrete moment will be affected by the duration changes of the former pieces. For a state $\mathbf{z}(t_k)$, assume that t_k is an absolute moment on the j th piece of the trajectory $\mathbf{z}_j(t)$, the relative time $t_r = (t_k - \sum_{i=1}^{j-1} \mathbf{T}_i)$ on $\mathbf{z}_j(t)$ is within the range

$$\sum_{i=1}^{j-1} \mathbf{T}_i \leq t_k \leq \sum_{i=1}^j \mathbf{T}_i. \quad (60)$$

With the denotation of $\mathcal{J}_D = \sum_{t \in \mathcal{T}} \mathcal{J}_H$ in (55), the gradients of \mathcal{J}_D w.r.t. \mathbf{c} and \mathbf{T} can be evaluated as

$$\frac{\partial \mathcal{J}_D}{\partial \mathbf{c}_i} = \begin{cases} \sum_{k=0}^{s-1} \boldsymbol{\beta}^{(k)} (t_r) \frac{\partial \mathcal{J}_D}{\partial \mathbf{z}_i^{(k)}}, & i = j \\ 0, & i \neq j \end{cases} \quad (61a)$$

$$\frac{\partial \mathcal{J}_D}{\partial T_i} = \begin{cases} \sum_{k=0}^{s-1} -\mathbf{z}_i^{(k+1)} (t_r) \frac{\partial \mathcal{J}_D}{\partial \mathbf{z}_i^{(k)}}, & i < j \\ 0, & i \geq j. \end{cases} \quad (61b)$$

Then, the problem of calculating gradients w.r.t \mathbf{c} and \mathbf{T} is further transformed into taking the gradients w.r.t the drone's flat-output states and their derivatives $\mathbf{z}^{[s-1]}$.

D. Temporal Constraints Elimination

Time slack constraint (53b) can be written as

$$\sum_{i=1}^M T_i \geq T_\ell. \quad (62)$$

We denote $\varsigma = (\varsigma_1, \dots, \varsigma_M) \in \mathbb{R}^M$ as new variables to be optimized and use the transformation

$$T_\Sigma = T_l + \varsigma_M^2 \quad (63a)$$

$$T_i = \frac{e^{\varsigma_i}}{1 + \sum_{j=1}^{M-1} e^{\varsigma_j}} T_\Sigma, 1 \leq i < M \quad (63b)$$

$$T_M = T_\Sigma - \sum_{i=1}^{M-1} T_i. \quad (63c)$$

The temporal constraints are eliminated by such substitution. Especially, when $T_\ell = 0$, we use a simpler transformation $T = e^\varsigma$ to eliminate the constraint (53b). Since the zero duration is invalid, here, constraint (53b) is changed to $T > T_\ell$.

E. Tracking Constraints Formulation

For trajectory optimization for tracking, we adopt $\mathfrak{T}_{\text{MINCO}}^3$ to represent position trajectory and $\mathfrak{T}_{\text{MINCO}}^2$ to represent yaw trajectory, guaranteeing sufficient optimization freedom. The differentiable visibility metrics have been presented in Section IV, and the constraints for tracking are further clarified here. Since the front end offers discrete drone and target series, the corresponding visibility costs forced at specific times are discrete absolute-time penalties. Then, the continuous relative-time and discrete absolute-time penalties are listed as

$$\mathcal{J}_G = \lambda_G [\mathcal{J}_o, \mathcal{J}_v, \mathcal{J}_a]^T \quad (64a)$$

$$\mathcal{J}_H = \lambda_H [\mathcal{J}_{OD}, \mathcal{J}_{OA}, \mathcal{J}_{OE}]^T \quad (64b)$$

where λ_G and λ_H are preset weight vectors. \mathcal{J}_{OD} is the observation distance penalty function defined as (9), \mathcal{J}_{OA} is the observation angle part defined as (12), and \mathcal{J}_{OE} is the occlusion effect avoidance part defined as (18). In addition, \mathcal{J}_o is obstacle avoidance cost defined as

$$\mathcal{J}_o(t) = g(d_{\text{thr}}^2 - \Xi(\mathbf{p}(t))^2) \quad (65)$$

where d_{thr} is the safety threshold, and $\Xi(\cdot)$ is the distance to the closest obstacle obtained from ESDF. $\mathcal{J}_v, \mathcal{J}_a$ are dynamic feasibility costs

$$\mathcal{J}_v(t) = g(\|\mathbf{p}^{(1)}(t)\|^2 - v_{\max}^2) \quad (66)$$

$$\mathcal{J}_a(t) = g(\|\mathbf{p}^{(2)}(t)\|^2 - a_{\max}^2) \quad (67)$$

where v_{\max} and a_{\max} are the maximum velocity and acceleration, respectively. For temporal constraint (53b), the duration of tracking trajectory should be equal to the prediction duration of the target motion T_p , ideally. However, enforcing the drone to reach the final states in a fixed duration may cause dynamic infeasibility, for instance, when the target moves faster than the drone. Therefore, we make a time slack $T \geq T_p$. For the final state constraint (53d), we fix it to the last viewpoint \mathbf{v}_K . For trajectory initialization, the initial guess of \mathbf{m} is obtained by sampling on the path provided by the occlusion-aware path-finding method, and the initial $T_i = T_p/M$.

F. Perching Constraints Formulation

For trajectory optimization for perching, we adopt $\mathfrak{T}_{\text{MINCO}}^4$ to represent position trajectory and $\mathfrak{T}_{\text{MINCO}}^2$ to represent yaw trajectory. When perching, it is necessary to force the terminal angular velocity to be 0, and $\mathfrak{T}_{\text{MINCO}}^4$ is the lowest order MINCO supporting to constrain the terminal angular velocity [48]. With the initial time set as $T_i = \|\mathbf{p} - \varrho\|/v_{\max}$, a boundary value problem is solved to obtain the initial guess of \mathbf{m} . Then, we summarize the penalty functions as

$$\mathcal{J}_G = \lambda_G [\mathcal{J}_c, \mathcal{J}_p, \mathcal{J}_\omega, \mathcal{J}_\tau, \mathcal{J}_{\Delta z}, \mathcal{J}_\nu]^T \quad (68a)$$

TABLE I
PARAMETERS SETTING FOR TRACKING SIMULATIONS

v_{max}	a_{max}	$\ \omega_{max}\ $	FoV	Image resolution	Tracking distance
Drone: 3.0 m	Drone: 6.0 m/s ²	3.0 rad/s	80° × 65°	640 × 480 px ²	5.5 m
Target: 1.5 m	Target: 2.0 m/s ²				

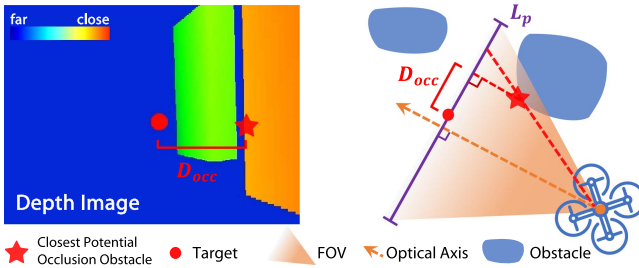


Fig. 9. Illustration of the occlusion criterion D_{occ} , which denotes the closest possible occluding obstacle. L_p is the projected plane crossing the target. Only obstacles on the camera image between the drone and L_p are recorded.

where \mathcal{J}_c is collision avoidance cost defined in (27), \mathcal{J}_p is perception cost defined in (32). \mathcal{J}_ω , \mathcal{J}_τ are dynamic feasibility cost defined in (38) and (37), $\mathcal{J}_{\Delta z}$ is relative height cost defined in (29), \mathcal{J}_v is the regulation for tangential relative speed defined in (47). For temporal constraint (53b), the low bound is set to $T_\ell = 0$.

VII. SIMULATION AND BENCHMARK

In this section, we conduct extensive simulations to validate the performance of our tracking and perching planning methods. As for benchmarks, cutting-edge works [18], [20], [21], [40], [41] in the tracking and perching fields are selected. All the simulations run on an Intel Core i5-9400F CPU with GeForce GTX 2060 GPU.

A. General Comparison of Visibility-Aware Tracking

We benchmark our method with the work of Jeon et al. [20] and Ji et al.'s Elastic-Tracker [21], which both consider the target's visibility. To further demonstrate the importance of visibility awareness, we also compare with Han's Fast-Tracker [18] without visibility consideration. These works are all open source and have not been modified. To compare the tracking performance fairly, we set the same parameters as listed in Table I with the same target trajectory. To compare the capability of occlusion avoidance, since the drone obtains target information directly from camera images, we record the projected distance between the target and the closest possible occluding obstacle (D_{occ}). The occlusion criterion is shown in Fig. 9.

We test all four methods in the same simulation environment as Elastic-Tracker. Since obstacle density has a significant impact on tracking performance, we test in scenarios with different obstacle densities. The sparse, medium, and dense density correspond to 6, 5, and 4 m average obstacle spacing, respectively. During tracking, we count the target positions projected to x - y plane in the tracking quadrotor's FoV. In Fig. 10(a), the heat map shows the distribution of the target positions, relative to

TABLE II
COMPUTATION TIME COMPARISON BETWEEN TRACKING METHODS

Methods	Average time (ms)		
	t_{path}	t_{opt}	t_{total}
Fast	9.56	0.38	9.94
Jeon's	11.32	3.20	14.32
Elastic	1.24	2.34	3.58
Ours	0.96	1.85	2.81

The boldface values indicate the optimal cases in the corresponding test scenario.

the tracking drone. Our method and Elastic-Tracker can both keep the target in the proper position of the FoV. Fig. 10(b) shows the distribution of D_{occ} . Since the main failures for Fast-Tracker are caused by tracking too close to the target or letting the target out of FoV, making the D_{occ} criterion meaningless, we do not include it in Fig. 10(b). Our method results in larger D_{occ} in all obstacle densities and is more effective at avoiding potential occlusion.

Furthermore, we record the failure reasons during tracking. Once the target is out of FoV, too near to the target, or occluded by obstacles, a failure is recorded. The failure reasons in the dense obstacle scene are counted in Fig. 10(c). We also benchmark the computation time, including path finding and trajectory optimization parts, as shown in Table II. Fast-Tracker consumes less time for trajectory optimization since it ignores visibility, resulting in more failures. In comparison, our proposed method consumes a much lower total computation budget, due to our lightweight path-finding method and concise metrics for trajectory optimization.

B. Case Study of Visibility-Aware Tracking

To better demonstrate and compare the tracking performance of different methods, we set up a representative scenario and present the whole process of tracking in Fig. 11. The parameter setting is the same as in Section VII-A. D_{occ} and the tracking distance are shown for all four methods. The occluded moments are indicated by the red lines connecting the drone and the target, and also correspond to the red background in the D_{occ} curve. For Fast-Tracker, due to the lack of visibility consideration, the quadrotor consistently follows the target closely. In the event of a sudden target turn, the drone often fails to adjust quickly, resulting in the target escaping from the FoV, as the moment shown in Fig. 11(a). As shown in Fig. 11(b), Jeon's method results in multiple occlusion moments and a less smooth trajectory, since the sequential graph-search-based path planner and smooth planner fail to jointly optimize visibility and smoothness and lack temporal optimization. As shown in Fig. 11(c), because Elastic-Tracker handles visibility by generating 2-D visible fans at a certain height, it fails to adjust visibility against the 3-D obstacle, which in this case is a two-layer instance. More importantly, when passing obstacle-rich areas, our method can adjust tracking distance elastically to reduce occlusion probability, as highlighted in green in Fig. 11(d). Especially when tracking the target passing the narrow gap, the drone with our method

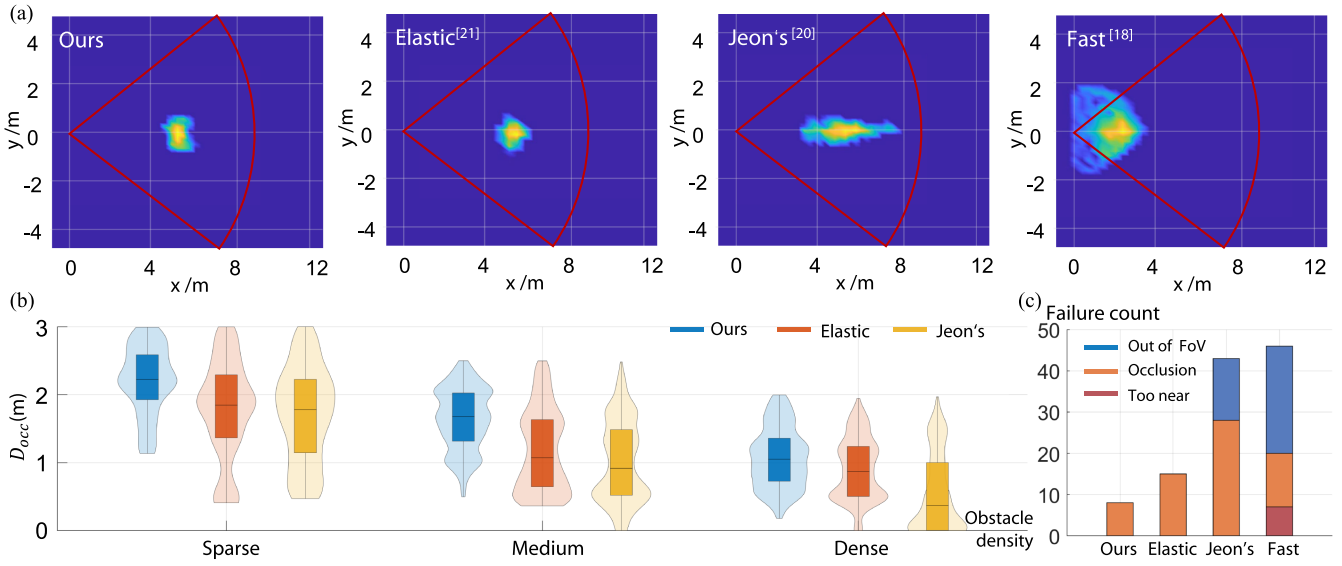


Fig. 10. (a) Comparison of the distribution heat map of the target position relative to the tracking quadrotor. The red sector represents the FoV of the drone. (b) Violin graph presenting a comparison of the distribution of the closest possible occluding obstacle on the image plane (D_{occ}) under different obstacle densities. (c) Failure reasons including out of view, too near (distance less than 1 m), occluded by obstacles.

TABLE III
PARAMETERS SETTING FOR PERCHING SIMULATIONS

τ_{\min}	τ_{\max}	$\ \omega_{\max}\ $	FoV	Image resolution
5.0 m/s ²	17.0 m/s ²	3.0 rad/s	80° × 65°	640 × 480 px ²

deployed elastically reduced the tracking distance to 4 m and avoid occlusion successfully. Consequently, our method shows reasonable visibility adjustment and has better performance at avoiding occlusion, due to the comprehensive and effective 3-D visibility metrics.

C. Perching Benchmark

We benchmark our perching method with the state-of-the-art perching methods proposed by Mao et al. [40] and Paneque et al. [41], which both consider visibility during perching. Paneque formulates a constrained discrete-time NLP problem and solves it using ForcesPRO [51]. They model the inputs of the system as the desired constant thrust derivatives and control each rotor thrust directly. To compare fairly, we constrain the thrust to be the same as ours so that the dynamics model of Paneque's and ours are similar. Since this work focuses on the perception of powerlines, we replace its perception cost with ours to compare fairly. Mao formulates a QP problem to constrain the terminal state and velocity bound. They increase the trajectories' time iteratively and recursively solve the QP problem until the thrust constraint is satisfied. We use the open-source code of Paneque's work and reimplement Mao's work, which is not open-source but not difficult to implement with the QP formulation. In the comparison, the terminal pitch angle is set to $\pi/2$ rad, and the trajectories are required to be rest-to-rest. The parameters of the drone are listed in Table III.

TABLE IV
COMPUTATION TIME COMPARISON BETWEEN PERCHING METHODS

Methods	Average time (ms)		
	30°	60°	90°
Paneque's	239.59	308.05	208.81
Mao's (A)	3.42	2.36	✗
Mao's (B)	16.65	13.73	✗
Ours	3.76	4.31	16.68

We compare both the trajectory quality and computation time of these methods, the results are presented in Fig. 12 and Table IV. Paneque's and our method successfully generate perching trajectories satisfying actuator and visibility constraints. Nevertheless, Paneque's method consumes much more computation time than ours, since a complex discrete-time multiple-shooting NLP problem formulation. Adopting MINCO, our method can optimize trajectories in the low-dimension flat-output space with high efficiency and can achieve real-time replanning during agile flight. Moreover, due to the finite discrete resolution, its thrusts and body rates are less smooth than ours. As shown in Fig. 13, Mao's method fails to guarantee dynamic feasibility even after sufficient iterations, which double the duration without providing any relief. Mao's method ignores that dynamic feasibility is affected by not only the temporal profile but also the spatial profile. As a result, its strategy narrows the solution space, leading to no solutions under such tight actuator constraints. Moreover, Mao's computation time depends on both initial duration and time sampling resolution. Thus, for Mao's (A), we set a better initial duration of 1.5 s and a coarser resolution 0.1 s, while for Mao's (B), a worse initial duration 1.0 s and a finer resolution 0.05 s are set. The results indicate that the computation time of Mao's method greatly increases with a

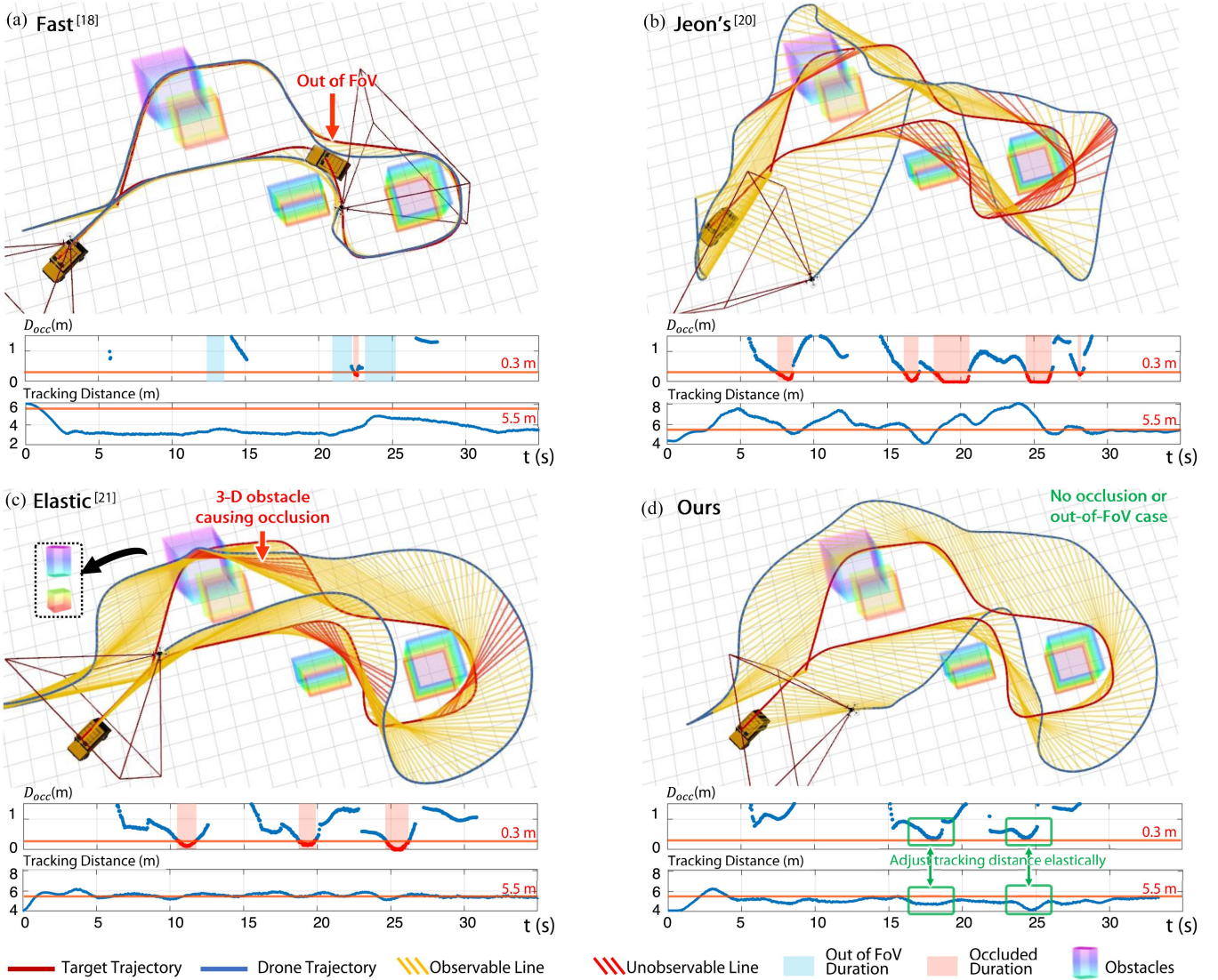


Fig. 11. Case study of visibility-aware tracking. Trajectories of the drone and the target, and the lines connecting their positions at the corresponding time are presented. The red lines show the occlusion moments. The D_{occ} and the tracking distance are shown for all four methods. We choose 0.3 m as the threshold at which the occlusion is likely to occur. An out-of-FoV failure of Fast-Tracker is shown in (a). (c) Shows that elastic-tracker fails to adjust visibility against the 3-D obstacle due to its pseudo-3-D visibility metric. (d) Shows that our method has no occlusion and out-of-FoV situations, and can adjust the relative distance elastically according to the environment.

worse initial value and a finer resolution. In comparison, our proposed method demonstrates high efficiency without greatly sacrificing the optimality of solutions.

Furthermore, we compare the capability of our perching planner with Panneque's planner, Mao's planner, and our previous planner [10]. The result is summarized in Table V. Both Panneque's and Mao's methods can only handle static targets. While ours can simultaneously handle collision avoidance, dynamic feasibility, and visibility constraints, and generate perching trajectories toward a moving target with a low computation budget. To further demonstrate our capability for adapting dynamic targets, Fig. 14 presents the generated trajectories for perching on moving targets with different speeds. Balanced aggressiveness and dynamic feasibility, our method drives the quadrotor perch on the target at proper contact moments. With different contact

TABLE V
CAPABILITY COMPARISON BETWEEN PERCHING METHODS

Capability Method	Collision Avoidance	Dynamic Feasibility	Visibility Awareness	Dynamic Target
Panneque's	✓	✓	✓	✗
Mao's	✗	✓	✓	✗
Ji's	✓	✓	✗	✓
Ours	✓	✓	✓	✓

The boldface values indicate the optimal cases in the corresponding test scenario.

moments and different terminal states, the quadrotor could still get full-state synchronization with the perching surface, presenting flexibility.

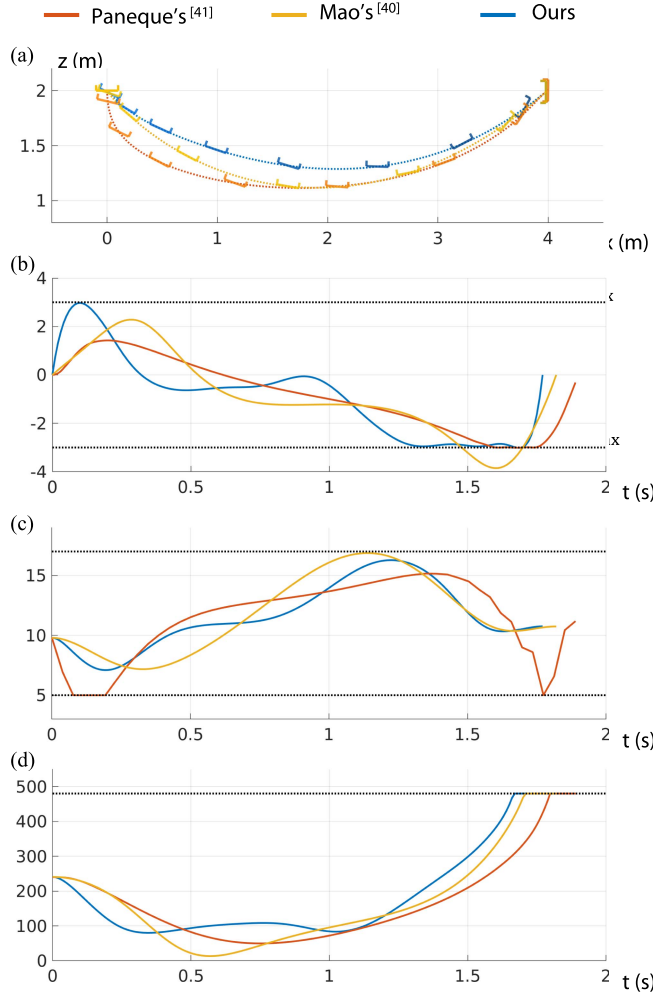


Fig. 12. Comparison of the trajectories generated by Paneque's, Mao's, and our planner for perching on vertical surfaces. (a) x - z trajectory shape. (b) Angular velocity. Mao's method exceeds the limitation. (c) Mass-normalized net thrust. Due to the finite discrete resolution of Paneque's method, its thrusts are less smooth than the others. (d) Target position on the u - v image space. All the methods guarantee that the target is visible.

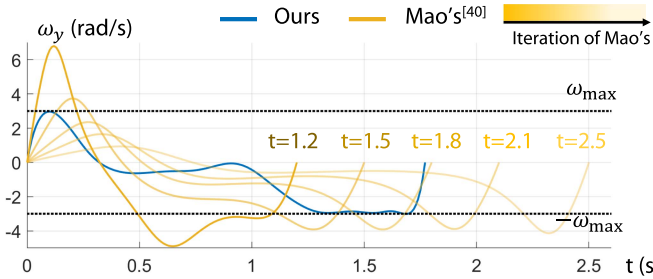


Fig. 13. Comparison of the angular velocity of the trajectories generated by our method and Mao's method. Mao's method fails to guarantee dynamic feasibility even after sufficient iterations to increase trajectory duration.

D. Ablation Study of the Visibility Awareness for Perching

Continuous and stable perception of targets is the foundation for perching planning. We validate our visibility-aware approach by comparing the perching trajectories with and without the visibility term. We use AprilTag [52] to mark the precise perching

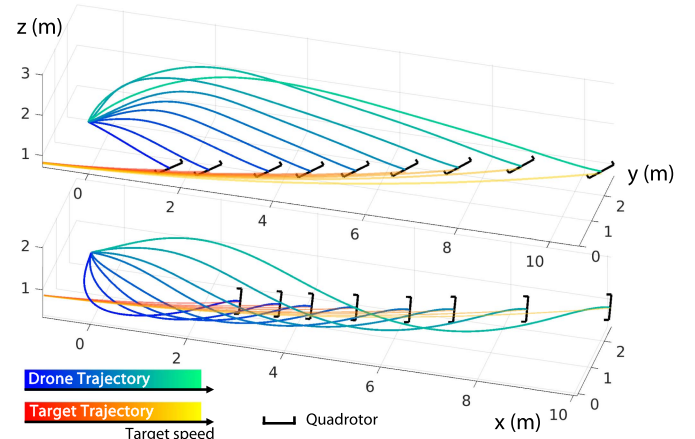


Fig. 14. Illustration of the 3-D trajectories generated for perching on a moving plane with different speeds. Top: 0.5 rad terminal pitch angle. Bottom: 1.5 rad terminal pitch angle. The target's velocity is ranged from 1.5 to 3.0 m/s. The kinematics of the target conforms to the CTRV model with $\omega = 0.2$ rad/s.

TABLE VI
ABLATION STUDY OF THE VISIBILITY AWARENESS FOR PERCHING

Terminal pitch angle	Visibility awareness	Observable distance (m)	Observable duration (s)
0.0 rd	w/o	0.64	0.60
	w/	1.96 (\uparrow 203%)	1.51 (\uparrow 152%)
0.5 rd	w/o	0.44	0.36
	w/	1.99 (\uparrow 352%)	1.68 (\uparrow 367%)
1.5 rd	w/o	3.61	2.2
	w/	4.15 (\uparrow 15%)	2.96 (\uparrow 35%)

The boldface values indicate the optimal cases in the corresponding test scenario.

position. As shown in Fig. 16, localization error increases with the observation angle θ . The quadrotor we used has front and down cameras for observation. Therefore, we choose the down camera for continuous detection when the terminal attitude is below 30° and the front camera when it is above 30° . Moreover, the decreasing error with decreasing distance also presents the necessity of replanning.

We conduct tests under different terminal attitudes, as shown in Fig. 15. The parameters are the same as in Section VII-C. The expected observation range is set to $\bar{d}_{\min} = 0.2$ m and $\bar{d}_{\max} = 2.0$ m. The orange and blue trajectories show quadrotor maneuvers with and without visibility considerations, respectively. For 0.0 and 0.5 rad terminal pitch angles, without visibility consideration, the drone can only observe the target at a short distance and a short duration. While with the perception cost, the quadrotor can keep continuous observation within the preset observe distance $\bar{d}_{\max} = 2.0$ m. For 1.5 rad pitch angle, the visibility-aware perching can keep the target at the center of the image space as long as possible. The observable distance and duration before touching the target plane are summarized in Table VI. Consequently, with our visibility-aware perching planning, the target visibility in terms of both space and time is dramatically improved.

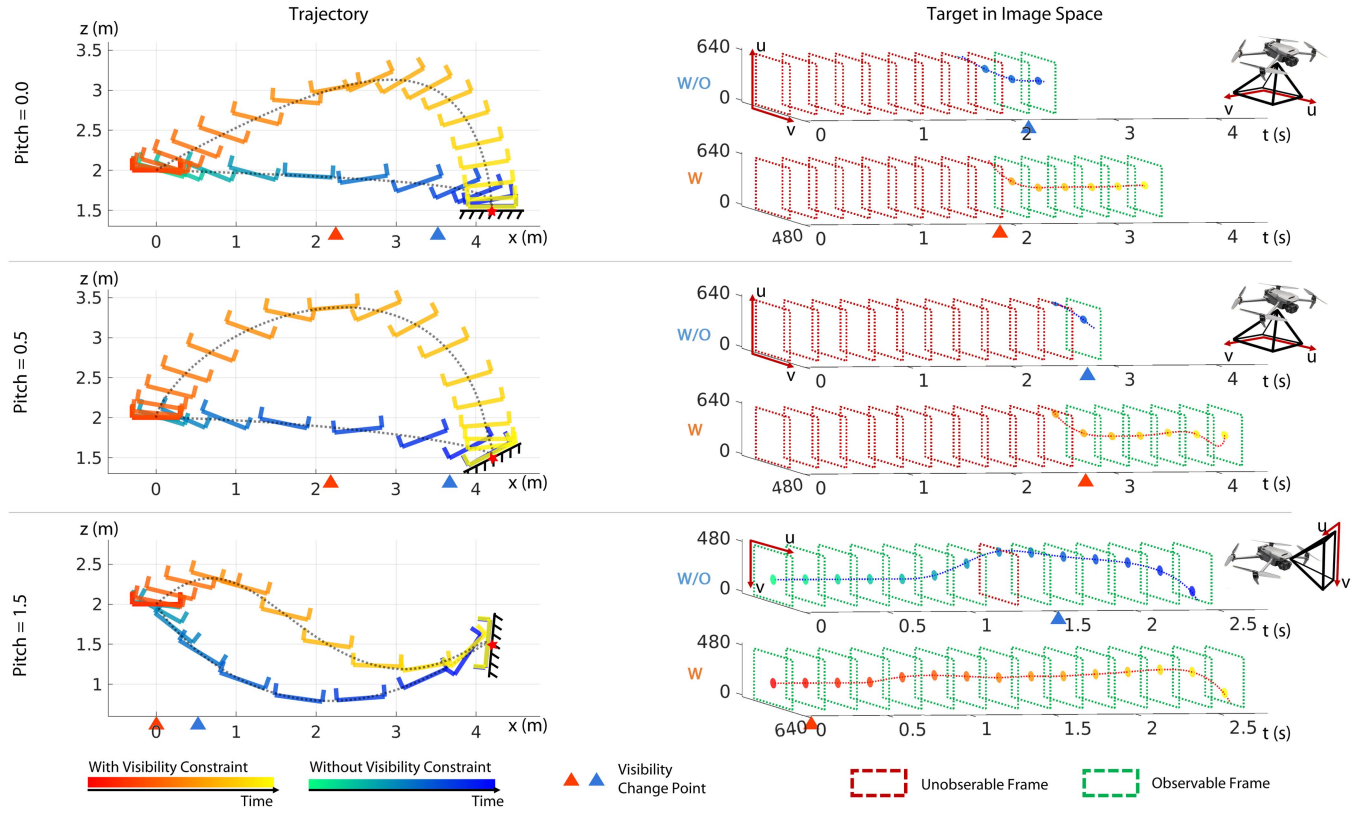


Fig. 15. Ablation study of the visibility awareness at different perching terminal angles. The quadrotor uses the down camera to observe the target at 0.0 and 0.5 rad terminal pitch angles, and the front camera for 1.5 rad terminal pitch angles. The expected observe distance is set to $\bar{d}_{\min} = 0.2$ m and $\bar{d}_{\max} = 2.0$ m. Left: The x - z trajectory w/ and w/o perception constraint. The triangles on the x -axis represent the position when the spatial visibility changes. The target is visible on the right side of the point. Right: The target position in the u - v image space. The target position is expected to be as close to the image's center as possible. The triangles on the x -axis represent the moment when the temporal visibility changes.

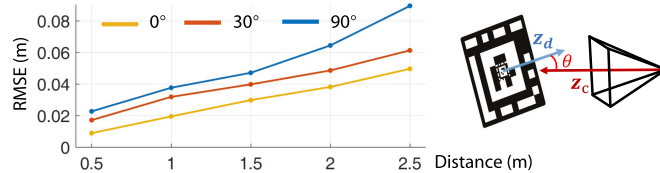


Fig. 16. Visual tag localization error at different distances and observation angles θ . \mathbf{z}_d is the normal vector of the tag plane and \mathbf{z}_c is the optical axis.

VIII. REAL WORLD EXPERIMENTS

A. System Configuration

We deploy our adaptive tracking and perching scheme on a commercial drone (DJI MAVIC3) shown in Fig. 18, with a full-size SUV as the moving platform. Our system operates outside the laboratory and is tested on the road, bringing it closer to real-world applications. The drone will attempt to track and perch on the SUV. The perching stage starts when receiving external perching order.

The target position is obtained by the fusion of finer visual detection and coarser nonstationary differential-GPS-based relative localization. We use the recursive visual fiducial tags [52] to mark the precise perching position. The software implementation of our scheme is integrated into the drone's embedded

processors, and interfaces with the existing modules to form a complete system. The localization and mapping functionality of the DJI MAVIC3 is retained as the foundation of the system. After the generation of the trajectory, control instructions are derived and transmitted to the flight controller for execution. Software modules, estimation, perception, planning, and control are all running onboard in real time. On the severely limited computing platform (8× slower than simulation settings), our planning scheme can still achieve 20 Hz replanning.

B. Visibility-Aware Tracking Validation

We select two common real-world scenarios to validate the visibility awareness of our tracking scheme. Static and moving impediments will appear in the path of the vehicle when it moves, stops, or turns. The drone is expected to track the vehicle without occlusion or target loss.

1) Scenario A: L-Shape Turn: The occlusion frequently happens when the target makes turns around obstacles. In this case, the target vehicle makes an L-shape turn, and two trucks are parked at the bend, which could easily block the view of the tracking drone. As shown in Fig. 17(a), due to our visibility-aware tracking scheme, the drone actively adjusts its relative position and keeps its FoV free of occlusion even when the vehicle makes sudden turns near obstacles.

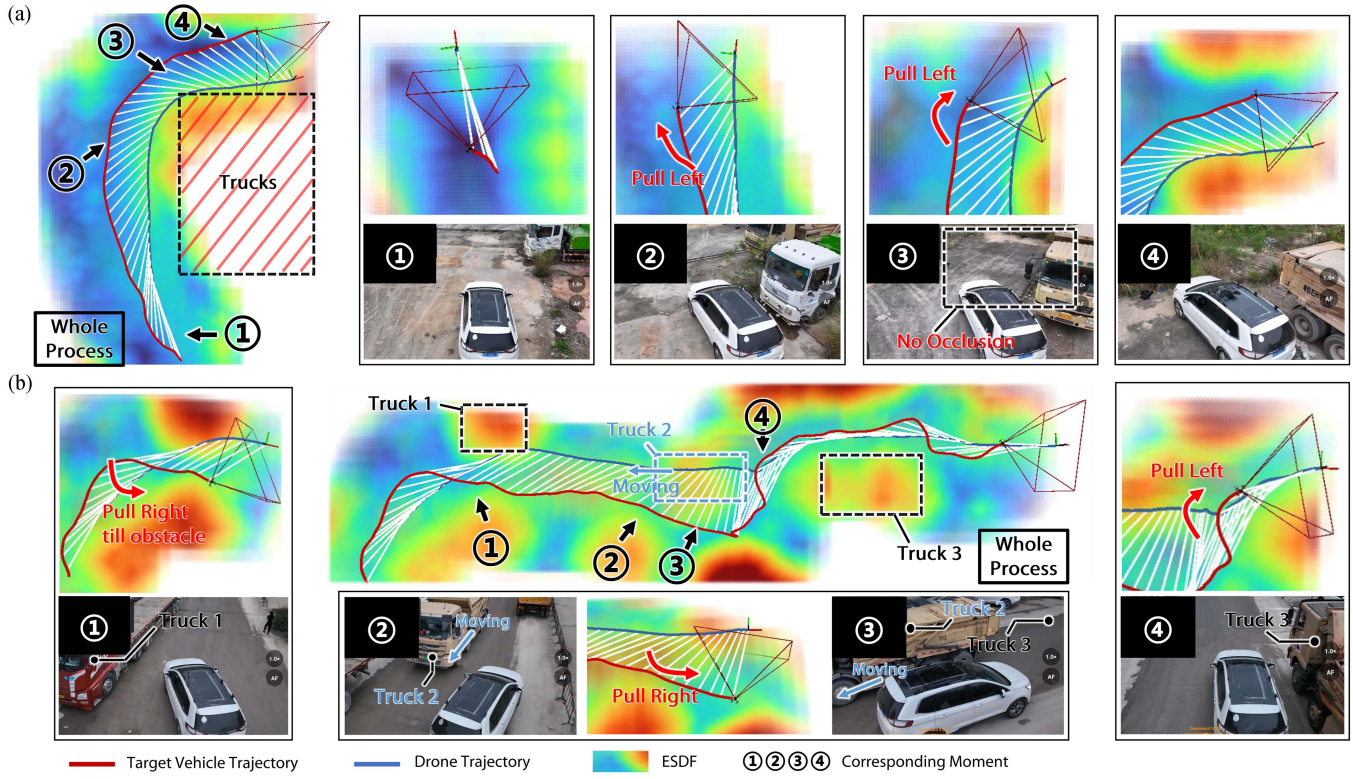


Fig. 17. Real-world visibility-aware tracking validation. (a) L-shape Turn: ① The drone tracks the SUV behind. ② A truck appears closely on the right. The drone pulls left to avoid occlusion. ③ The SUV turns right along the trunk, easily causing occlusion. The drone pulls left to avoid it. ④ Constantly tracking on the left for better visibility. (b) Bilateral staggered obstacles: ① The SUV heading straight, truck 1 appears on the left, and the drone pulls right. ② Trunk 2 is approaching the target SUV from the left. ③ The SUV stops to make way for truck 2. The tracking drone keeps pulling right as truck 2 gets closer. ④ The SUV passes truck 3, and the drone pulls left for less occlusion.



Fig. 18. Illustration of the quadrotor platform (DJI MAVIC3). The front and bottom cameras are used for detection. The gimbal camera was not selected for detection since its dedicated designed for photography and with high link delay. The drone and the surface are secured with velcro after perching.



Fig. 19. Comparison with the origin DJI tracking under scenario 2. (a) Active tracking: The target car is lost at the turning. (b) Our tracking scheme enhances visibility actively, tracking successfully.

2) Scenario B: Bilateral Staggered Obstacles: While the SUV is moving, static or dynamic trucks will appear alternately on the left and right sides. The target vehicle will either stop or move forward. In this experiment, not only the active adjustment of the drone to the static surroundings is demonstrated, but also the ability to avoid dynamic obstacles affecting the observation line of sight. As shown in Fig. 17(b), the tracking drone maintains high visibility of the target SUV throughout the process.

3) Comparative Experiment: We compare our tracking scheme with the mature commercial *Active Tracking* function of DJI MAVIC3 under Scenario A, as shown in Fig. 19. When the target SUV turns right near the truck, the drone with an *active tracking* is unaware of the potential occlusion and loses the target at the turning. While our method drives the drone to avoid the occlusion effect of the truck, and allows the drone to continuously receive visual information of the target.

In these experiments, the drone observes the target SUV at a certain distance with a straight-forward angle and effectively avoids the occlusion of obstacles. Consequently, our scheme drives the drone to maintain a stable relative state and high-quality observation with the target.

C. High-Speed Dynamic Tracking and Perching Validation

Extensive experiments are conducted to validate dynamic tracking and perching in multiple scenarios. The system is tested

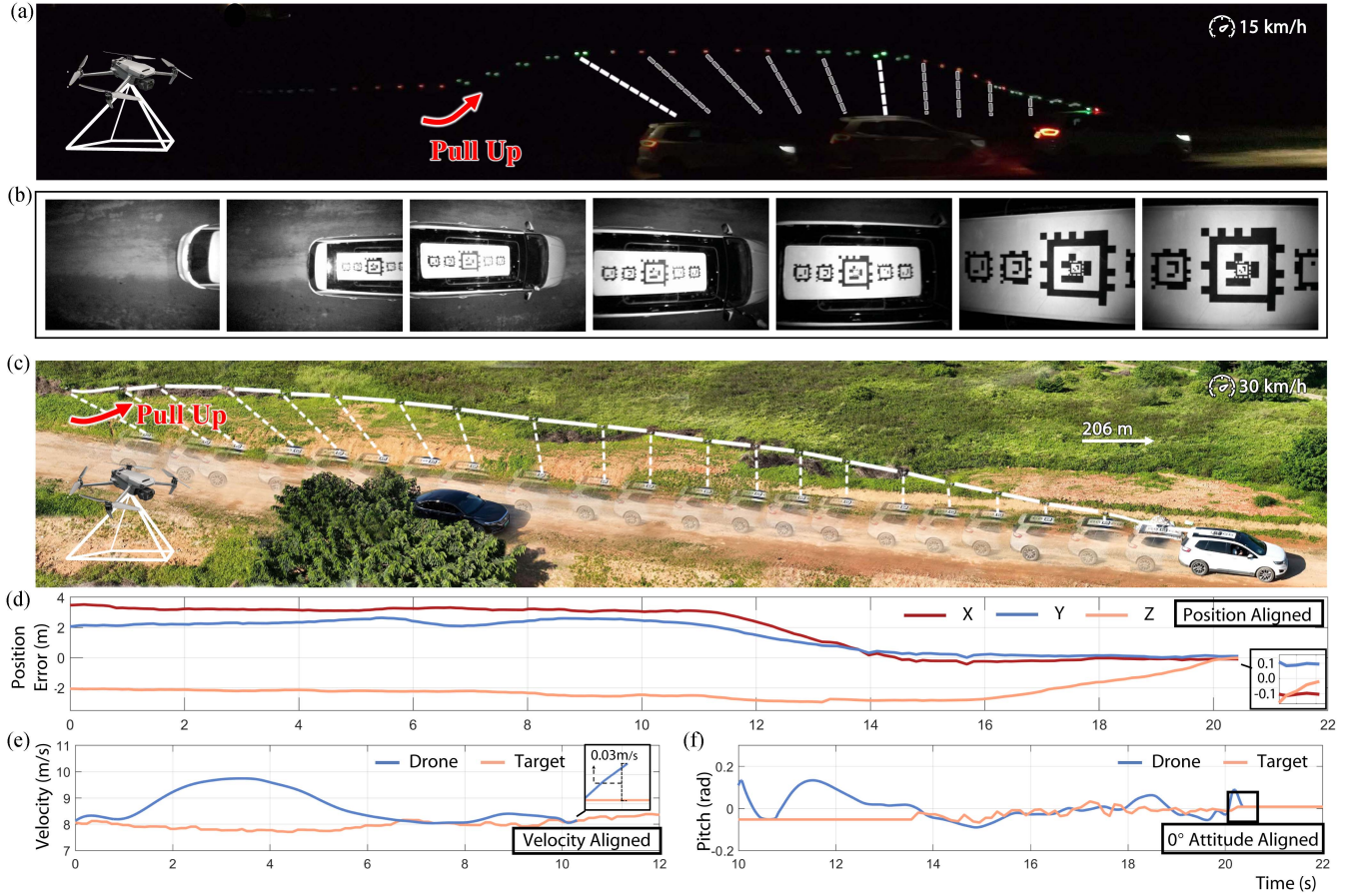


Fig. 20. (a) and (b) Illustration of the 15 km/h (4.2 m/s) tracking and horizontal perching real-world experiment in the night scene. (b) Images obtained by the down camera of the drone. (c)–(f) Illustration of the 30 km/s (8.3 m/s) high-speed tracking and horizontal perching. (d) Position error between the drone and the desired perching point. (e) Velocity curve of the drone and the SUV. (f) Pitch angle curve of the drone and the perching surface on the SUV.

TABLE VII
MULTIPLE SCENES REAL-WORLD EXPERIMENTS

Scene	Target Vel. (m/s)	Drone Vel. (m/s) (Max. / Avg.)	Target Acc. (m/s ²)	Error (cm)
Indoor	1.5	2.65 / 2.21	0.65	3.31
Road	4.0	5.13 / 4.76	1.01	4.47
Field Night	4.0	5.22 / 4.47	1.67	8.36
	4.0	5.37 / 4.69	1.12	5.87
Field	6.0	7.53 / 6.87	1.18	10.92
	8.0	9.51 / 8.44	1.31	14.19

The boldface values indicate the optimal cases in the corresponding test scenario.

in high-speed situations that require an efficient, robust, and accurate tracking and perching scheme. The following tests present the system's high precision, system-level robustness, and active visibility enhancement. We first test horizontal perching in multiple scenarios. The results of the experiments are summarized in Table VII. Indoor and road scenarios have good road conditions, yet the field road provides for safe high-speed tests but with more uneven ground causing target shaking. These abundant scenes also demonstrate the application value. And the multiple desire terminal attitudes with different target speeds are also tested and summarized in Table VIII. For both tables, the maximum and average velocity of the drone during perching are

TABLE VIII
MULTIPLE ATTITUDE DYNAMIC PERCHING EXPERIMENTS

Pitch angle	Target Vel. (m/s)	Drone Vel. (m/s) (Max. / Avg.)	Target Acc. (m/s ²)	Error (cm)
0.5 rd	0.0	1.63 / 0.82	0.27	2.05
	1.0	1.73 / 1.51	0.49	4.85
	2.0	3.04 / 2.33	0.60	6.29
1.0 rd	0.0	2.37 / 1.43	0.26	2.86
	1.0	2.84 / 1.91	0.42	7.01
	2.0	3.87 / 2.86	0.41	9.33

recorded. The average target acceleration estimation shows both real velocity changes and perception disturbance. Moreover, the final perching errors are listed in the table. We present three cases for more details as follows.

1) *Case 1: 15 km/h Tracking and Perching at Night:* In this case, we present the visibility-aware behavior resulting from our approach. Thanks to the spotlight on the bottom of the drone, the bottom detection camera is adaptable to night scenes. The visual perception range is set to [0.0 m, 2.0 m].

As shown in Fig. 20(a), the initial relative height is less than 2.0 m, so the drone pulls itself up to ensure the observation of the target within the set range. Such behavior is not intentionally designed but rather emerges automatically due to the perception

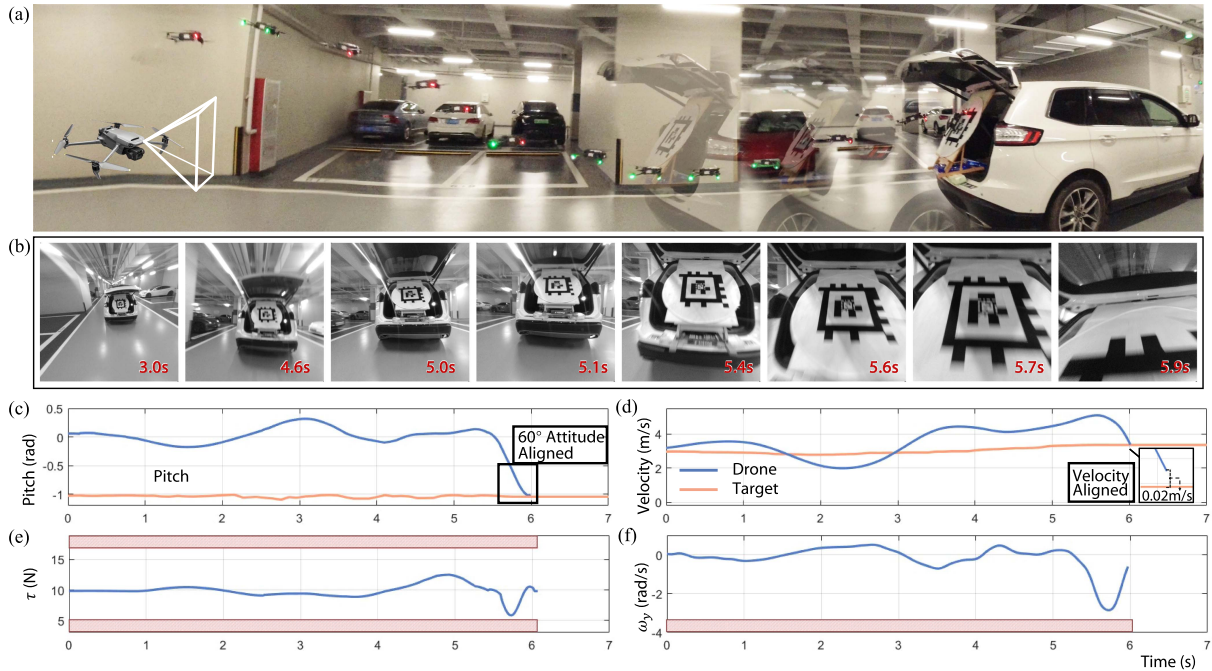


Fig. 21. Illustration of the large attitude dynamic tracking and perching real-world experiment. (a) Snapshot of the whole process. The vehicle moves at approximately 3.5 m/s, and the perching surface is 60° inclined. (b) Images obtained by the front camera of the quadrotor. (c) Pitch angle of the drone and the moving plane. (d) Velocity curve of the drone and the moving plane. (e) Thrust curve of the drone. (f) Angular velocity curve.

metric. The target tag is kept in the center of the image space as much as possible since its initial detection, which can enhance the target state estimation.

2) *Case 2: 30 km/h High-Speed Tracking and Perching:* In this case, we conduct high-speed tracking and perching on the top of the SUV. During the perching process, as shown in Fig. 20(b), the SUV's speed is 30 km/h (8.3 m/s), while the maximum speed of the drone reaches about 10 m/s. The final perching error on the $x - y$ plane is 10.7 cm. The inaccuracy is mostly caused by poor target estimating (due to detection and system link delays) and trajectory tracking errors. The wind and the ground effect are countered by the integrator control. Due to the turbulence of the vehicle, the attitude of the perching surface is shaking. The drone can obtain the plane's attitude during continuous observation and constantly replan, and finally ensure the attitude alignment at the end.

3) *Case 3: Large Attitude Dynamic Tracking and Perching:* In this case, we set a 60° inclined plane in the trunk of the SUV as the perching surface to validate the large attitude perching ability. Fig. 21 shows the snapshot of the whole process. For the sake of perception enhancement, the trajectory shape is similar to the simulated one with 1.5 rad pitch angle shown in Fig. 15. During the time interval from 3.0 to 5.7 s, the drone keeps the tag in the center of the image space as much as possible. The angular velocity and the thrust are both within the dynamic feasible region.

IX. CONCLUSION

In this article, we analyzed the core dilemmas to achieve tracking and perching in the dynamic scenario in detail and summarized five aspects of requirement accurately to solve

the above problems. Then we, respectively, designed metrics to enhance visibility, guarantee safety, and dynamic feasibility in both tracking and perching stages. To adapt to the dynamic target state, we adjusted the terminal state of the drone accordingly to achieve state alignment. High-frequency spatiotemporal SE(3) trajectory optimization provided feasible tracking and perching trajectories. Finally, we deployed the adaptive tracking and perching scheme systematically on the commercial drone with a full-size SUV as the moving platform for real-world experiments. The results verified that our scheme was effective and had great application value.

ACKNOWLEDGMENT

The authors would like to thank colleagues at DJI for their strong support for this work: Z. Lu, Z. Xu, B. Wu, J. Nong, and J. Ying.

REFERENCES

- [1] D. N. Das, R. Sewani, J. Wang, and M. K. Tiwari, "Synchronized truck and drone routing in package delivery logistics," *IEEE Trans. Intell. Transp. Syst.*, vol. 22, no. 9, pp. 5772–5782, Sep. 2021.
- [2] G. Wu, N. Mao, Q. Luo, B. Xu, J. Shi, and P. N. Suganthan, "Collaborative truck-drone routing for contactless parcel delivery during the epidemic," *IEEE Trans. Intell. Transp. Syst.*, vol. 23, no. 12, pp. 25077–25091, Dec. 2022.
- [3] Y. Liu, Z. Liu, J. Shi, G. Wu, and W. Pedrycz, "Two-echelon routing problem for parcel delivery by cooperated truck and drone," *IEEE Trans. Syst. Man Cybern. Syst.*, vol. 51, no. 12, pp. 7450–7465, Dec. 2021.
- [4] G. Wu, W. Pedrycz, H. Li, M. Ma, and J. Liu, "Coordinated planning of heterogeneous earth observation resources," *IEEE Trans. Syst. Man Cybern. Syst.*, vol. 46, no. 1, pp. 109–125, Jan. 2016.
- [5] P. Tokekar, J. Vander, D. H. Mulla, and V. Isler, "Sensor planning for a symbiotic UAV and UGV system for precision agriculture," *IEEE Trans. Robot.*, vol. 32, no. 6, pp. 1498–1511, Dec. 2016.

- [6] C. Shen, Y. Zhang, Z. Li, F. Gao, and S. Shen, "Collaborative air-ground target searching in complex environments," in *Proc. IEEE Int. Symp. Saf. Secur. Rescue Robot.*, 2017, pp. 230–237.
- [7] J. Delmerico, E. Mueggler, J. Nitsch, and D. Scaramuzza, "Active autonomous aerial exploration for ground robot path planning," *IEEE Robot. Autom. Lett.*, vol. 2, no. 2, pp. 664–671, Apr. 2017.
- [8] S. Wu, W. Xu, F. Wang, G. Li, and M. Pan, "Distributed federated deep reinforcement learning based trajectory optimization for air-ground cooperative emergency networks," *IEEE Trans. Veh. Tech.*, vol. 71, no. 8, pp. 9107–9112, Aug. 2022.
- [9] M. Mittal, R. Mohan, W. Burgard, and A. Valada, "Vision-based autonomous UAV navigation and landing for urban search and rescue," in *Proc. Int. Symp. Robot. Res.*, 2022, pp. 575–592.
- [10] J. Ji, T. Yang, C. Xu, and F. Gao, "Real-time trajectory planning for aerial perching," in *Proc. IEEE/RSJ Int. Conf. Intell. Robots Syst.*, 2022, pp. 10516–10522.
- [11] Q. Wang, Y. Gao, J. Ji, C. Xu, and F. Gao, "Visibility-aware trajectory optimization with application to aerial tracking," in *Proc. IEEE/RSJ Int. Conf. Intell. Robots Syst.*, 2021, pp. 5249–5256.
- [12] H. Cheng, L. Lin, Z. Zheng, Y. Guan, and Z. Liu, "An autonomous vision-based target tracking system for rotorcraft unmanned aerial vehicles," in *Proc. IEEE/RSJ Int. Conf. Intell. Robots Syst.*, 2017, pp. 1732–1738.
- [13] A. G. Kendall, N. N. Salvapantula, and K. A. Stol, "On-board object tracking control of a quadcopter with monocular vision," in *Proc. IEEE Int. Conf. Unmanned Aircr. Syst.*, 2014, pp. 404–411.
- [14] T. Nägeli, J. Alonso-Mora, A. Domahidi, D. Rus, and O. Hilliges, "Real-time motion planning for aerial videography with dynamic obstacle avoidance and viewpoint optimization," *IEEE Robot. Autom. Lett.*, vol. 2, no. 3, pp. 1696–1703, Jul. 2017.
- [15] B. Penin, P. R. Giordano, and F. Chaumette, "Vision-based reactive planning for aggressive target tracking while avoiding collisions and occlusions," *IEEE Robot. Autom. Lett.*, vol. 3, no. 4, pp. 3725–3732, Oct. 2018.
- [16] J. Thomas, J. Welde, G. Loianno, K. Daniilidis, and V. Kumar, "Autonomous flight for detection, localization, and tracking of moving targets with a small quadrotor," *IEEE Robot. Autom. Lett.*, vol. 2, no. 3, pp. 1762–1769, Jul. 2017.
- [17] R. Bonatti, Y. Zhang, S. Choudhury, W. Wang, and S. Scherer, "Autonomous drone cinematographer: Using artistic principles to create smooth, safe, occlusion-free trajectories for aerial filming," in *Proc. Int. Symp. Exp. Robot.*, 2018, pp. 119–129.
- [18] Z. Han, R. Zhang, N. Pan, C. Xu, and F. Gao, "Fast-tracker: A robust aerial system for tracking agile target in cluttered environments," in *Proc. IEEE Int. Conf. Robot. Autom.*, 2021, pp. 328–334.
- [19] B. F. Jeon and H. J. Kim, "Online trajectory generation of a MAV for chasing a moving target in 3D dense environments," in *Proc. IEEE/RSJ Int. Conf. Intell. Robots Syst.*, 2019, pp. 1115–1121.
- [20] B. Jeon, Y. Lee, and H. J. Kim, "Integrated motion planner for real-time aerial videography with a drone in a dense environment," in *Proc. IEEE Int. Conf. Robot. Autom.*, 2020, pp. 1243–1249.
- [21] J. Ji, N. Pan, C. Xu, and F. Gao, "Elastic tracker: A spatio-temporal trajectory planner for flexible aerial tracking," in *Proc. IEEE Int. Conf. Robot. Autom.*, 2022, pp. 47–53.
- [22] A. Borowczyk, D.-T. Nguyen, A. P.-V. Nguyen, D. Q. Nguyen, D. Saussié, and J. L. Ny, "Autonomous landing of a multirotor micro air vehicle on a high velocity ground vehicle," *IFAC-PapersOnline*, vol. 50, no. 1, pp. 10488–10494, 2017.
- [23] Y. Qi, J. Jiang, J. Wu, J. Wang, C. Wang, and J. Shan, "Autonomous landing solution of low-cost quadrotor on a moving platform," *Robot. Auton. Syst.*, vol. 119, pp. 64–76, 2019.
- [24] J. Ghommam and M. Saad, "Autonomous landing of a quadrotor on a moving platform," *IEEE Trans. Aerosp. Elec. Syst.*, vol. 53, no. 3, pp. 1504–1519, Jun. 2017.
- [25] P. Serra, R. Cunha, T. Hamel, D. Cabecinhas, and C. Silvestre, "Landing of a quadrotor on a moving target using dynamic image-based visual servo control," *IEEE Trans. Robot.*, vol. 32, no. 6, pp. 1524–1535, Dec. 2016.
- [26] J. Thomas, G. Loianno, K. Sreenath, and V. Kumar, "Toward image based visual servoing for aerial grasping and perching," in *Proc. IEEE Int. Conf. Robot. Autom.*, 2014, pp. 2113–2118.
- [27] D. Lee, T. Ryan, and H. J. Kim, "Autonomous landing of a VTOL UAV on a moving platform using image-based visual servoing," in *Proc. IEEE Int. Conf. Robot. Autom.*, 2012, pp. 971–976.
- [28] J. A. Macés-Hernández, F. Defay, and C. Chauffaut, "Autonomous landing of an UAV on a moving platform using model predictive control," in *Proc. 11th Asian Control Conf.*, 2017, pp. 2298–2303.
- [29] A. Mohammadi, Y. Feng, C. Zhang, S. Rawashdeh, and S. Baek, "Vision-based autonomous landing using an MPC-controlled micro UAV on a moving platform," in *Proc. Int. Conf. Unmanned Aircr. Syst.*, 2020, pp. 771–780.
- [30] A. Paris, B. T. Lopez, and J. P. How, "Dynamic landing of an autonomous quadrotor on a moving platform in turbulent wind conditions," in *Proc. IEEE Int. Conf. Robot. Autom.*, 2020, pp. 9577–9583.
- [31] D. Falanga, A. Zanchettin, A. Simovic, J. Delmerico, and D. Scaramuzza, "Vision-based autonomous quadrotor landing on a moving platform," in *Proc. IEEE Int. Symp. Saf. Secur. Rescue Robot.*, 2017, pp. 200–207.
- [32] P. Wang, C. Wang, J. Wang, and M. Q.-H. Meng, "Quadrotor autonomous landing on moving platform," *Procedia Comput. Sci.*, vol. 209, pp. 40–49, 2022.
- [33] J. M. Daly, Y. Ma, and S. L. Waslander, "Coordinated landing of a quadrotor on a skid-steered ground vehicle in the presence of time delays," *Auton. Robots*, vol. 38, pp. 179–191, 2015.
- [34] T. Muskardin, G. Balmer, S. Wlach, K. Kondak, M. Laiacker, and A. Ollero, "Landing of a fixed-wing UAV on a mobile ground vehicle," in *Proc. IEEE Int. Conf. Robot. Autom.*, 2016, pp. 1237–1242.
- [35] H. Tsukagoshi, M. Watanabe, T. Hamada, D. Ashlih, and R. Iizuka, "Aerial manipulator with perching and door-opening capability," in *Proc. IEEE Int. Conf. Robot. Autom.*, 2015, pp. 4663–4668.
- [36] L. Daler, A. Klaptocz, A. Briod, M. Sitti, and D. Floreano, "A perching mechanism for flying robots using a fibre-based adhesive," in *Proc. IEEE Int. Conf. Robot. Automat.*, 2013, pp. 4433–4438.
- [37] A. Kalantari, K. Mahajan, D. Ruffatto, and M. Spenko, "Autonomous perching and take-off on vertical walls for a quadrotor micro air vehicle," in *Proc. IEEE Int. Conf. Robot. Autom.*, 2015, pp. 4669–4674.
- [38] E. Barrett et al., "Autonomous battery exchange of UAVs with a mobile ground base," in *Proc. IEEE Int. Conf. Robot. Autom.*, 2018, pp. 699–705.
- [39] J. Thomas et al., "Aggressive flight with quadrotors for perching on inclined surfaces," *J. Mechanisms Robot.*, vol. 8, no. 5, 2016, Art. no. 051007.
- [40] J. Mao, S. Nogar, C. M. Kroninger, and G. Loianno, "Robust active visual perching with quadrotors on inclined surfaces," *IEEE Trans. Robot.*, vol. 39, no. 3, pp. 1836–1852, Jun. 2023.
- [41] J. L. Paneque et al., "Perception-aware perching on powerlines with multirotors," *IEEE Robot. Automat. Lett.*, vol. 7, no. 2, pp. 3077–3084, Apr. 2022.
- [42] P. Vlantis, P. Marantos, C. P. Bechlioulis, and K. J. Kyriakopoulos, "Quadrotor landing on an inclined platform of a moving ground vehicle," in *Proc. IEEE Int. Conf. Robot. Autom.*, 2015, pp. 2202–2207.
- [43] B. Hu and S. Mishra, "Time-optimal trajectory generation for landing a quadrotor onto a moving platform," *IEEE/ASME Trans. Mechatronics*, vol. 24, no. 2, pp. 585–596, Apr. 2019.
- [44] S. Liu, Z. Wang, X. Sheng, and W. Dong, "Hitchhiker: A quadrotor aggressively perching on a moving inclined surface using compliant suction cup gripper," *IEEE Trans. Autom. Sci. Eng.*, to be published, doi: [10.1109/TASE.2023.3263558](https://doi.org/10.1109/TASE.2023.3263558).
- [45] M. W. Mueller, M. Hehn, and R. D'Andrea, "A computationally efficient motion primitive for quadcopter trajectory generation," *IEEE Trans. Robot.*, vol. 31, no. 6, pp. 1294–1310, Dec. 2015.
- [46] Y. Huang, J. Du, Z. Yang, Z. Zhou, L. Zhang, and H. Chen, "A survey on trajectory-prediction methods for autonomous driving," *IEEE Trans. Intell. Veh.*, vol. 7, no. 3, pp. 652–674, Sep. 2022.
- [47] M. Watterson and V. Kumar, "Control of quadrotors using the Hopf fibration on $SO(3)$," in *Robotics Research*. Berlin, Germany: Springer, 2020, pp. 199–215.
- [48] Z. Wang, X. Zhou, C. Xu, and F. Gao, "Geometrically constrained trajectory optimization for multicopters," *IEEE Trans. Robot.*, vol. 38, no. 5, pp. 3259–3278, Oct. 2022.
- [49] L. S. Jennings and K. L. Teo, "A computational algorithm for functional inequality constrained optimization problems," *Automatica*, vol. 26, no. 2, pp. 371–375, 1990.
- [50] W. H. Press, S. A. Teukolsky, W. T. Vetterling, and B. P. Flannery, *Numerical Recipes 3rd Edition: The Art of Scientific Computing*, 3rd ed. New York, NY, USA: Cambridge Univ. Press, 2007.
- [51] A. Domahidi and J. Jerez, "Forces professional," Embotech AG, 2014. [Online]. Available: <https://embotech.com/FORCES-Pro>
- [52] M. Krogius, A. Haggenmüller, and E. Olson, "Flexible layouts for fiducial tags," in *Proc. IEEE/RSJ Int. Conf. Intell. Robots Syst.*, 2019, pp. 1898–1903.



Yuman Gao received the graduation degree in control science and engineering in 2021 from Zhejiang University, Hangzhou, China, where he is concurrently pursuing a minor in advanced honor class of engineering education (ACEE), with Chu Kochen Honors College. He is currently working toward the Ph.D. degree in automation under the supervision of Fei Gao, with the FAST Lab, Zhejiang University.

His research interests include motion planning and autonomous navigation for multirobot systems.



Zhimeng Shang received the master's degree in mechanical engineering and automation from Beihang University, Beijing, China, in 2015.

Since 2015, he has been with DJI, Nanshan, China, focusing on multirotor control and planning. He participated in the development of DJI's Mavic/Phantom/Inspire/FPV series, as well as flight controllers like A3/N3. His research interests include classic and optimal control, motion planning, and UAV design and control.



Jialin Ji received the graduation degree in mechatronic engineering in 2019 from the School of Mechanical Engineering, Zhejiang University, Hangzhou, China, and a minor in advanced honor class of engineering education (ACEE) from Chu Kochen Honors College, Hangzhou, China. He is currently working toward the Ph.D. degree in automation under the supervision of Fei Gao, with FAST Lab, Zhejiang University, working on motion planning and autonomous navigation for aerial robotics.



Yanjun Cao received the Ph.D. degree in computer and software engineering from the University of Montreal, Montreal, Canada, in 2020.

He is currently an Associate Researcher with the Center of Swarm Navigation, Huzhou Institute, Zhejiang University, Hangzhou, China. He leads the Field Intelligent Robotics Engineering (FIRE) group of the Field Autonomous System and Computing Lab (FAST Lab). His research interests include key challenges in multirobot systems, such as collaborative localization, autonomous navigation, perception, and communication.



Qianhao Wang (Student Member, IEEE) received the M.Eng. degree in 2022 in control science and engineering from Zhejiang University, Hangzhou, China, where he is currently working toward the Ph.D. degree in control science and engineering.

His research interests include motion planning, computational geometry, LiDAR SLAM, and autonomous navigation for aerial robotics.



Shaojie Shen received the B.Eng. degree in electronic engineering from the Hong Kong University of Science and Technology, Hong Kong, (HKUST) in 2009, the M.S. degree in robotics and the Ph.D. degree in electrical and systems engineering from the University of Pennsylvania, PA, USA, in 2011 and 2014, respectively.

In 2014, he joined the Department of Electronic and Computer Engineering, HKUST as an Assistant Professor, and was promoted to Associate Professor in 2020. His research interests include robotics and unmanned aerial vehicles, with focus on state estimation, sensor fusion, computer vision, localization and mapping, and autonomous navigation in complex environments.



Rui Jin received the B.E. degree in mechanical design & manufacturing and their automation from Northwestern Polytechnical University, Xi'an, China, in 2021. He is currently working toward the M.Eng. degree in robotics with the FAST Lab, Zhejiang University, Hangzhou, China.

Her research interests include the design, control, and motion planning of coaxial helicopters.



Chao Xu (Senior Member, IEEE) received the Ph.D. degree in mechanical engineering from Lehigh University, Bethlehem, PA, USA, in 2010.

He is currently an Associate Dean and Professor with the College of Control Science and Engineering, Zhejiang University, Hangzhou, China. He is also the inaugural Dean of ZJU Huzhou Institute, and plays the role of a Managing Editor for *IET Cyber-Systems and Robotics*. He has authored or coauthored more than 100 papers in international journals, including *Science Robotics*, *Nature Machine Intelligence*, etc.

His research interests include flying robotics and control-theoretic learning.



Yi Lin received the B.Eng. degree in software engineering from the Harbin Institute of Technology, Harbin, China, in 2015, and the M.Phil. degree in electronic and computer engineering from the Hong Kong University of Science and Technology, Hong Kong, in 2017.

He is currently a Senior Engineer with DJI Technology Company, Ltd., Nanshan, China. His research interests include computer vision, simultaneous localization and mapping, 3-D reconstruction, autonomous navigation, unmanned aerial vehicles, motion planning, and optimization.



Fei Gao (Member, IEEE) received the Ph.D. degree in electronic and computer engineering from the Hong Kong University of Science and Technology, Hong Kong, in 2019.

He is currently a tenured Associate Professor with the Department of Control Science and Engineering, Zhejiang University, Hangzhou, China, where he leads the Flying Autonomous Robotics (FAR) group affiliated with the Field Autonomous System and Computing (FAST) Laboratory. His research interests include aerial robots, autonomous navigation, motion planning, optimization, and localization and mapping.

Design and Stiffness Control of a Variable-Length Continuum Robot for Endoscopic Surgery

Jingyu Zhang, *Member, IEEE*, Qin Fang^{ID}, Lilu Liu^{ID}, Rui Jin, Pingyu Xiang^{ID}, Rong Xiong^{ID}, *Senior Member, IEEE*, Yue Wang^{ID}, *Member, IEEE*, and Haojian Lu^{ID}, *Member, IEEE*

Abstract—Continuum robots, owing to their inherent compliance, have become essential in endoscopic surgical procedures, such as mucosal ablation. However, the prevalent design of endoscopic manipulators, which typically features only a single active bending segment, often results in limited dexterity and accessibility. Additionally, the incorporation of variable stiffness in these robots has attracted significant interest, with the aim to improve manipulation capabilities in confined spaces. In the paper, we propose a novel variable-length continuum robot with variable stiffness for endoscopic surgery. The robot's stiffness can be altered either by modifying the catheter's length or solid-liquid transition of low-melting-point alloy (LMPA). The design and fabrication methods of the robot are meticulously detailed. Additionally, a quasi-static stiffness model along with a learning-based stiffness compensation approach for accurate stiffness estimation are proposed. Leveraging this model, a contact force controller is designed for ablation procedure. The experimental results show that our robot possesses good flexibility and accessibility, making it highly adept at manipulating in confined spaces. Its variable stiffness feature significantly enhances its ability to counteract external disturbance and prevent tip deformation (with a average position change of 1.1mm). Finally, through force control experiments and a surgical demonstration in a gastrointestinal model, we have further validated the robot's applicability in surgical contexts.

Note to Practitioners—This paper proposed a variable-length continuum robot with variable stiffness for endoscopic surgery.

Manuscript received 5 February 2024; revised 2 May 2024; accepted 17 June 2024. This article was recommended for publication by Associate Editor H. Wang and Editor L. Zhang upon evaluation of the reviewers' comments. This work was supported in part by Zhejiang Provincial Natural Science Foundation of China under Grant LD22E050007, in part by the National Natural Science Foundation of China under Grant 62303407 and Grant 62103363, and in part by the Key Research and Development Program of Zhejiang under Grant 2022C01022 and Grant 2023C01176. (Jingyu Zhang and Qin Fang contributed equally to this work.) (Corresponding authors: Haojian Lu; Yue Wang.)

Jingyu Zhang, Qin Fang, Lilu Liu, Rui Jin, Pingyu Xiang, Rong Xiong, and Yue Wang are with the State Key Laboratory of Industrial Control and Technology and the Institute of Cyber-Systems and Control, Zhejiang University, Hangzhou 310027, China (e-mail: ywang24@zju.edu.cn).

Haojian Lu is with the State Key Laboratory of Industrial Control and Technology and the Institute of Cyber-Systems and Control, Zhejiang University, Hangzhou 310027, China, and also with Stomatology Hospital, the School of Stomatology, Zhejiang Provincial Clinical Research Center for Oral Diseases, the Key Laboratory of Oral Biomedical Research of Zhejiang Province, the Cancer Center of Zhejiang University, and the Engineering Research Center of Oral Biomaterials and Devices of Zhejiang Province, Zhejiang University School of Medicine, Hangzhou 310000, China (e-mail: luhaojian@zju.edu.cn).

This article has supplementary material provided by the authors and color versions of one or more figures available at <https://doi.org/10.1109/TASE.2024.3418092>.

Digital Object Identifier 10.1109/TASE.2024.3418092

The robot can achieve axial elongation and omnidirectional bending motion, having better dexterity and accessibility than traditional medical continuum robots with one active bending segment. The robot's stiffness can be adjusted by the length changes or solid-liquid transition of low-melting-point alloy (LMPA). Besides, an accurate stiffness model and a contact force controller are proposed for endoscopic ablation surgery. By experimental results, the robot shows high flexibility and accessibility, allowing access to confined spaces for manipulation, and good control accuracy and variable stiffness capability for endoscopic surgery.

Index Terms—Soft robots, small-scale robot, variable length, variable stiffness, endoscopic surgery.

I. INTRODUCTION

CONTINUUM robots, drawing inspiration from the snakes [1], elephant trunks [2], and tendrils [3], [4], are becoming increasingly prevalent in the realm of endoscopic surgery [5]. Their unique ability to bend flexibly and form continuous shapes allows them to navigate through confined spaces. Recent developments have seen the creation of several continuum robots with a single active bending segment, aimed at transforming treatment methodologies in various medical fields such as cardiology [6], [7], pulmonology [8], [9], and urology [10]. Nonetheless, these robots still face challenges related to their limited dexterity and accessibility, which can hinder effective disease diagnosis and treatment within the confined confines of human anatomy.

To expand their operational range and enhance flexibility, advancements in continuum robot design have led to the development of models featuring two or more active bending segments. For instance, Hong et al. developed a two-segment continuum robot for maxillary sinus surgery [11], Wang et al. developed a flexible tendon-driven continuum manipulator for laparoscopic surgery [12], Zeng et al. developed a two-segment notched continuum Robot for sinus surgery [13], and Alfalahi et al. developed a three-segment hand-held concentric tube robot for minimally invasive surgery [14]. However, the tracking errors of these robots will gradually accumulate with an increasing number of segments, and more actuators are necessary, leading to a larger and more cumbersome actuation system. In response to these challenges, recent innovations have introduced advanced structures and actuators to improve the flexibility of continuum robots for medical application [15], [16]. Noteworthy developments

include an origami-inspired actuator designed for upper gastrointestinal endoscopy [17], ferromagnetic soft continuum robots for cerebral vascular aneurysm treatments [18], [19], and shape memory alloy (SMA)-actuated spring-based continuum robot for MRI-guided neurosurgery [20], [21]. These advancements demonstrate a concerted effort to refine the functionality and application of continuum robots in the medical field, addressing previous limitations related to flexibility and system size.

Besides, variable stiffness technologies of continuum robots have also attracted extensive attention for their potential to enhance surgical performance in confined spaces of the human body [22]. Specifically, lower stiffness at the tip (or the whole body) of the robot facilitates safe navigation in narrow spaces, while higher stiffness facilitates the manipulation ability for lesions. Currently, there are three primary methods to change the stiffness of the robot. The first is material-based stiffness adjustment. This approach involves filling the robot with materials that can alter stiffness in response to physical or chemical factors, such as LMPA [23] or shape memory polymer (SMP) [24], [25]. However, the process of changing stiffness with these materials can take time and effort. The second is internal friction changing. The friction of the internal components of the robot can be increased by particle [26] or layer jamming [27], leading to a greater force to deform. While effective, this method may lead to increased mechanical wear and a reduction in the robot's lifespan. The third is a structural configuration change. Typical examples are the continuum robots with pre-programmed tensegrity structure [28], or nonuniform patterns [29]. This approach often requires the robot to maintain a certain configuration and has limited flexibility.

In conclusion, to address the trade-offs between the limited flexibility of single-segment active bending continuum robots and the challenges in maintaining precise control over multi-segment functional bending robots, we propose a novel design: a variable-length single-segment active bending continuum robot. This design significantly expands the robot's operational space. Furthermore, by employing a combination of material-based and structure-based methods for adjusting stiffness, the robot can adopt various stiffness configurations to suit different surgical tasks, enhancing its overall flexibility. At the algorithmic level, we have developed a stiffness model for the robot and designed a learning-based stiffness compensation algorithm. This algorithm is tailored to compensate for the errors induced by friction or gravity. Additionally, we have engineered a contact force controller specifically for ablation force control within the human body. These advancements collectively aim to refine the robot's performance, making it more adaptable and efficient for endoscopic surgical application, as depicted in Fig. 1. The main contributions of this paper can be summarized in the following three points:

- A variable-length single-segment active bending continuum robot with variable stiffness is proposed, which can achieve omnidirectional bending and axial elongation. The robot uses material solid-liquid transition and structural changes to adjust its stiffness.
- The stiffness model and a learning-based stiffness compensation approach of the variable-length continuum

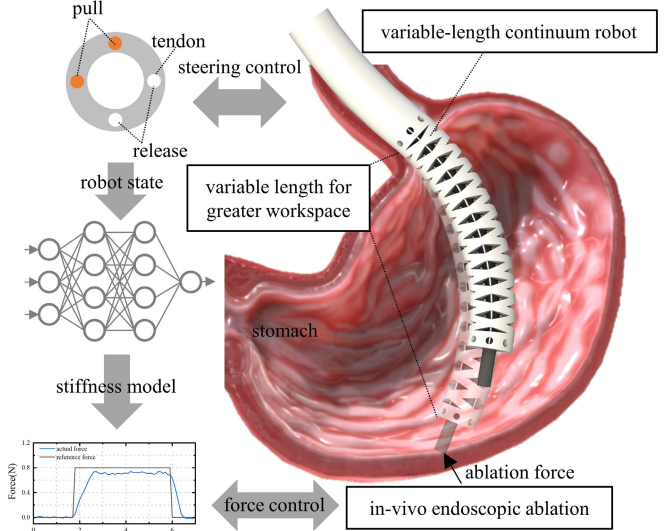


Fig. 1. Force control diagram of the variable-length continuum robot for endoscopic mucosal ablation. The robot is controlled to reach the target area, showing large workspace and high dexterity. During the ablation procedure, the neural network outputs the compensation to improve the accuracy of the stiffness model used for contact force control.

robot are proposed to establish the relationship between the robot stiffness, material properties, and driving force. In addition, a force controller is proposed for ablation surgery.

- The robot integrates a magnetic positioning sensor, a micro camera, and surgical tools and has been comprehensively validated in the in vitro experiments in a gastrointestinal model, confirming its surgical application potential.

The article is organized as follows. In Section II, the design and fabrication of a quasi-static stiffness model, along with a learning-based stiffness compensation approach, are introduced. Besides, a contact force controller is proposed for ablation surgery. In Section III, the characterization experiment, variable stiffness analysis, force control experiment, and gastrointestinal surgical demonstration are carried out to assess the performance of the proposed robot comprehensively. In Section V, the main achievements and improvements of this work are briefly concluded.

II. METHODS

A. Design and Fabrication

The design and fabrication of the variable-length continuum robot are depicted in Fig. 2(a). The robot mainly consists of a robotic arm to adjust the robot pose, a variable-length catheter with an outer diameter (OD) of 12.6 mm used for endoscopic surgery, and an actuation system to control the catheter. The catheter is designed to achieve omnidirectional steering and axial elongation under the actuation of the rod (made of Nitinol). The actuation system consists of four linear motors mounted on the motor fixture (Fig. 2(b)), which are used to pull the rod to steer or elongate the variable-length catheter. Each linear motor is installed with a force sensor through the motor flange and sensor connector, and the force

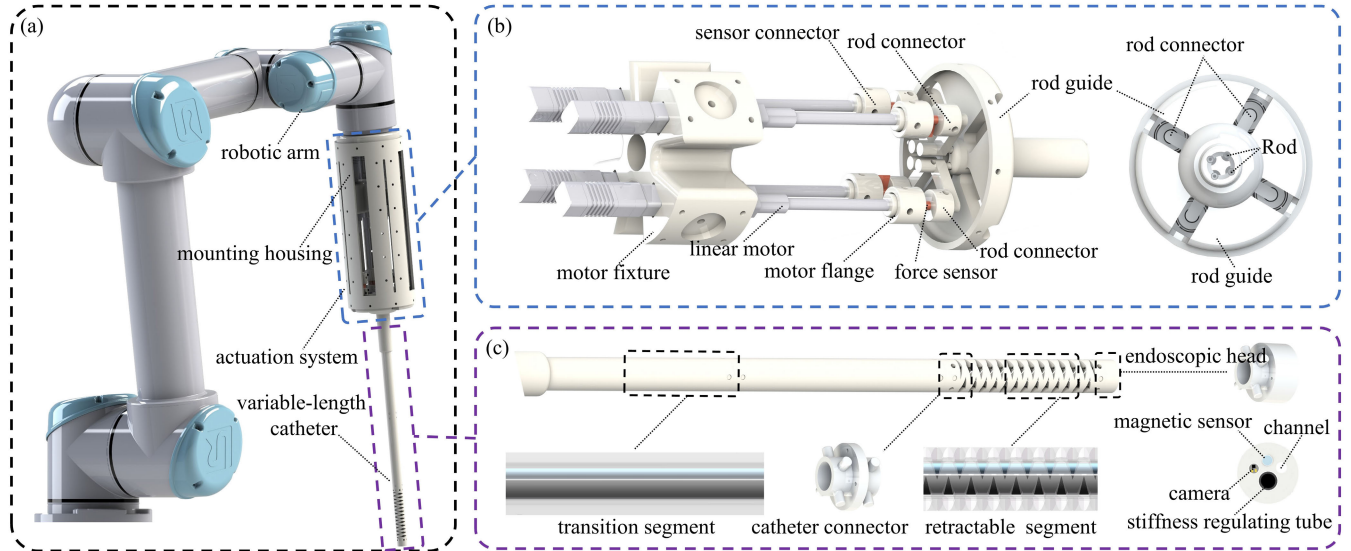


Fig. 2. The design and fabrication of the variable-length continuum robot. (a) The CAD model of the variable-length continuum robot. It consists of a robotic arm to adjust the robot pose, a variable-length catheter used for endoscopic surgery, and the actuation system for the shape control of the catheter. (b) The CAD model of the actuation system. It consists of four linear motors to pull the rods to steer or extend the variable-length catheter. Each linear motor is installed with a force sensor to measure the driving force. (c) The CAD model of the variable-length catheter. It mainly consists of a retractable segment and a transition segment used for passive compliance.

sensor connects with the rod through the rod connector. During movement, the force sensors are used to measure the driving force in real-time.

The detailed structure of the variable-length catheter is depicted in Fig. 2(c). It consists of a retractable segment used for steering or elongation control, a transition segment used for passive compliance, an endoscopic head used to install endoscopic equipment, and a catheter connector used to bond the retractable segment and transition segment. In this robot, a magnetic positioning sensor (610060, Northern Digital Inc., Canada), a micro camera (OCHTA10, OmniVision Technologies Inc., America), a working channel (made of polycarbonate), and a stiffness regulating tube (with an OD of 4mm) are installed on the endoscopic head. The transition and retractable segments are made of silicone materials but have different stiffnesses. Besides, the retractable segment has many triangle-shaped incisions, resulting in much lower stiffness than the transition segment.

The structure of the stiffness regulating tube is depicted in Fig. 3(a). It is filled with LMPA, wound with the heating wire (made of 0.1 mm copper wire), and then encapsulated by a TPU layer. It can adjust the stiffness of the variable-length catheter by switching the state of the LMPA (melt by heating and solidify by cooling). Additionally, the detailed fabrication of the retractable segment is also introduced, as depicted in Fig. 3(b). Firstly, two fluted parts (bottom and top) made of resin materials are closed to form a groove. Secondly, seal the fluted parts with one end cap and pour the liquid silica gel (Polydimethylsiloxane material) into the groove. When filled with liquid, put on the other end cap. Thirdly, insert the spindle and pins to form a working channel and four holes for placing the push rods. After high-temperature curing, the spindle, pins, end caps, and fluted parts are successively removed, and

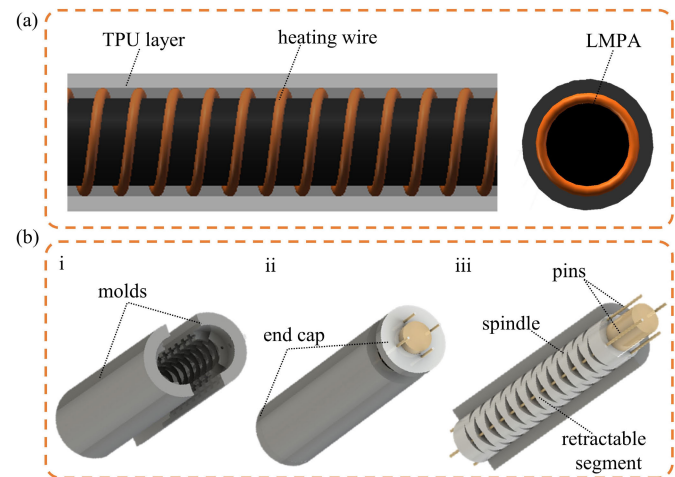


Fig. 3. The design and fabrication of stiffness regulating tube.(a) The CAD model of the stiffness regulating tube. (b) The detailed fabrication process for the variable-length catheter.

the retractable segment is obtained. Similarly, the transition segment can be fabricated by the same fabrication process.

B. Kinematic Model

To analyze the movement of the variable-length catheter, the kinematic analysis is conducted, as shown in Fig. 3. The coordinate system $\{o_b x_b y_b z_b\}$ and $\{o_t x_t y_t z_t\}$ are established on the base and tip of the variable-length catheter. The coordinate system $\{o_{rt} x_{rt} y_{rt} z_{rt}\}$ and $\{o_{rb} x_{rb} y_{rb} z_{rb}\}$ are established on the tip and base of the retractable segment. Four tendons are fixed on the catheter tip and run parallel to the centroidal axis of the catheter at a radius d .

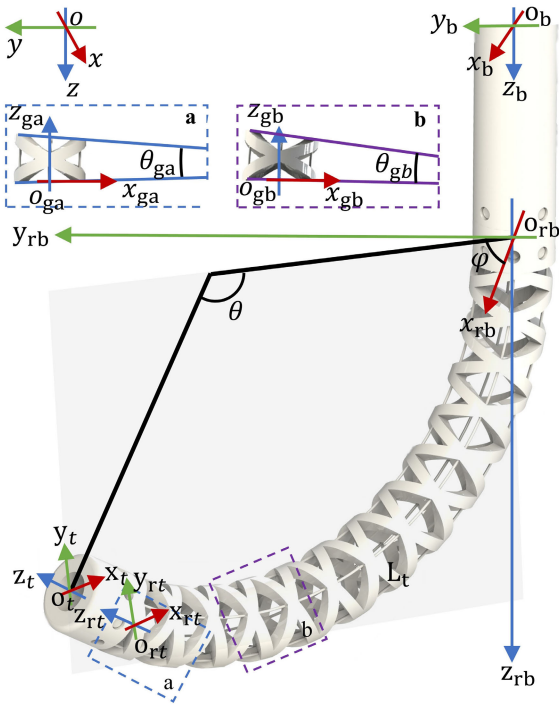


Fig. 4. Kinematic schematic diagram of the variable-length catheter.

To simplify the kinematic model, assume that the retractable segment deforms in constant curvature [30], [31] under the actuation of the rods. As depicted in Fig. 4, the configuration parameters include the bending angle θ , bending plane angle φ and the length L_t (initial length L_0), relative to the coordinate system $\{O_{rb}x_{rb}y_{rb}z_{rb}\}$. The retractable segment has N triangle-shaped incisions in vertical directions respectively. We have

$$\theta_{ga} = \frac{1}{N} \theta \cos(\varphi) \quad (1)$$

$$\theta_{gb} = \frac{1}{N} \theta \sin(\varphi) \quad (2)$$

The transformation matrix ${}^t_b\mathbf{T}$ between the catheter base and the tip can be represented as follows.

$${}^t_b\mathbf{T} = {}^r_b\mathbf{T} \cdot {}^{rt}_b\mathbf{T} \cdot {}^t_{rt}\mathbf{T} = {}^r_b\mathbf{T} \cdot \begin{bmatrix} {}^{rt}_b\mathbf{R} & {}^{rt}_b\mathbf{p} \\ 0 & 1 \end{bmatrix} \cdot {}^t_{rt}\mathbf{T} \quad (3)$$

where ${}^r_b\mathbf{T}$ and ${}^{rt}_b\mathbf{T}$ are respectively the transformation matrix from the base to tip of the transition segment and retractable segment. ${}^{rt}_b\mathbf{R}$ and ${}^{rt}_b\mathbf{p}$ are respectively the rotation matrix and position vector. We have

$${}^t_b\mathbf{p} = {}^r_b\mathbf{p} + {}^r_b\mathbf{R} \cdot {}^{rt}_b\mathbf{p} + {}^r_b\mathbf{R} \cdot {}^{rt}_b\mathbf{R} \cdot {}^t_{rt}\mathbf{p} \quad (4)$$

$${}^t_b\mathbf{R} = {}^r_b\mathbf{R} \cdot {}^{rt}_b\mathbf{R} \cdot {}^t_{rt}\mathbf{R} \quad (5)$$

where ${}^t_{rt}\mathbf{p} = [0, 0, h]^T$, and h is the length of the catheter tip. By deploying sensors on the catheter, the parameters of the above equations can be obtained in real time. Based on the constant curvature assumption, ${}^{rt}_b\mathbf{R}$ and ${}^{rt}_b\mathbf{p}$ could be solved

by the parameters L_t , θ , and φ as follows.

$${}^{rt}_{rb}\mathbf{p} = \frac{L_t}{\theta} \begin{bmatrix} c_\varphi(s_\theta - 1) \\ -s_\varphi(s_\theta - 1) \\ -c_\theta \end{bmatrix} \quad (6)$$

$${}^{rt}_{rb}\mathbf{R} = e^{-\varphi[\hat{\mathbf{w}} \times]} e^{-\theta[\hat{\mathbf{v}} \times]} e^{\varphi[\hat{\mathbf{w}} \times]} \quad (7)$$

where s_α and c_α are abbreviated form of the cosine and sine, respectively $s_\alpha = \sin \alpha$, $c_\alpha = \cos \alpha$, and $\hat{\mathbf{v}} = [0, 1, 0]^T$, $\hat{\mathbf{w}} = [0, 0, 1]^T$

Define the actuation state \mathbf{q} as

$$\mathbf{q} = [L_1, L_2, L_3, L_4]^T \quad (8)$$

where $L_i, i = 1, \dots, 4$ is tendon displacement. We have

$$L_i = -L_c + d\theta \cos(\alpha_i), i = 1, \dots, 4 \quad (9)$$

where L_c is the extension length of the retractable segment and α_i is defined as

$$\alpha_i = \varphi - \pi \frac{i-1}{2} \quad (10)$$

The twist \mathbf{t} of the retractable segment can be obtained by the rate of change of the configurations state $\dot{\psi} = [\dot{\theta}, \dot{\varphi}, \dot{L}_c]$, and the rate of change of the actuation state $\dot{\mathbf{q}}$, as

$$\dot{\mathbf{t}} = \mathbf{J}_{t\psi} \dot{\psi} \quad (11)$$

$$\dot{\mathbf{q}} = \mathbf{J}_{q\psi} \dot{\psi} \quad (12)$$

where $\mathbf{J}_{t\psi}$ is the geometric Jacobian relating configuration space and task space velocities, while $\mathbf{J}_{q\psi}$ is the Jacobian relating configuration space and joint space velocities [32].

C. Stiffness Model

During motion control, the retractable segment would steer or elongate actively under the actuation of the rods, while the transition segment passively deforms. In instantaneous time, only the potential energy variation of the retractable segment, along with the driving rods, is considered. Neglecting gravity [33], the potential energy consists of the bending energy U_b and axial compression energy U_c , then the potential energy U_b can be defined using Euler-Bernoulli beam element analysis as

$$\begin{aligned} U_b = & \frac{1}{2} N EI \int_0^{\frac{L_t}{2N}} \left(\frac{d\theta_{pa}}{ds} \right)^2 + \left(\frac{d\theta_{pb}}{ds} \right)^2 ds \\ & + \sum_{i=1}^4 \frac{1}{2} E_r I_r \int_0^{L_i} \left(\frac{d\theta_{pi}}{ds} \right)^2 ds \\ = & \frac{1}{2} \frac{EI}{L_t} \theta^2 + \frac{1}{2} \sum_{i=1}^4 \frac{E_r I_r}{L_i} \theta^2 \end{aligned} \quad (13)$$

where L_t is the current length of the retractable segment. E , I , and E_r , I_r are, respectively, Young's modulus, area moment of inertia of the retractable segment, and the push rod. θ_{pa} , θ_{pb} are respectively the bending angle of any point along the length of the triangle-shaped incisions, while θ_{pi} is the bending angle of any point along the length of the i -th rod. We have

$$\theta_{pa} = s \frac{2N\theta_{ga}}{L_t}$$

$$\begin{aligned}\theta_{pb} &= s \frac{2N\theta_{gb}}{L_t} \\ \theta_{pi} &= s \frac{\theta}{L_i}\end{aligned}\quad (14)$$

where s is the distance of the point to the base along the centerline. The potential energy due to the axial extension of the retractable segment can be derived by

$$U_c = \frac{1}{2}EA \int_0^{L_0} \left(\frac{du_p}{ds} \right)^2 ds = \frac{1}{2}EA(L_t - L_0)^2 \quad (15)$$

where A , and $u_p = s \frac{L_t - L_0}{L_0}$ are the cross-section area of the retractable segment and the axial extension of any point p along the length of the segment, respectively. Thus, the total potential energy U can be represented as

$$U = U_b + U_c \quad (16)$$

The generalized force perturbation δf_ψ associated with the retractable segment with respect to its configuration space perturbation $\delta \psi$ is described as follows.

$$\delta f_\psi = \mathbf{K}_\psi \delta \psi \quad (17)$$

where \mathbf{K}_ψ is the stiffness matrix. The elements of \mathbf{K}_ψ can be solved [34] as follows.

$$\mathbf{K}_\psi = \frac{\partial}{\partial \psi} [\nabla U - \mathbf{J}_{q\psi}^T \tau] \quad (18)$$

where τ represents the actuation force state.

The wrench acting on the tip of the retractable segment can be projected by the generalized force as follows.

$$\mathbf{f}_\psi = \mathbf{J}_{t\psi}^T \mathbf{w} \quad (19)$$

D. MLNN-Based Stiffness Compensation

In the above section, due to the neglected gravitational potential energy, fabrication, and assembly errors, and the frictions between the rods and the catheter, along with the unconsidered variation of elastic modulus during elongation of the catheter, there might result in a deviation \mathbf{K}_e of the stiffness model. Thus, the actual stiffness matrix takes the form.

$$\widehat{\mathbf{K}}_\psi = \mathbf{K}_\psi + \mathbf{K}_e \quad (20)$$

To compensate for the stiffness matrix, a multi-layer neural network (MLNN) is used to establish a stiffness compensation function h_e . The MLNN consists of an input layer, two hidden layers, and an output layer. Each hidden layer is composed of a fully connected layer (with 50 neurons) with the Rectified Linear Unit activation function and a BatchNorm layer to standardize the outputs. The actuation state \mathbf{q} can be implicitly expressed by the configuration states ψ and its derivative $\dot{\psi}$, thus the input \mathbf{I}_e of the MLNN can be represented as follows.

$$\mathbf{I}_e = [\dot{\psi}^T \psi^T \tau]^T \quad (21)$$

The output of the MLNN is the systematic deviation \mathbf{K}_e , could be represented by

$$\mathbf{K}_e = h_e(\mathbf{I}_e) \quad (22)$$

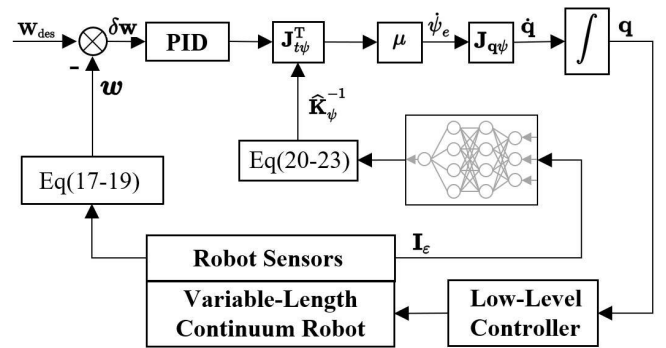


Fig. 5. Force controller for the variable-length continuum robot.

Define the loss function $l_c(\mathbf{I}_e, \mathbf{q})$ as follows

$$l_c(\mathbf{I}_e, \mathbf{q}) = |\mathbf{J}_{t\psi} (\mathbf{K}_\psi + \mathbf{K}_e) \dot{\psi} - \delta \mathbf{w}| \quad (23)$$

where $\delta \mathbf{w}$ is the external force perturbation. \mathbf{K}_ψ is the solved stiffness matrix by equation (18), and \mathbf{K}_e is the compensation matrix outputted by MLNN. During the training process, the Adam solver is used to minimize the loss function and optimize the network parameters. The learning rate is set as 0.001, and the early stopping technique is applied to avoid overfitting. To collect sufficient data, we discretized sampling within the interval of each configuration parameter: 10 points were discretized for bending angle, 36 points for bending plane angle, and 10 points were discretized for elongation. Due to the strong nonlinear fitting ability of neural networks, the predictive stiffness of any configuration can be obtained based on the trained neural networks.

E. Contact Force Controller

During endoscopic surgery, particularly during ablation procedures, it's crucial for the catheter tip to contact with the tissue while maintaining a stable force. Thus, based on the proposed stiffness model, a force controller is proposed for the variable-length catheter. Define the desired force as \mathbf{w}_{des} , we have

$$\delta \mathbf{w} = \mathbf{K}_p(\mathbf{e}_n - \mathbf{e}_{n-1}) + \mathbf{K}_i \mathbf{e}_n + \mathbf{K}_d(\mathbf{e}_n - 2\mathbf{e}_{n-1} + \mathbf{e}_{n-2}) \quad (24)$$

where $\mathbf{e} = \mathbf{w}_{des} - \mathbf{w}$, \mathbf{e}_n is the force error at step n, and \mathbf{w} is the external force. \mathbf{K}_p , \mathbf{K}_i and \mathbf{K}_d are respectively the proportional, integral, and differential coefficient matrix. Thus, the control law could be written as

$$\dot{\psi}_e = \mu \widehat{\mathbf{K}}_\psi^{-1} \mathbf{J}_{t\psi}^T \delta \mathbf{w} \quad (25)$$

where μ is the adjustment coefficient, and $\dot{\psi}_e$ is the desired configuration space velocity vector.

Based on the proposed control law, the force controller is designed as depicted in Fig. 5. The force error \mathbf{e} is calculated by the estimated external force \mathbf{w} and the desired force \mathbf{w}_{des} . After amplified by the incremental PID coefficients, it is converted into the configuration space velocity vector $\dot{\psi}_e$ and transferred to the actuation state \mathbf{q} . By the low-level controller, the variable-length continuum robot reaches the desired force.

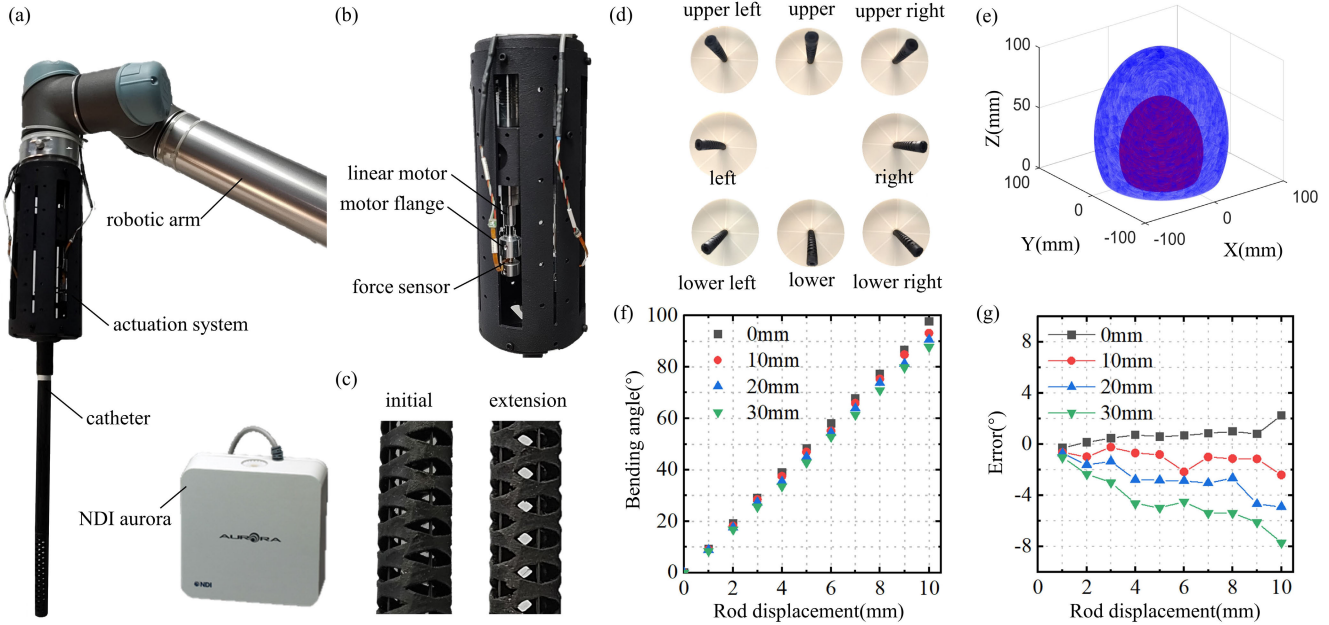


Fig. 6. Characterization experiments of the variable-length continuum robot. (a) Hardware system integration. (b) The integration of the actuation system. (c) The catheter structure before and after elongation. (d) Steering experiment. (e) Workspace analysis. (f) The relationship between the driving displacement and the bending angle of the retractable segment under 0mm, 10mm, 20mm, and 30mm elongations. (g) The bending angle error under 0mm, 10mm, 20mm, and 30mm elongations.

III. RESULTS

A. Characterization Experiments

To assess the performance of the proposed variable-length continuum robot, the experimental system is integrated, as shown in Fig. 6(a). This system includes a robotic arm for pose adjustment, a variable-length continuum robot for endoscopic surgery, and a magnetic positioning sensor to track the pose of the catheter tip. Fig. 6(b) shows the integration of the actuation system. It includes four linear motors dedicated to steering or elongating the catheter alongside four force sensors tasked with measuring the driving force. The catheter structure before and after elongation is shown in Fig. 6(c).

To evaluate the robot's maneuverability, an active steering experiment was conducted, as depicted in Fig. 6(d). The experiment's snapshots reveal the catheter bending in eight directions, driven by the rods, with an elongation of 30mm (maximum elongation). This demonstrates the catheter's good steering capabilities, as the orientation of the catheter closely aligns with the direction of the notch on the base. In addition, the robot's workspace before and after the elongation is plotted in Fig. 6(e). The red scatter points represent the area reachable by the catheter tip before elongation, whereas the blue scatter points depict the expanded reachable region following a 30mm elongation. The area between these two points indicates the enhanced accessible region for the variable-length catheter. These experimental results unequivocally show that the variable-length catheter boasts an expanded workspace and superior flexibility.

Next, kinematic characterization experiments are carried out to verify the model accuracy for the continuum robot. Fig. 6(f) depicts the relationship between the rod displacement and the

bending angle of the retractable segment under 0mm, 10mm, 20mm, and 30mm elongations. The results demonstrated a linear relationship between the rods' driving displacement and the retractable segment's bending angle, confirming the linear behavior predicted by the kinematic model. The scatter points representing the bending angle at different elongations closely overlapped, indicating that the robot's behavior remains consistent across different lengths of elongation and aligns well with the proposed kinematic model. Fig. 6(g) depicts the error variation under 0mm, 10mm, 20mm, and 30mm elongations. It can be seen that as the elongation increases, the error in the model's predictions gradually rises. The main reason is that elongating the catheter by applying force through the rods introduces additional stresses within the catheter structure. These stresses lead to increased friction between the rod and the catheter, which, in turn, impacts the model's accuracy. The phenomenon demonstrates the complexity of accurately modeling the behavior of continuum robots, especially when considering the dynamic interactions between mechanical components under stress.

To evaluate the control accuracy of the robot, a trajectory tracking experiment is carried out. The catheter tip is controlled to move along a circle based on the proposed kinematic model, while the magnetic positioning sensor is used to record the actual trajectory. Fig. 7(a) and (b) respectively show the real and ideal trajectory points projected on the XY plane and XZ plane. It is observed that the two trajectories have a reasonable degree of overlap in most directions, but there are some differences in specific directions. By calculation, the average position error is 1.78 mm (4.45% relative to the radius of 40 mm), and the maximum position error is 3.91 mm. Overall, the tracking error still fluctuates within a controllable

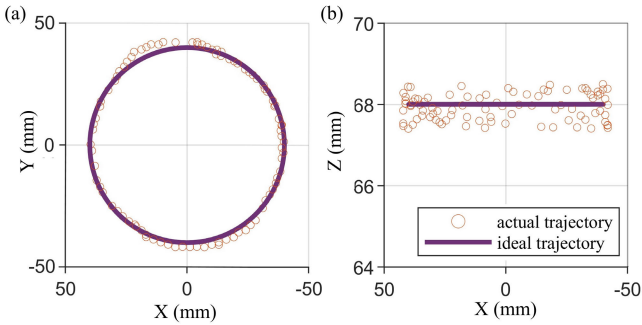


Fig. 7. Trajectory tracking experiments. (a) The actual and ideal trajectory points projected on the XY plane. (b) The actual and ideal trajectory points projected on the XZ plane.

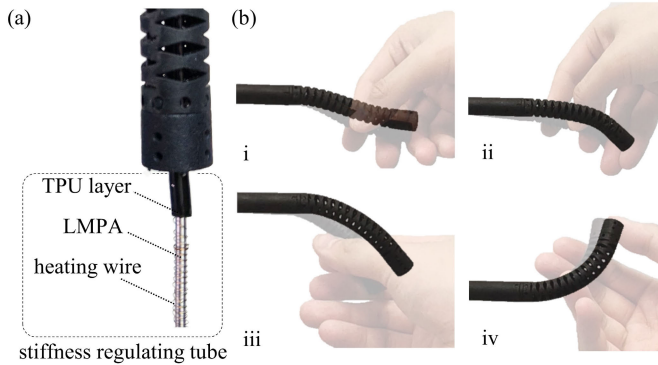


Fig. 8. Catheter shaping experiment. (a) Integration of the variable-length catheter with variable stiffness. (b) Snapshots of the catheter shaping experiment.

range, showing the good open control performance of the proposed controller.

B. Variable Stiffness Analysis

To validate the catheter's variable stiffness capability, enabled by the solid-liquid transition of Low Melting Point Alloy (LMPA), a catheter shaping experiment is conducted. Initially, LMPA (with a melting point of 47 degrees Celsius) is cooled to a solid state and encased within a Thermoplastic Polyurethane (TPU) layer, forming the stiffness-regulating tube. This tube is then integrated into the variable-length catheter, with its tip securely attached (Fig. 8(a)). During the experiment, the catheter's shape is manually altered and subsequently released, showcasing the catheter's ability to maintain any given configuration post-manipulation (Fig. 8(b)). The comparison of translucent (before release) and opaque (after shaping) images illustrates the catheter's capacity to hold a stable shape once the LMPA solidifies. This feature is particularly beneficial for ensuring stability when surgical tools are inserted into the catheter.

Next, the variable stiffness capability of the catheter, enabled by the changes in its length, is tested by controlling the catheter to steer at varying elongations, as depicted in Fig. 9(a). The relationship between driving force and driving displacement is plotted in Fig. 9(b). The purple, red, blue, and green curves, respectively, represent the curves under 0mm, 10mm, 20mm, and 30mm elongations. It is observed that with

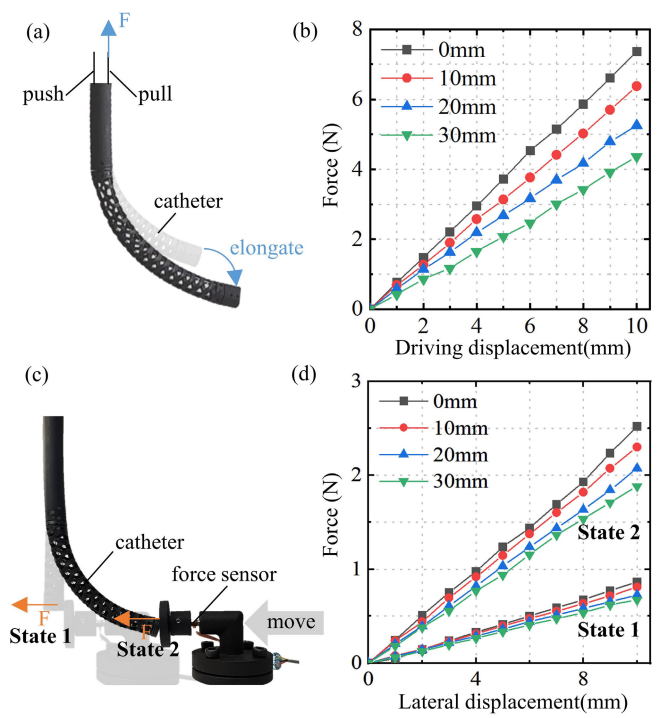


Fig. 9. Variable stiffness analysis under different elongations.(a) Steering control diagram under different elongations. (b) Force-driving displacement relationship under different elongations. (c) Experimental setting of lateral stiffness measurement. (d) Force-lateral displacement relationship under two configurations.

the increase of elongation, the driving force under the same driving displacement decreases. This decrease is attributed to the reduction in deformation per unit length after elongation, thereby lowering the stress and required driving force. Notably, the consistency across the relationship curves for all four elongations suggests uniform material and mechanical properties of the catheter in all directions. Additionally, the catheter's lateral stiffness is analyzed by controlling it to respectively maintain axial deformation and the same unilateral steering at different elongations, with a force sensor measuring the lateral stiffness (see Fig. 9(c)). The relationship between the lateral displacement and force is plotted in Fig. 9(d). It is observed that the lateral stiffness diminishes as elongation increases, and notably, the lateral stiffness after bending significantly exceeds that observed during mere elongation. The main reason is that the driving force of the rod increases when bending, which increases the stress distribution of the catheter and changes its transverse stiffness. The above experiments fully verify the variable stiffness ability of the catheter after length changes and material solid-liquid transition.

C. Force Control Experiment on Stomach Model

To test the force control accuracy of the variable-length continuum robot, force tracking experiments are carried out, as depicted in Fig. 10(a). The catheter equipped with an ablation probe on its tip is controlled to apply force to the force measurement platform installed with a force sensor, following triangle and sinusoidal reference forces. The control frequency of the robot is set as 50Hz. Two trials of actual force and

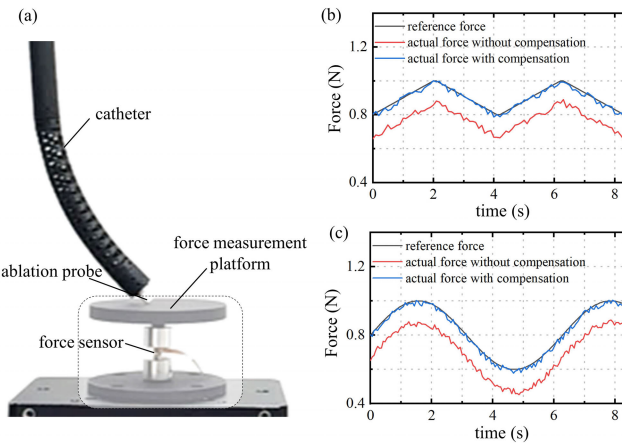


Fig. 10. Force tracking experiment. (a) The experimental setup. (b) The tracking force and reference triangle force variation curves. (c) The tracking force and reference sinusoidal force variation curves.

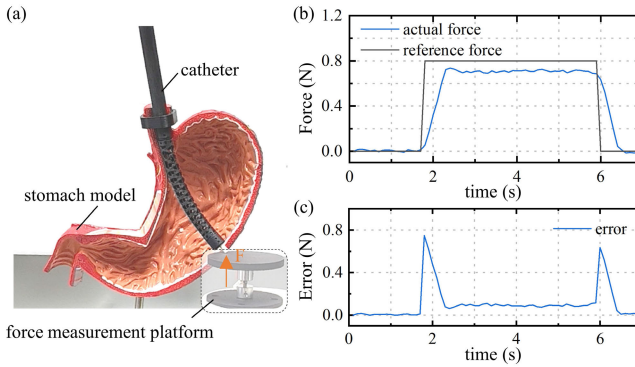


Fig. 11. Ablation force control experiment. (a) The experimental setup. (b) The actual force and reference force variation curves. (c) The force error variation curve.

reference force are plotted in Fig. 10(b) and (c). Notably, there is a certain deviation between the actual force without stiffness compensation and the reference force. However, with stiffness compensation, the actual forces are closely aligned with the reference forces, significantly improving tracking performance. The mean errors of the two signals without compensation are 133 mN and 129 mN for the triangle and sinusoidal signals, respectively, but dropped to 21 mN and 23 mN with compensation. The results demonstrate the force controller's high accuracy and the substantial impact of stiffness compensation on enhancing force-tracking capabilities in surgical applications.

To demonstrate the robot's potential in endoscopic surgery, an ablation force control experiment is carried out, as depicted in Fig. 11(a). The variable-length catheter, equipped with an ablation probe, is controlled to insert into the stomach model to simulate a surgical procedure. Due to the ample workspace and high flexibility, it can reach most areas of the stomach model. Upon making contact with the force measuring platform (mimic lesion tissues), an ablation force control task is initiated with a set desired force of 0.8 N. It can be seen from Fig. 11(b) that the catheter quickly achieved the target force. However, the contacts between the catheter body and the stomach model introduced challenges, diminishing

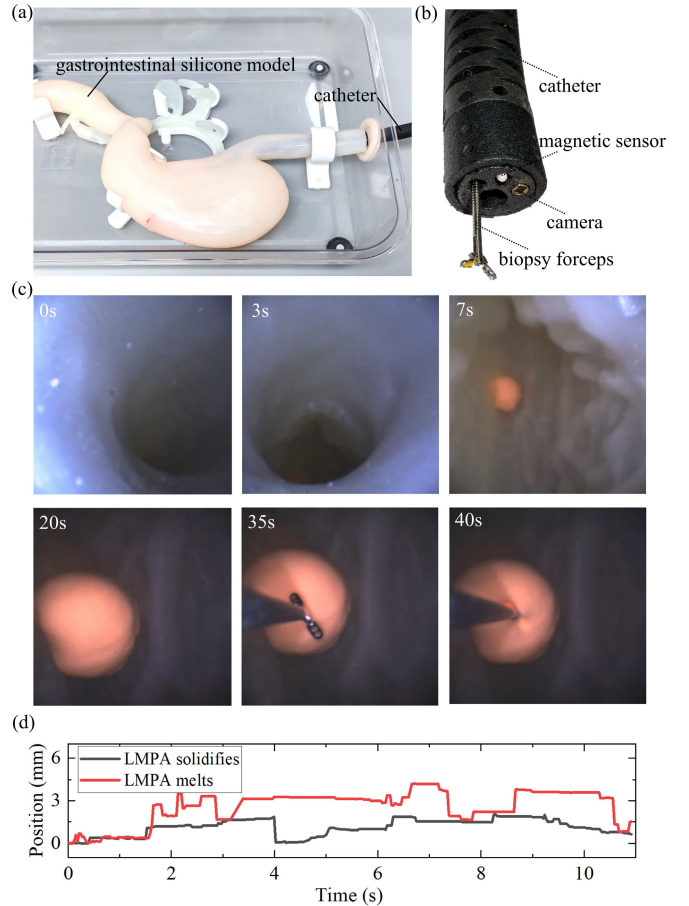


Fig. 12. Gastrointestinal surgical demonstration. (a) The experimental scene. (b) The catheter integrated with a working channel and a micro camera. (c) Snapshots of surgical process in the gastrointestinal model. (d) The changes in position of the catheter tip when performing tissue sampling with LMPA in a solid versus a liquid state.

the stiffness model's accuracy and leading to the deviation between the actual and the desired forces. Fig. 11(c) shows the error variation during the experiment. It can be seen that the force error is particularly noticeable during the rise and fall phases, with a mean error of about 0.09 N throughout the process. The experiment highlighted the robot's potential to perform endoscopic surgery in confined spaces.

D. Gastrointestinal Surgical Demonstration

To further demonstrate the endoscopic surgical capability of the robot, a tissue sampling experiment is conducted in a gastrointestinal model, as depicted in Fig. 12(a). The variable-length catheter, equipped with a working channel, a magnetic sensor and a micro camera, allows for the insertion of surgical tools, such as biopsy forces (see Fig. 12(b)). During the experiment, the LMPA is initially heated for about 15s (the heating wire is applied to a voltage of 10V) to change into a liquid state, at this time, the catheter has low stiffness, and can be controlled to locate the lesion (simulated by a silly putty ball) within the gastrointestinal model. Upon identifying a lesion, the catheter's tip is precisely directed toward the target area, followed by the solidification of the LMPA (cool for about 10s) within the catheter to enhance its stiffness for

TABLE I
COMPARISON BETWEEN THIS WORK AND THE OTHER STUDIES

Ref	Actuation	Dimension	Variable stiffness principle	Variable length	Control frequency	Application
[26]	pneumatic	$\varnothing 30$ mm	granular jamming	no	-	minimally invasive surgery
[29]	tube-driven	$\varnothing 1.8$ mm	nonuniform tubes movement	yes	-	steerable needle
[35]	tendon-driven	$\varnothing 15$ mm	material glass transition	no	-	endoscopic manipulator
[36]	magnetic driven	$\varnothing 1$ mm	material solid-liquid transition	no	10 Hz	ophthalmic surgery
[37]	pneumatic/cable-driven	$\varnothing 18$ mm	pressure-based jamming	no	1000 Hz	gastrointestinal endoscopy
[38]	tendon-driven	$\varnothing 14.5$ mm	fiber jamming	no	-	surgical manipulator
[39]	pneumatic	$\varnothing 3.6\text{--}21$ mm	sandpaper jamming	no	-	endoscopic surgery
[40]	rod-driven	$\varnothing 8$ mm	tube-based mechanism	no	-	transoral Surgery
[41]	magnetic driven	10×2 mm	sliding nitinol backbone	no	1 Hz	gastric surgery
[42]	magnetic driven	$\varnothing 0.8$ mm	tube length adjustment	yes	130 Hz	coronary intervention
[43]	tube-driven	$\varnothing 8$ mm	temperature changes of SMA and length changes	yes	-	transoral robotic surgery
ours	rod-driven	$\varnothing 12.6$ mm	material solid-liquid transition and length changes	yes	50 Hz	endoscopic surgery

stable surgical intervention. Subsequently, the biopsy forceps is inserted through the working channel to carry out the surgical task, as shown in Fig. 12(c).

To demonstrate the benefits of variable stiffness capability, the changes in position of the catheter tip are compared when performing tissue sampling with LMPA in a solid versus a liquid state, as depicted in Fig. 12(d). The average position change is 1.1mm when LMPA solidifies, while that is 2.6mm when LMPA melts. It is observed that the solidification of LMPA improves the stiffness of the catheter, reduces the disturbance of the surgical tool during procedures, and increases the stability of the surgical process. This experiment showcases the robot's potential to significantly impact endoscopic surgical practices by enabling precise, flexible, and controlled interventions in complex anatomical regions.

IV. DISCUSSION AND CONCLUSION

This paper proposed a variable-length continuum robot with variable stiffness for endoscopic surgery. The robot can bend omnidirectionally and elongate along its axis under the actuation of the rods. Compared with the continuum robots with one active bending segment, the robot has higher flexibility and accessibility. Besides, a quasi-static stiffness model and a learning-based stiffness compensation approach are proposed for accurate stiffness estimation; then, a model-based force controller is designed for ablation surgery. According to the experimental results, the robot shows high flexibility, accessibility, and good force control accuracy.

To more comprehensively highlight the advantages of the work in this paper, we summarized the variable-stiffness surgical continuum robots that have been developed, as shown in Table I. Due to their large load capacity, most existing surgical robots adopt tendon-driven or pneumatic methods. For miniaturizing the robots, magnetic and tube-driven methods have also been adopted, with concentric tube robots being a subset of tube-driven designs. The prevalent robots adopt material-based (glass transition) or Jamming-based approaches to achieve variable stiffness. A few robots employ the structure-based approaches, such as the tube relative movement. Despite these varied approaches, the paper highlights a notable gap:

few robots can simultaneously adjust their length and stiffness in real time, a capability integral to enhancing surgical precision and adaptability. The existing approaches to achieve variable length generally adopt a structure similar to that of the concentric tube robots, relying on the elongation of the backbone. Our robot uses the deformation of the hollow structure of the catheter to achieve the variable length capacity, and depends on the length change and the solid-liquid transition of LMPA to change the stiffness, marking a significant step forward in developing surgical continuum robots by combining online length variability with variable stiffness functionality.

However, it is worth noting that the retractable segment of the catheter is complicated and challenging to manufacture, and there are some differences in the material properties of the formed segments, reducing the model accuracy. Furthermore, the increase in the catheter's elongation also reduces the robot model's accuracy. It is worth studying to develop more accurate mechanical models for high-precision control of robots in the future.

REFERENCES

- [1] G. Qin et al., "A snake-inspired layer-driven continuum robot," *Soft Robot.*, vol. 9, no. 4, pp. 788–797, Aug. 2022.
- [2] J. Zhang et al., "A preprogrammable continuum robot inspired by elephant trunk for dexterous manipulation," *Soft Robot.*, vol. 10, no. 3, pp. 636–646, Jun. 2023.
- [3] F. Meder, S. P. Murali Babu, and B. Mazzolai, "A plant tendril-like soft robot that grasps and anchors by exploiting its material arrangement," *IEEE Robot. Autom. Lett.*, vol. 7, no. 2, pp. 5191–5197, Apr. 2022.
- [4] J. Zhang et al., "A survey on design, actuation, modeling, and control of continuum robot," *Cyborg Bionic Syst.*, vol. 2022, pp. 1–12, Jan. 2022.
- [5] J. Burgner-Kahrs, D. C. Rucker, and H. Choset, "Continuum robots for medical applications: A survey," *IEEE Trans. Robot.*, vol. 31, no. 6, pp. 1261–1280, Dec. 2015.
- [6] X. Zhang et al., "Robotic actuation and control of a catheter for structural intervention cardiology," in *Proc. IEEE/RSJ Int. Conf. Intell. Robots Syst. (IROS)*, 2022, pp. 5907–5913.
- [7] M. A. Zenati and M. Mahvash, "Robotic systems for cardiovascular interventions," in *Medical Robotics*. Amsterdam, The Netherlands: Elsevier, 2012, pp. 78–89.
- [8] J. Zhang et al., "AI co-pilot bronchoscope robot," *Nature Commun.*, vol. 15, no. 1, p. 241, Jan. 2024.
- [9] X. Duan et al., "A novel robotic bronchoscope system for navigation and biopsy of pulmonary lesions," *Cyborg Bionic Syst.*, vol. 4, p. 0013, Jan. 2023.

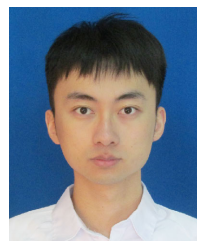
- [10] A. Bajo, R. B. Pickens, S. Duke. Herrell, and N. Simaan, "Constrained motion control of multisegment continuum robots for transurethral bladder resection and surveillance," in *Proc. IEEE Int. Conf. Robot. Autom.*, May 2013, pp. 5837–5842.
- [11] W. Hong, F. Feng, L. Xie, and G.-Z. Yang, "A two-segment continuum robot with piecewise stiffness for maxillary sinus surgery and its decoupling method," *IEEE/ASME Trans. Mechatronics*, vol. 27, no. 6, pp. 4440–4450, Dec. 2022.
- [12] F. Wang et al., "FIORA : A flexible tendon-driven continuum manipulator for laparoscopic surgery," *IEEE Robot. Autom. Lett.*, vol. 7, no. 2, pp. 1166–1173, Apr. 2022.
- [13] W. Zeng, J. Yan, X. Huang, and S. Shin Cheng, "Motion coupling analysis for the decoupled design of a two-segment notched continuum robot," in *Proc. IEEE Int. Conf. Robot. Autom. (ICRA)*, May 2021, pp. 7665–7671.
- [14] C. Girerd and T. K. Morimoto, "Design and control of a hand-held concentric tube robot for minimally invasive surgery," *IEEE Trans. Robot.*, vol. 37, no. 4, pp. 1022–1038, Aug. 2021.
- [15] D. Liu et al., "Magnetically driven soft continuum microrobot for intravascular operations in microscale," *Cyborg Bionic Syst.*, vol. 2022, Jan. 2022, Art. no. 9850832.
- [16] J. Liu, T. Xu, and X. Wu, "Model predictive control of magnetic helical swimmers in two-dimensional plane," *IEEE Trans. Autom. Sci. Eng.*, vol. 21, no. 2, pp. 1–10, Apr. 2024.
- [17] M. Chauhan, J. H. Chandler, A. Jha, V. Subramaniam, K. L. Obstein, and P. Valdastri, "An origami-based soft robotic actuator for upper gastrointestinal endoscopic applications," *Frontiers Robot. AI*, vol. 8, pp. 1–12, May 2021.
- [18] Y. Kim, G. A. Parada, S. Liu, and X. Zhao, "Ferromagnetic soft continuum robots," *Sci. Robot.*, vol. 4, no. 33, pp. 1–10, Aug. 2019.
- [19] Y. Kim et al., "Telerobotic neurovascular interventions with magnetic manipulation," *Sci. Robot.*, vol. 7, no. 65, Apr. 2022, Art. no. eabg9907.
- [20] Y. Kim, S. S. Cheng, M. Diakite, R. P. Gullapalli, J. M. Simard, and J. P. Desai, "Toward the development of a flexible mesoscale MRI-compatible neurosurgical continuum robot," *IEEE Trans. Robot.*, vol. 33, no. 6, pp. 1386–1397, Dec. 2017.
- [21] S. S. Cheng, Y. Kim, and J. P. Desai, *Towards Real-Time SMA Control for a Neurosurgical Robot: MINIR-II*. Springer, 2018, pp. 187–200.
- [22] Y. Zhong, L. Hu, and Y. Xu, "Recent advances in design and actuation of continuum robots for medical applications," *Actuators*, vol. 9, no. 4, p. 142, Dec. 2020.
- [23] Y. Hao, J. Gao, Y. Lv, and J. Liu, "Low melting point alloys enabled stiffness tunable advanced materials," *Adv. Funct. Mater.*, vol. 32, no. 25, Jun. 2022, Art. no. 2201942.
- [24] M. Mattmann et al., "Thermoset shape memory polymer variable stiffness 4D robotic catheters," *Adv. Sci.*, vol. 9, no. 1, Jan. 2022, Art. no. 2103277.
- [25] J. Delaey, P. Dubruel, and S. Van Vlierberghe, "Shape-memory polymers for biomedical applications," *Adv. Funct. Mater.*, vol. 30, no. 44, 2020, Art. no. 1909047.
- [26] I. De Falco, M. Cianchetti, and A. Menciassi, "A soft multi-module manipulator with variable stiffness for minimally invasive surgery," *Bioinspiration Biomimetics*, vol. 12, no. 5, Sep. 2017, Art. no. 056008.
- [27] Y.-J. Kim, S. Cheng, S. Kim, and K. Iagnemma, "A novel layer jamming mechanism with tunable stiffness capability for minimally invasive surgery," *IEEE Trans. Robot.*, vol. 29, no. 4, pp. 1031–1042, Aug. 2013.
- [28] J. Zhang et al., "Bioinspired continuum robots with programmable stiffness by harnessing phase change materials," *Adv. Mater. Technol.*, vol. 8, no. 6, Mar. 2023, Art. no. 2201616.
- [29] J. Kim, W.-Y. Choi, S. Kang, C. Kim, and K.-J. Cho, "Continuously variable stiffness mechanism using nonuniform patterns on coaxial tubes for continuum microsurgical robot," *IEEE Trans. Robot.*, vol. 35, no. 6, pp. 1475–1487, Dec. 2019.
- [30] R. J. Webster and B. A. Jones, "Design and kinematic modeling of constant curvature continuum robots: A review," *Int. J. Robot. Res.*, vol. 29, no. 13, pp. 1661–1683, 2010.
- [31] B. A. Jones and I. D. Walker, "Kinematics for multisegment continuum robots," *IEEE Trans. Robot.*, vol. 22, no. 1, pp. 43–55, Feb. 2006.
- [32] A. Bajo and N. Simaan, "Kinematics-based detection and localization of contacts along multisegment continuum robots," *IEEE Trans. Robot.*, vol. 28, no. 2, pp. 291–302, Apr. 2012.
- [33] M. M. Dalvand, S. Nahavandi, and R. D. Howe, "An analytical loading model for n -tendon continuum robots," *IEEE Trans. Robot.*, vol. 34, no. 5, pp. 1215–1225, Oct. 2018.
- [34] R. E. Goldman, A. Bajo, and N. Simaan, "Compliant motion control for multisegment continuum robots with actuation force sensing," *IEEE Trans. Robot.*, vol. 30, no. 4, pp. 890–902, Aug. 2014, doi: 10.1109/TRO.2014.2309835.
- [35] H. M. Le, P. T. Phan, C. Lin, L. Jiajun, and S. J. Phee, "A temperature-dependent, variable-stiffness endoscopic robotic manipulator with active heating and cooling," *Ann. Biomed. Eng.*, vol. 48, no. 6, pp. 1837–1849, Jun. 2020.
- [36] J. Lussi et al., "A submillimeter continuous variable stiffness catheter for compliance control," *Adv. Sci.*, vol. 8, no. 18, Sep. 2021, Art. no. 2101290.
- [37] X. Luo, D. Song, Z. Zhang, S. Wang, and C. Shi, "A novel distal hybrid pneumatic/cable-driven continuum joint with variable stiffness capacity for flexible gastrointestinal endoscopy," *Adv. Intell. Syst.*, vol. 5, no. 6, Jun. 2023, Art. no. 2200403.
- [38] M. Brancadoro, M. Manti, F. Grani, S. Tognarelli, A. Menciassi, and M. Cianchetti, "Toward a variable stiffness surgical manipulator based on fiber jamming transition," *Frontiers Robot. AI*, vol. 6, p. 12, Mar. 2019.
- [39] H. Wang and S. Zuo, "A novel variable-diameter-stiffness guiding sheath for endoscopic surgery," *IEEE Robot. Autom. Lett.*, vol. 8, no. 1, pp. 89–96, Jan. 2023.
- [40] C. Li, X. Gu, X. Xiao, C. M. Lim, and H. Ren, "Flexible robot with variable stiffness in transoral surgery," *IEEE/ASME Trans. Mechatronics*, vol. 25, no. 1, pp. 1–10, Feb. 2020.
- [41] P. Lloyd et al., "A magnetically-actuated coiling soft robot with variable stiffness," *IEEE Robot. Autom. Lett.*, vol. 8, no. 6, pp. 3262–3269, Jun. 2023.
- [42] Z. Li, J. Li, Z. Wu, Y. Chen, M. Yeerbulati, and Q. Xu, "Design and hierarchical control of a homocentric variable stiffness magnetic catheter for multi-arm robotic ultrasound-assisted coronary intervention," *IEEE Trans. Robot.*, vol. 40, pp. 2306–2326, Mar. 2024.
- [43] J. Chen et al., "A variable length, variable stiffness flexible instrument for transoral robotic surgery," *IEEE Robot. Autom. Lett.*, vol. 7, no. 2, pp. 3835–3842, Apr. 2022.



Jingyu Zhang (Member, IEEE) received the M.Eng. degree from Nanjing University of Science and Technology, Nanjing, Jiangsu, China. He is currently pursuing the Ph.D. degree in robotics with the Soft Medical Robotics Laboratory, Zhejiang University, Hangzhou, China. Previously, he has worked on medical ultrasound scanning systems. He is also developing novel different scale of soft continuum to augment the operation ability of surgeons.



Qin Fang is currently pursuing the Ph.D. degree with the School of Control Science and Engineering, Zhejiang University. During the master's degree, she studied with the School of Aeronautics and Astronautics, Zhejiang University. Her current research interests focus on the design, fabrication, and control of biomimetic soft robots.



Lilu Liu received the B.Eng. degree from the School of Electrical Engineering and Automation, Harbin Institute of Technology, Harbin, China, in 2019. He is currently pursuing the Ph.D. degree with the College of Control Science and Engineering, Zhejiang University, Hangzhou, China. His research interests include medical image analysis, object pose estimation, and surgical robotics.



Rui Jin received the B.E. degree in mechanical design, manufacturing and automation from Northwestern Polytechnical University. He is currently pursuing the master's degree in control science and engineering with Zhejiang University under the supervision of Prof. Lu and Prof. Gao. His research interests include coaxial helicopter and autonomous flight.



Yue Wang (Member, IEEE) received the Ph.D. degree in control science and engineering from the Department of Control Science and Engineering, Zhejiang University, Hangzhou, China, in 2016. He is currently an Associate Professor with the Department of Control Science and Engineering, Zhejiang University. His latest research interests include mobile robotics and robot perception.



Pingyu Xiang received the B.E. degree in mechatronic engineering from the School of Mechanical Engineering, Zhejiang University, where he is currently pursuing the M.E. degree in control science and engineering with the College of Control Science and Engineering. His research interests include continuum robotics, medical robotics, and machine learning.



Rong Xiong (Senior Member, IEEE) received the Ph.D. degree in control science and engineering from the Department of Control Science and Engineering, Zhejiang University, Hangzhou, China, in 2009. She is currently a Professor with the Department of Control Science and Engineering, Zhejiang University. Her latest research interests include motion planning and SLAM.



Haojian Lu (Member, IEEE) received the B.Eng. degree in mechatronical engineering from Beijing Institute of Technology in 2015 and the Ph.D. degree in robotics from the City University of Hong Kong in 2019. He is currently a Professor with the State Key Laboratory of Industrial Control and Technology and Institute of Cyber-Systems and Control, Zhejiang University. His research interests include micro/nanorobotics, bioinspired robotics, medical robotics, micro aerial vehicle, and soft robotics.

Soft Lightweight Small-Scale Parallel Robot With High-Precision Positioning

Qin Fang , Jingyu Zhang, Danying Sun, Yanan Xue, Rui Jin, Nenggan Zheng , Senior Member, IEEE,
 Yue Wang , Member, IEEE, Rong Xiong , Member, IEEE, Zhefeng Gong ,
 and Haojian Lu , Member, IEEE

Abstract—Small-scale (from centimeters down to micrometers) parallel robots with high precision are widely utilized in various industrial and biomedical settings, while such superiorities remain challenges for soft parallel robots (SPRs). In this work, we propose an integrated design and fabrication strategy to make up a soft lightweight (3.5 g) small-scale ($\phi 60 \times 40$ mm) parallel robot based on the dielectric elastomer actuator. Then, a hybrid model is established to describe the mapping between driving space and workspace, taking advantage of the robustness and security of the model-based method and the strong nonlinear fitting ability of the data-driven neural network method. The stiffness and workspace of the robot are analyzed. The results of trajectory tracking experiments demonstrate the accuracy and robustness of the proposed hybrid model. The average positioning error of the different trajectories is 13.4–16.6 μm . Finally, the zebrafish embryo puncture experiment is carried out to show the ability of micromanipulation. This research paves a new avenue for designing and controlling high-positioning SPRs, which is expected to be applied in the micromanipulation field.

Index Terms—Dielectric elastomer actuator, micro positioning, small-scale robot, soft parallel robot (SPR).

I. INTRODUCTION

THE parallel robots usually have higher stiffness, greater load capacity and higher accuracy compared with the classical serial robots, attracting the extensive interest of researchers and developing rapidly. The earliest parallel robot was designed by Gough in 1947, which was used to detect tire wear under various load conditions [1], [2]. In the following decades, various parallel robots have been proposed, such as delta robots [3], [4]. The advantages of parallel robots come from their closed kinematic structure. The positioning error of one kinematic chain will be reduced by other kinematic chains rather than accumulated and amplified. At the same time, the parallel configuration of multiple actuators endows the robot with sufficient rigidity to restrict external loads. In recent years, parallel robots have been widely used in various industrial applications, such as food packaging [5], machining [6], pick-and-place assembly [7], and so on.

However, the connecting rods of most parallel robots are rigid, making it unsuitable for applications requiring high biocompatibility. Some control methods could endow these robots with compliance [8], [9], but they are limited to use in special scenarios. In contrast, soft parallel robots (SPRs) composed of soft materials or flexible links have intrinsic compliance to be used in restricted or interactive environments [10], [11], [12], [13], [14].

Currently, a variety of SPRs have been developed. Yang et al. [15] developed a pneumatic robot, which is composed of three silicone chambers to achieve parallel configuration. Jiang et al. [16] developed a planar parallel robot based on the combination of tendon-driven continuum link and rigid link, which has a large workspace and high repeated positioning accuracy. Li et al. [17] used shape memory alloy (SMA) to develop a soft parallel arm made of soft silicone, and it has good operation and movement ability. Webster III and Jones [18] developed a 3-DOF soft parallel drawing robot employed with three tube-type dielectric elastomer actuators (DEAs). Godage et al. [19] proposed a SPR based on three linear DEAs with springs inside, which can achieve horizontal, vertical, and circular motions for the application of robotic eyeballs. However,

Manuscript received 4 November 2022; revised 20 February 2023; accepted 8 April 2023. Date of publication 10 May 2023; date of current version 15 December 2023. This work was supported in part by the Key R&D Program of Ministry of Science and Technology of China under Grant 2021ZD0114500, in part by the National Natural Science Foundation of China under Grant T2293724, in part by the Key R&D Program of Zhejiang under Grant 2022C01022, in part by the Zhejiang Provincial Natural Science Foundation of China under Grant LD22E050007, in part by the Fundamental Research Funds for the Zhejiang Provincial Universities under Grant 2021XZZX021, and in part by the Science and Technology on Space Intelligent Control Laboratory under Grant 2021-JCJQ-LB-010-13. Recommended by Technical Editor Mohammad Al Janaideh and Senior Editor Gursel Alici. (Corresponding authors: Haojian Lu; Zhefeng Gong.)

Qin Fang, Jingyu Zhang, Danying Sun, Yanan Xue, Rui Jin, Yue Wang, Rong Xiong, and Haojian Lu are with the State Key Laboratory of Industrial Control and Technology, and the Institute of Cyber-Systems and Control, Zhejiang University, Hangzhou 310027, China (e-mail: qinfang@zju.edu.cn; 12132011@zju.edu.cn; danyingsun@zju.edu.cn; xueyanan2020@zju.edu.cn; bbbbigrui@zju.edu.cn; wangyue@iipc.zju.edu.cn; rxiong@zju.edu.cn; luhaojian@zju.edu.cn).

Nenggan Zheng is with the Qiushi Academy for Advanced Studies, Zhejiang University, Hangzhou 310027, China (e-mail: zng@cs.zju.edu.cn).

Zhefeng Gong is with the Key Laboratory of Neurobiology, Zhejiang University School of Medicine, Hangzhou 310027, China (e-mail: zf-gong@zju.edu.cn).

Color versions of one or more figures in this article are available at <https://doi.org/10.1109/TMECH.2023.3270633>.

Digital Object Identifier 10.1109/TMECH.2023.3270633

currently developed SPRs typically have relatively large sizes and weights and have submillimeter positioning accuracy. It is still challenging to design a 3-DOF SPR with the advantages of small scale, lightweight, and high precision at the same time.

On the other hand, considering the complex coupling between material nonlinearity and the kinematic chains of SPRs, the modeling and control face great challenges. The modeling methods could be roughly divided into three categories. The first is the geometric model. The shape of the robot skeleton is fitted by piecewise constant curvature (PCC) approximation [20], modal shape function approximation [21], Bessel curve approximation [22], and other methods, regardless of the materials and driving characteristics. Due to its high computation efficiency, it is widely used on various occasions requiring real-time control [23]. The second is the continuum model, such as the Cosserat model [24] and Euler–Bernoulli beam model [25], which considers the coupling of elastic force and various constraints and can accurately describe the deformation of the robots. However, due to the almost infinite degrees of freedom of the SPRs, it is difficult to be applied to the actual robot control due to the low computation efficiency. The third is the data-driven model, which learns the hidden rules from large amounts of data (input and output) without the guidance of physical models and has received a lot of attention in recent years [26]. The neural network [27] model is the most commonly used approximate mapping model. However, it is difficult to adapt to the time-varying complex environment, which limits its use.

In this article, we developed a soft lightweight small-scale parallel robot composed of three symmetrically distributed DEAs based on the integrated design and fabrication strategy. A data-driven method based on the neural network is adopted to analyze the electrodeformation characteristics of DEAs. By the kinematic model of the robot, the mapping from the driving space (input voltage) to the task space (position of the robot end effector) is established. In addition, we also carried out trajectory tracking experiments and micromanipulation experiments to verify the reliability of the model and the overall motion performance of the robot. The contribution of this work can be summarized as follows.

- 1) An integrated design and fabrication strategy of the 3-DOF SPR is proposed. The robot is composed of three DEAs and has a lightweight and compact structure.
- 2) Taking advantage of the robustness of the model-based method and the strong nonlinear fitting ability of the data-driven method, a control strategy is proposed to achieve high-precision positioning based on the hybrid model.
- 3) The proposed robot achieves micron-level control accuracy as well as micromanipulation capabilities, as demonstrated in trajectory tracking and zebrafish embryo puncture experiments.

The rest of this article is organized as follows. Section II describes the integrated design and fabrication strategy to make up the SPR. In Section III, a hybrid model and an open-loop controller of the robot are proposed to achieve high positioning accuracy. In Section IV, the trajectory tracking experiments and zebrafish embryo puncture experiments are carried out to

TABLE I
STRUCTURAL PARAMETERS OF THE SUPPORTING FRAME

Parameter	Value	Parameter	Value
L	196 mm	d	5 mm
H	70 mm	e	10 mm
a	50 mm	h	10 mm
b	50 mm	r	10 mm
c	2 mm	t	0.188 mm

analyze the performance of the robot. Finally, Section V concludes this article.

II. INTEGRATED DESIGN AND FABRICATION

This section presents an integrated design and fabrication strategy to make up the SPR. Conventional SPRs tend to first process multiple actuators, and then, assemble them through the output stage to achieve a parallel configuration. The process is cumbersome and prone to greater processing errors and assembly errors. In contrast, our proposed design method achieves the fabrication and assembly of three DEAs simultaneously. The robot has an ultralightweight, compact structure, and a simplified manufacturing process.

To obtain the DEAs with superior performance, the manufacturing materials are seriously considered. The selection criterion of the dielectric elastomer (DE) is that the material should be soft enough to produce large deformation. The selection criteria of electrodes are low stiffness, lightweight, good adherence (not easy to slip off from the DE membrane), and maintaining high conductivity when the DE membrane deforms. These criteria for selecting materials listed previously can help increase the deformation ability of DEAs.

As for dielectric elastomer, the VHB material provides several benefits over silicone membrane material in terms of low price, good adhesion, and easy fabrication, so we choose VHB 4910 (3 M Company, USA) with an initial thickness of 1 mm as the DE membrane. And we chose carbon grease (MG chemicals, USA) as the electrode. As for flexible supporting structures, a high bending modulus will increase the deformation resistance, but if the bending modulus is too low, the actuator will quickly shrink and will not be capable of achieving the desired configuration. As a result, we choose the PET film with a thickness of $t = 0.188$ mm as the supporting frame.

After selecting the materials for the main structures, the fabrication process of the SPR can be started, as illustrated in Fig. 1(a). The PET supporting frame needs to be cut into a preset shape on the laser cutter, and the structural parameters are shown in Table I. We design the electrode area, hollow area, and bonding area on the flexible supporting structure. The shape of the electrode area is rectangular, and rounded corners are designed to reduce concentrated stress. The function of the hollowed-out area is to disperse the three actuators and reduce the interaction of the three actuators. Four minor marks are designed on the bonding area for accurate assembly of the robot. Then, the VHB membrane is prestretched at the rate of $300\% \times 300\%$ and is put on the clean bench for about six hours.

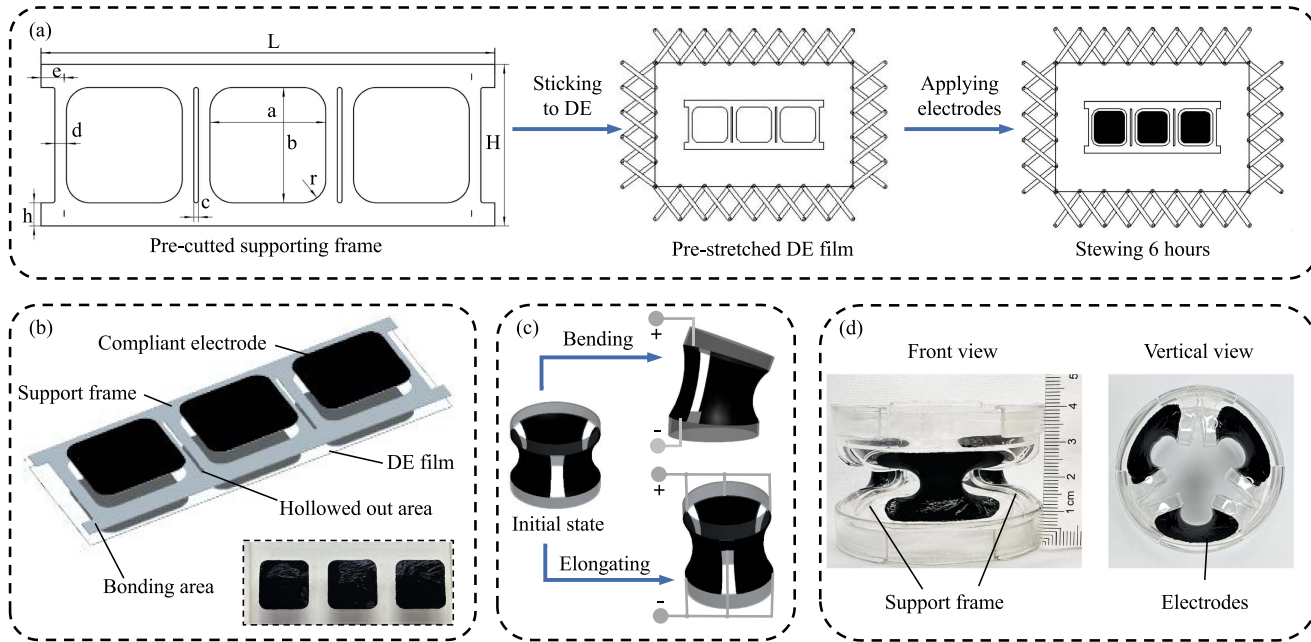


Fig. 1. Design, manufacturing, and driving principle of the SPR. (a) Manufacturing process of the SPR with the structural parameters of the supporting frame. (b) Structural composition diagram of the SPR. (c) Three modes of the SPR and deformation principle. (d) Photos of the SPR with visual reference.

Prestretching can suppress the electromechanical instability and alleviate the high viscoelasticity of the DE membrane, which is the main reason for the SPR to obtain fast response speed and stable strain under an external electric field. Then, the electrode mask is necessary for machining standard shape electrodes. A laser cutter cuts the electrode mask on the release paper. It is worth noting that there should be a distance of 2–3 mm from the edge of the electrode to the edge of the supporting frame because a large strain will occur at the edge when a high voltage is loaded. After confirming that the supporting frame is well bonded with the DE membrane, carefully cover the mask on the supporting frame, coat the carbon grease electrode, and remove the mask to obtain an electrode with a predesigned shape [the photo is shown in Fig. 1(b)]. Cutting the DE membrane in the hollow areas, and then, the three actuators will be separated. After carefully connecting the bonding area along with the minor preset marks, three actuators are evenly distributed along the circumferential direction of the robot. The front view and top view photos of the robot are shown in Fig. 1(d).

When high voltage is applied, the saddle-shaped DEA expands gradually, increasing the length of the actuator, and then, the whole robot bends. When high voltage is applied to the three DEAs simultaneously, the SPR elongates along its axes, as shown in Fig. 1(c). Theoretically, the robot could bend in any direction by adjusting the voltage on the three actuators. The frequency of elongation or bending of the robot depends on the driving voltage frequency and the DE membrane's material characteristics. To the best of our knowledge, the 3-DOF SPR based on the DEAs with lightweight and small scale is proposed for the first time. Next, we will carry out kinematic modeling of the robot.

III. HYBRID MODELING AND CONTROL METHOD

A. Learning-Based Electromechanical Modeling

It is necessary to characterize the electrical deformation ability of DEAs. Most of the previous research on the electric deformation of DEAs is based on the nonlinear large deformation theory of soft materials and the electromechanical coupling characteristics between the dielectric elastomer and supporting structure. However, it is difficult to accurately predict the effective output deformation of the actuator due to the following factors.

- 1) The complex structure and nonuniform deformation: The DE membrane forms a complex spatial structure due to the synergistic interplay between the elastic supporting frame and the electric field. At the same time, the strain distribution across the DE membrane surface is heterogeneous, with the peripheral strain of the DE membrane surpassing the strain at the center [28].
- 2) Material nonlinearity: The DE material demonstrate a highly nonlinear behavior [29], characterized by a substantial increase in elastic modulus as strain increases.
- 3) Electric field nonlinearity: As stretch rate increases, the relative permittivity of DE material decreases [30], and the uneven thickness of carbon grease electrodes may further contribute to a nonuniform electric field distribution.
- 4) Electromechanical coupling: There is a strong coupling between electrical and mechanical properties. The external electric fields induce deformation in the thin DE membrane and the support frame, which in turn affects the distribution of electric fields, further exacerbating the nonlinearity of DEA [31].

In summary, considering the complex electromechanical deformation of DEAs, developing a precise analytical model for DEAs remains challenging. Consequently, we chose to employ the learning-based method to model the electromechanical deformation behavior of DEAs. A neural network model is utilized to characterize the mapping relationship, circumventing the need to consider the mechanical and electrical properties of the DE membrane, support frame and compliant electrodes, and has been demonstrated to be accurate and efficient in subsequent experimental verification.

A typical neural network framework usually includes an input layer, hidden layers, and an output layer. The nonlinearity of neural networks is mainly reflected in neurons. Each neuron contains the weight w_i and bias b as well as an activation function σ . The output y of a neuron satisfies the following equation:

$$y = \sigma \left(b + \sum_{i=1}^n x_i w_i \right) \quad (1)$$

where x_i represents the neuron input.

For the SPR, the input of the neural network is the elongation of DEAs and the output is the actuation voltage. Before training the neural network model, the dataset was divided into the training set, verification set, and test set by the ratio of 0.7: 0.15: 0.15. The optimization algorithm is Levenberg–Marquardt, the nonlinear activation function is the sigmoid function, and the training loss mean squared error (MSE) is as follows:

$$\text{MSE} = \frac{1}{m} \sum_{i=1}^m (V_i - \bar{V}_i)^2 \quad (2)$$

where V_i is the actual voltage, and \bar{V}_i is the predicted voltage by the neural network.

We make the following assumptions: The first is that the three DEAs have almost consistent electromechanical characteristics. The second is that the electrodeformation model of DEAs does not change with the deformation of the robot. When applying the same voltage to the three DEAs at the same time, the upper plane of the robot will remain horizontal during the elongation process. The elongation is acquired by a high-precision laser displacement sensor (HG-C1030, Panasonic Industry (China) Co., Ltd., Shanghai, China) with a resolution of $10\text{ }\mu\text{m}$ and a dynamic range of $\pm 5\text{ mm}$. It is noteworthy that in the process of collecting electrodeformation data, a thin cap (2.5 g) is placed on the robot for reflecting the laser and a marked paper sheet is placed on the cap for subsequent trajectory tracking experiments.

In order to further improve the generalization ability of neural networks, the neural network with different numbers of hidden neurons was trained over 50 times, respectively. The root means square error (RMSE) and the regression coefficient R were calculated and compared, as shown in Table II. It is observed that the training error decreases, and then, increases with the increase in the number of neurons. This can be attributed to the increasing complexity of the neural network, which eventually leads to overfitting. Therefore, it is of great significance to select the appropriate number of neurons. By the results, a neural network comprising ten hidden neurons is chosen, given its minimal RMSE of 0.6332 V, and its training results are detailed in Section IV.

TABLE II
TRAINING RESULTS OF DIFFERENT NUMBER OF HIDDEN NEURONS

Neurons	RMSE _{min} (V)	RMSE _{mean} (V)	RMSE _{max} (V)	R _{mean}
4	0.6588	0.6611	0.6663	0.999890
6	0.6496	0.6535	0.6626	0.999891
8	0.6458	0.6580	0.6935	0.999894
10	0.6332	0.6519	0.6797	0.999896
12	0.6395	0.6595	0.7176	0.999893
14	0.6395	0.6595	0.6986	0.999892
16	0.6458	0.6708	0.7036	0.999887

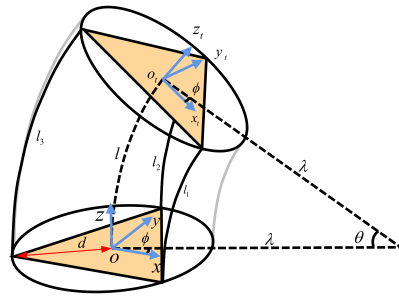


Fig. 2. Diagram of kinematic model of the SPR.

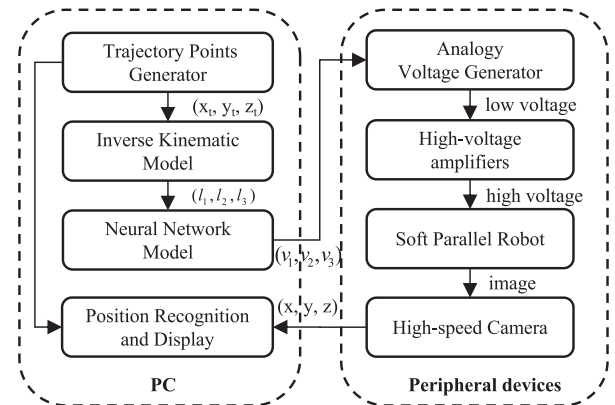


Fig. 3. Control strategy of the SPR.

B. Kinematic Modeling

After obtaining the mapping relationship between the actuation voltage and the elongation of DEAs, the kinematic model between the elongation and the motion of the center point on the top plane of the SPR is necessary to be derived. According to Fig. 2, three DEAs are fixed to the support frame at a radius d from the center at the distribution of $2\pi/3$ radian. Due to the restricted arrangement of the DEAs, the robot either exhibited pure extension or curved arcuately when a driving voltage is applied. The configuration space is defined by three spatial parameters: circle radius $\lambda \in (0, \infty)$, bending angle $\theta \in [-\pi, \pi]$, and the angle of the bending plane with respect to the X-axis, $\phi \in [0, 2\pi]$. The lengths of the three actuators are denoted as l_1 , l_2 , and l_3 , respectively.

First, we establish the robot coordinate systems as shown in Fig. 3. The $\{OXYZ\}$ reference frame is fixed on the center of the bottom plane of the SPR, and the $\{O_tX_tY_tZ_t\}$ reference

frame is fixed on the center of the top plane. The transformation between the two reference frames could be obtained by the following steps. At first, rotate the $\{OXYZ\}$ reference frame by ϕ along the Z-axis. Next, translate the reference frame by λ along the X-axis. Next, rotate the new reference frame by θ along the Y-axis. Finally, rotate the coordinate system in the opposite direction of the first two steps, and the transformation is finished. By these steps, the original reference frame $\{OXYZ\}$ is coincident with the coordinate system $\{O_tX_tY_tZ_t\}$. This process could be described as follow:

$$\begin{aligned}\mathbf{T}_c(\mathbf{q}) &= \mathbf{R}_Z(\phi) \mathbf{P}_X(\lambda) \mathbf{R}_Y(\theta) \mathbf{P}_X(-\lambda) \mathbf{R}_Z(-\phi) \\ &= \begin{bmatrix} \mathbf{R}_c(\mathbf{q}) & \mathbf{p}_c(\mathbf{q}) \\ \mathbf{0}_{1 \times 3} & 1 \end{bmatrix} \quad (3)\end{aligned}$$

where $\mathbf{R}_Z \in SO(3)$, $\mathbf{R}_Y \in SO(3)$ are homogeneous rotation matrix, respectively, along the Z- and Y-axes, $\mathbf{P}_X \in \mathbb{R}$ is the homogeneous translation matrix along the X-axis, $\mathbf{R}_c \in SO(3)$ and $\mathbf{p}_c \in \mathbb{R}^3$ are the rotational and translation components of the transformation matrix \mathbf{T}_c , and $\mathbf{q} = \{\lambda, \phi, \theta\}$ is the spatial curve parameters unnumbered equation shown at the bottom of this page.

Finally, we could solve the complete transformation matrix \mathbf{T}_c . The aforementioned transformation matrix describes the mapping relationship between the spatial curve parameters and the pose of the center on the top plane of the robot.

In order to intuitively describe how the position of the top plane is influenced, we also need to establish the relationship between the lengths of DEAs (l_1, l_2, l_3) and the spatial configuration parameters \mathbf{q} . Based on the PCC model, the spatial configuration parameters of the robot can be solved by the following formulas.

$$l = \frac{1}{3}(l_1 + l_2 + l_3) \quad (4)$$

$$\phi = \tan^{-1} \left(\frac{\sqrt{3}(l_3 + l_1 - 2l_2)}{3(l_3 - l_1)} \right) \quad (5)$$

$$\lambda = \frac{d(l_1 + l_2 + l_3)}{2\sqrt{l_1^2 + l_2^2 + l_3^2 - l_1l_2 - l_1l_3 - l_2l_3}} \quad (6)$$

$$\theta = l/\lambda. \quad (7)$$

Through the forward kinematics established previously, we can obtain the position of center on the top plane of the robot according to the lengths of DEAs. Furthermore, we derive the inverse kinematics of the robot as follows:

$$\phi = \arctan \frac{y}{x} \quad (8)$$

$$\lambda = \frac{x^2 + y^2 + z^2}{2\sqrt{x^2 + y^2}} \quad (9)$$

$$\mathbf{T}_c(\mathbf{q}) = \begin{bmatrix} \cos^2 \phi (\cos \theta - 1) + 1 & \sin \phi \cos \phi (\cos \theta - 1) & \cos \phi \sin \theta & \lambda \cos \phi (1 - \cos \theta) \\ \sin \phi \cos \phi (\cos \theta - 1) & \cos^2 \phi (1 - \cos \theta) + \cos \theta & \sin \phi \sin \theta & \lambda \sin \phi (1 - \cos \theta) \\ -\cos \phi \sin \theta & -\sin \phi \sin \theta & \cos \theta & \lambda \sin \theta \\ 0 & 0 & 0 & 1 \end{bmatrix}.$$

$$\theta = \arccos \left(\frac{\lambda - \sqrt{x^2 + y^2}}{\lambda} \right) \quad (10)$$

$$l_i = l - \theta d \cdot \cos \left(\phi + \frac{\pi}{6} - \frac{2(i-1)}{3}\pi \right) \quad (11)$$

where $l_i, i = 1, 2, 3$ represents the length of the i th DEA.

With the aforementioned equation, we could quickly compute the length of each DEA by the desired position of the robot center.

To sum up, in Section III-A, we obtain the mapping relationship between the elongation of DEA and the driving voltage by the electrodeformation model. In Section III-B, the forward and inverse kinematics between the lengths of the DEAs and the position coordinates of the robot are established. Combining the aforementioned two models, we can solve the lengths of the DEAs by the end position, and then, get the corresponding driving voltage. This is the foundation for controlling the robot to track desired trajectories accurately.

C. Control Strategy

As shown in Fig. 3, the control strategy of the SPR is designed. Through the user-defined interface, we can select different desired trajectories. The trajectory coordinate generator is used to generate the dense coordinate sequence of the desired trajectory (x_t, y_t, z_t) in the workspace. Then, the elongation and the length of the three actuators (l_1, l_2, l_3) could be solved by the inverse kinematic model. According to the neural network model, the related analogy control voltages could be obtained. Next, the voltage generator provides the voltage sequence (v_1, v_2, v_3) and amplified by the high-voltage amplifiers. The high control voltages are applied to the SPR to obtain the desired motion. With the high-speed camera, the motion trajectory of the robot (x, y, z) could be captured and shown with the desired trajectory (x_t, y_t, z_t) in real time.

IV. RESULTS

A. Experiment Setup

In order to test the performance of the designed SPR, an experimental system is established, as shown in Fig. 4(a). This system consists of the following parts. The NI controller module (NI 9174; National Instruments, Austin, TX, USA) is used to communicate with the PC and three voltage output boards (NI 9263; National Instruments, Austin, TX, USA) for generating the low analog voltage sequence range from 0 to 5 V. In order to check whether the control voltage is correct during the experiment, a voltage acquisition module (USB-31110, Smacq Technologies. Co., Ltd., Beijing, China) is used to monitor the

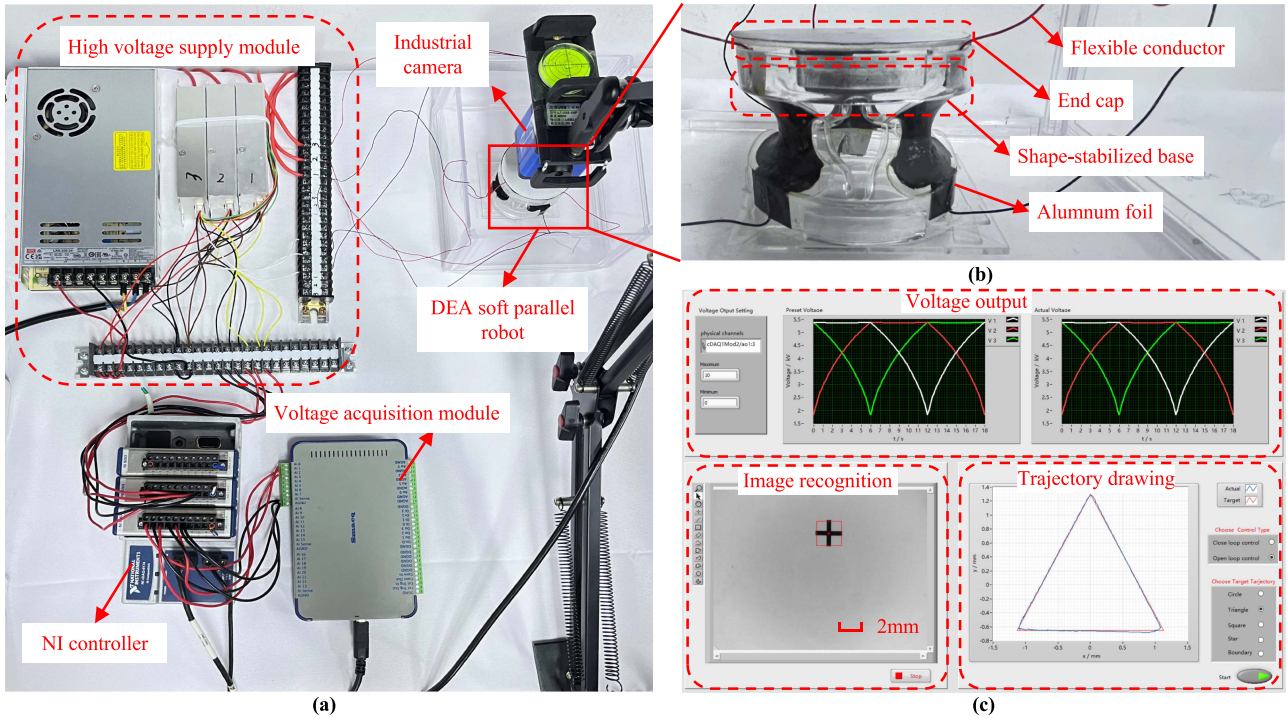


Fig. 4. Experiment Setup. (a) Robot system consists of the NI controller to generate the low analog voltage, a high-voltage supply module to amplify the low voltage to high control voltage, an industrial camera to capture the motion of the soft robot and a voltage acquisition module to measure the control voltage. (b) SPR with an end cap and two shape-stabilized bases and aluminum foil pasted. (c) Software consists of the voltage output chart, image recognition window, and the trajectory drawing chart.

voltage generated by the NI controller in real time. A high-voltage supply module (P103-1FU1, Dongwen High Voltage Power Supply Corp, Tianjin, China) is used to amplify (2000 times) the analog voltage generated by the NI controller to actuate the DEAs. Moreover, an industrial camera (LT-H8179, Qingdao Blue Sky Technology Co., Ltd., Qingdao, China) is used for capturing the motion of the robot.

Fig. 4(b) shows the SPR, two shape-stabilized bases, and an end cap. The flexible conductor is pasted on the two bases through aluminum foil. A small cross mark is designed on the end cap for image recognition and real-time motion display. Besides, we designed a front panel based on LABVIEW for operation and display, as shown in Fig. 4(c). The front panel consists of the voltage output chart to show the actual actuation voltage, an image recognition window to track the designed cross mark based on the template matching method, and a trajectory drawing chart to plot the actual and desired trajectories. To ensure the accuracy of the experiment, we adjusted the camera view, and the observable region is about $16 \text{ mm} \times 12 \text{ mm}$, while the resolution is 1600×1200 , so the pixel accuracy is about $10 \mu\text{m}$.

B. Stiffness Analysis

In this section, we test the axial stiffness and bending stiffness of the proposed SPR, respectively, as shown in Fig. 5(a). The digital force gauge (WD-2/0.2, Wenzhou WeDo Electronics Co., Ltd., Wenzhou, China) has a measuring range of $\pm 0.2 \text{ N}$ and

a measuring accuracy of $\pm 0.5\%$. Fig. 5(b) shows the bending stiffness of the SPR in different directions. The red, blue, yellow, and green curves represent the stress curves when the robot's edge is compressed by 2, 4, 6, and 8 mm. It can be seen that the forces in all directions are basically the same under the same compression, so the bending stiffness of the SPR is almost uniform in all directions. In order to further quantitatively analyze the bending stiffness of SPR, we chose two special directions, $\varphi = 90^\circ$ and $\varphi = -90^\circ$. As shown in Fig. 5(d), it can be seen that the curves are approximately straight, demonstrating that a proportional increment in force corresponds to an increase in edge compression.

Fig. 5(c) shows the relationship curves between the force and displacement in the process of compression and extension at the center of the SPR. It can be seen that the axial stiffness is greater than the bending stiffness by comparing with Fig. 5(d). The two curves closely resemble linear relationships, and the tensile and compressive stiffness are roughly equivalent. According to the least-square method, the axial stiffness of the robot is about 0.11 N/mm .

C. Training Result of the Neural Network Model

In this part, we train our neural network model with the collected dataset and plot relative results shown in Fig. 6. As mentioned previously, we use the neural network method for electromechanical modeling due to its excellent nonlinear fitting and generalization ability. In order to show the training accuracy,

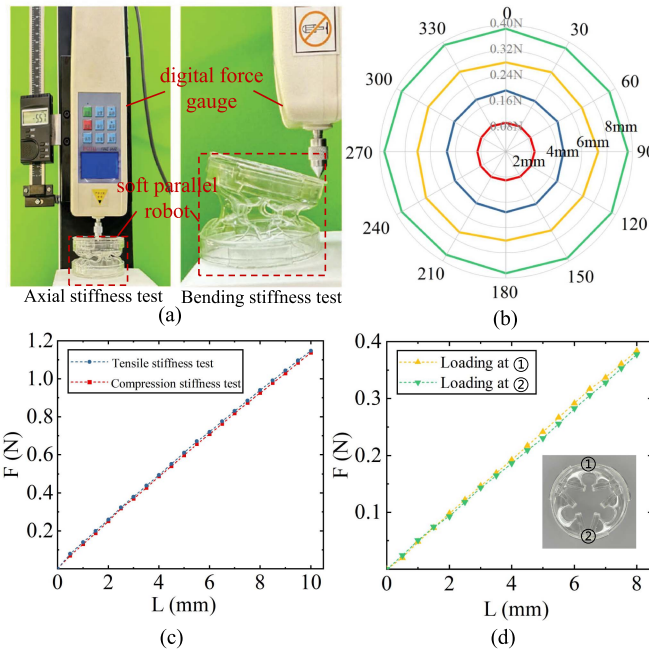


Fig. 5. (a) Stiffness Analysis experimental settings. (b) Bending stiffness analysis of the SPR in different directions. (c) Axial stiffness analysis of the SPR. (d) Bending stiffness analysis of the SPR in two special directions.

we plot several curves to show the relationship between the elongation and the actuation voltage [see Fig. 6(a)]. When the voltage is lower than 1 kV, there is no obvious elongation of the actuator. As the voltage gradually increases, the length of the actuator is also elongated gradually, and the elongation growth rate also increases. It is because the thickness of the DE membrane is getting smaller, and according to the deformation principle of the DEA mentioned previously, the stress of the DE membrane is increased. The target and output curves are almost coincident on the training set, validation set, and test set. To make the errors between curves more observable, Fig. 6(b) shows the error distribution curves of different datasets. The maximum error does not exceed $15 \mu\text{m}$, and the large error mainly occurs in the initial stage of deformation as the elongation is less than 0.5 mm. When the elongation exceeds 0.5 mm, the error is greatly reduced and gradually stabilized within a small range.

In order to further analyze the predicted error of the neural network, we plot the error histogram with 20 bins [see Fig. 6(c)]. It is observed that more than 70% of errors are in the bin that less than $1 \mu\text{m}$. Besides, the curves in Fig. 6(d) also show that the neural network has great fitting accuracy with a regression coefficient of 0.9999. The overall results verify that the neural network could be able to learn the nonlinearity deformation of the SPR and establish a solid foundation for robot control.

D. Workspace Analysis

In this subsection, we analyze the workspace of the robot based on the forward kinematics model. Under the maximum safe energization voltage of 6 kV, the SPR could reach the elongation of 4 mm with the original height of 40 mm (including

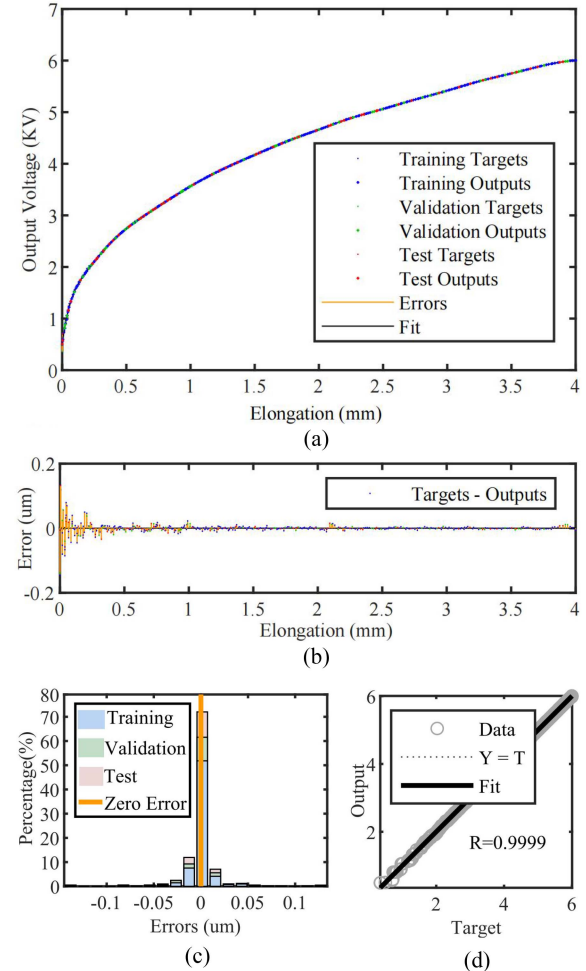


Fig. 6. Training result of the neural network. (a) Output voltage curves relative to elongation of different training sets. (b) Error distribution curves of different datasets. (c) Error distribution histogram. (d) Regression curve between target value and predicted value of neural network.

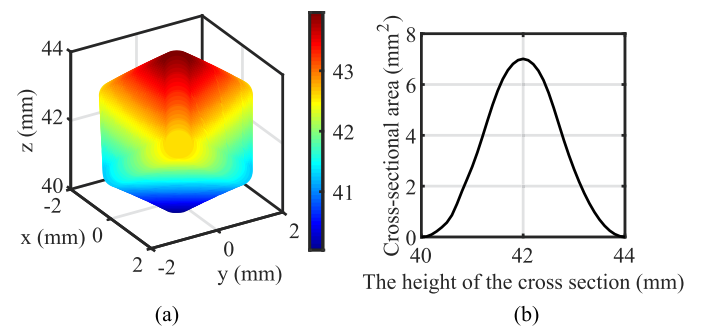


Fig. 7. Workspace analysis. (a) 3-D kinematic workspace of the SPR. (b) Z-axis cross-sectional area relative to the Z-axis height.

the length of the two shape-stabilized bases). The initial height of the DE membrane is 20 mm, so the elongation rate is 20%. Taking the original length and the elongation of the DEA into the forward kinematics, we could obtain the workspace of the SPR, as shown in Fig. 7(a). The workspace volume is 12 mm^3 . We also analyzed the Z-axis cross-sectional area relative to the

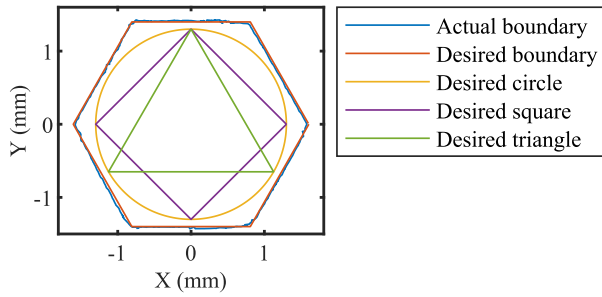


Fig. 8. Actual and desired boundary curves, and different trajectories within the boundary.

Z-axis height, as shown in Fig. 7(b). The results show that when the height is 42 mm, the section area is the largest at 6.8 mm^2 , providing a theoretical guide to choosing the trajectory plane.

We design several different trajectories on the maximum cross section of the workspace, including triangle, circle, and square, shown in Fig. 8. We also carried out experiments to obtain the actual boundary and compared it with the target boundary. The results show that the two boundary curves almost coincide, verifying the accuracy of the proposed hybrid model.

E. Trajectory Tracking Performance

In Section III, a control strategy is proposed based on the hybrid model for the SPR. To evaluate the control accuracy, trajectory tracking experiments are carried out. The robot is controlled to track three patterns (see Fig. 8) at different speeds and under different loads. The three patterns have the same circumscribed circle with a radius of 1.3 mm. The starting point of the three trajectories is (0, 1.3 mm), and the movement direction is counterclockwise. During the experiments, a 2-D camera is used to capture the position of the robot center in real time. It is worth mentioning that the maximum inclination angle of the robot's upper plane is 0.0619 rad when moving along different trajectories. The origin length of the “cross” mark is 2 mm, so the maximum change in length caused by the inclination is about 0.00383 mm, which is almost negligible. Therefore, a 2-D camera can meet the accuracy requirements for trajectory tracking.

First, set the velocity to 0.375 mm/s without load, and the control voltage sequences are generated to actuate the DEAs. The experimental results are shown in Fig. 9(a), where the solid black line is the desired trajectory, and the green line is the actual trajectory. It can be seen that the two trajectories basically coincide, indicating that the robot has good motion performance at this velocity. The tracking error distribution is shown as a green bar in Fig. 9(d). The errors mainly source from two aspects. The first is the neural network model error and the assumption based on the constant curvature. The second is the fabrication error, which can be caused by different electrodeformation characteristics of the DE membrane and the uneven area and thickness of the hand-painted carbon grease electrode.

Next, the load capacity of the robot is tested. 14 and 21 g (4 times and 6 times the weight of robot) loads are installed,

respectively, on the upper plane of the robot, and trajectory planning experiments are carried out for the three patterns. The results are shown in Fig. 9(b), where the black line is the desired trajectory, and the orange and purple lines are the actual trajectories with the load of 14 and 21 g, respectively. It can be seen that when the load changes, the robot's trajectory coincides with the preset trajectory, indicating that the increase in load does not reduce the robot's tracking performance. This is because the robot is designed in a parallel configuration. Compared with the serial robot, the stiffness is greater. Even under the external load, the robot can still produce preset deformation, indicating that the robot has a good load capacity.

Next, the control performance of the robot at different tracking velocities is also tested. The results are shown in Fig. 9(c), where the black line is the desired trajectory, and the red and blue lines are the actual trajectories with the velocity of 0.75 and 1.5 mm/s, respectively. It can be seen that when the velocity increases, the motion range of the robot becomes significantly smaller. As the tracking velocity of the robot increases gradually, the charging and discharging speed of the DEA increases. Due to the hysteresis of the DEA, the deformation of the robot cannot reach the preset goal in real time.

Finally, to quantitatively analyze the trajectory tracking error, the mean error and standard deviation are calculated and plotted in Fig. 9(d). When the speed of the robot is 0.375 mm/s without any additional load, the mean positioning error of different trajectories is 13.4–16.6 μm . When the external load increases, the error of the robot increases, but it still maintains a high positioning accuracy. With loads of 14 and 21 g at a speed of 0.375 mm/s, the mean errors are 14.8–17.6 and 15.9–18.2 μm , respectively. When there is no additional load, the mean errors of three trajectories with the velocity of 0.75 and 1.5 mm/s are 98.2–103.4 μm and 231.8–236.2 μm , respectively. It can be seen from Fig. 9(c) that although the range of the three trajectories becomes smaller, there is no significant distortion in shape.

F. Micromanipulation Experiment

To further verify the micromanipulation capability of the SPR, a microneedle is mounted in the upper plane of the robot, and zebrafish embryo puncture experiments are carried out, as depicted in Fig. 10. The puncture procedure includes the following steps: first, the SPR is controlled to bring the microneedle close to the zebrafish embryo; second, the surface of the embryo begins to deform after being touched by the microneedle; third, the microneedle advances until it penetrates the zebrafish embryo; and finally, the microneedle is withdrawn from the embryo and return to the initial position. The experimental results demonstrate that the proposed robot has high control accuracy and the potential for application in the field of micromanipulation.

G. Discussion

Compared with the conventional soft serial robots, the SPRs have great application prospects in micromanipulation, microassembly, and microsurgery due to their higher stiffness, greater load capacity, and higher precision. This work presents a lightweight (3.5 g) small-scale ($\phi 60 \times 40 \text{ mm}$) SPR made up

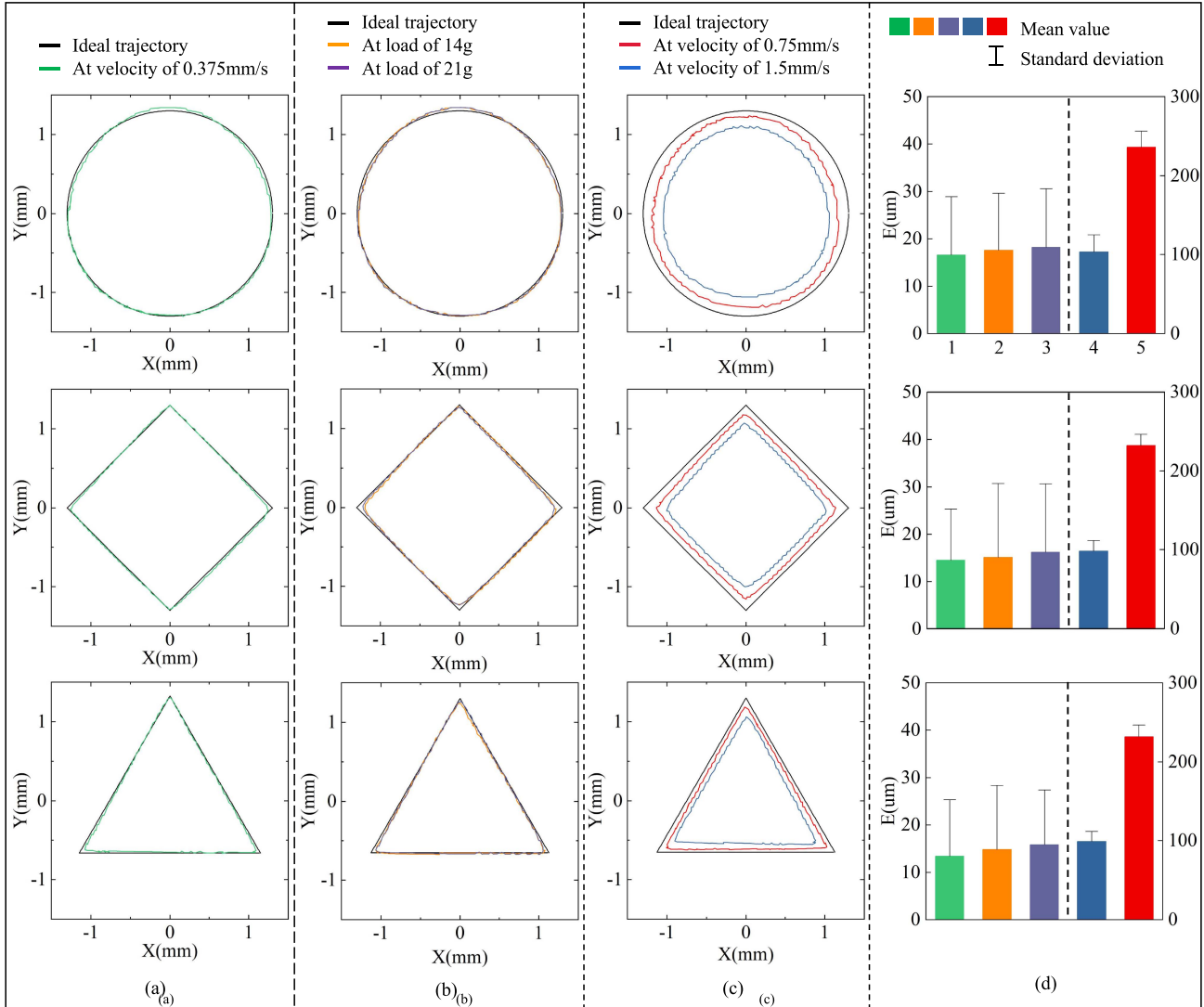


Fig. 9. Trajectory tracking experiments. (a) Tracking trajectory of circle, triangle, and square patterns at the velocity of 0.375 mm/s without load. (b) Tracking trajectory of circle, square, and triangle patterns at the velocity of 0.375 mm/s with the load of 14 and 21 g. (c) Tracking trajectory of circle, square, and triangle patterns at the velocity of 0.75 and 1.5 mm/s without load. (d) Tracking error distributions of circle, square, and triangle patterns, respectively, under different conditions [one-to-one correspondence with the same color in Fig. 9(a)–(c)].

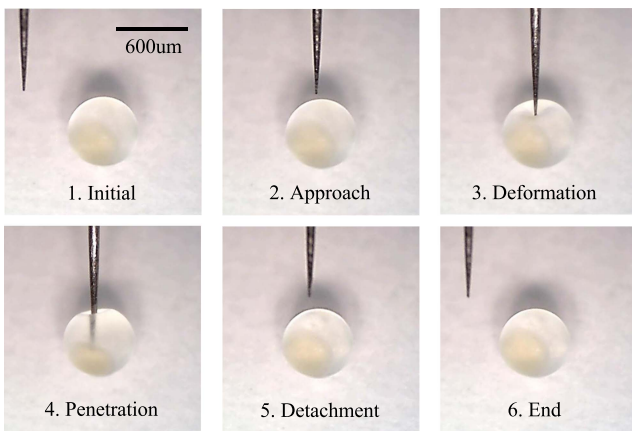


Fig. 10. Zebrafish embryo puncture experiments with the SPR.

of three symmetrically arranged DEAs and a lot of experiments have been carried out to analyze the performance of the robot. The results show that the robot has high control accuracy and the potential to be applied in the field of micromanipulation.

In order to further demonstrate the performance of robots, Table III shows the comparison between the proposed SPR and other existing SPRs. Few SPRs can achieve micron-level precision control. In terms of driving method: pneumatic SPRs often need to be equipped with multiple silicone chambers and solenoid valves, resulting in bulky and complex robot systems, and the response speed is usually limited by the ability to pump air in and out of the actuator [15], [32]; tendon-actuated SPRs are usually limited to planar motion for better control accuracy and need to occupy a large area [16], [33]; SMA-actuated SPRs are slow in response, and the temperature dependence makes it difficult to control [17], [34], [35]; DE-actuated SPRs

TABLE III
COMPARISON BETWEEN THIS WORK AND SOME SPRS

Reference	Link type	Size ¹	NOA ²	Accuracy	Actuation method
SPR [15]	flexible	$\approx \phi 200 \times 150 \text{mm}$	3	6.4–9.2cm	Pneumatic
Wrist rehabilitation robot [32]	flexible	$\approx \phi 100 \times 440 \text{mm}$	6	—	Pneumatic
Extracorporeal ultrasound robot [37]	flexible	$\approx \phi 170 \times 130 \text{mm}$	3	0.39mm	Pneumatic
Planar continuum robot [16]	flexible & rigid	$>\phi 580 \text{mm}$	3	1.8mm	Tendon-actuated
Reconfigurable continuum robot [33]	flexible	$>\phi 200 \text{mm}$	6	3.3mm	Tendon-actuated
Soft parallel Stewart platform [34]	flexible	$\approx \phi 170 \times 90 \text{mm}$	6	—	SMA-actuated
Multi-DoF continuum robot [35]	flexible	$\phi 80 \times 345 \text{mm}$	9	1.42mm	SMA-actuated
Soft robotic arm [17]	flexible	$\phi 26 \times 80 \text{mm}$	3	0.16mm	SMA-actuated
Bionic eyeball motion actuator [19]	flexible	$\approx \phi 50 \times 150 \text{mm}$	3	1.086–1.719mm	DE-actuated
Drawing robot [18]	flexible	$\approx \phi 200 \times 160 \text{mm}$	3	—	DE-actuated
Cone actuator [36]	flexible & rigid	$\phi 60 \times 50 \text{mm}$	8	$\pm 4.45 \text{ mm}$	DE-actuated
ours	flexible	$\phi 60 \times 40 \text{mm}$	3	13.4–16.6μm	DE-actuated

¹ The overall size not clearly provided in the literature is estimated based on the scale and the given size.

² NOA: Number of actuators.

have fast response speed and compact structure. However, the existing DE-actuated SPRs need to be equipped with additional structures inside for support and restoration, such as spring [19] and connecting rod [36], which increases the weight of the robot and limits its application. Moreover, an integrated design and manufacturing method is proposed. The actuators can be fabricated and assembled simultaneously rather than fabricating several actuators individually, and then, assembling them with connectors. The integrated method overcomes the limitations of conventional manufacturing methods, take advantage of lower material costs and processing time costs, reduces processing errors, endows the robot with a compact structure and ultralightweight mass, and lays the foundation for high-precision positioning.

This study opens up a new path for the design and control of the soft lightweight small-scale parallel robot with high-precision positioning. In the future, the closed-loop control of the robot will be further studied to compensate for the inevitable errors in manufacturing and modeling.

V. CONCLUSION

Due to the great application potential in the industrial production and biomedical field, this article proposed a DE-actuated soft lightweight small-scale parallel robot. With the integrated design and fabrication strategy, the robot has a compact structure, low manufacturing cost, and a simplified manufacturing process. A hybrid-model-based open-loop controller is established, and the proposed robot achieves high trajectory tracking accuracy. The average positioning error of the different trajectories is 13.4–16.6 μm . The zebrafish embryo puncture experiments have proved that the robot has micromanipulation capabilities.

REFERENCES

- [1] V. Gough, "Contribution to discussion to papers on research in automobile stability and control and in tire performance," *Proc. Automot. Division Inst. Mech. Eng.*, vol. 180, pp. 392–394, 1957.
- [2] V. E. Gough, "Universal tyre test machine," in *Proc. FISITA 9th Int. Tech. Congr.*, London, U.K., 1962, pp. 117–137.
- [3] H. McClintock, F. Z. Temel, N. Doshi, J.-s. Koh, and R. J. Wood, "The milidelta: A high-bandwidth, high-precision, millimeter-scale delta robot," *Sci. Robot.*, vol. 3, no. 14, 2018, Art. no. eaar3018.
- [4] F. Pierrot, C. Reynaud, and A. Fournier, "Delta: A simple and efficient parallel robot," *Robotica*, vol. 8, no. 2, pp. 105–109, 1990.
- [5] W. Xu, J.-S. Pap, and J. Bronlund, "Design of a biologically inspired parallel robot for foods chewing," *IEEE Trans. Ind. Electron.*, vol. 55, no. 2, pp. 832–841, Feb. 2008.
- [6] S. Briot, A. Pashevich, and D. Chablat, "Optimal technology-oriented design of parallel robots for high-speed machining applications," in *Proc. IEEE Int. Conf. Robot. Automat.*, 2010, pp. 1155–1161.
- [7] J. Mo, Z.-F. Shao, L. Guan, F. Xie, and X. Tang, "Dynamic performance analysis of the x4 high-speed pick-and-place parallel robot," *Robot. Comput.-Integr. Manuf.*, vol. 46, pp. 48–57, 2017.
- [8] Z. Li, X. Li, Q. Li, H. Su, Z. Kan, and W. He, "Human-in-the-loop control of soft exosuits using impedance learning on different terrains," *IEEE Trans. Robot.*, vol. 38, no. 5, pp. 2979–2993, Oct. 2022.
- [9] W. He, C. Xue, X. Yu, Z. Li, and C. Yang, "Admittance-based controller design for physical human–robot interaction in the constrained task space," *IEEE Trans. Automat. Sci. Eng.*, vol. 17, no. 4, pp. 1937–1949, Oct. 2020.
- [10] T. Xu, Z. Hao, C. Huang, J. Yu, L. Zhang, and X. Wu, "Multimodal locomotion control of needle-like microrobots assembled by ferromagnetic nanoparticles," *IEEE/ASME Trans. Mechatron.*, vol. 27, no. 6, pp. 4327–4338, Dec. 2022.
- [11] J. Zhang et al., "A survey on design, actuation, modeling, and control of continuum robot," *Cyborg Bionic Syst.*, vol. 2022, 2022, Art. no. 9754697.
- [12] C. Laschi, B. Mazzolai, and M. Cianchetti, "Soft robotics: Technologies and systems pushing the boundaries of robot abilities," *Sci. Robot.*, vol. 1, no. 1, 2016, Art. no. eaah3690.
- [13] D. Liu et al., "Magnetically driven soft continuum microrobot for intravascular operations in microscale," *Cyborg Bionic Syst.*, vol. 2022, 2022, Art. no. 9850832.
- [14] I. L. Sander, N. Dvorak, J. A. Stebbins, A. J. Carr, and P.-A. Mouthuy, "Advanced robotics to address the translational gap in tendon engineering," *Cyborg Bionic Syst.*, vol. 2022, 2022, Art. no. 9842169.
- [15] X. Huang, X. Zhu, and G. Gu, "Kinematic modeling and characterization of soft parallel robots," *IEEE Trans. Robot.*, vol. 38, no. 6, pp. 3792–3806, Dec. 2022.
- [16] K. Nuelle, T. Sterneck, S. Lilge, D. Xiong, J. Burgner-Kahrs, and T. Ortmaier, "Modeling, calibration, and evaluation of a tendon-actuated planar parallel continuum robot," *IEEE Robot. Automat. Lett.*, vol. 5, no. 4, pp. 5811–5818, Oct. 2020.
- [17] H. Yang, M. Xu, W. Li, and S. Zhang, "Design and implementation of a soft robotic arm driven by SMA coils," *IEEE Trans. Ind. Electron.*, vol. 66, no. 8, pp. 6108–6116, Aug. 2019.
- [18] C. Jiang et al., "Flexible parallel link mechanism using tube-type dielectric elastomer actuators," *J. Robot. Mechatron.*, vol. 27, no. 5, pp. 504–512, 2015.
- [19] L. Li, H. Godaba, H. Ren, and J. Zhu, "Bioinspired soft actuators for eyeball motions in humanoid robots," *IEEE/ASME Trans. Mechatron.*, vol. 24, no. 1, pp. 100–108, Feb. 2019.
- [20] R. J. Webster III and B. A. Jones, "Design and kinematic modeling of constant curvature continuum robots: A review," *Int. J. Robot. Res.*, vol. 29, no. 13, pp. 1661–1683, 2010.
- [21] I. S. Godage, G. A. Medrano-Cerda, D. T. Branson, E. Guglielmino, and D. G. Caldwell, "Modal kinematics for multisection continuum arms," *Bioinspiration Biomimetics*, vol. 10, no. 3, 2015, Art. no. 035002.

- [22] P. S. Gonthina, A. D. Kapadia, I. S. Godage, and I. D. Walker, "Modeling variable curvature parallel continuum robots using euler curves," in *Proc. Int. Conf. Robot. Automat.*, 2019, pp. 1679–1685.
- [23] W. McMahan, B. A. Jones, and I. D. Walker, "Design and implementation of a multi-section continuum robot: Air-octor," in *Proc. IEEE/RSJ Int. Conf. Intell. Robots Syst.*, 2005, pp. 2578–2585.
- [24] F. Janabi-Sharifi, A. Jalali, and I. D. Walker, "Cosserat rod-based dynamic modeling of tendon-driven continuum robots: A tutorial," *IEEE Access*, vol. 9, pp. 68703–68719, 2021.
- [25] M. M. Dalvand, S. Nahavandi, and R. D. Howe, "An analytical loading model for n -tendon continuum robots," *IEEE Trans. Robot.*, vol. 34, no. 5, pp. 1215–1225, Oct. 2018.
- [26] G. Fang, Y. Tian, Z.-X. Yang, J. M. Geraedts, and C. C. Wang, "Efficient Jacobian-based inverse kinematics with sim-to-real transfer of soft robots by learning," *IEEE/ASME Trans. Mechatron.*, vol. 27, no. 6, pp. 5296–5306, Dec. 2022.
- [27] Z. Geng and L. Haynes, "Neural network solution for the forward kinematics problem of a stewart platform," in *Proc. IEEE Int. Conf. Robot. Automat.*, 1991, pp. 2650–2651.
- [28] T. Lu, C. Ma, and T. Wang, "Mechanics of dielectric elastomer structures: A review," *Extreme Mechanics Lett.*, vol. 38, 2020, Art. no. 100752.
- [29] Y. Li, I. Oh, J. Chen, H. Zhang, and Y. Hu, "Nonlinear dynamic analysis and active control of visco-hyperelastic dielectric elastomer membrane," *Int. J. Solids Struct.*, vol. 152, pp. 28–38, 2018.
- [30] Z. Suo, "Theory of dielectric elastomers," *Acta Mechanica Solidica Sinica*, vol. 23, no. 6, pp. 549–578, 2010.
- [31] M. Wissler and E. Mazza, "Electromechanical coupling in dielectric elastomer actuators," *Sensors Actuators A, Phys.*, vol. 138, no. 2, pp. 384–393, 2007.
- [32] Y. Wang and Q. Xu, "Design and testing of a soft parallel robot based on pneumatic artificial muscles for wrist rehabilitation," *Sci. Rep.*, vol. 11, no. 1, 2021, Art. no. 1273.
- [33] G. Böttcher, S. Lilge, and J. Burgner-Kahrs, "Design of a reconfigurable parallel continuum robot with tendon-actuated kinematic chains," *IEEE Robot. Automat. Lett.*, vol. 6, no. 2, pp. 1272–1279, Apr. 2021.
- [34] E. L. White, J. C. Case, and R. Kramer-Bottiglio, "A soft parallel kinematic mechanism," *Soft Robot.*, vol. 5, no. 1, pp. 36–53, 2018.
- [35] C. Cheng, J. Cheng, and W. Huang, "Design and development of a novel SMA actuated multi-DOF soft robot," *IEEE Access*, vol. 7, pp. 75073–75080, 2019.
- [36] A. T. Conn and J. Rossiter, "Towards holonomic electro-elastomer actuators with six degrees of freedom," *Smart Mater. Struct.*, vol. 21, no. 3, 2012, Art. no. 035012.
- [37] L. Lindenroth, R. J. Housden, S. Wang, J. Back, K. Rhode, and H. Liu, "Design and integration of a parallel, soft robotic end-effector for extracorporeal ultrasound," *IEEE Trans. Biomed. Eng.*, vol. 67, no. 8, pp. 2215–2229, Aug. 2020.



Qin Fang received the M.S. degree in aircraft design in 2021 from the School of Aeronautics and Astronautics, Zhejiang University, Hangzhou, China, where she is currently working toward the Ph.D. degree in control science and engineering with the Department of Control Science and Engineering.

Her research interests include soft robots, small-scale robots, and bionic robots.



Jingyu Zhang received the M.S. degree in mechanical manufacturing in 2021 from the School of Mechanical Engineering, Zhejiang University, Hangzhou, China, where he is currently working toward the Ph.D. degree in control science and engineering with the Department of Control Science and Engineering.

His research interests include medical robots and soft continuum robots.



Danying Sun received the B.Eng. degree in automation from the Nanjing University of Science and Technology, Nanjing, China, in 2020. She is currently working toward the M.S. degree in control science and engineering with the Department of Control Science and Engineering, Zhejiang University, Hangzhou, China.

Her research interests include soft magnetic robots and untethered sensing systems.



Yanan Xue received the M.D. degree in plastic surgery from the Zhejiang University School of Medicine, Hangzhou, China, in 2023.

She is currently working with the Plastic Surgery Department, Zhejiang Provincial People's Hospital and the Department of Control Science and Engineering, Zhejiang University, Hangzhou. Her research interests include micromedical robots, tissue regeneration repair, and scar treatment.



Rui Jin received the B.E. degree in mechanical design, manufacturing, and automation from Northwestern Polytechnical University, Xian, China, in 2021. He is currently working toward the M.S. degree in control science and engineering with the Department of Computer Science and Technology, Zhejiang University, Hangzhou, China.

His research interests include coaxial helicopters and autonomous flight.



Nenggan Zheng (Senior Member, IEEE) received the B.E. degree in biomedical engineering and the Ph.D. degree in computer science, both from Zhejiang University, Hangzhou, China, in 2002 and 2009, respectively.

He is currently a Professor with the Department of Computer Science and Technology, Zhejiang University. His research interests include artificial intelligence, software engineering, and electronic engineering.



Yue Wang (Member, IEEE) received the Ph.D. degree in control science and engineering from the Department of Control Science and Engineering, Zhejiang University, Hangzhou, China, in 2016.

He is currently an Associate Professor with the Department of Control Science and Engineering, Zhejiang University. His research interests include mobile robotics and robot perception.



Rong Xiong (Member, IEEE) received the Ph.D. degree in control science and engineering from the Department of Control Science and Engineering, Zhejiang University, Hangzhou, China, in 2009.

She is currently a Professor with the Department of Control Science and Engineering, Zhejiang University. Her research interests include motion planning and SLAM.



Haojian Lu (Member, IEEE) received the B.Eng. degree in mechatronical engineering from the Beijing Institute of Technology, Beijing, China, in 2015, and the Ph.D. degree in robotics from the City University of Hong Kong, Kowloon, Hong Kong, in 2019.

He is currently a Professor with the State Key Laboratory of Industrial Control and Technology, and the Institute of Cyber-Systems and Control, Zhejiang University, Hangzhou, China. His research interests include micro/nanorobotics, medical robotics, micro aerial vehicle, and soft robotics.



Zhefeng Gong received the Ph.D. degree in biophysics from the Institute of Biophysics, Chinese Academy of Sciences, Beijing, China, in 2000.

He is currently a Professor with the Medical School of Zhejiang University, Hangzhou, China. His research interest includes sensorimotor transformation in animals and neural control of animal movements.

Review Article

A Survey on Design, Actuation, Modeling, and Control of Continuum Robot

Jingyu Zhang,^{1,2} Qin Fang,^{1,2} Pingyu Xiang,^{1,2} Danying Sun,^{1,2} Yanan Xue,^{1,2,3} Rui Jin,^{1,2} Ke Qiu,^{1,2} Rong Xiong,^{1,2} Yue Wang,^{1,2} and Haojian Lu^{1,2}

¹State Key Laboratory of Industrial Control and Technology, Zhejiang University, Hangzhou 310027, China

²Institute of Cyber-Systems and Control, The Department of Control Science and Engineering, Zhejiang University, Hangzhou 310027, China

³Department of Plastic Surgery, Sir Run Run Shaw Hospital, Zhejiang University of Medicine, Hangzhou 310016, China

Correspondence should be addressed to Yue Wang; ywang24@zju.edu.cn and Haojian Lu; luhaojian@zju.edu.cn

Received 26 April 2022; Accepted 27 June 2022; Published 26 July 2022

Copyright © 2022 Jingyu Zhang et al. Exclusive Licensee Beijing Institute of Technology Press. Distributed under a Creative Commons Attribution License (CC BY 4.0).

In this paper, we describe the advances in the design, actuation, modeling, and control field of continuum robots. After decades of pioneering research, many innovative structural design and actuation methods have arisen. Untethered magnetic robots are a good example; its external actuation characteristic allows for miniaturization, and they have gotten a lot of interest from academics. Furthermore, continuum robots with proprioceptive abilities are also studied. In modeling, modeling approaches based on continuum mechanics and geometric shaping hypothesis have made significant progress after years of research. Geometric exact continuum mechanics yields apparent computing efficiency via discrete modeling when combined with numerical analytic methods such that many effective model-based control methods have been realized. In the control, closed-loop and hybrid control methods offer great accuracy and resilience of motion control when combined with sensor feedback information. On the other hand, the advancement of machine learning has made modeling and control of continuum robots easier. The data-driven modeling technique simplifies modeling and improves anti-interference and generalization abilities. This paper discusses the current development and challenges of continuum robots in the above fields and provides prospects for the future.

1. Introduction

Inspired by the tentacles of elephant trunks, snakes, and octopuses, continuum robots use a series of continuous arcs structurally rather than skeletal structures to generate bending motion [1], with flexibility, lightweight, inherent safety, scalability, and potential for low-cost parts. This design approach was initially applied primarily in industrial scenarios such as large-scale grasping, movement, and positioning [2] and even urban search and rescue operations in confined environments [3]. With the development of some advanced materials, the scale of the continuum robot is getting smaller and smaller [4]. With its soft characteristics, it has been widely used in the field of medical surgery.

In addition to the robots composed entirely of continuum medium, super-redundant robots with many discrete links are also regarded as continuum robots. The earliest work can be

located in 1967, when Anderson [5] studied the first tensor arm composed of stacked plates that can generate motion by stretching tendons. After that, there is a lot of research on super-redundant continuum robots [6–8]. A typical example is the super-redundant robot developed by CardioARM [9], which is a highly redundant serpentine arm for cardiac ablation. In recent years, parallel designs of continuum robots have also been developed. This kind of robot uses multiple elastic rods connected in parallel arrangement and has higher accuracy and stiffness than the serially connected continuum robot [10–12]. Some typical examples of parallel continuum robots include the multispine snake robot proposed by Ding et al. [13], Festo bionic tripod manipulator [14], and Stewart-Gough continuum design [15].

In general, the actuation mechanism of continuum robots [16, 17] can be divided into internal and external actuation mechanism [18]. Internal actuation mechanism

refers to the robot actuator being located inside and as part of the ontology [19]. A typical example is pneumatic robots, where deformation is caused by the expansion of an internal elastic chamber [20]. External actuation mechanism refers to the use of external components to change the robot configuration, such as the magnetic continuum robot. Different actuation mechanisms would bring different characteristics to robots [21]. For instance, the magnetic robot is easy to miniaturize while the tendon-driven robot has a relatively large load capacity. In addition, even if the same design prototype is used, different degrees of manufacturing error will bring different model parameters to the robot. As time goes by, the wear effect will further damage the modeling accuracy of the robot.

Considering the nonlinear deformations caused by actuation, material elasticity, and sensitivity to contact with the environment, continuum robots face great challenges in precise analytical modeling. Although the kinematic modeling of traditional rigid linkage robots is completely defined by the size of linkage and joint coordinates, the almost unlimited freedom of continuum robots greatly increases the complexity of its modeling. One of the major challenges in modeling soft continuum robots is to simplify the models and compromise the relationship between computation complexity and model accuracy. At present, the main modeling methods of continuum robots include the continuum model, geometric model, and data-driven model [22]. In the continuum model, the continuum robot is represented by an infinite number of infinitesimal microsolids in continuous accumulation [23], with geometric accuracy. The geometric model assumes that the continuum robot deforms in a certain geometric form, and the piecewise constant curvature modeling method is the most commonly used assumption for the continuum robot at present [24]. Recently, data-driven modeling, in which the model of the system is derived by using datasets and learning processes without making such physical simplification assumptions, has also been widely studied [25–27].

The control problem for the continuum robot is to find the proper actuation value to reach the desired state to perform a given task. In the control field, most research works focus on the positioning control and force control of the end-effector, but the control of the whole body configuration is rarely studied [16, 28]. Due to the kinematic redundancy of the continuum robot, a hierarchical control strategy could be adopted to achieve the optimal control to perform a certain task and simultaneously achieve the optimal configuration of the body. Currently, the control methods could be mainly divided into model-based, model-free, and hybrid model control [29]. Among them, model-based control is highly dependent on the precise modeling of the continuum robot and the perception accuracy of the sensor, showing better performance in motion accuracy [30]. The model-free control method is a data-driven control method, which is based on the neural network to learn the model of the robot, so as to achieve efficient control [31]. The hybrid model control method is generally combined with the neural network and physical model, and the neural network model is used to compensate for nonlinear factors to achieve effi-

cient control accuracy [32, 33]. In addition, remote operation is often used to control the continuum robot in the medical field [34, 35]. Through the user's visual perception, with the help of intraoperative images, the robot's state can be estimated, and the user can correct its movement accordingly.

This paper is aimed at summarizing and discussing the representative work in design, actuation, modeling, and control of continuum robots, as well as conducting a thorough and systematic analysis. This paper, in contrast to other review publications [21, 24, 36, 37], focuses more on major technical concerns rather than its application in a certain field. Thus, it could provide a relatively wide perspective on the development of continuum robots. Furthermore, this paper is expected to enlighten researchers to pay more attention to the immature field of continuum robots. This paper is organized as follows. In Chapter 2, this paper introduces the design and actuation method of the continuum robots in detail. In Chapter 3, this paper introduces the development of the continuum model, geometric model, and data-driven model in detail. In Chapter 4, several control methods of continuum robots, including model-based, model-free, and hybrid model control strategies, are introduced. In Chapter 5, some prospects and challenges are offered in order to motivate researchers to address some new issues. In Chapter 6, we conclude this paper and hope to give the researcher inspiration and a general understanding of continuum robots.

2. Design and Actuation Methods

2.1. Classification of the Design and Actuation Principle. Many alternative design and actuation approaches of continuum robots have been presented to fulfill the application in many sectors. Tendon-driven continuum robots are currently the most commonly used [38–40]. This kind of robots has a relatively rigid body [41], can easily obtain the analytical solution of the kinematics model, and is widely applied in multitask operation of various small surgical instruments [42]. Besides, it can usually achieve bending angles in excess of 100 degrees, achieving positioning accuracy of around 2.0 mm [43]. However, traditional tendon-driven continuum robots are constrained by traditional manufacturing processes and are difficult to be scaled down to smaller scales.

In order to reduce the stiffness of the continuum robot while maintaining a larger workspace, the fluid actuation mechanism [55–57] is proposed to replace the tendon actuation. Although its soft body gives the robot the advantages of safe contact and a large bending angle, it is difficult to achieve accurate positioning due to its highly nonlinear characteristics and the increasing complexity of the control system [58]. In addition, fluid-driven robots are larger than tendon-driven robots due to their limited actuation mode in shape.

In order to realize the miniaturization configuration of continuum robots, many cutting-edge materials have been developed and used to realize the actuation of robots, showing unique advantages [38, 59–61]. The soft continuum robots embedded with micromagnet or made of ferromagnetic composite material have accurate steering ability under

an external controllable magnetic field; its bending angle could exceed 180 degrees and has high positioning accuracy up to $10\text{ }\mu\text{m}$ [49]. Magnetically soft continuum robots, on the other hand, can achieve small diameters, up to the micron scale, which ensures their ability to conduct targeted therapy in bronchi or in cerebral vessels [62]. However, it is difficult for magnetically soft continuum robots to maintain stability under external forces, and the tiny rigid magnet tips risk falling off inside the body during operation. To achieve safer and more reliable control, shape memory materials are used to drive the continuum robot and for cardiovascular examination and nasopharyngeal administration [63]. The key advantage of this self-deforming material is that it provides extension, bending, and torsion for the main stem and can achieve overall actuation while maintaining a small scale, but its inherent hysteresis makes it difficult to achieve rapid response and precise positioning at the same time, and it has a low load capacity and quite complex pipeline wiring. Recently, combined with the ionic liquid conductors and tendon-driven method, a kind of continuum robot with proprioception has been studied. This robot shows a promising prospect toward low-cost, scalable position feedback for small-scale continuum robots [64].

In order to achieve accurate position prediction and variable stiffness for different environments, researchers have developed a number of hybrid actuated continuum robots. By integrating the pneumatic and tendon actuation methods, the robot exhibited great characteristics and achieved bending angles greater than 90° [65, 66]. In order to achieve the interventional treatment of human stenosis, a continuum robot integrating magnetic- and tendon-driven methods is proposed [51]. The robot can achieve relatively large angle steering under tendon actuation and high-precision position control of $10\text{ }\mu\text{m}$ under the external magnetic field. It takes the full advantage of both actuation methods and demonstrates excellent steering and accurate tracking capabilities.

Recently, some new design and actuation methods of continuum robots have been studied. A stretchable origami continuum robot [53] with omnidirectional bending and twisting has been developed. This kind of robot could achieve more sophisticated motions such as continuous stretching and contracting, reconfigurable bending, and multiaxis twisting with the foundation of the basic integrated motion. Besides, this robot has good scalability that could be assembled into a multisection continuum robot. A soft pneumatic robot [67, 68] has been studied that is able to navigate their environments not through locomotion but through growth. This motion is achieved by two principles: the increasing pressure of the thin-walled vessel allows rapid and substantial extension of the tip and asymmetric lengthening of the tip allows directional control. By validation, this kind of robot shows the abilities to navigate through constrained environments by exploiting passive deformations. The Table 1 summarizes some different design and actuation method of continuum robots.

2.2. Optimization Method of the Structure Parameters. For some specific occasions, the structure of continuum robots needs to be specially designed to meet the needs of use.

Two important principles need to be considered: the size of the workspace and the stiffness. In general, the workspace and stiffness should be as large as possible, so that the robot could reach the desired position and apply the required operating force. The two properties mainly depend on the structural design and constituent material. In general, a small diameter and high elastic modulus would take a large range of workspace; however, small cross-sectional diameter would reduce the stiffness of the robots. Therefore, there is a basic compromise between the workspace and the stiffness of a continuum robot. The super-elastic NiTi skeleton has high stiffness in a small diameter (about 3 mm), which has been widely adopted as the backbone skeleton of robots [38, 69, 70]. Moreover, it has good biocompatibility and is widely used in the medical field.

In recent years, there have been some studies on the structure optimization of continuum robots [71, 72]. The optimization parameters include material properties, whole length, diameter, and curvature that affect robot capabilities and properties. It is significant to obtain optimal design parameters for concentric tube robot [73], considering surgical task requirements, anatomical constraints, and any other desired indicators. Heuristics algorithms have been proposed to solve the design optimization problem on workspace of the robots [74]. However, it has been proven that this method is actually suboptimal [75]. Recently, a systematic set of the evolutionary design algorithm by integrating a theoretical model and the genetic algorithm is proposed [76]. The experimental results validate that designed magnetic soft continuum robots have a counterintuitive nonuniform distribution of magnetic particles to achieve an unprecedented workspace. Besides, some researcher also appropriately integrates sampling-based motion planning in configuration space into stochastic optimization in design space to obtain the optimal continuum robot for medical application [77] and provide the asymptotic optimality.

3. Modeling Method

Many researchers have contributed to the development of mathematical modeling methods capable of describing the kinematics and dynamics of such robots with infinite degrees of freedom since the field's inception. However, addressing the needs of robotics applications remains a challenge. The kinematics and dynamics modeling of the traditional rigid linkage robot can be defined by the size of the linkage and the coordinate of the joint. However, continuum robots have almost unlimited degrees of freedom, which greatly increases the complexity of modeling. In order to meet the standard of traditional rigid robot technology, the model of continuum robots should have low computational costs and sufficient accuracy. It should be able to clarify mathematical submodels, include them in a unified framework, and provide a systematic modeling process. At present, one of the main challenges of continuum robot modeling is to study and set up reasonable model assumptions and simplify modeling, which can accurately predict robot behavior while improving computational efficiency. The tradeoff between model complexity, computational cost,

TABLE 1: Summary of different design and actuation methods.

Literature	Design principle	DOF	Actuation	Diameter (mm)	Accuracy	Characteristics
[44]	Parallel	5	Rod driven	—	2.3%	Large workspace and high precision
[45]	Backbone	2	SMA driven	5	0.98 mm	Modular; teleoperation
[39]	Backbone	4	Tendon driven	38	<2 mm	Passive structural flexibility
[46]	Backbone	6	Fluid driven	30	—	Variable stiffness
[47]	Concentric tube	12	Motor driven	2.74; 1.92; 1.21	1%	Dual-arm
[48]	Backbone	4	Fluid driven	32	1.3%	Soft and has variable stiffness
[49]	Backbone	6	Magnetic driven	—	<7.86	Combination of soft and hard joints
[50]	Backbone	5	Magnetic driven	2.5	—	Variable stiffness
[51]	Backbone	5	Tendon and magnetic driven	3	10 μm	Large workspace and high precision
[52]	Backbone	5	Fluid and tendon driven	25	—	High load capacity
[53]	Backbone	5	Magnetic driven	20	—	Omnidirectional bending and twisting
[54]	Concentric tube	4	Motor driven	4.36; 2.265	—	3D printed

and accuracy is the main principle that must be considered when modeling continuum robots. This paper investigates the modeling techniques that have been proposed so far and introduces the development of the continuum model, geometric model, and proxy model, which are relatively representative in current academia.

3.1. Continuum Model. The continuum model is an infinite degree of freedom model in which a robot is represented by a continuous stack of infinite infinitesimal particles (Cosserat bar theory, see [78]). In the field of robotics, the Cosserat theory consisting of a finite number of solids projected on a continuous backbone has been applied to the dynamics of hyperredundant robots [79]. Recently, the Cosserat theory has been explicitly applied to soft robot motion and operation under static and dynamic conditions [79–81]. The Cosserat model treats the continuum robot as a deformable curve in which each particle is rigidly connected to a set of orthogonal vectors (controllers) to characterize its direction [82].

In Cosserat theory [79], the configuration of a microsolid with material abscissa $X \in [0, L]$ on the continuum robot with respect to the base frame of a continuum robot can be represented by position vector \mathbf{P} and rotation matrix \mathbf{R} . Therefore, the configuration space is defined as a curve $\mathbf{g}(\cdot): X \mapsto \mathbf{g}(X) \in \text{SE}(3)$ and

$$\mathbf{g} = \begin{pmatrix} \mathbf{R} & \mathbf{P} \\ 0^T & 1 \end{pmatrix}. \quad (1)$$

The strain state of the soft arm is defined by the vector field along the curve $\mathbf{g}(X)$ given as $X \mapsto \hat{\xi}(X) = \mathbf{g}^{-1} \frac{d}{dX} \mathbf{g} \in \text{se}(3)$ where the hat is the isomorphism between the twist vector representation and the matrix representation of the Lie algebra $\text{se}(3)$. It could be defined as

$$\hat{\xi} = \begin{pmatrix} \tilde{k} & q \\ 0^T & 0 \end{pmatrix} \in \text{se}(3), \xi = \begin{pmatrix} k^T & q^T \end{pmatrix}^T \in R^6, \quad (2)$$

where $q(X)$ represents the linear strains and $k(X)$ represents the angular strains.

The time derivation of the configuration curve $\mathbf{g}(\cdot)$ is represented by the twisted vector field $X \mapsto \eta(X) \in R^6$ given by $\hat{\eta}(X) = \mathbf{g}^{-1} \partial \mathbf{g} / \partial t = \mathbf{g}^{-1} \dot{\mathbf{g}}$. This field can be detailed in terms of its components in the (micro)body frames as

$$\hat{\eta} = \begin{pmatrix} \tilde{w} & v \\ 0^T & 0 \end{pmatrix} \in \text{se}(3), \eta = (w^T, v^T)^T \in R^6, \quad (3)$$

where $v(X)$ represents the linear velocity and $w(X)$ represents the angular velocity at a given time instant.

The time derivation of continuous media (see Figure 1) can be used to describe the dynamics that relates the time evolution of stress to the time evolution of strain. It could be obtained based on Newton's law, Alembert's law, and Hamilton's law; a set of geometric boundary conditions; and the constitutive law as follows.

$$\begin{cases} M\dot{\eta} - ad_{\eta}^T M\eta = \Lambda' - ad_{\xi}^T \Lambda + \bar{F}, \\ \Lambda(0) = -F_0, \Lambda(1) = F_1, \end{cases} \quad (4)$$

where ad is the adjoint representation of the Lie algebra, M is the inertia tensor of the cross section, $\Lambda = ((R^T m)^T, (R^T n)^T)^T$, $\bar{F} = ((R^T l)^T, (R^T f)^T)^T$, and it simulates the stress field on the beam which is the double counterpart of the strain field.

In order to simplify the modeling complexity, a discrete Cosserat model based on piecewise-constant strain (PCS) hypothesis has been proposed in recent years [22]. Compared with finite element simulation and other methods, this model can express the motion characteristics of discrete beams by explicit integration. The strain assumptions of the Cosserat continuous model (including torsion, shear, curvature, and elongation) are considered. The discrete modeling framework has excellent modeling accuracy under different driving conditions and external load models and can represent the deformation under the interaction with

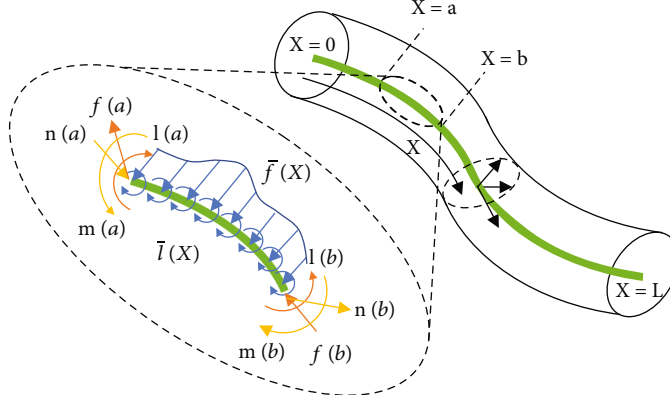


FIGURE 1: Diagram of force analysis of continuous media [83].

the medium, which promotes the development of modeling theory in the field of continuum robots.

3.2. Geometric Model. Compared with the Cosserat model, the geometric model does not consider the material properties of the robot and assumes that the deformation of the robot is a specific geometric shape. Therefore, the configuration of the continuum robot can be represented by a curve and a vector defining the direction of the robot tip. By far, the most widely used geometric model in the soft robot field adopts the piecewise constant curvature assumption [24]. The soft robot is expressed as a finite set of arc and described by circle parameters (radius of curvature, arc angle, and bending plane). By this method, the dimension of the state vector of continuum robot is simplified, and it is widely used in all kinds of real-time control algorithms and other occasions requiring high-speed computation [84–86].

As shown in Figure 2, the kinematics of the robot is decomposed into two mappings: One mapping is f_{specific} from the joint or actuator space q to a configuration space parameter (κ, φ, l) describing a constant curvature section; it is robotic specific because each actuator in a unique continuum robot

would affect circle parameters in different ways. The other mapping $f_{\text{independent}}$ is from the configuration space to the task space; it is robot independent and used to represent the characteristics of piecewise constant curvature deformation.

As is shown in Figure 3(a), the continuum robot can be described by a spatial curve, which describes the position and direction of any point on the body. Kinematic models of robots can be derived in a variety of ways, including Denavit-Hartenberg (D-H) parameters [87], Frenet-Serret (F-S) framework [88], and exponential coordinates [89]. At present, the kinematic characterization method using the DH parameter and exponential coordinate is widely used. In the section, we mainly introduce the two-representation method.

As shown in Figure 3(b), the continuum robot can be represented as the relative rotation and translation motion between multiple rigid links, and the corresponding DH parameters are given. According to the assumption of constant curvature deformation, the transformation matrix T_c between the tip coordinate system and the base coordinate system can be represented as

$$T_c = \begin{bmatrix} \cos^2 \varphi (\cos \kappa s - 1) + 1 & \sin \varphi \cos \varphi (\cos \kappa s - 1) & \cos \varphi \sin \kappa s & \frac{\cos \varphi (1 - \cos \kappa s)}{\kappa} \\ \sin \varphi \cos \varphi (\cos \kappa s - 1) & \cos^2 \varphi (1 - \cos \kappa s) + \cos \kappa s & \sin \varphi \sin \kappa s & \frac{\sin \varphi (1 - \cos \kappa s)}{\kappa} \\ -\cos \varphi \sin \kappa s & -\sin \varphi \sin \kappa s & \cos \kappa s & \frac{\sin \kappa s}{\kappa} \\ 0 & 0 & 0 & 1 \end{bmatrix}. \quad (5)$$

Similar results can be obtained using exponential coordinates based on the Lie group theory [90, 91]. The homogeneous transformation of the constant curvature curve can be decomposed into rotation transformation φ and in-plane transformation ℓ , and we can write the twist vector associated with each transformation using the notations and conventions outlined by Murray [92] as follows.

$$\begin{aligned} \mathbf{x}_{\text{rot}} &= \begin{bmatrix} \mathbf{v}_{\text{rot}} \\ w_{\text{rot}} \end{bmatrix} = [0 \ 0 \ 0 \ 0 \ 0 \ 1]^T, \\ \mathbf{x}_{\text{inp}} &= \begin{bmatrix} \mathbf{v}_{\text{inp}} \\ w_{\text{inp}} \end{bmatrix} = [0 \ 0 \ 1 \ 0 \ \kappa \ 0]^T. \end{aligned} \quad (6)$$

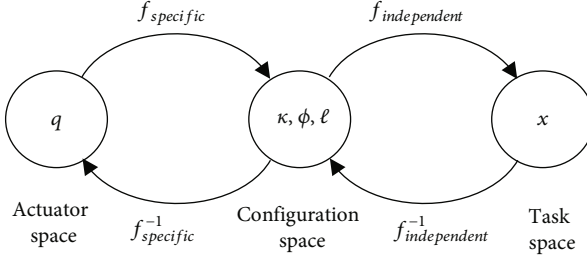


FIGURE 2: Mapping relationship of geometric model.

It can be written as follows.

$$\hat{\mathbf{x}}_{\text{rot}} = \begin{bmatrix} \hat{w}_{\text{rot}} & \mathbf{v}_{\text{rot}} \\ 0 & 0 \end{bmatrix} = \begin{bmatrix} 0 & -1 & 0 & 0 \\ 1 & 0 & 0 & 0 \\ 0 & 0 & 0 & 0 \\ 0 & 0 & 0 & 0 \end{bmatrix}, \quad (7)$$

$$\hat{\mathbf{x}}_{\text{inp}} = \begin{bmatrix} \hat{w}_{\text{inp}} & \mathbf{v}_{\text{inp}} \\ 0 & 0 \end{bmatrix} = \begin{bmatrix} 0 & 0 & \kappa & 0 \\ 0 & 0 & 0 & 0 \\ -\kappa & 0 & 0 & 1 \\ 0 & 0 & 0 & 0 \end{bmatrix}^T.$$

Using the exponential product formula, the transformation matrix T could be solved by the following equation.

$$T = e^{(\hat{\mathbf{x}}_{\text{rot}}\varphi)} e^{(\hat{\mathbf{x}}_{\text{inp}}\ell)}. \quad (8)$$

Similarly, if a set of twist vector is denoted by

$$\mathbf{x} = [0 \ 0 \ 1 \ -\kappa \sin \varphi \ \kappa \cos \varphi \ 0]^T. \quad (9)$$

Its exponential coordinate has the same form with (5).

3.3. Data-Driven Model. Because of the significant nonlinearities in the motion process of continuum robots, successful modeling of robots necessitates a significant amount of work and experience in continuum mechanics. To tackle these challenges, data-driven techniques, in which systems are modeled by learning from vast volumes of data (inputs and outputs) from external sources, have gotten a lot of attention recently [93–96]. At present, the neural network (NN) is the most commonly used approximate mapping regression model. By weighting the hidden layer, information always flows from the input to the output [97]. Furthermore, various regression approaches have shown to be effective in the field of continuum robotics, and the representative method can be locally weighted projection regression (LWPR) and (local) Gaussian process regression (GPR) [98]. One of the main benefits of these solutions is that they do not require physical models, but they rely on large amounts of representative data, which is sometimes difficult to collect. It is worth noting that for both data-driven and model-based approaches, each has a unique strength and is

preferred over the other in certain scenarios. Due to the possibility of hybrid approaches, combining both of them should also be explored in the future. Neural network models, on the other hand, are often pretrained and difficult to adapt to dynamic contexts. As a result, online learning is likely to become a new research topic.

4. Control Method

Robot control is the study of how to determine the right amount of drive to achieve the required state to perform a given task. The state of the continuum robot includes the position and orientation of the end-effector, the configuration of the robot, the stiffness of the robot, and its related motion performance. Current control methods of continuum robots mainly focus on achieving accurate position and posture control of end-effector and impedance control of the end-effector [16, 28, 99–101], which are mainly solved at the level of actuation and design optimization. There are few studies on control methods of overall configuration and distributed stiffness. On the other hand, the continuum robot has a redundant degree of freedoms, and the optimal control method can be used to achieve the optimal configuration of its configuration while performing the required tasks [102, 103].

Currently, control methods for the continuum robots can be divided into model-free, model-based, and hybrid model controls [29]. The accuracy of the robot model is critical for model-based control approaches. In order to obtain satisfactory control effects, complex models are usually derived to explain the numerous physical phenomena experienced by the robot. It is challenging to implement high-performance control algorithms in real time when using sophisticated nonlinear models, such as the variable curvature model. Control accuracy can be improved by using electromagnetic sensors [104, 105] or analytical calculation [106], visual feedback [107, 108], and other feedback techniques. The measured data is used to compensate the model error in the control process and achieve higher control accuracy. A typical closed-loop control strategy for a magnetic continuum robot is proposed by Campisano et al. based on the real-time Cosserat rod theory [109]. It utilized the actuation feedback to compensate for nonlinearities that can result in a kinematic model error. Pose feedback is utilized to maintain accurate path following. Experimental results demonstrate that the closed-loop control scheme has a significant performance.

Several studies have shown that using a closed-loop control strategy with feedback information can significantly increase control accuracy, stability, and robustness in low-frequency environments [110–113]. However, for extremely miniaturized continuous robotics, feedback control poses significant technical problems in sensor integration. It incorporates compatibility with anatomy, preoperative imaging technologies, and surgical equipment, especially in medical applications [105, 114]. Contact constraints in the environment also bring uncertainty to the control of the continuum robots [26, 37]. In order to overcome the inaccuracy of the model, some advanced control methods, such as adaptive

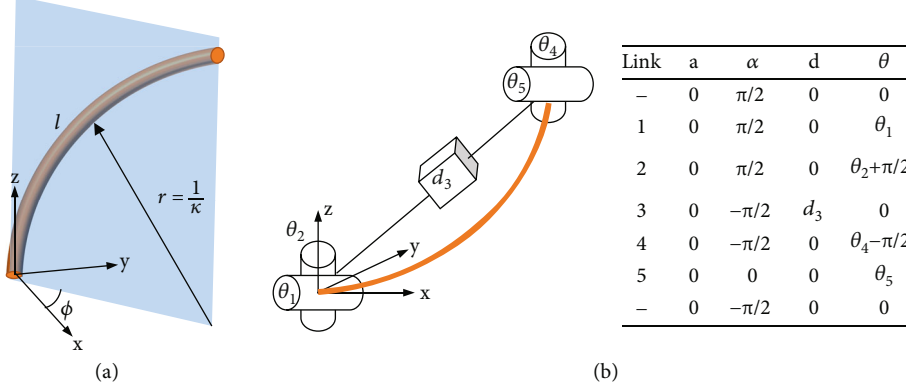


FIGURE 3: Parameter description of the configuration space continuum robot. (a) Arc parameter description of one section of continuum robots. (b) Denavit-Hartenberg (D-H) parameter description of one section of continuum robots.

control, have emerged in the field of continuous robots. The earliest application of this method was to compensate the kinematic inaccuracy of concentric robots [115] and to realize the automatic adjustment of model parameters by using model parameter estimation, so as to achieve high-performance control [116].

Due to the high complexity and high computation time of continuum robot kinematics, the model-free method (see Figure 4(a)) is used as an alternative method in recent studies. Direct strategy learning for robot control is an effective method, which is suitable for situations where dynamic modeling is difficult or the environment is unstructured. This method can be applied to high-dimensional systems and has a higher speed than traditional model-based controllers [93, 120, 121]. Strategy learning can be divided into model-free reinforcement learning and model-based reinforcement learning; we focus on model-based reinforcement learning because it can generate more effective strategy learning samples. In [122], the model-based strategy search uses a learning control algorithm called probabilistic reasoning, which takes into account the model uncertainty of the learned dynamic model (provided by a nonparametric Gaussian process) in long-term planning. Recently, there has been a strong interest in using traditional trajectory optimization methods to generate samples for strategy learning [123]. In addition, it can also combine the function approximation ability of the neural network to learn and represent these strategies [124, 125]. The most advanced methods of using this variant of the idea involve the use of local models of learning [126], composite multistep controllers [127], and deep representations of control strategies [128]. A model-based policy learning algorithm is proposed for closed-loop predictive control of a continuum robot. The closed loop control is obtained by trajectory optimization and supervised learning strategy, which shows good performance on control accuracy.

However, high computational time, low compatible rate of change in environment/interference, and complexity of learning methods (due to the nonlinearity and redundancy of continuum robots) seriously hinder the use of model-free methods in complex scenarios. The adaptability of different continuum robot structures presents additional chal-

lenges to the learning approach due to the particularity of each structure and inconsistencies in actuation and model descriptions. Therefore, a hybrid model control method (see Figure 4(b)) is proposed, which takes into account both model control reliability and data-driven robustness. One representative work is the hybrid adaptive control framework proposed by Wang et al. [116]; it combined offline trained robot inverse kinematics with neural network and online adaptive PID controller to compensate the positioning error caused by external disturbance. The experiment results validated that the proposed hybrid adaptive control framework has great performance to compensate for uncertain factors such as friction, driving tendon relaxation and external load during robot movement. Another representative work is the control method based on the Koopman operator theory [119, 129], which can not only avoid the physical simplification hypothesis but also produce a clear control-oriented model. This method uses the linear structure of the Koopman operator to construct a linear model of a nonlinear controlled dynamical system from input-output data and uses an established linear control method [130, 131] to control it. Koopman modeling and control methods are well suited to soft robots because they pose less physical threat to themselves or their surroundings, which allows the model to safely collect input-output data under a variety of operating conditions and do so in an automated manner. In addition, because the Koopman program is entirely data-driven, it inherently captures input-output behavior, avoiding the ambiguity involved in selecting discrete sets of states for structures with infinite degrees of freedom [119]. The Table 2 summarizes some different control methods for continuum robots.

5. Prospects and Challenges

In this paper, we have reviewed the state of the art of continuum robots, focusing particularly on the design, actuation, modeling, and control. The design and actuation of continuum robots is evolved from single actuation to hybrid actuation combining the advantages of different actuation methods. On the other hand, some new type of continuum

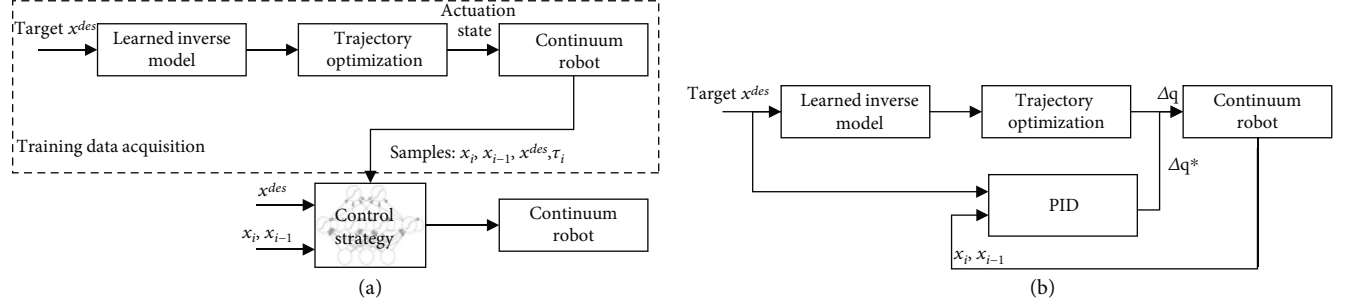


FIGURE 4: Several control strategies for continuum robots. (a) Schematic diagram of learning-based control strategy. (b) Schematic diagram of hybrid control strategy.

TABLE 2: Summary of different control methods.

Literature	Design principle	Actuation	Model based or free	Control method	Accuracy
[116]	Backbone	Tendon driven	Model based	Hybrid control based on the adaptive PID and NN model	<2.14 mm
[26]	Backbone	Tendon driven	Model free	Optimal control considering contacts	—
[110]	Backbone	Tendon driven	Model based	Closed control based on the mechanics model	<1.07 mm
[111]	Backbone	Magnetic driven	Model based	Closed control based on the mechanics model	0.42 mm
[117]	Backbone	Tendon driven	Model based	Open control based on the FEM model	<2.14 mm
[112]	Backbone	Fluid driven	Model based	Closed control based on the inverse kinematics	12.3 mm
[113]	Concentric tube	Motor driven	Model based	Closed control based on the Cosserat rod model	<1.67 mm
[118]	Backbone	Magnetic driven	Model based	Closed control based on the inverse kinematics	<5.41 mm
[93]	Backbone	Tendon driven	Model based	Closed control based on the reinforcement learning	<0.029 mm
[119]	Backbone	Fluid driven	Model based	Closed control based on the Koopman operator theory	<0.43 mm
[120]	Backbone	Fluid driven	Model based	Closed control based on the online learning kinematic	16.8 pixels

robot including soft pneumatic growing robot or origami-inspired continuum robot shows excellent abilities in motion flexibility or expansibility. On the field of modeling, the most widely used method includes Cosserat model and geometric model. The former is geometric exact but has low computation efficiency. The latter simplifies the modeling complexity and has very high computation efficiency but has lower accuracy if there is large deformation. However, considering the requirements of many applications, the geometric model is still popular. Recently, the data-driven method has been studied and applied into the modeling of continuum robots due to its ability of nonlinear fitting and generalization. However, the generalization ability of dynamic scenarios is still a problem worth studying. On the field of control, the closed control strategy with feedback information shows great improvement on the control accuracy, stability, and robustness under low frequency environment; however, it depends mostly on the sensor accuracy. Recently, the model-free control method which is used as an alternative method has been studied. Direct strategy learning for robot control is an effective method and shows good control accuracy and robustness. However, these methods have low adaptability to the change in environment/interference.

The hybrid model control method attracts the attention of researchers. The Koopman algorithm uses the linear structure of the Koopman operator to construct a linear model from input-output data to describe the dynamics of a complex system. Thus, many linear model controllers could be applied to the motion control of some complex continuum robot.

However, there are some serious significant challenges for the development of continuum robots, and there is no good solution so far.

- (1) The first is the miniaturization of continuum robots. At present, only magnetic-driven, optical-driven, or thermal-driven methods are most likely to achieve the miniaturization of continuum robots, but they often have highly nonlinear complex mechanical models, which makes it difficult to achieve robust control
- (2) The second is to enhance continuum robot perception. Ideally, the optimal awareness should be able to reconstruct the configurations of the robot with infinite degrees of freedom; however, only expensive FBG optical fibers can currently realize a high degree

- of freedom reconstruction. In the future, it is expected to combine with optical, mechanical, and electrical technologies to develop sensors that are cheaper and more suitable for continuum robots
- (3) The third is to develop the physics simulation engine of the continuum robots. The traditional rigid robot has a number of relatively mature simulation frameworks; however, they are not suitable to the continuum robots with infinite degrees of freedom. Nowadays, the validation of control algorithms must depend on the real robot platform which increases the costs. It is urgent for academia and industry to develop a real-time physics simulation engine for soft continuum robots

6. Conclusion

In summary, the development of continuum robots is rapid in recent years, and there have been many representative achievements on the design, actuation, modeling, and control of continuum robots. These great improvements promote the application of continuum robots in many fields such as surgical robot, nursing robot, continuum-limbed vehicles, ship-to-ship refueling, and exploration of extraterrestrial surfaces. It is expected that the continuum robot would play a more and more important role in social production and human life.

Conflicts of Interest

The authors declare that they have no competing interests.

Authors' Contributions

Jingyu Zhang analyzed the data and wrote the manuscript. Yue Wang, Haojian Lu, and Rong Xiong conceived the idea and led the project. The others collected the references and surveyed the development.

Acknowledgments

This work was supported by the Fundamental Research Funds for the Zhejiang Provincial Universities (2021XZZX021), Science and Technology on Space Intelligent Control Laboratory (2021-JCJQ-LB-010-13), and Zhejiang Provincial Natural Science Foundation of China (LD22E050007).

References

- [1] Y. Zhao, X. Song, X. Zhang, and X. Lu, "A hyper-redundant elephant's trunk robot with an open structure: design, kinematics, control and prototype," *Chinese Journal of Mechanical Engineering*, vol. 33, no. 1, pp. 1–19, 2020.
- [2] G. Robinson and J. B. C. Davies, "Continuum robots-a state of the art," in *Proceedings 1999 IEEE International Conference on Robotics and Automation (Cat. No.99CH36288C)*, pp. 2849–2854, Detroit, MI, USA, 1999.
- [3] B. A. Jones and I. D. Walker, "Practical kinematics for real-time implementation of continuum robots," *IEEE Transactions on Robotics*, vol. 22, no. 6, pp. 1087–1099, 2006.
- [4] J. Hwang, J.-y. Kim, and H. Choi, "A review of magnetic actuation systems and magnetically actuated guidewire- and catheter-based microrobots for vascular interventions," *Intelligent Service Robotics*, vol. 13, no. 1, pp. 1–14, 2020.
- [5] V. C. Anderson, "Tensor arm manipulator design," *American Society of Mechanical Engineers*, vol. 67, pp. 1–12, 1967.
- [6] T. Kato, I. Okumura, H. Kose, K. Takagi, and N. Hata, "Tendon-driven continuum robot for neuroendoscopy: validation of extended kinematic mapping for hysteresis operation," *International Journal of Computer Assisted Radiology and Surgery*, vol. 11, no. 4, pp. 589–602, 2016.
- [7] Z. Wu, Q. Li, J. Zhao, J. Gao, and K. Xu, "Design of a modular continuum-articulated laparoscopic robotic tool with decoupled kinematics," *IEEE Robotics and Automation Letters*, vol. 4, no. 4, pp. 3545–3552, 2019.
- [8] B. Zhao, W. Zhang, Z. Zhang, X. Zhu, and K. Xu, "Continuum manipulator with redundant backbones and constrained bending curvature for continuously variable stiffness," in *2018 IEEE/RSJ International Conference on Intelligent Robots and Systems (IROS)*, pp. 7492–7499, Madrid, Spain, 2018.
- [9] T. Ota, A. Degani, D. Schwartzman et al., "A highly articulated robotic surgical system for minimally invasive surgery," *The Annals of Thoracic Surgery*, vol. 87, no. 4, pp. 1253–1256, 2009.
- [10] C. E. Bryson and D. C. Rucker, "Toward parallel continuum manipulators," in *2014 IEEE International Conference on Robotics and Automation (ICRA)*, pp. 778–785, Hong Kong, China, 2014.
- [11] C. B. Black, *Modeling, Analysis, Force Sensing and Control of Continuum Robots for Minimally Invasive Surgery*, Tennessee Research and Creative Exchange (TRACE), 2017.
- [12] C. B. Black, J. Till, and D. C. Rucker, "Parallel continuum robots: modeling, analysis, and actuation-based force sensing," *IEEE Transactions on Robotics*, vol. 34, no. 1, pp. 29–47, 2018.
- [13] J. Ding, R. E. Goldman, K. Xu, P. K. Allen, D. L. Fowler, and N. Simaan, "Design and coordination kinematics of an insertable robotic effectors platform for single-port access surgery," *IEEE/ASME Transactions on Mechatronics*, vol. 18, no. 5, pp. 1612–1624, 2012.
- [14] J. A. Rivera and C. J. Kim, "Spatial parallel soft robotic architectures," in *2014 IEEE/RSJ International Conference on Intelligent Robots and Systems*, pp. 548–553, Chicago, IL, USA, 2014.
- [15] A. L. Orekhov, V. A. Alois, and D. C. Rucker, "Modeling parallel continuum robots with general intermediate constraints," in *2017 IEEE International Conference on Robotics and Automation (ICRA)*, pp. 6142–6149, Singapore, 2017.
- [16] M. C. Yip, J. A. Sganga, and D. B. Camarillo, "Autonomous control of continuum robot manipulators for complex cardiac ablation tasks," *Journal of Medical Robotics Research*, vol. 2, no. 1, article 1750002, 2017.
- [17] Y. Ansari, M. Manti, E. Falotico, Y. Mollard, M. Cianchetti, and C. Laschi, "Towards the development of a soft manipulator as an assistive robot for personal care of elderly people," *International Journal of Advanced Robotic Systems*, vol. 14, no. 2, 2017.

- [18] Y. Zhong, L. Hu, and Y. Xu, "Recent advances in design and actuation of continuum robots for medical applications," *Actuators*, vol. 9, no. 4, p. 142, 2020.
- [19] H.-C. Fu, J. D. L. Ho, K. H. Lee et al., "Interfacing soft and hard: a spring reinforced actuator," *Soft Robotics*, vol. 7, no. 1, pp. 44–58, 2020.
- [20] N. Farrow and N. Correll, "A soft pneumatic actuator that can sense grasp and touch," in *2015 IEEE/RSJ International Conference on Intelligent Robots and Systems (IROS)*, pp. 2317–2323, Hamburg, Germany, 2015.
- [21] S. Li and G. Hao, "Current trends and prospects in compliant continuum robots: a survey," *Actuators*, vol. 10, no. 7, p. 145, 2021.
- [22] F. Renda, F. Boyer, J. Dias, and L. Seneviratne, "Discrete Cosserat approach for multisection soft manipulator dynamics," *IEEE Transactions on Robotics*, vol. 34, no. 6, pp. 1518–1533, 2018.
- [23] S. S. Antman, "Problems in nonlinear elasticity," in *Nonlinear Problems of Elasticity*, vol. 107 of Applied Mathematical Sciences, pp. 513–584, Springer, New York, NY, 2005.
- [24] R. J. Webster III and B. A. Jones, "Design and kinematic modeling of constant curvature continuum robots: a review," *The International Journal of Robotics Research*, vol. 29, no. 13, pp. 1661–1683, 2010.
- [25] W. Xu, J. Chen, H. Y. Lau, and H. Ren, "Data-driven methods towards learning the highly nonlinear inverse kinematics of tendon-driven surgical manipulators," *The International Journal of Medical Robotics and Computer Assisted Surgery*, vol. 13, no. 3, article e1774, 2017.
- [26] M. C. Yip and D. B. Camarillo, "Model-less feedback control of continuum manipulators in constrained environments," *IEEE Transactions on Robotics*, vol. 30, no. 4, pp. 880–889, 2014.
- [27] X. You, Y. Zhang, X. Chen et al., "Model-free control for soft manipulators based on reinforcement learning," in *2017 IEEE/RSJ International Conference on Intelligent Robots and Systems (IROS)*, pp. 2909–2915, Vancouver, BC, Canada, 2017.
- [28] M. Li, R. Kang, S. Geng, and E. Guglielmino, "Design and control of a tendon-driven continuum robot," *Transactions of the Institute of Measurement and Control*, vol. 40, no. 11, pp. 3263–3272, 2018.
- [29] M. T. Chikhaoui and J. Burgner-Kahrs, "Control of continuum robots for medical applications: state of the art," in *ACTUATOR 2018; 16th International Conference on New Actuators*, pp. 1–11, Bremen, Germany, 2018.
- [30] R. S. Penning, J. Jung, N. J. Ferrier, and M. R. Zinn, "An evaluation of closed-loop control options for continuum manipulators," in *2012 IEEE International Conference on Robotics and Automation*, pp. 5392–5397, Saint Paul, MN, USA, 2012.
- [31] J. Back, L. Lindenroth, K. Rhode, and H. Liu, "Model-free position control for cardiac ablation catheter steering using electromagnetic position tracking and tension feedback," *Frontiers in Robotics and AI*, vol. 4, p. 17, 2017.
- [32] A. D. Marchese, R. K. Katzeckmann, and D. Rus, "Whole arm planning for a soft and highly compliant 2d robotic manipulator," in *2014 IEEE/RSJ International Conference on Intelligent Robots and Systems*, pp. 554–560, Chicago, IL, USA, 2014.
- [33] A. D. Marchese and D. Rus, "Design, kinematics, and control of a soft spatial fluidic elastomer manipulator," *The International Journal of Robotics Research*, vol. 35, no. 7, pp. 840–869, 2016.
- [34] C. G. Frazelle, A. Kapadia, and I. Walker, "Developing a kinematically similar master device for extensible continuum robot manipulators," *Journal of Mechanisms and Robotics*, vol. 10, no. 2, article 025005, 2018.
- [35] C. Fellmann, D. Kashi, and J. Burgner-Kahrs, "Evaluation of input devices for teleoperation of concentric tube continuum robots for surgical tasks," in *Medical Imaging 2015: Image Guided Procedures, Robotic Interventions, and Modeling*, pp. 411–419, Orlando, FL, USA, 2015.
- [36] J. Burgner-Kahrs, D. C. Rucker, and H. Choset, "Continuum robots for medical applications: a survey," *IEEE Transactions on Robotics*, vol. 31, no. 6, pp. 1261–1280, 2015.
- [37] T. da Veiga, J. H. Chandler, P. Lloyd et al., "Challenges of continuum robots in clinical context: a review," *Progress in Biomedical Engineering*, vol. 2, no. 3, article 032003, 2020.
- [38] T.-D. Nguyen and J. Burgner-Kahrs, "A tendon-driven continuum robot with extensible sections," in *2015 IEEE/RSJ International Conference on Intelligent Robots and Systems (IROS)*, pp. 2130–2135, Hamburg, Germany, 2015.
- [39] S. Geng, Y. Wang, C. Wang, and R. Kang, "A space tendon-driven continuum robot," in *Advances in Swarm Intelligence. ICSI 2018*, Lecture Notes in Computer Science, Y. Tan, Y. Shi, and Q. Tang, Eds., pp. 25–35, Springer, Cham, 2018.
- [40] J. Liu, C. Zhang, Z. Liu et al., "Design and analysis of a novel tendon-driven continuum robotic dolphin," *Bioinspiration & Biomimetics*, vol. 16, no. 6, article 065002, 2021.
- [41] T. Liu, Z. Mu, W. Xu et al., "Improved mechanical design and simplified motion planning of hybrid active and passive cable-driven segmented manipulator with coupled motion," in *2019 IEEE/RSJ International Conference on Intelligent Robots and Systems (IROS)*, pp. 5978–5983, Macau, China, 2019.
- [42] F. Qi, F. Ju, D. Bai, Y. Wang, and B. Chen, "Kinematic analysis and navigation method of a cable-driven continuum robot used for minimally invasive surgery," *The International Journal of Medical Robotics and Computer Assisted Surgery*, vol. 15, no. 4, article e2007, 2019.
- [43] T. Liu, Z. Mu, H. Wang, W. Xu, and Y. Li, "A cable-driven redundant spatial manipulator with improved stiffness and load capacity," in *2018 IEEE/RSJ International Conference on Intelligent Robots and Systems (IROS)*, pp. 6628–6633, Madrid, Spain, 2018.
- [44] G. Wu and G. Shi, "Design, modeling, and workspace analysis of an extensible rod-driven parallel continuum robot," *Mechanism and Machine Theory*, vol. 172, article 104798, 2022.
- [45] Q. Ding, Y. Lu, A. Kyme, and S. S. Cheng, "Towards a multi-imager compatible continuum robot with improved dynamics driven by modular SMA," in *2021 IEEE International Conference on Robotics and Automation (ICRA)*, pp. 11930–11937, Xi'an, China, 2021.
- [46] I. De Falco, M. Cianchetti, and A. Menciassi, "A soft multi-module manipulator with variable stiffness for minimally invasive surgery," *Bioinspiration & Biomimetics*, vol. 12, no. 5, article 056008, 2017.
- [47] M. T. Chikhaoui, J. Granna, J. Starke, and J. Burgner-Kahrs, "Toward motion coordination control and design optimization for dual-arm concentric tube continuum robots," *IEEE*

- Robotics and Automation Letters*, vol. 3, no. 3, pp. 1793–1800, 2018.
- [48] T. Ranzani, G. Gerboni, M. Cianchetti, and A. Menciassi, “A bioinspired soft manipulator for minimally invasive surgery,” *Bioinspiration & Biomimetics*, vol. 10, no. 3, article 035008, 2015.
- [49] T. Greigarn, N. L. Poirot, X. Xu, and C. Cavusoglu, “Jacobian-based task-space motion planning for MRI-actuated continuum robots,” *IEEE Robotics and Automation Letters*, vol. 4, no. 1, pp. 145–152, 2019.
- [50] C. Chautems, A. Tonazzini, D. Floreano, and B. J. Nelson, “A variable stiffness catheter controlled with an external magnetic field,” in *2017 IEEE/RSJ International Conference on Intelligent Robots and Systems (IROS)*, pp. 181–186, Vancouver, BC, Canada, 2017.
- [51] T. Zhang, L. Yang, X. Yang, R. Tan, H. Lu, and Y. Shen, “Millimeter-scale soft continuum robots for large-angle and high-precision manipulation by hybrid actuation,” *Advanced Intelligent Systems*, vol. 3, no. 2, article 2000189, 2021.
- [52] A. Shiva, A. Stilli, Y. Noh et al., “Tendon-based stiffening for a pneumatically actuated soft manipulator,” *IEEE Robotics and Automation Letters*, vol. 1, no. 2, pp. 632–637, 2016.
- [53] S. Wu, Q. Ze, J. Dai, N. Udupi, G. H. Paulino, and R. Zhao, “Stretchable origami robotic arm with omnidirectional bending and twisting,” *Proceedings of the National Academy of Sciences of the United States of America*, vol. 118, no. 36, 2021.
- [54] T. K. Morimoto and A. M. Okamura, “Design of 3-d printed concentric tube robots,” *IEEE Transactions on Robotics*, vol. 32, no. 6, pp. 1419–1430, 2016.
- [55] R. Kang, Y. Guo, L. Chen, D. T. Branson, and J. S. Dai, “Design of a pneumatic muscle based continuum robot with embedded tendons,” *IEEE/ASME Transactions on Mechatronics*, vol. 22, no. 2, pp. 751–761, 2017.
- [56] J. D. Greer, T. K. Morimoto, A. M. Okamura, and E. W. Hawkes, “Series pneumatic artificial muscles (spams) and application to a soft continuum robot,” in *2017 IEEE International Conference on Robotics and Automation (ICRA)*, pp. 5503–5510, Singapore, 2017.
- [57] C. Sun, L. Chen, J. Liu, J. S. Dai, and R. Kang, “A hybrid continuum robot based on pneumatic muscles with embedded elastic rods,” *Proceedings of the Institution of Mechanical Engineers, Part C: Journal of Mechanical Engineering Science*, vol. 234, no. 1, pp. 318–328, 2020.
- [58] J. Y. Loo, K. C. Kong, C. P. Tan, and S. G. Nurzaman, “Non-linear system identification and state estimation in a pneumatic based soft continuum robot,” in *2019 IEEE Conference on control technology and applications (CCTA)*, pp. 39–46, Hong Kong, China, 2019.
- [59] Y. Goergen, G. Rizzello, S. Seelecke, and P. Motzki, “Modular design of an SMA driven continuum robot,” in *Proceedings of the ASME 2020 Conference on Smart Materials, Adaptive Structures and Intelligent Systems. ASME 2020 Conference on Smart Materials, Adaptive Structures and Intelligent Systems*, Orlando, FL, USA, 2020.
- [60] M. A. Mandolino, Y. Goergen, P. Motzki, and G. Rizzello, “Design and characterization of a fully integrated continuum robot actuated by shape memory alloy wires,” in *2022 IEEE 17th International Conference on Advanced Motion Control (AMC)*, pp. 6–11, Padova, Italy, 2022.
- [61] H. Guo, F. Ju, Y. Cao et al., “Continuum robot shape estimation using permanent magnets and magnetic sensors,” *Sensors and Actuators A: Physical*, vol. 285, pp. 519–530, 2019.
- [62] L. Wang, C. F. Guo, and X. Zhao, “Magnetic soft continuum robots with contact forces,” *Extreme Mechanics Letters*, vol. 51, article 101604, 2022.
- [63] S. Jiang et al. et al., “A variable-stiffness continuum manipulators by an SMA-based sheath in minimally invasive surgery,” *The International Journal of Medical Robotics and Computer Assisted Surgery*, vol. 16, no. 2, article e2081, 2020.
- [64] D. Alatorre, D. Axinte, and A. Rabani, “Continuum robot proprioception: the ionic liquid approach,” *IEEE Transactions on Robotics*, vol. 38, no. 1, pp. 526–535, 2022.
- [65] J. Liu, J. Wei, G. Zhang, S. Wang, and S. Zuo, “Pneumatic soft arm based on spiral balloon weaving and shape memory polymer backbone,” *Journal of Mechanical Design*, vol. 141, no. 8, 2019.
- [66] R. Kang, D. T. Branson, T. Zheng, E. Guglielmino, and D. G. Caldwell, “Design, modeling and control of a pneumatically actuated manipulator inspired by biological continuum structures,” *Bioinspiration & biomimetics*, vol. 8, no. 3, article 036008, 2013.
- [67] E. W. Hawkes, L. H. Blumenschein, J. D. Greer, and A. M. Okamura, “A soft robot that navigates its environment through growth,” *Science Robotics*, vol. 2, no. 8, article eaan3028, 2017.
- [68] J. D. Greer, L. H. Blumenschein, A. M. Okamura, and E. W. Hawkes, “Obstacle-aided navigation of a soft growing robot,” in *2018 IEEE International Conference on Robotics and Automation (ICRA)*, pp. 4165–4172, Brisbane, QLD, Australia, 2018.
- [69] J. Tian, T. Wang, X. Fang, and Z. Shi, “Design, fabrication and modeling analysis of a spiral support structure with superelastic Ni-Ti shape memory alloy for continuum robot,” *Smart Materials and Structures*, vol. 29, no. 4, article 045007, 2020.
- [70] H. Liu, Z. Ji, J. Li, Y. Zhou, C. Wang, and P. Ba, “As shape continuum robot with a single actuation structured by NiTi slices,” in *2017 IEEE International Conference on Robotics and Biomimetics (ROBIO)*, pp. 401–405, Macau, Macao, 2017.
- [71] H. Cheong, M. Ebrahimi, and T. Duggan, “Optimal design of continuum robots with reachability constraints,” *IEEE Robotics and Automation Letters*, vol. 6, no. 2, pp. 3902–3909, 2021.
- [72] P. Lloyd, G. Pittiglio, J. H. Chandler, and P. Valdastri, “Optimal design of soft continuum magnetic robots under follow-the-leader shape forming actuation,” in *2020 International Symposium on Medical Robotics (ISMR)*, pp. 111–117, Atlanta, GA, USA, 2020.
- [73] H. B. Gilbert, D. C. Rucker, and R. J. Webster III, “Concentric tube robots: the state of the art and future directions,” *Robotics Research*, vol. 114, pp. 253–269, 2016.
- [74] J. Burgner-Kahrs, “Task-specific design of tubular continuum robots for surgical applications,” in *Soft Robotics*, pp. 222–230, Springer, Berlin, Heidelberg, 2015.
- [75] T. Anor, J. R. Madsen, and P. Dupont, “Algorithms for design of continuum robots using the concentric tubes approach: a neurosurgical example,” in *2011 IEEE international conference on robotics and automation*, pp. 667–673, Shanghai, China, 2011.

- [76] L. Wang, D. Zheng, P. Harker, A. B. Patel, C. F. Guo, and X. Zhao, "Evolutionary design of magnetic soft continuum robots," *Proceedings of the National Academy of Sciences of the United States of America*, vol. 118, no. 21, 2021.
- [77] C. Baykal and R. Alterovitz, "Asymptotically optimal design of piecewise cylindrical robots using motion planning," in *Robotics: Science and Systems*, Orlando, FL, USA, 2017.
- [78] F. Boyer and F. Renda, "Poincaré's equations for Cosserat media: application to shells," *Journal of Nonlinear Science*, vol. 27, no. 1, pp. 1–44, 2017.
- [79] F. Janabi-Sharifi, A. Jalali, and I. D. Walker, "Cosserat rod-based dynamic modeling of tendon-driven continuum robots: a tutorial," *IEEE Access*, vol. 9, pp. 68703–68719, 2021.
- [80] M. T. Chikhaoui, S. Lilge, S. Kleinschmidt, and J. Burgner-Kahrs, "Comparison of modeling approaches for a tendon actuated continuum robot with three extensible segments," *IEEE Robotics and Automation Letters*, vol. 4, no. 2, pp. 989–996, 2019.
- [81] B. A. Jones, R. L. Gray, and K. Turlapati, "Three dimensional statics for continuum robotics," in *2009 IEEE/RSJ International Conference on Intelligent Robots and Systems*, pp. 2659–2664, St. Louis, MO, USA, 2009.
- [82] A. Doroudchi and S. Berman, "Configuration tracking for soft continuum robotic arms using inverse dynamic control of a Cosserat rod model," in *2021 IEEE 4th International Conference on Soft Robotics (Robo Soft)*, pp. 207–214, New Haven, CT, USA, 2021.
- [83] C. Armanini, C. Messer, A. T. Mathew, F. Boyer, C. Duriez, and F. Renda, "Soft robots modeling: a literature unwinding," 2021, <https://arxiv.org/abs/2112.03645>.
- [84] W. McMahan, B. A. Jones, and I. D. Walker, "Design and implementation of a multi-section continuum robot: air-actor," in *2005 IEEE/RSJ International Conference on Intelligent Robots and Systems*, pp. 2578–2585, Edmonton, AB, Canada, 2005.
- [85] B. A. Jones and I. D. Walker, "Kinematics for multisection continuum robots," *IEEE Transactions on Robotics*, vol. 22, no. 1, pp. 43–55, 2006.
- [86] V. Falkenhahn, T. Mahl, A. Hildebrandt, R. Neumann, and O. Sawodny, "Dynamic modeling of constant curvature continuum robots using the Euler-Lagrange formalism," in *2014 IEEE/RSJ International Conference on Intelligent Robots and Systems*, pp. 2428–2433, Chicago, IL, USA, 2014.
- [87] P. I. Corke, "A simple and systematic approach to assigning Denavit-Hartenberg parameters," *IEEE Transactions on Robotics*, vol. 23, no. 3, pp. 590–594, 2007.
- [88] G. Arreaga, R. Capovilla, and J. Guven, "Frenet-Serret dynamics," *Classical and Quantum Gravity*, vol. 18, no. 23, pp. 5065–5083, 2001.
- [89] D. Arnal, B. Currey, and B. Dali, "Construction of canonical coordinates for exponential lie groups," *Transactions of the American Mathematical Society*, vol. 361, no. 12, pp. 6283–6348, 2009.
- [90] A. Müller, "Screw and Lie group theory in multibody dynamics," *Multibody System Dynamics*, vol. 42, no. 2, pp. 219–248, 2018.
- [91] S. Grazioso, G. D. Gironimo, and B. Siciliano, "From differential geometry of curves to helical kinematics of continuum robots using exponential mapping," in *Advances in Robot Kinematics 2018. ARK 2018*, vol. 8 of Springer Proceedings in Advanced Robotics, pp. 319–326, Springer, Cham, 2018.
- [92] R. M. Murray, Z. Li, and S. S. Sastry, *A Mathematical Introduction to Robotic Manipulation*, CRC press, 2017.
- [93] T. G. Thuruthel, E. Falotico, F. Renda, and C. Laschi, "Model-based reinforcement learning for closed-loop dynamic control of soft robotic manipulators," *IEEE Transactions on Robotics*, vol. 35, no. 1, pp. 124–134, 2018.
- [94] C. Bergeles, F. Lin, and G. Yang, "Concentric tube robot kinematics using neural networks," *Hamlyn Symposium on Medical Robotics*, vol. 6, pp. 1–2, 2015.
- [95] J. D. Ho, K. H. Lee, W. L. Tang et al., "Localized online learning-based control of a soft redundant manipulator under variable loading," *Advanced Robotics*, vol. 32, no. 21, pp. 1168–1183, 2018.
- [96] G. Wu, G. Shi, and Y. Shi, "Modeling and analysis of a parallel continuum robot using artificial neural network," in *2017 IEEE International Conference on Mechatronics (ICM)*, pp. 153–158, Churchill, VIC, Australia, 2017.
- [97] K. Chen, Y. Tzeng, G. Chen, and W. Kao, "Dynamic learning neural network," *Photogrammetric Engineering & Remote Sensing*, vol. 6, no. 4, pp. 403–408, 1995.
- [98] E. Schulz, M. Speekenbrink, and A. Krause, "A tutorial on gaussian process regression: modelling, exploring, and exploiting functions," *Journal of Mathematical Psychology*, vol. 85, pp. 1–16, 2018.
- [99] M. Dehghani and S. A. A. Moosavian, "Modeling and control of a planar continuum robot," in *2011 IEEE/ASME International Conference on Advanced Intelligent Mechatronics (AIM)*, pp. 966–971, Budapest, Hungary, 2011.
- [100] B. Ouyang, Y. Liu, H.-Y. Tam, and D. Sun, "Design of an interactive control system for a multisegment continuum robot," *IEEE/ASME Transactions on Mechatronics*, vol. 23, no. 5, pp. 2379–2389, 2018.
- [101] R. E. Goldman, A. Bajo, and N. Simaan, "Compliant motion control for continuum robots with intrinsic actuation sensing," in *2011 IEEE international conference on robotics and automation*, pp. 1126–1132, Shanghai, China, 2011.
- [102] F. Piltan and S. T. Haghighi, "Design gradient descent optimal sliding mode control of continuum robots," *IAES International Journal of Robotics and Automation*, vol. 1, no. 4, 2012.
- [103] R. E. Goldman, A. Bajo, and N. Simaan, "Compliant motion control for multisegment continuum robots with actuation force sensing," *IEEE Transactions on Robotics*, vol. 30, no. 4, pp. 890–902, 2014.
- [104] R. S. Penning, J. Jung, J. A. Borgstadt, N. J. Ferrier, and M. R. Zinn, "Towards closed loop control of a continuum robotic manipulator for medical applications," in *2011 IEEE International Conference on Robotics and Automation*, pp. 4822–4827, Shanghai, China, 2011.
- [105] G. Chen, M. T. Pham, and T. Redarce, "Sensor-based guidance control of a continuum robot for a semi-autonomous colonoscopy," *Robotics and Autonomous Systems*, vol. 57, no. 6–7, pp. 712–722, 2009.
- [106] Q. Zhao, J. Lai, K. Huang, X. Hu, and H. K. Chu, "Shape estimation and control of a soft continuum robot under external payloads," *IEEE/ASME Transactions on Mechatronics*, 2021.
- [107] J. M. Croom, D. C. Rucker, J. M. Romano, and R. J. Webster, "Visual sensing of continuum robot shape using self-

- organizing maps,” in *2010 IEEE International Conference on Robotics and Automation*, pp. 4591–4596, Anchorage, AK, USA, 2010.
- [108] S. Norouzi-Ghazbi and F. Janabi-Sharifi, “A switching image-based visual servoing method for cooperative continuum robots,” *Journal of Intelligent & Robotic Systems*, vol. 103, no. 3, 2021.
- [109] F. Campisano, S. Caló, A. A. Remirez et al., “Closed-loop control of soft continuum manipulators under tip follower actuation,” *The International Journal of Robotics Research*, vol. 40, no. 6-7, pp. 923–938, 2021.
- [110] Z. Dong, X. Wang, G. Fang et al., “Shape tracking and feedback control of cardiac catheter using MRI-guided robotic platform—validation with pulmonary vein isolation simulator in MRI,” *IEEE Transactions on Robotics*, 2022.
- [111] J. Edelmann, A. J. Petruska, and B. J. Nelson, “Magnetic control of continuum devices,” *The International Journal of Robotics Research*, vol. 36, no. 1, pp. 68–85, 2017.
- [112] S. Mbakop, G. Tagne, M.-H. Frouin, A. Melingui, and R. Merzouki, “Inverse dynamics model-based shape control of soft continuum finger robot using parametric curve,” *IEEE Robotics and Automation Letters*, vol. 6, no. 4, pp. 8053–8060, 2021.
- [113] R. Xu, A. Asadian, A. S. Naidu, and R. V. Patel, “Position control of concentric-tube continuum robots using a modified Jacobian-based approach,” in *2013 IEEE International Conference on Robotics and Automation*, pp. 5813–5818, Karlsruhe, Germany, 2013.
- [114] C. Shi, X. Luo, P. Qi et al., “Shape sensing techniques for continuum robots in minimally invasive surgery: a survey,” *IEEE Transactions on Biomedical Engineering*, vol. 64, no. 8, pp. 1665–1678, 2017.
- [115] M. N. Boushaki, C. Liu, and P. Poignet, “Task-space position control of concentric-tube robot with inaccurate kinematics using approximate Jacobian,” in *2014 IEEE International Conference on Robotics and Automation (ICRA)*, pp. 5877–5882, Hong Kong, China, 2014.
- [116] Z. Wang, T. Wang, B. Zhao et al., “Hybrid adaptive control strategy for continuum surgical robot under external load,” *IEEE Robotics and Automation Letters*, vol. 6, no. 2, pp. 1407–1414, 2021.
- [117] C. Duriez, “Control of elastic soft robots based on real-time finite element method,” in *2013 IEEE International Conference on Robotics and Automation*, pp. 3982–3987, Karlsruhe, Germany, 2013.
- [118] T. Liu, R. Jackson, D. Franson et al., “Iterative Jacobian-based inverse kinematics and open-loop control of an MRI-guided magnetically actuated steerable catheter system,” *IEEE/ASME Transactions on Mechatronics*, vol. 22, no. 4, pp. 1765–1776, 2017.
- [119] D. Bruder, X. Fu, R. B. Gillespie, C. D. Remy, and R. Vasudevan, “Data-driven control of soft robots using Koopman operator theory,” *IEEE Transactions on Robotics*, vol. 37, no. 3, pp. 948–961, 2021.
- [120] G. Fang, X. Wang, K. Wang et al., “Vision-based online learning kinematic control for soft robots using local gaussian process regression,” *IEEE Robotics and Automation Letters*, vol. 4, no. 2, pp. 1194–1201, 2019.
- [121] J. Peters and S. Schaal, “Reinforcement learning of motor skills with policy gradients,” *Neural Networks*, vol. 21, no. 4, pp. 682–697, 2008.
- [122] M. P. Deisenroth, C. E. Rasmussen, and D. Fox, “Learning to control a low-cost manipulator 739 using data-efficient reinforcement learning,” in *Robotics: Science and Systems VII*, vol. 7, pp. 57–64, Orlando, FL, USA, 2011.
- [123] S. Levine and V. Koltun, “Guided policy search,” in *International conference on machine learning*, pp. 1–9, Orlando, FL, USA, 2013.
- [124] S. Levine and P. Abbeel, “Learning neural network policies with guided policy search under unknown dynamics,” *Advances in Neural Information Processing Systems*, vol. 27, 2014.
- [125] I. Mordatch and E. Todorov, “Combining the benefits of function approximation and trajectory optimization,” in *Robotics: Science and Systems X*, vol. 4, Orlando, FL, USA, 2014.
- [126] V. Kumar, E. Todorov, and S. Levine, “Optimal control with learned local models: Application to dexterous manipulation,” in *2016 IEEE International Conference on Robotics and Automation (ICRA)*, pp. 378–383, Stockholm, Sweden, 2016.
- [127] W. Han, S. Levine, and P. Abbeel, “Learning compound multi-step controllers under unknown dynamics,” in *2015 IEEE/RSJ International Conference on Intelligent Robots and Systems (IROS)*, pp. 6435–6442, Hamburg, Germany, 2015.
- [128] T. Zhang, G. Kahn, S. Levine, and P. Abbeel, “Learning deep control policies for autonomous aerial vehicles with MPC-guided policy search,” in *2016 IEEE International Conference on Robotics and Automation (ICRA)*, pp. 528–535, Stockholm, Sweden, 2016.
- [129] I. Abraham and T. D. Murphey, “Active learning of dynamics for data-driven control using Koopman operators,” *IEEE Transactions on Robotics*, vol. 35, no. 5, pp. 1071–1083, 2019.
- [130] I. Abraham, G. De La Torre, and T. D. Murphey, “Model-based control using Koopman operators,” 2017, <https://arxiv.org/abs/1709.01568>.
- [131] M. Korda and I. Mezić, “Linear predictors for nonlinear dynamical systems: Koopman operator meets model predictive control,” *Automatica*, vol. 93, pp. 149–160, 2018.